Synthesis and Investigation of Low Valent Transition Metal Nitrides as Electrocatalysts for the Hydrogen Evolution Reaction

Youyi Sun

Submitted in fulfilment of the requirements of the Degree of Doctor of philosophy

School of Chemistry

College of Science and Engineering

September 2022

Abstract

With the help of renewable electricity, a device called electrolyser can split water into main components: O_2 and H_2. Hydrogen is a good fuel and can be used on demand in a range of energy applications as well as feedstock for chemicals. The hydrogen evolution reaction from water is commonly assisted by Pt-group metal electrocatalysts. The high cost of Pt-group metals makes the search for cheaper alternatives important. The presented work aims to assess the suitability of low valent transition metal nitrides as electrocatalysts for the hydrogen evolution reaction (HER) and compare their performance with transition metal alloys.

After brief introduction and experimental sections, the synthesis, crystal structure and electronic properties of two common ordered Co-Mo intermetallics (Co_3Mo and Co_7Mo_6) are discussed. These were tested in both acidic and alkaline conditions to have a reliable benchmark for comparison with metal nitrides. Despite relatively good electrocatalytic performance the stability of the intermetallic was found limited which is consistent with previous literature reports.

The following chapter is focused on comparison of three isostructural ternary nitrides (Co_3Mo_3N, Fe_3Mo_3N and Co_6Mo_6N) which crystallize in the η-carbide structure type. As the focus is given to the comparative investigation a great care was given to isolate them as phase pure materials which was confirmed by Rietveld refinement of PXRD data. The synthesis was carried out by reduction of the relevant metal oxides in H_2/N_2 gas mixtures while Co_6Mo_6N was prepared through topotactic reaction from Co_3Mo_3N in H_2/Ar gas mixture. Co_3Mo_3N delivered a relatively low overpotential of just 108 mV at 10 mA cm^{-2} while it also showed high current densities when immobilised on Ni-foam substrate. The stability of the nitride was excellent as was evidenced by chronoamperometric studies. Remarkably, Co_6Mo_6N showed a similar electrocatalytic properties with slightly higher overpotential but poor electrochemical stability. Hence, the initial hypothesis that the introduction of N atoms within the lattice could lead to higher stability was confirmed. Replacing Co for Fe into isostructural Fe_3Mo_3N on the other hand led to deteriorated performance suggesting that Co sites are catalytically active. This observation was also supported by computational DFT studies presented in this work. Overall, it was shown that low valent nitrides are probably superior catalyst than similar metal alloys.

To study the effect of Mo substitution a previously unreported nitride with a composition Co_6W_6N was isolated. The additional use of urea precursor along with H_2/N_2 was required with elemental analysis unambiguously pointing out that the resulting compound was pure nitride

as no traces of carbon were found. In comparison, isostructural Fe_6W_6N showed poor electrochemical performance confirming that the Co-sites are probably responsible for catalytic activity in these low valent nitrides.

To pursue the hypothesis about crucial role of late transition metals play in catalytic performance Co_2Mo_3N and the isostructural solid solutions with the compositions $Ni_{2-x}Fe_xMo_3N$ (x= 0 – 1.25) were investigated. The substitution of Ni for Fe led to a deterioration in the performance further suggesting that d^8/d^9 metals are essential for good electrocatalytic properties. An additional XPS investigation suggested that preserving low oxidation state of the metals is important. As Co_2Mo_3N showed higher overpotential than Co_3Mo_3N at a benchmark current density this suggested that higher number of d^8/d^9 transition metals per formula unit could be a way forward for improving the catalytic properties.

To test the hypothesis that increased number of late transition metal per formula unit would lead to improved catalytic activity several ternary nitrides with anti-perovskite structure were synthesised, including Co_3SnN, Fe_3SnN, Co_3ZnN and Co_3InN. These were prepared with the help of melamine as a nitrogen source and were found phase pure according to the Rietveld refinement of the PXRD data. The nitrides showed poor stability in acidic electrolyte but demonstrated a good stability in alkaline conditions. Among these nitrides, despite relatively higher number of Co atoms per formula unit, the lowest overpotential of 128 mV was achieved on Co_3InN. However, this was higher than that of 108 mV demonstrated by Co_3Mo_3N at a benchmark current density of 10 mA cm^{-2}. From this perspective it was not possible to determine whether increasing the number of late-transition metal sites could lead to an improved catalytic performance.

Overall, the results pointed out that ternary low valent transition metal nitrides are promising targets for application in electrocatalytic water splitting. Ni_2Mo_3N was identified as the most cost-effective material due to a relative simplicity of immobilizing it on a high surface area nickel foam substrate. This creates future opportunities for further research that could lead to an implementation of nitrides in proton exchange electrolysers.

Acknowledgements

Most of all, I would like to express my genuine gratitude to Dr. Alexey Ganin for his guidance and support. I could not have expected for a better supervisor, and I appreciate everything you have done for me. Your passion for work, enthusiasm and friendship for your students made me feel happy to work with you. I still remember the first day when I met you in the university and you helped me to register and pick up my student card. I will greatly miss working with you.

I would also like to thank the wonderful collaborators throughout the course of my PhD. In particular, Mr. James Gallagher, a very friendly Scottish person, who trained and helped me obtain the SEM and EDX measurements in his lab. Every time we were talking, I felt incredibly welcomed to Scotland. Also, Dr Mark Symes and Abdulhai Faqeeh for their help to characterize my materials in flow cell toward HER. Additionally, many thanks for Angela Daisley and Professor Justin Hargreaves, for helping me synthesize some nitrides via ammonia gas. Finally, I'd like to thank Dr. David MacDonald and Jingyi Zhang for their help to measure my samples for SEM images.

I'm extremely grateful to the members of the Ganin group, past and present, who have made my time in C2-02 and C5-21 such an enjoyable experience. So, thanks to Jessica, James, Liudvika, Yuanshen, Santhosh and Weihao Li for your friendship and support.

I'd like to thank Odysseas Dimitrios Keramidas for showing me how to make Pizza, going for hotpot, hiking and playing videogames together. Also thank my friend Bradly Wilson (王瑞博) for the refinement of my writing and spending time to try to make dumplings with me.

Of course, I'm grateful for the support and encouragement I've received from my parents and my little brother over the years as I wouldn't have got where I am today without it. I'd like to thank them for talking through video during the hard times of Covid-19.

Lastly, I'd like to thank my friends, in particular Tianxue Cheng (陈天雪) for his encouragement over last 4 years. Also many thank for Xian Zhou (周详) for his time playing league of legends (LOL) with me, carry me every time and let my account from silver to gold level.

Abbreviations

HER	Hydrogen Evolution Reaction
ECSA	Electrochemical Active Surface Area
CV	Cyclic Voltammetry
LSV	Linear Sweep Voltammetry
R_{CT}	Charge Transfer Resistance
DFT	Density Functional Theory
C_{dl}	Double Layer Capacitance
EIS	Electrochemical Impedance Spectroscopy
OVP	Overpotential
PXRD	Powder X-ray diffraction
SEM	Scanning Electron Microscopy
EDX	Energy Dispersive X-Ray Spectroscopy
BET	Brunauer-Emmet-Teller
GC	Gas Chromatography
XPS	X-Ray Photoelectron Spectroscopy
ICSD	Inorganic Crystal Structure Database
DOS	Density of States
rGO	Reduced graphene oxide
DMF	N,N-Dimethylformamide
PBE	Perdew–Burke–Ernzerhof

Thesis Contribution

Some of the work details in this thesis was performed in collaboration with others. Listed below are the details of collaboration.

• The DFT experiments were designed and carried out by Lewen Wang, Yecheng Zhou and Núria López at Sun Yat-Sen University in China and Institute of Chemical Research of Catalonia in Spain.

• The XPS was carried out and analysed by Olga Guselnikova and Oleg Semyonov at Tomsk Polytechnic University in Russia.

• Some SEM images were measured by James Fraser and Jingyi Zhang at Glasgow University.

Author's Declaration

I declare that, except where explicit reference is made to the contribution of others, that this dissertation is the result of my own work and has not been submitted for any other degree at the university of Glasgow or any other institution.

Printed name: Youyi Sun

Signature:

Publications and Conferences

The following manuscripts were published as a result of work undertaken over the course of this PhD:

Youyi Sun, Lewen Wang, Olga Guselnikova, Oleg Semyonov, James Fraser, Yecheng Zhou, Nuria Lopez and Alexey Y. Ganin, *J. Mater. Chem. A*, 2022, 10, 855.

Youyi Sun and Alexey Y. Ganin, *Hydrogen* **2020**, *1*(1), 11-21.

The following conference were attended over the course of this PhD:

University of Scotland Inorganic Conference 2019 (Glasgow, UK) – Poster Presentation.

H2FC Supergen Research Conference 2022 (University of St Andrews, UK) – Poster Presentation.

Table of Contents

Chapter 1. Introduction

Fossil fuels such as oil, coal and natural gas (that the world currently uses as prime sources of energy) emit CO_2 and thus, are main contributors to global warming.[1] The increase of the carbon dioxide content in the atmosphere is believed the main cause of the climate change, resulting in a significant change in typical weather patterns. In addition, fossil fuels are not renewable and in limited supply. They are key to production of plastics and high-value chemical products. Therefore, it is impractical to burn them as fuels. Alternative energy vectors, which can support a growing quality of life but also become scalable with growing population, are required.[2,3]

1.1. Major renewable energy systems

Photovoltaics (PVs or solar cells), solar thermal (electric and thermal), wind, biomass (plants and trees), hydroelectric, ocean and geothermal are major systems to supply renewable energy. Due to rapidly increasing prices for fossil fuels, electricity generated by solar cells and wind turbines has become cost-comparative with the traditional electricity generation from fossil fuels. The main drawback of wind / solar energy generation is that they are weather dependent. Back-up solution from gas or coal powered electricity power plants are required when sun does not shine and wind does not blow.

1.2 Hydrogen use

Energy vectors that can be used to store the excess renewable energy when there is little demand from consumers or industry are a practical way to eliminate the fossil fuel from renewable energy generation. Hydrogen, compressed gas and batteries are three emerging and complementary technologies that can be used in the future. Among this storing electricity as hydrogen fuel is particularly attractive. H_2 can be converted to electrical energy via a fuel cell and the only waste product is water.[4] Furthermore, it can be utilized not only as energy carrier but also as industrial feedstock, for example in production of fertilizers. Hydrogen can be used in transportation to substitute fossil fuel when sustainable energy is not available.

Currently, commercial hydrogen is most generated through the steam reforming of natural gas, as shown in Equation 1.[5] To increase the hydrogen yield, the reforming the CO product further with water vapour can be achieved as shown in Equation 2:

$$CH_4 + H_2O \rightarrow CO + 3H_2 \qquad (1)$$

$$CO + H_2O \leftrightarrow CO_2 + H_2 \quad (2)$$

However, CO_2 is produced during these processes making hydrogen not particularly green. As shown in Figure 1-1 there are a range of options to create green hydrogen using renewable electricity and solar energy. Among these technologies, water electrolysis (in a device called electrolyser) is probably the most reliable and practical way of generating hydrogen.

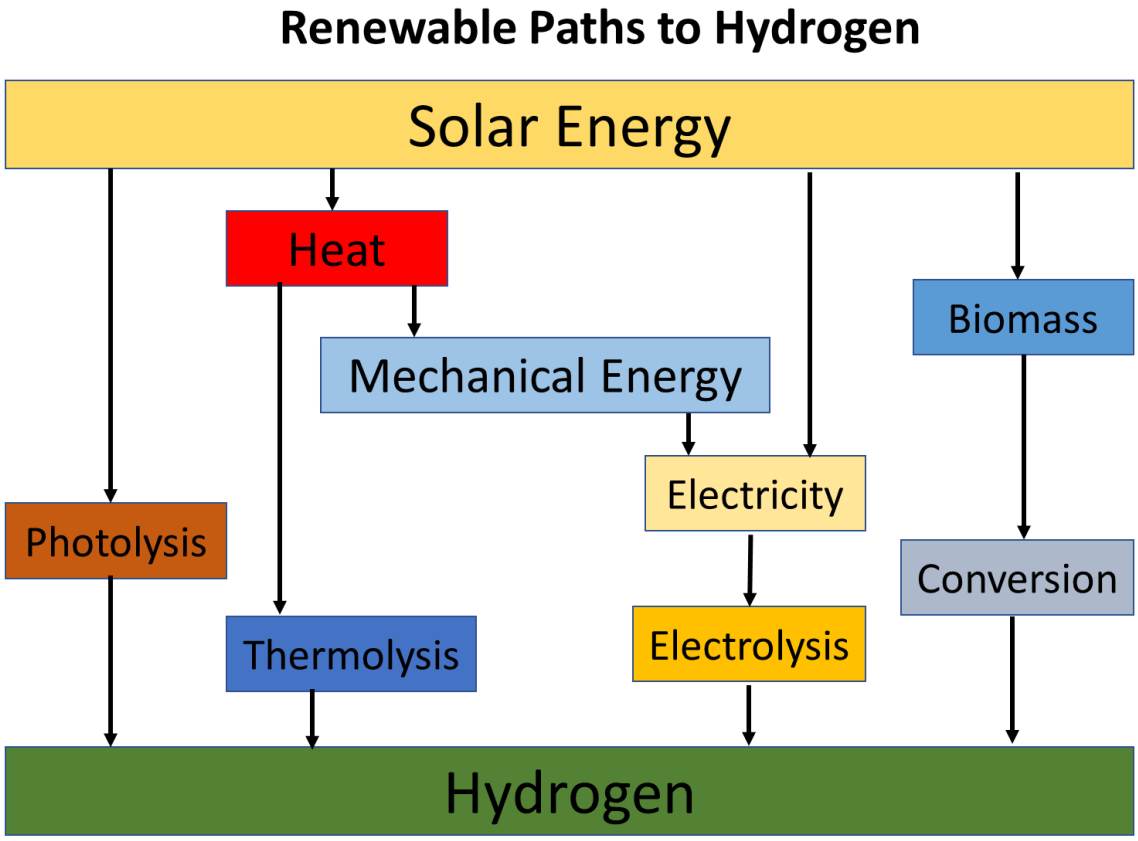

Figure 1-1: Renewable pathways from solar power to hydrogen.

1.3. Water electrolysis

Water electrolysis industrially is carried out at the proton exchange membrane which imposes highly acidic conditions. Therefore, the electrochemical processes could be presented through some relatively simple equations:

Cathode reaction: $4H^+ + 4e^- \rightarrow 2H_2$ $\quad E^0_{cathode} = 0.00\,V$ (3)

Anode reaction: $2H_2O \rightarrow O_2 + 4H^+ + 4e^-$ $\quad E^0_{anode} = -1.23\,V$ (4)

Overall reaction: $2H_2O \rightarrow 2H_2 + O_2$ $\quad E^0_{cell} = -1.23\,V$ (5)

Electricity is applied to split water into hydrogen and oxygen gas, the reactions of water electrolysis as shown in Figure 1-2.

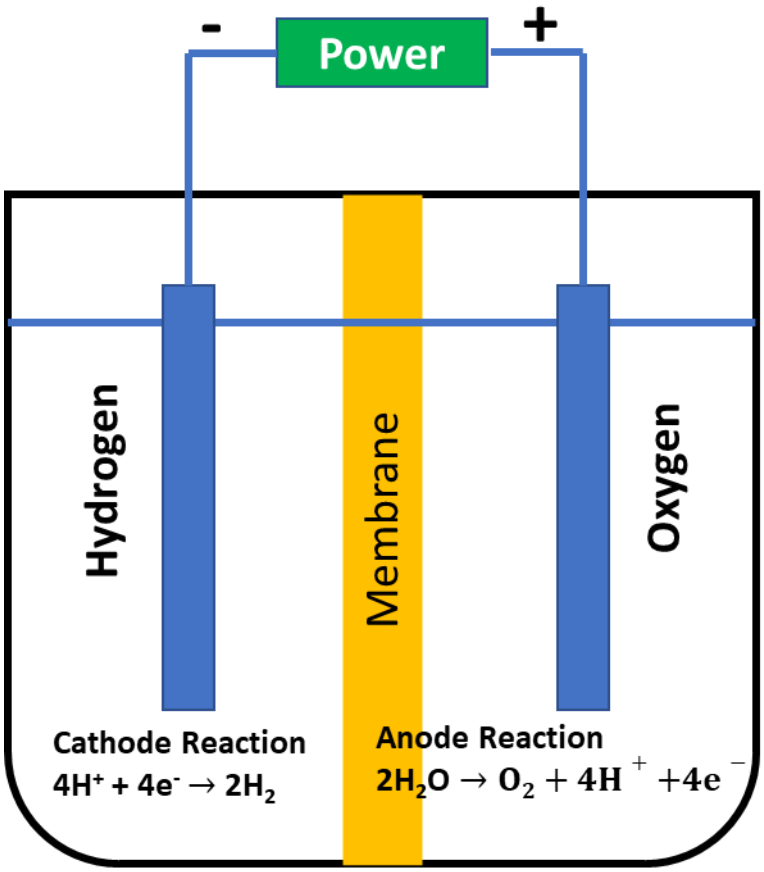

Figure 1-2: General water electrolysis setup. The left hand side illustrates hydrogen evolution at the cathode, while the right hand side shows water oxidation at the anode.

Oxygen production takes place at the anode (Equation 3), this reaction is known as the oxygen evolution reaction (OER). Then the protons pass through the membrane towards the cathode to form hydrogen (Equation 4), known as the hydrogen evolution reaction (HER). The overall process is shown in Equation 5.

The production of hydrogen by electrolysis only accounts for about 5% of the world's hydrogen supply, as it is more cost demanding comparing to steam reforming of fossil fuels.[6] The electrolysis could also be carried in alkaline conditions. However, alkaline electrolysers (AEL) have long start up times making it very difficult for integration with renewable energy sources.[7] As mentioned above, proton-exchange membrane electrolysers (PEM) are more versatile, compact and thus, easier to operate in tandem with wind turbine or solar cells. With the PEM offering load-flexibility and short start-up times, it is important to reduce the cost of PEM to make it in a large-scale hydrogen production. As will be discussed below the PEM electrolyser requires substantial amount of Pt that contributes to the cost of PEM equipment.[8] Finding cheap, earth-abundant alternatives to Pt is the key to future integration of PEM into renewable energy networks and research in this thesis focus on this aspect.

1.4. Thermodynamics

Water electrolysis is not a spontaneous process, which is demonstrated by a positive Gibbs free energy value of $\Delta G^0 = +237.23\ kJ\ mol^{-1}$, as calculated by Equation 6.[9]

$$\Delta G^0 = \Delta H^0 - T\Delta S^0 = -zFE^0_{cell} \quad (6)$$

Where ΔG^0 is the difference in Gibbs free energy, ΔH^0 is the difference in enthalpy (285.8 kJ mol^{-1}), ΔS^0 is the difference in entropy (163 J K^{-1} mol^{-1}), T is the temperature (K), z is the stoichiometric number of moles of electrons involved in the reaction, F is the Faraday constant (96485 C mol^{-1}) and E^0_{cell} is the cell potential.

The minimum potential required for the overall reaction is governed by the conditions within the electrolyser equipment, like temperature and pH value. For example, the potential of 1.48 V is required when temperature is 0 K, while at room temperature, the minimum potential is lowered to 1.23 V. Therefore, the splitting of water is easier to take place with increasing temperature.

Similarly, pH also has a profound effect on the required potential. In accordance with shifting away from standard conditions, the Nernst equation can be written as Equation 7. Then, the potential under non-standard conditions is defined as the Equation 8.

$$G = \Delta G^0 + RTlnQ \quad (7)$$

$$E = E^0 - \frac{RT}{zF} lnQ \quad (8)$$

Where R is the gas constant, T is the absolute temperature and Q is the reaction quotient. Q is defined as the ratio of activities of the oxidant and reductant species. Therefore, the effect of pH can be investigated by setting Q equal to the concentration of protons, $[H^+]$, and converting the natural log to $\log_{10}$. At standard temperature, the equation can be rewritten into the following (Equation 9):

$$E = E^0 - \frac{0.059}{z} log\,[H^+] = E^0 - \frac{0.059}{z} pH \quad (9)$$

Accordingly, the potential will shift by 0.059 V for every 1 pH unit change. Therefore, the potentials required for HER at varying pH values can be written as Equation 10.

$$E = 0.00 - 0.059\,pH \quad (10)$$

1.5. Hydrogen Evolution Reaction Electrocatalysts

1.5.1. Background

PEM electrolysis, as mentioned in Section 1.3. is the most promising electrolytic method for generation of hydrogen due to its high-energy efficiencies. It allows to produce pure hydrogen (about 99.999 vol %) at high-pressures which again simplifies the integration with renewable energy sources as no need for post-purification is required.[10–12] As mentioned in Section 1.4, the potential required for water splitting is 1.23 V is theoretical. However, in practice, this potential is governed by the nature of the electrode material. Depending on the material used an extra voltage needs to be applied which is known as the overpotential. The overpotential is

the difference between the experimentally observed potential and the thermodynamically required potential. This requirement could be reduced close to zero if optimal electrocatalysts are used.

1.5.2. Electrocatalysts for Hydrogen Evolution Reaction (HER)

As shown in Figure 1-3 the most effective metal catalysts in the field for HER electrocatalysis are noble metals, such as platinum, ruthenium, rhodium and iridium. Non-noble metals usually deliver a poor performance for driving hydrogen evolution.

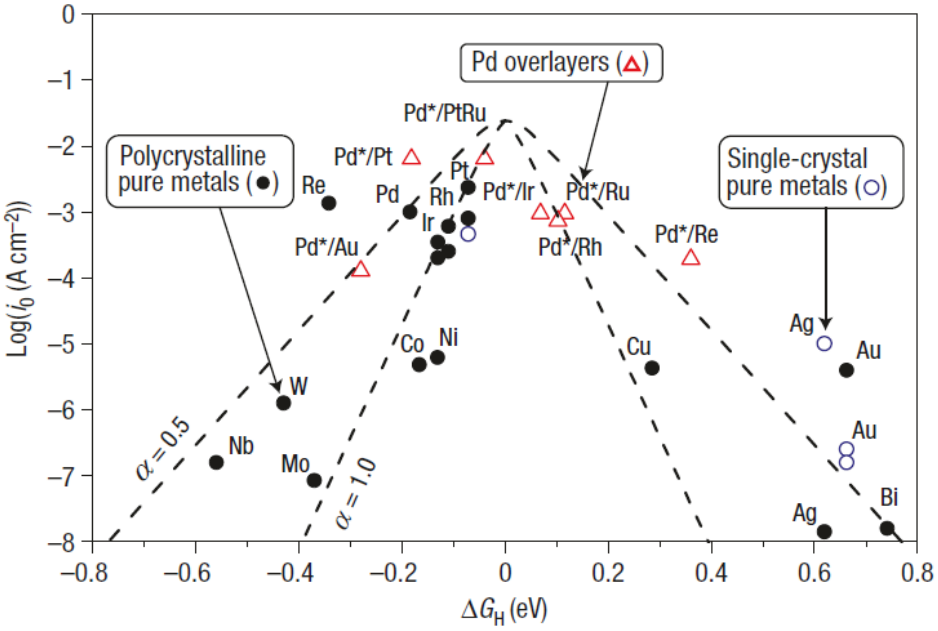

Figure 1-3: Previous experimental values of exchange current for the electrolytic evolution of hydrogen on various metals, all data have been collected from over 40 years of publications. The ΔG_H values are calculated by Jeff *et al.*[13]

The price of noble metals metal has increased in last 20 years, and the trend of this increasing price is set to continue over the coming years.[14] Hydrogen generation via electrolyser technologies containing these precious metals will also have a corresponding price increase.

Given the aim of reducing the cost of hydrogen generation through PEM electrolysis, some attempts were carried out to produce non-precious metal-based catalyst to replace noble metals for efficient hydrogen production. For a good hydrogen-producing electrocatalyst, some effective catalytic properties are required, such as high electronic conductivity, a large number of electrocatalytically active sites and good surface structure. Thus, an electrocatalytic

materials toward the HER must be (i) active, (ii) cheap and (iii) stable[15] to design a viable electrocatalyst, these factors should be considered.

The combination of non-noble metals with other elements as substitute electrocatalysts may be beneficial towards the effectiveness of the HER.[16] Based on these finding, it was determined that transition metals could provide a favourable alternative, owing to their relative abundance in nature, low cost, stability and reportedly corresponding low overpotentials. For example, Co, Ni and their alloys have been identified as the most efficient catalytic materials for the replacement of noble metals catalysts.[17–22] Nevertheless, whilst their alloys are capable of operating in alkaline mediums, the same success is not reflected when facilitating hydrogen gas formation in acidic media (required for PEM electrolysis), where, in spite of high production rates and low energy consumption, the poor corrosion stability of metal or their alloys presents a considerable challenge within the reaction system.[23]

Extending on from the limited success of non-noble metals alloys, multiple research groups have devised a variety of non-noble metal compounds that permit the HER to take place at relatively low overpotentials, such as transition metal selenides,[24–26] nitrides,[27–29] and carbides.[30–33] These noble-metal free catalysts display shared properties that could see them potentially replace platinum-based materials and metal-based alloys. Such as resistance to corrosion in acidic and alkaline environments, high stabilities, high melting points and mechanical strength. Out of these candidates, transition metal nitrides stand out for their remarkable catalytic activities and durability as alternative catalysts in the wider field of electrocatalysis, where some of reports have already obtained a comparable result to noble metals catalysts.[27] This is attributed to the presence of non-metal atoms within the metal lattice, which appears to promote distinctive electronic assemblies within the host lattice structures.[27]

In the family of transition metal nitrides (although there exist a number of different structure types which interstitial nitrides can adopt) two of the most significant are the η-carbide and filled β-manganese phases. The crystal structure of η-carbides (often as found an impurity in steels) has been known for a long time.[34–36] Using the Fe_3Mo_3N as an example, its structure can be described by two diamondoid subunits as shown in Figure 1-4.

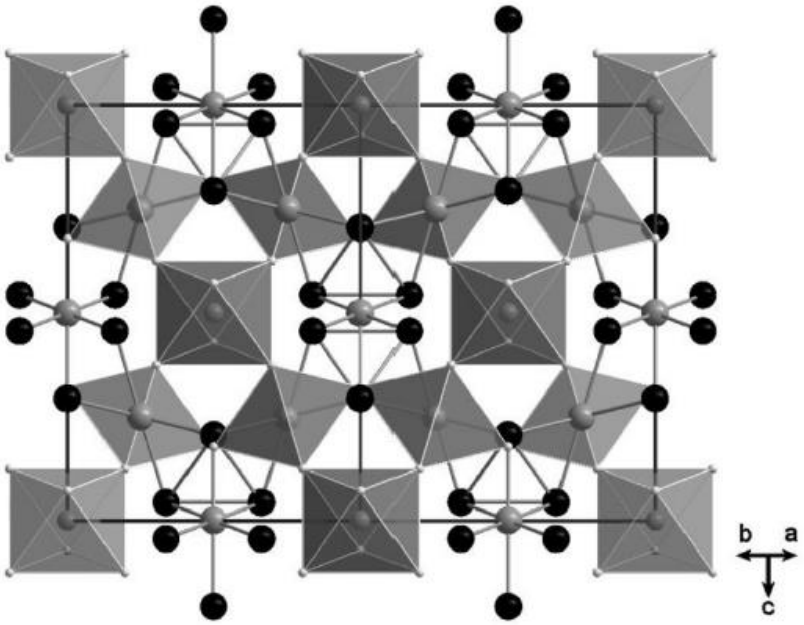

Figure 1-4: Relationship between the two diamondoid nets of the η-carbide structure. The corner-sharing Mo_6N octahedra fill the space in the Fe supertetrahedra net. (Colours: Fe 32*e* black; Fe16*d* grey; Mo_6N octahedral grey).[37]

The first of these units comprises tetrahedra of iron atoms on the 32*e* site. The tetrahedra are capped over each face by the iron atoms of the 16*d* site, forming supertetrahedra. These supertetrahedra share corners to form a diamondoid net. The second subunit consist of corner-sharing Mo_6N octahedra, forming clusters which are orientated into a second diamond net. The nitrogen atoms fill the octahedral holes of the η-carbide structure. However, it is not essential for stability that all of octahedral holes are filled. The composition with less nitrogen is known, such as the η-carbide structure Co_3Mo_3N and Co_6Mo_6N are known and conversion between two phases is workable.[38]

An array of metal atoms could form certain interstitial compounds which are similar to that in β-Mn.[39] Using the example of Ni_2Mo_3N, the structure can also be described as two sub-units. The nickel atoms lie on the positions of 8*c* Wyckoff in space group $P4_132$, forming a (10,3)-a network of atoms as shown in Figure 1-5. The space within the network of nickel atoms is filled with a net of corner-sharing Mo_6N octahedra. All the octahedral holes within the structure at the 4*a* Wyckoff positions are occupied by nitrogen atoms.

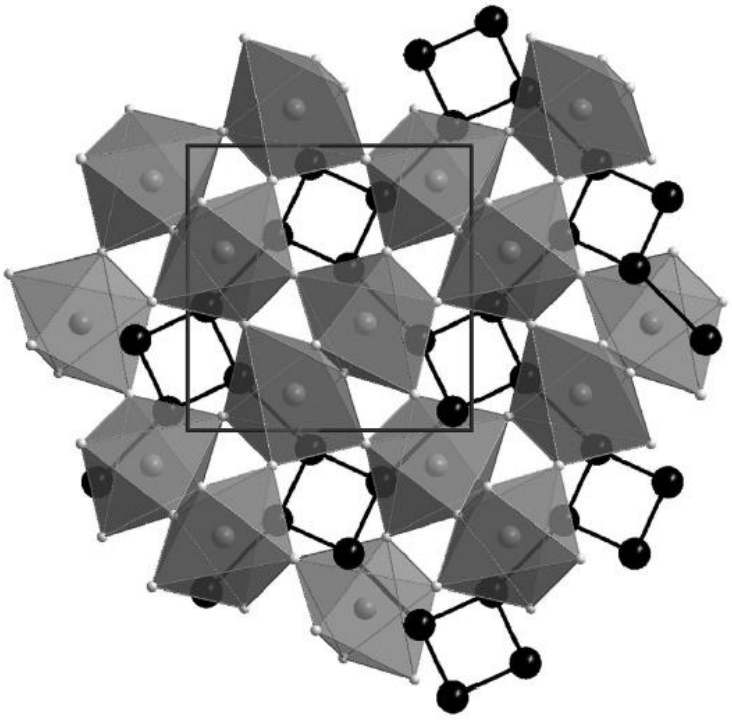

Figure 1-5: The filled β-Mn structure (Ni_2Mo_3N). Nickel atoms (black) adopt a (10,3)-a network; Mo_6N octahedra (grey) occupy the space in this network.[37]

1.5.3. Transition metal nitrides for Hydrogen Evolution reaction

The synthesis method plays a major role in producing the transition metal nitrides with desired high surface area and composition. These synthetic conditions are affected by the nature of chemical precursor, reaction temperature, the heating rate and time duration. The commonly methods of synthesis transition metal nitrides are listed in below Table 1-1.

Table1-1: Two common methods for synthesis of metal nitrides.

Methods	Nitrogen source	Precursor	Ref
1, The temperature programmed reaction	Ammonia gas, N_2/H_2 gas mixture, or urea	Metals, metal oxides, metal halides and organometallic	[40–42]
2, Urea glass route	urea	Metal-ortho-ester mixture	[43–45]

Transition metals nitrides are commonly prepared by heating metal precursors (like metals, metal oxides, metal halides and organometallic compounds) in NH_3 or N_2/H_2 gas mixture flow at high temperature. In addition, using urea up-stream of the tube furnace also can be utilized as nitrogen source to synthesise nitrides.[40–42]

The urea used as the nitrogen source to synthesise metal nitrides. Firstly, the metal precursor synthesised by dissolving one of the abovementioned chemicals into ethanol to form a metal-ortho-ester mixture. Then the urea power is added at various molar ratios and mixture into a gel-like metal/urea precursor under a continue magnetic stirrer. The resulting precursor is collected in the crucible and heated at high temperature under an N_2 or Ar gas atmosphere.

1.5.4. Transition metals nitrides as HER electrocatalysts

Cobalt and nickel based nitride materials can surpass noble metal electrocatalysts for driving HER and studied by many researchers comparing iron-based nitride. Low overpotential usually could be observed from cobalt and nickel based bimetallic or ternary nitrides. Xing *et al.*[28] developed a Ni_3N thin film by direct nitridation of Ni foam under an NH_3 atmosphere. In this approach, the Ni foam played a dual role as substrate and Ni source. The obtained Ni_3N thin film delivered high HER activity with an overpotential of 121 mV at 10 mA cm^{-2} in alkaline solution. Lai *et al.* [46] synthesized NiCoN/C by a two-step process of chemical etching with nickel nitrate in a zeolitic–imidazolate framework, followed by nitridation. The prepared NiCoN/C electrocatalysts exhibited high HER activity with an overpotential of 142 mV at 20 mA cm^{-2} in alkaline solution. Moreover, some ternary nitrides deposited on nickel form or carbon or mixed with other compound to form a composited catalytic materials could achieved overpotential of less than 100 mV at j = -10 mA cm^{-2}, such as Mo-doped Ni_3FeN/Ni form,[47] Ni_{foam}@Ni-$Ni_{0.2}Mo_{0.8}N$,[48] Cr-Co_4N,[49] Co-NiMoN-400,[50] Ni_4N/Cu_3N nanotube,[51]

Ni_3FeN/r-GO-20.[52] Those composited materials usually own a high electrochemically active surface area and low charge transfer resistance.

The family of tungsten and molybdenum-based materials has attracted much attention in electrocatalytic applications. tungsten and molybdenum nitrides of compositions WN, W_2N, MoN or Mo_2N could deliver a reasonable performance of electrocatalysts for HER.[18,53–55] However, their catalytic activity could be enhanced by adding Co or Ni metals to form composition; such as the overpotential of WN/Co was 76 mV at 10 mA cm^{-2}, lower than WN (332 mV).[53] The authors assumed this improvement was considered from contribution from synergetic effect between the components and a large number of electrocatalytically active surface sites. Similarly, the overpotential observed on $Co_{0.6}Mo_{1.4}N_2$ composition also lower than MoN.[56] In addition, an improved performance also could be received by immobilized the tungsten and molybdenum nitrides on substrate. Shi *et al.* fabricated WN nanorods on carbon cloth (WN/CC) by hydrothermal synthesis of precursor (WO_3 nanorods/CC) followed by nitridation with NH_3 gas at 600 °C for 2 h. When employed as an advanced electrocatalyst for HER in acidic conditions, the WN/CC exhibited good HER activity with an overpotential of 198 mV at 10 mA cm^{-2}, and excellent stability (maintaining its initial activity for approximately 60 h).[57] Yan *et al.* synthesized P-incorporated WN/GO (P–WN/rGO) from an $H_3[PO_4(W_3O_9)_4]$ precursor, thereby developing an efficient and low-cost electrocatalyst for HER. The P atoms synergistically interacted with rGO and WN, achieving a low overpotential (85 mV at 10 mA cm^{-2}). Zhu *et al.* [58] constructed nano-octahedrons of MoN–N doped C (MoN–NC) from a metal–organic framework by a controlled calcination approach. The obtained composite delivered excellent electrocatalytic performance, with an overpotential of only 62 mV at 10 mA cm^{-2}.

Recently, researchers have proposed various Fe-based electrocatalysts with high electrical conductivity and rapid electron transfer. As electrocatalytic HER materials, iron nitrides are superior to noble metals owing to their high chemical stability, high melting points, good wear resistance, and high electrical conductivity. The nitridation of iron sources yield various iron nitrides with different phases, such as Fe_2N, Fe_3N, Fe_4N, and $Fe_{16}N_2$. However, most pure iron nitrides deliver a higher overpotential. Zhang *et al.*[59] synthesised Fe_2N/N-doped reduced graphene oxide (rGO) composite by a two-step process of sol-gel followed by NH_3 nitridation. The fabricated Fe_2N/N-doped rGO composite showed excellent HER activity comparing to pure Fe_2N. In addition, Ojha et al.[60] fabricated a composite nitride system (FeN_x/Mo_2N/carbon nanotubes) by reacting Fe and Mo-nitrates as the Fe and Mo sources,

respectively, with melamine as the nitrogen source. The mixed metal precursors and nitrogen sources were heat-treated at 600 °C under an Ar atmosphere for 10 h. The carbon nanotubes, formed together with FeN*x*/Mo_2N during the nitridation process. The FeN_x/Mo_2N delivered an enhanced HER performance.

Thus far, we found that those nitrides that had delivered reasonably good catalytic performance for HER were generally synthesized with poorly defined crystal structure and compositions. Many investigated nitride catalysts contained impurity phases and/or were composite materials, with for example, high surface area metal-foam or carbon cloth as shown in Table 1-2.

Table 1-2: Electrochemical properties of selected transition metal nitrides for HER in acidic media.

Reported material description	η, mV at 10 mA cm^{-2}	ECSA, mF cm^{-2}	Catalyst loading, mg/cm^2	Ref.
$NiMoN_x$ / C nanosheet	220 (0.1M $HClO_4$) @5 mA cm^{-2}	N/A	0.25	[61]
$Co_{0.6}Mo_{1.4}N_2$	200 (0.1M $HClO_4$)	N/A	0.24	[62]
Co_3Mo_3N	<400 (0.1M $HClO_4$) @5 mA cm^{-2}	N/A	N/A	[62]
W-doped MoN	129 (0.5M H_2SO_4)	N/A	0.4	[63]
Pt-TiN NTAs	71 (0.5M H_2SO_4)	67.9	N/A	[64]
Ru-VN	134 (0.5M H_2SO_4)	N/A	N/A	[65]
Co/WN	208 (0.5M H_2SO_4)	308	N/A	[66]
P-MoP/Mo_2N	89 (0.5M H_2SO_4)	N/A	N/A	[67]
MoS_2/Mo_3N_2 hybrid	196 (0.5M H_2SO_4)	14.15	N/A	[68]
Co_3ZnC/Co-NCCP	–0.188 V (1 M KOH)@10 mA cm^{-2}	10.4	0.21	[69]
Mo-doped Ni_3FeN/Ni form	–0.069 V (1 M KOH)@10 mA cm^{-2}	38.06	N/A	[47]
Ni_3FeN-NPs	-0.158 (1 M KOH)	N/A	0.35	[70]
Cr-Co_4N	-0.021(1M KOH)	138	3.5	[49]
Ni_{foam}@Ni-$Ni_{0.2}Mo_{0.8}N$	-0.015 (1M KOH) @10 mA cm^{-2}	2.93	0.28	[48]
Mo_2N/CeO_2@NF	-0.026 (1M KOH) @10 mA cm^{-2}	80	N/A	[71]
NiMoN	-0.109(1M KOH) @10 mA cm^{-2}	21	2.5	[72]
Ni_3N	-0.208(1M KOH) @10 mA cm^{-2}	5.8	2.5	[72]
MoON	-0.146(1M KOH) @10 mA cm^{-2}	2.0	2.5	[72]
MoN_x/NF	-0.125(0.1M KOH) @10 mA cm^{-2}	12.4	N/A	[54]
Mo-C/N@MoS_2	-0.117(1M KOH) @10 mA cm^{-2}	9.03	N/A	[73]
$CoFeN_x$	-0.200(1M KOH) @10 mA cm^{-2}	26.57	N/A	[74]
Co_3N	-0.230(1M KOH) @10 mA cm^{-2}	N/A	N/A	[75]
$Co_{3.2}Fe_{0.8}N$/MNC-100	-0.523(1M KOH) @10 mA cm^{-2}	60.24	0.25	[50]
Co-NiMoN-400	-0.045(1M KOH) @10 mA cm^{-2}	14.86	3.5	[50]
NiMoN-400	-0.090(1M KOH) @10 mA cm^{-2}	10.46	3.5	[50]
Ni_4N/Cu_3N nanotube	-0.098(1M KOH) @10 mA cm^{-2}	186.5	1.8	[51]
Co1Ni1N	-0.1445(1M KOH) @10 mA cm^{-2}	15.02	N/A	[76]
Co2Ni1N	-0.1026(1M KOH) @10 mA cm^{-2}	19.16	N/A	[76]
Co1Ni2N	-0.183.3(1M KOH) @10 mA cm^{-2}	13.89	N/A	[76]
Co-N/GF-900	-0.165(1M KOH) @10 mA cm^{-2}	41.6	N/A	[77]
Ni_3FeN/CC	-0.105(1M KOH) @10 mA cm^{-2}	52.55	0.5	[78]
Ni_3FeN/r-GO-20	-0.094(1M KOH) @10 mA cm^{-2}	15.9	0.5	[79]

This makes the understanding the intrinsic catalyst's performance a complex task due to multiphase nature of samples. On the other hand, the electrochemical tests on materials that are free from substrates and secondary phases can provide a robust benchmark for comparison between existing and development of future nitride materials. However, despite being detrimental (especially when it comes to multicomponent systems), the studies of phase-pure, free-standing nitrides are rare[61,62]and attempts to decouple the role of confounding factors (such as impurities and substrates) from the intrinsic catalyst's performance are urgently needed.

Since phase pure ternary transition metals nitrides could be synthesised in particular the η-carbide, filled β-manganese or anti-perovskite structures[61,80–82] there are opportunities to understand properly whether these nitrides are suitable electrocatalysts. Understanding the role chemical composition plays would provide a way for predictive research which could lead to better understanding how good HER catalysts could be made.

1.6 Aims

This thesis aims to understand the origin of catalytic activity in phase pure ternary transition nitrides. To do this, a strategic investigation of the role the active sites need to be employed. Work in this thesis, therefore, seeks to identify and comparatively test catalytic materials with the same crystal structure and morphology if possible. In this way, the electrocatalytic activity of different nitrides may be investigated without confusing effect of impurities and substrates. It is believed that this would help to gain insight into the correlation between various elements and the electrochemical performance which could help with future design of optimal catalysts.

1.7 References

[1] G.A. Olah, Beyond oil and gas: The methanol economy, *Angew. Chemie - Int. Ed*. 44 (**2005**) 2636–2639. https://doi.org/10.1002/anie.200462121.

[2] J.A. Turner, A realizable renewable energy future, *Science* (80-.). 285 (**1999**) 687–689. https://doi.org/ 10.1126/science.285.5428.687.

[3] H.W. Schiffer, WEC energy policy scenarios to 2050, *Energy Policy*. 36 (**2008**) 2464–2470. https://doi.org/10.1016/J.ENPOL.2008.02.045.

[4] X. Cheng, Z. Shi, N. Glass, L. Zhang, J. Zhang, D. Song, Z.S. Liu, H. Wang, J. Shen, A review of PEM hydrogen fuel cell contamination: Impacts, mechanisms, and mitigation, *J. Power Sources*. 165 (**2007**) 739–756. https://doi.org/10.1016/J.JPOWSOUR.2006.12.012.

[5] D.K. Liguras, D.I. Kondarides, X.E. Verykios, Production of hydrogen for fuel cells by steam reforming of ethanol over supported noble metal catalysts, *Appl. Catal. B Environ*. 43 (**2003**) 345–354. https://doi.org/10.1016/S0926-3373(02)00327-2.

[6] G. Chisholm, L. Cronin, Hydrogen From Water Electrolysis, Storing Energy With Spec. Ref. to Renew. *Energy Sources*. (**2016**) 315–343. https://doi.org/10.1016/B978-0-12-803440-8.00016-6.

[7] S. Zhao, Thermochemical processes for biohydrogen production, Waste to Renew. *Biohydrogen* Vol. 1 Adv. Theory Exp. (**2021**) 139–177. https://doi.org/10.1016/B978-0-12-821659-0.00011-3.

[8] A. Buttler, H. Spliethoff, Current status of water electrolysis for energy storage, grid balancing and sector coupling via power-to-gas and power-to-liquids: A review, *Renew. Sustain. Energy Rev*. 82 (**2018**) 2440–2454. https://doi.org/10.1016/j.rser.2017.09.003.

[9] N.A. Kelly, Hydrogen production by water electrolysis, *Adv. Hydrog. Prod. Storage Distrib*. (**2014**) 159–185. https://doi.org/10.1533/9780857097736.2.159.

[10] P. Millet, R. Ngameni, S.A. Grigoriev, N. Mbemba, F. Brisset, A. Ranjbari, C. Etiévant, PEM water electrolyzers: From electrocatalysis to stack development, *Int. J. Hydrogen Energy*. 35 (**2010**) 5043–5052. https://doi.org/10.1016/j.ijhydene.2009.09.015.

[11] P. Nikolaidis, A. Poullikkas, A comparative overview of hydrogen production processes, *Renew. Sustain. Energy Rev*. 67 (**2017**) 597–611. https://doi.org/10.1016/j.rser.2016.09.044.

[12] D. Symes, B. Al-Duri, A. Dhir, W. Bujalski, B. Green, A. Shields, M. Lees, Design for on-site Hydrogen production for hydrogen fuel cell vehicle refueling station at University of Birmingham, U.K., *Energy Procedia*. 29 (**2012**) 606–615. https://doi.org/10.1016/j.egypro.2012.09.070.

[13] J. Greeley, T.F. Jaramillo, J. Bonde, I. Chorkendorff, J.K. Nørskov, Computational high-throughput screening of electrocatalytic materials for hydrogen evolution, *Nat. Mater*. 5 (**2006**) 909–913. https://doi.org/10.1038/NMAT1752.

[14] LBMA Precious Metal Prices | LBMA, (n.d.). https://www.lbma.org.uk/prices-and-data/precious-metal-prices#/ (accessed 21 September **2022**).

[15] J.D. Benck, T.R. Hellstern, J. Kibsgaard, P. Chakthranont, T.F. Jaramillo, Catalyzing the hydrogen evolution reaction (HER) with molybdenum sulfide nanomaterials, *ACS Catal*. 4 (**2014**) 3957–3971. https://doi.org/10.1021/CS500923C.

[16] M. Kozejova, V. Latyshev, V. Kavecansky, H. You, S. Vorobiov, A. Kovalcikova, V. Komanicky, Evaluation of hydrogen evolution reaction activity of molybdenum nitride thin films on their nitrogen content, *Electrochim. Acta*. 315 (**2019**) 9–16. https://doi.org/10.1016/J.ELECTACTA.2019.05.097.

[17] X. Zhang, Y. Li, Y. Guo, A. Hu, M. Li, T. Hang, H. Ling, 3D hierarchical nanostructured Ni–Co alloy electrodes on porous nickel for hydrogen evolution reaction, *Int. J. Hydrogen Energy*. 44 (**2019**) 29946–29955. https://doi.org/10.1016/J.IJHYDENE.2019.09.193.

[18] D. Goranova, E. Lefterova, R. Rashkov, Electrocatalytic activity of Ni-Mo-Cu and Ni-Co-Cu alloys for hydrogen evolution reaction in alkaline medium, *Int. J. Hydrogen Energy*. 42 (**2017**) 28777–28785. https://doi.org/10.1016/J.IJHYDENE.2017.10.002.

[19] K. Mech, P.R. Zabinski, T. Tokarski, R. Kowalik, T. Tokarski, K. Fitzner, Electrodeposition of Co–Pd alloys from ammonia solutions and their catalytic activity for hydrogen evolution reaction, *J. Appl. Electrochem*. 44 (**2013**) 97–103. https://doi.org/10.1007/s10800-013-0605-7.

[20] C. Lupi, A. Dell'Era, M. Pasquali, In situ activation with Mo of Ni–Co alloys for hydrogen evolution reaction, *Int. J. Hydrogen Energy*. 39 (**2014**) 1932–1940. https://doi.org/10.1016/J.IJHYDENE.2013.11.093.

[21] M.A. Domínguez-Crespo, M. Plata-Torres, A.M. Torres-Huerta, E.M. Arce-Estrada, J.M. Hallen-López, Kinetic study of hydrogen evolution reaction on $Ni_{30}Mo_{70}$, $Co_{30}Mo_{70}$, $Co_{30}Ni_{70}$ and $Co_{10}Ni_{20}Mo_{70}$ alloy electrodes, *Mater. Charact*. 55 (**2005**) 83–91. https://doi.org/10.1016/j.matchar.2005.03.003.

[22] M.J. De Giz, G. Tremiliosi-Filho, E.R. Gonzalez, S. Srinivasan, A.J. Appleby, The hydrogen evolution reaction on amorphous nickel and cobalt alloys, *Int. J. Hydrogen Energy*. 20 (**1995**) 423–427. https://doi.org/10.1016/0360-3199(94)00068-B.

[23] W.F. Chen, J.T. Muckerman, E. Fujita, Recent developments in transition metal carbides and nitrides as hydrogen evolution electrocatalysts, *Chem Commun*. 49 (**2013**) 8896–8909. https://doi.org/10.1039/C3CC44076A.

[24] W. Feng, W. Pang, Y. Xu, A. Guo, X. Gao, X. Qiu, W. Chen, Transition metal selenides for electrocatalytic hydrogen evolution reaction, *ChemElectroChem*. 7 (**2020**) 31–54. https://doi.org/10.1002/celc.201901623.

[25] X. Xia, L. Wang, N. Sui, V.L. Colvin, W.W. Yu, Recent progress in transition metal selenide electrocatalysts for water splitting, *Nanoscale*. 12 (**2020**) 12249–12262. https://doi.org/10.1039/D0NR02939D.

[26] C.T. Zeng, L. Dai, Y.H. Jin, J.B. Liu, Q.Q. Zhang, H. Wang, Design strategies toward transition metal selenide-based catalysts for electrochemical water splitting, *Sustain. Energy Fuels*. 5 (**2021**) 1347–1365. https://doi.org/10.1039/D0SE01722A.

[27] J. Theerthagiri, S.J. Lee, A.P. Murthy, J. Madhavan, M.Y. Choi, Fundamental aspects and recent advances in transition metal nitrides as electrocatalysts for hydrogen evolution reaction: A review, Curr. Opin. *Solid State Mater. Sci*. 24 (**2020**). https://doi.org/10.1016/j.cossms.2020.100805.

[28] Z. Xing, Q. Li, D. Wang, X. Yang, X. Sun, Self-supported nickel nitride as an efficient high-performance three-dimensional cathode for the alkaline hydrogen evolution reaction, *Electrochim. Acta*. 191 (**2016**) 841–845. https://doi.org/10.1016/J.ELECTACTA.2015.12.174.

[29] Y. Abghoui, E. Skúlason, Hydrogen Evolution Reaction Catalyzed by Transition-Metal Nitrides, *J. Phys. Chem. C*. 121 (**2017**) 24036–24045. https://doi.org/10.1021/acs.jpcc.7b06811.

[30] H. Jun, S. Kim, J. Lee, Development strategies in transition metal carbide for hydrogen evolution reaction: A review, *Korean J. Chem. Eng*. 2020 378. 37 (**2020**) 1317–1330. https://doi.org/10.1007/S11814-020-0612-4.

[31] S.K. Kim, Y. Qiu, Y.J. Zhang, R. Hurt, A. Peterson, Nanocomposites of transition-metal carbides on reduced graphite oxide as catalysts for the hydrogen evolution reaction, *Appl. Catal. B Environ*. 235 (**2018**) 36–44. https://doi.org/10.1016/j.apcatb.2018.04.032.

[32] S. Meyer, A. V. Nikiforov, I.M. Petrushina, K. Köhler, E. Christensen, J.O. Jensen, N.J. Bjerrum, Transition metal carbides (WC, Mo_2C, TaC, NbC) as potential electrocatalysts for the hydrogen evolution reaction (HER) at medium temperatures, *Int. J. Hydrogen Energy*. 40 (**2015**) 2905–2911. https://doi.org/10.1016/J.IJHYDENE.2014.12.076.

[33] Y.W. Cheng, J.H. Dai, Y.M. Zhang, Y. Song, Two-Dimensional, Ordered, Double Transition Metal Carbides (MXenes): A New Family of Promising Catalysts for the Hydrogen Evolution Reaction, *J. Phys. Chem. C*. 122 (**2018**) 28113–28122. https://doi.org/10.1021/ACS.JPCC.8B08914.

[34] A. Taylor, K. Sachs, A new complex eta-carbide, *Nature*. 169 (**1952**) 411. https://doi.org/10.1038/169411A0.

[35] N. Karlsson, Metallic oxides with the structure of high-speed steel carbide [8], *Nature*. 168 (**1951**) 558. https://doi.org/10.1038/168558A0.

[36] G.A. Yurko, J.W. Barton, J.G. Parr, The crystal structure of Ti_2Ni, *Acta Crystallogr*. 12 (**1959**) 909–911. https://doi.org/10.1107/S0365110X59002559.

[37] J.O. Conway, T.J. Prior, Interstitial nitrides revisited – A simple synthesis of M_xMo_3N (M = Fe, Co, Ni), *J. Alloys Compd*. 774 (**2019**) 69–74. https://doi.org/10.1016/J.JALLCOM.2018.09.307.

[38] S.M. Hunter, D. McKay, R.I. Smith, J.S.J. Hargreaves, D.H. Gregory, Topotactic nitrogen transfer: Structural transformation in cobalt molybdenum nitrides, *Chem.*

Mater. 22 (**2010**) 2898–2907. https://doi.org/10.1021/CM100208A.

[39] T.J. Prior, D. Nguyen-Manh, V.J. Couper, P.D. Battle, Ferromagnetism in the beta-manganese structure: $Fe_{1.5}Pd_{0.5}Mo_3N$, *J. Phys. Condens. Matter*. 16 (**2004**) 2273–2281. https://doi.org/10.1088/0953-8984/16/13/008.

[40] A.K. Tareen, G.S. Priyanga, S. Behara, T. Thomas, M. Yang, Mixed ternary transition metal nitrides: A comprehensive review of synthesis, electronic structure, and properties of engineering relevance, *Prog. Solid State Chem*. 53 (**2019**) 1–26. https://doi.org/10.1016/J.PROGSOLIDSTCHEM.2018.11.001.

[41] Q. Chen, X. Li, R. Xie, L. Xu, L. Liu, Novel rapid synthesis of nanoscale tungsten nitride using non-toxic nitrogen source, *Ceram. Int*. 46 (**2020**) 2580–2584. https://doi.org/10.1016/J.CERAMINT.2019.09.221.

[42] J.B. Claridge, A.P.E. York, A.J. Brungs, M.L.H. Green, Study of the temperature-programmed reaction synthesis of early transition metal carbide and nitride catalyst materials from oxide precursors, *Chem. Mater*. 12 (**2000**) 132–142. https://doi.org/10.1021/CM9911060.

[43] L. Ma, L.R.L. Ting, V. Molinari, C. Giordano, B.S. Yeo, Efficient hydrogen evolution reaction catalyzed by molybdenum carbide and molybdenum nitride nanocatalysts synthesized via the urea glass route, *J. Mater. Chem. A*. 3 (**2015**) 8361–8368. https://doi.org/10.1039/C5TA00139K.

[44] J. Theerthagiri, S.B. Dalavi, M. Manivel Raja, R.N. Panda, Magnetic properties of nanocrystalline ε-Fe_3N and Co_4N phases synthesized by newer precursor route, *Mater. Res. Bull*. 48 (**2013**) 4444–4448. https://doi.org/10.1016/J.MATERRESBULL.2013.07.043.

[45] C. Giordano, C. Erpen, W. Yao, M. Antonietti, Synthesis of Mo and W carbide and nitride nanoparticles via a simple 'urea glass' route, *Nano Lett*. 8 (**2008**) 4659–4663. https://doi.org/10.1021/nl8018593.

[46] J. Lai, B. Huang, Y. Chao, X. Chen, S. Guo, J. Lai, S. Guo, Y. Chao, B. Huang, H. Hom, H.Y. Kong SAR Chao, X. Chen, Strongly coupled nickel–cobalt nitrides/carbon hybrid nanocages with Pt-like activity for hydrogen evolution catalysis, *Adv. Mater.* 31 (**2018**). https://doi.org/10.1002/adma.201805541.

[47] X. Liu, X. Lv, P. Wang, Q. Zhang, B. Huang, Z. Wang, Y. Liu, Z. Zheng, Y. Dai, Improving the HER activity of Ni_3FeN to convert the superior OER electrocatalyst to an efficient bifunctional electrocatalyst for overall water splitting by doping with molybdenum, *Electrochim. Acta*. 333 (**2020**). https://doi.org/10.1016/J.ELECTACTA.2019.135488.

[48] J. Jia, M. Zhai, J. Lv, B. Zhao, H. Du, J. Zhu, Nickel Molybdenum Nitride Nanorods Grown on Ni Foam as Efficient and Stable Bifunctional Electrocatalysts for Overall Water Splitting, *ACS Appl. Mater. Interfaces*. 10 (**2018**) 30400–30408. https://doi.org/10.1021/ACSAMI.8B09854.

[49] N. Yao, P. Li, Z. Zhou, Y. Zhao, G. Cheng, S. Chen, W. Luo, Synergistically Tuning Water and Hydrogen Binding Abilities Over Co_4N by Cr Doping for Exceptional Alkaline Hydrogen Evolution Electrocatalysis, *Adv. Energy Mater*. 9 (**2019**). https://doi.org/10.1002/aenm.201902449.

[50] K. Zhang, W. Mai, J. Li, G. Li, L. Tian, W. Hu, Bimetallic $Co_{3.2}Fe_{0.8}N$-Nitrogen-Carbon Nanocomposites for Simultaneous Electrocatalytic Oxygen Reduction, Oxygen Evolution, and Hydrogen Evolution, *ACS Appl. Nano Mater*. 2 (**2019**) 5931–5941. https://doi.org/10.1021/ACSANM.9B01361.

[51] J. Li, C. Yao, X. Kong, Z. Li, M. Jiang, F. Zhang, X. Lei, Boosting hydrogen production by electrooxidation of urea over 3D hierarchical Ni_4N/Cu_3N nanotube arrays, *ACS Sustain. Chem. Eng*. 7 (**2019**) 13278–13285. https://doi.org/10.1021/ACSSUSCHEMENG.9B02510.

[52] Y. Gu, S. Chen, J. Ren, Y.A. Jia, C. Chen, S. Komarneni, D. Yang, X. Yao, Electronic Structure Tuning in Ni_3FeN/r-GO Aerogel toward Bifunctional Electrocatalyst for Overall Water Splitting, *ACS Nano*. 12 (**2018**) 245–253. https://doi.org/10.1021/ACSNANO.7B05971.

[53] H. Jin, H. Zhang, J. Chen, S. Mao, Z. Jiang, Y. Wang, A general synthetic approach for hexagonal phase tungsten nitride composites and their application in the hydrogen evolution reaction, *J. Mater. Chem. A*. 6 (**2018**) 10967–10975. https://doi.org/10.1039/C8TA02595A.

[54] R. Ramesh, D.K. Nandi, T. Hyun Kim, T. Cheon, J. Oh, S.-H. Kim, Atomic-Layer-Deposited MoN_x Thin Films on Three-Dimensional Ni Foam as Efficient Catalysts for

the Electrochemical Hydrogen Evolution Reaction, *ACS Publ.* 11 (**2019**) 17321–17332. https://doi.org/10.1021/acsami.8b20437.

[55] H. Jin, X. Liu, A. Vasileff, Y. Jiao, Y. Zhao, Y. Zheng, S.Z. Qiao, Single-Crystal Nitrogen-Rich Two-Dimensional Mo_5N_6 Nanosheets for Efficient and Stable Seawater Splitting, *ACS Nano.* 12 (**2018**) 12761–12769. https://doi.org/10.1021/ACSNANO.8B07841.

[56] G. Zhang, G. Wang, Y. Liu, H. Liu, J. Qu, J. Li, Highly Active and Stable Catalysts of Phytic Acid-Derivative Transition Metal Phosphides for Full Water Splitting, *J. Am. Chem. Soc.* 138 (**2016**) 14686–14693. https://doi.org/10.1021/jacs.6b08491.

[57] J. Shi, Z. Pu, Q. Liu, A.M. Asiri, J. Hu, X. Sun, Tungsten nitride nanorods array grown on carbon cloth as an efficient hydrogen evolution cathode at all pH values, *Electrochim. Acta*. 154 (**2015**) 345–351. https://doi.org/10.1016/J.ELECTACTA.2014.12.096.

[58] Y. Zhu, G. Chen, X. Xu, G. Yang, M. Liu, Z. Shao, Enhancing Electrocatalytic Activity for Hydrogen Evolution by Strongly Coupled Molybdenum Nitride@Nitrogen-Doped Carbon Porous Nano-Octahedrons, *ACS Catal*. 7 (**2017**) 3540–3547. https://doi.org/10.1021/ACSCATAL.7B00120.

[59] Y. Zhang, Y. Xie, Y. Zhou, X. Wang, K. Pan, Well dispersed Fe_2N nanoparticles on surface of nitrogen-doped reduced graphite oxide for highly efficient electrochemical hydrogen evolution, *J. Mater. Res.* 32 (**2017**) 1770–1776. https://doi.org/10.1557/JMR.2017.138/FIGURES/8.

[60] K. Ojha, S. Banerjee, A.K. Ganguli, Facile charge transport in FeN_x/Mo_2N/CNT nanocomposites for efficient hydrogen evolution reactions, *J. Chem. Sci*. 129 (**2017**) 989–997. https://doi.org/10.1007/S12039-017-1302-6/FIGURES/6.

[61] W.-F. Chen, K. Sasaki, C. Ma, A.I. Frenkel, N. Marinkovic, J.T. Muckerman, Y. Zhu, R.R. Adzic, W. Chen, K. Sasaki, J.T. Muckerman, R.R. Adzic, C. Ma, Y. Zhu, A.I. Frenkel, N. Marinkovic, Hydrogen-Evolution Catalysts Based on Non-Noble Metal Nickel–Molybdenum Nitride Nanosheets, *Angew. Chemie Int. Ed*. 51 (**2012**) 6131–6135. https://doi.org/10.1002/ANIE.201200699.

[62] B. Cao, G.M. Veith, J.C. Neuefeind, R.R. Adzic, P.G. Khalifah, Mixed close-packed

cobalt molybdenum nitrides as non-noble metal electrocatalysts for the hydrogen evolution reaction, *J. Am. Chem. Soc*. 135 (**2013**) 19186–19192. https://doi.org/10.1021/ja4081056.

[63] H. Jin, Q. Gu, B. Chen, C. Tang, Y. Zheng, H. Zhang, M. Jaroniec, S.Z. Qiao, Molten Salt-Directed Catalytic Synthesis of 2D Layered Transition-Metal Nitrides for Efficient Hydrogen Evolution, *Chem*. 6 (**2020**) 2382–2394. https://doi.org/10.1016/J.CHEMPR.2020.06.037.

[64] J. Zhao, Y. Zeng, J. Wang, Q. Xu, R. Chen, H. Ni, G.J. Cheng, Ultrahigh electrocatalytic activity with trace amounts of platinum loadings on free-standing mesoporous titanium nitride nanotube arrays for hydrogen evolution reactions, *Nanoscale*. 12 (**2020**) 15393–15401. https://doi.org/10.1039/d0nr01316a.

[65] W. Wang, Y. Shao, Z. Wang, Z. Yang, Z. Zhen, Z. Zhang, C. Mao, X. Guo, G. Li, Synthesis of Ru-Doped VN by a Soft-Urea Pathway as an Efficient Catalyst for Hydrogen Evolution, *ChemElectroChem*. 7 (**2020**) 1201–1206. https://doi.org/10.1002/CELC.202000072.

[66] Z. Liu, X. Zhang, H. Song, Y. Yang, Y. Zheng, B. Gao, J. Fu, P.K. Chu, K. Huo, Electronic Modulation between Tungsten Nitride and Cobalt Dopants for Enhanced Hydrogen Evolution Reaction at a Wide Range of pH, *ChemCatChem*. 12 (**2020**) 2962–2966. https://doi.org/10.1002/CCTC.202000391.

[67] Y. Gu, A. Wu, Y. Jiao, H. Zheng, X. Wang, Y. Xie, L. Wang, C. Tian, H. Fu, Two-Dimensional Porous Molybdenum Phosphide/Nitride Heterojunction Nanosheets for pH-Universal Hydrogen Evolution Reaction, *Angew. Chemie - Int. Ed*. 60 (**2021**) 6673–6681. https://doi.org/10.1002/ANIE.202016102.

[68] J. Tan, Y. Mei, H. Shen, H. Liu, T. Azhagan, W. Song, T. Thomas, J. Liu, M. Yang, M. Gao, Experimental and Theoretical Insights of MoS_2/Mo_3N_2 Nanoribbon-Electrocatalysts for Efficient Hydrogen Evolution Reaction, *ChemCatChem*. 12 (**2020**) 122–128. https://doi.org/10.1002/CCTC.201901874.

[69] Z. Yu, Y. Bai, S. Zhang, Y. Liu, N. Zhang, G. Wang, J. Wei, Q. Wu, K. Sun, Metal-Organic Framework-Derived Co_3ZnC/Co Embedded in Nitrogen-Doped Carbon Nanotube-Grafted Carbon Polyhedra as a High-Performance Electrocatalyst for Water Splitting, *ACS Appl. Mater. Interfaces*. 10 (**2018**) 6245–6252.

https://doi.org/10.1021/ACSAMI.7B16130.

[70] X. Jia, Y. Zhao, G. Chen, L. Shang, R. Shi, X. Kang, G.I.N. Waterhouse, L.-Z. Wu, C.-H. Tung, T. Zhang, Water Splitting: Ni_3FeN Nanoparticles Derived from Ultrathin NiFe-Layered Double Hydroxide Nanosheets: An Efficient Overall Water Splitting Electrocatalyst (Adv. Energy Mater. 10/2016) , *Adv. Energy Mater.* 6 (**2016**). https://doi.org/10.1002/AENM.201670063.

[71] C. Wang, X. Lv, P. Zhou, X. Liang, Z. Wang, Y. Liu, P. Wang, Z. Zheng, Y. Dai, Y. Li, M.H. Whangbo, B. Huang, Molybdenum Nitride Electrocatalysts for Hydrogen Evolution More Efficient than Platinum/Carbon: Mo_2N/CeO_2@Nickel Foam, *ACS Appl. Mater. Interfaces*. 12 (**2020**) 29153–29161. https://doi.org/10.1021/ACSAMI.0C02851.

[72] Y. Zhang, B. Ouyang, J. Xu, S. Chen, R. Singh Rawat, H. Jin Fan, Y.Q. Zhang, J. Xu, S. Chen, H.J. Fan, B. Ouyang, R.S. Rawat, 3D porous hierarchical nickel–molybdenum nitrides synthesized by RF plasma as highly active and stable hydrogen-evolution-reaction electrocatalysts, *Adv. Energy Mater*. 6 (**2016**) 1600221. https://doi.org/10.1002/aenm.201600221.

[73] I.S. Amiinu, Z. Pu, X. Liu, K.A. Owusu, H.G.R. Monestel, F.O. Boakye, H. Zhang, S. Mu, Multifunctional Mo–N/C@MoS_2 Electrocatalysts for HER, OER, ORR, and Zn–Air Batteries, *Adv. Funct. Mater*. 27 (**2017**). https://doi.org/10.1002/ADFM.201702300.

[74] D. Li, Y. Xing, R. Yang, T. Wen, D. Jiang, W. Shi, S. Yuan, Holey Cobalt-Iron Nitride Nanosheet Arrays as High-Performance Bifunctional Electrocatalysts for Overall Water Splitting, *ACS Appl. Mater. Interfaces*. 12 (**2020**) 29253–29263. https://doi.org/10.1021/ACSAMI.0C05219.

[75] Z. Xu, W. Li, Y. Yan, H. Wang, H. Zhu, M. Zhao, S. Yan, Z. Zou, In-Situ Formed Hydroxide Accelerating Water Dissociation Kinetics on Co_3N for Hydrogen Production in Alkaline Solution, *ACS Appl. Mater. Interfaces*. 10 (**2018**) 22102–22109. https://doi.org/10.1021/ACSAMI.8B04596.

[76] X. Feng, H. Wang, X. Bo, L. Guo, Bimetal-Organic Framework-Derived Porous Rodlike Cobalt/Nickel Nitride for All-pH Value Electrochemical Hydrogen Evolution, *ACS Appl. Mater. Interfaces*. 11 (**2019**) 8018–8024.

https://doi.org/10.1021/ACSAMI.8B21369.

[77] Y. Tong, X. Yu, H. Wang, B. Yao, C. Li, G. Shi, Trace Level Co-N Doped Graphite Foams as High-Performance Self-Standing Electrocatalytic Electrodes for Hydrogen and Oxygen Evolution, *ACS Catal*. 8 (**2018**) 4637–4644. https://doi.org/10.1021/acscatal.8b01131.

[78] Z. Liu, H. Tan, J. Xin, J. Duan, X. Su, P. Hao, J. Xie, J. Zhan, J. Zhang, J.J. Wang, H. Liu, Metallic Intermediate Phase Inducing Morphological Transformation in Thermal Nitridation: Ni_3FeN-Based Three-Dimensional Hierarchical Electrocatalyst for Water Splitting, ACS Appl. Mater. *Interfaces*. 10 (**2018**) 3699–3706. https://doi.org/10.1021/acsami.7b18671.

[79] Y. Gu, S. Chen, J. Ren, Y.A. Jia, C. Chen, S. Komarneni, D. Yang, X. Yao, Electronic Structure Tuning in Ni_3FeN/r-GO Aerogel toward Bifunctional Electrocatalyst for Overall Water Splitting, *ACS Nano*. 12 (**2018**) 245–253. https://doi.org/10.1021/acsnano.7b05971.

[80] L.A. Sviridov, P.D. Battle, F. Grandjean, G.J. Long, T.J. Prior, Magnetic ordering in nitrides with the η-carbide structure, $(Ni,Co,Fe)_2(Ga,Ge)Mo_3N$, *Inorg. Chem*. 49 (**2010**) 1133–1143. https://doi.org/10.1021/IC902069W.

[81] R. Niewa, Metal-Rich Ternary Perovskite Nitrides, *Eur. J. Inorg. Chem*. (**2019**) 3647–3660. https://doi.org/10.1002/EJIC.201900756.

[82] T.J. Prior, P.D. Battle, Superparamagnetism and metal-site ordering in quaternary nitrides with the *η*-carbide structure, *J. Mater. Chem*. 14 (**2004**) 3001–3007. https://doi.org/10.1039/B408040H.

Chapter 2. Experimental Methods

2.1. Synthesis

The specific details experiments are given in each chapter. However, the general protocol was as follows. All materials (nitrides) were prepared in a tube furnace as schematically shown in Figure 2-1. Certain amounts of the relevant precursor were placed into a ceramic boat within a tube furnace under flow of 5% H_2 in N_2 gas mixture with a flow rate of 10 mL min^{-1}. The heating rate was set at 5 ^oC/min and after 5 hours of reaction time at given reaction temperature, then the furnace was cooled naturally to the ambient temperature. The detailed synthesis will be discussed in a corresponding chapter, due to the differences of experimental operation conditions of the prepared samples.

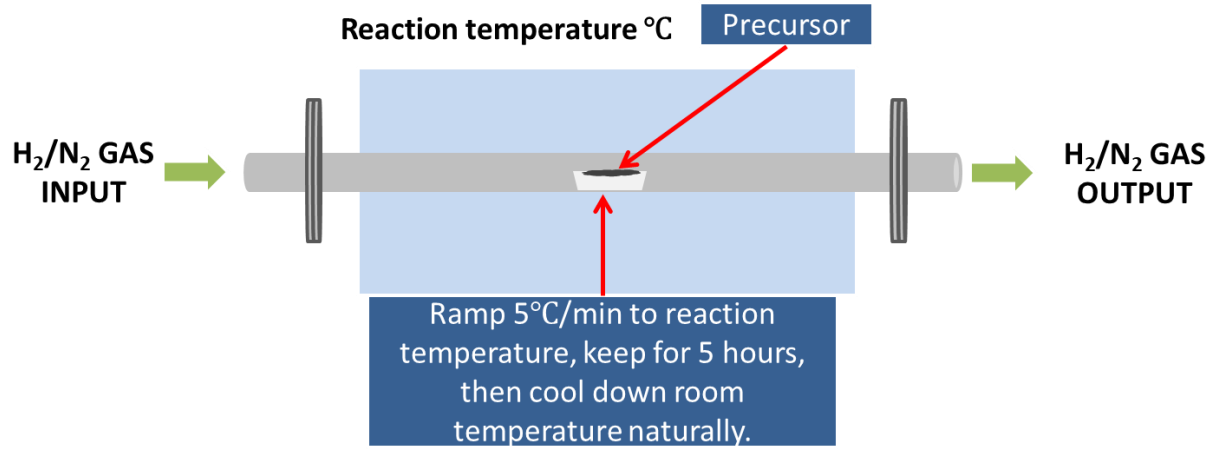

Figure 2-1: A schematic of an equipment for synthesis of samples under 5% H_2 in N_2 gas mixture flow.

2.2 Materials Characterisation

2.2.1. Powder X-Ray Diffraction (PXRD)

Throughout the duration of the whole project, the primary method of characterisation used to determine the phase composition and purity of the synthesised compounds was PXRD, a form of X-ray crystallography. X-ray crystallography operates on the basis that the atomic and molecular properties of crystals can be discerned upon exposure of the sample to X-rays, which will diffract in a specified fashion suggestive of the sample structure. These diffraction patterns can then be compared to pre-calculated patterns from the inorganic crystal structure database (ICSD) and hence the composition and purity of the synthesised compound can be confirmed. X-ray radiation is generated by bombarding a copper target with a high energy electron beam.

These electrons will collide with the electrons housed within the inner K shell of the copper target, ejecting core electrons from this inner shell. In response, high energy outer electrons within L shells will drop into the vacant site left behind in the K shell, emitting excess energy in the process as photons of X-ray radiation, Kα. The Kα radiation that is produced is a form of short wavelength radiation, making it ideal for the study of atoms which are generally spaced around 1 Å apart.[1] The patterns produced by crystalline solids upon exposure to X-ray radiation is defined by Bragg diffraction, which envisages a crystalline material as a layered, regular repeating structure, where, in order for diffraction to take place, the perpendicular distance between the crystal planes is in the same range of the wavelength of the oncoming X-ray radiation (Figure 2-2).[1]

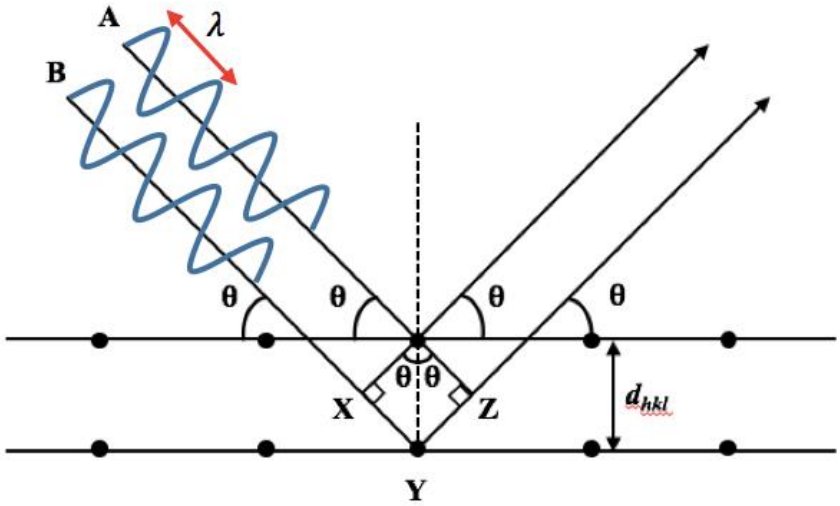

Figure2-2: illustration of Bragg's law and the path of X-rays through a crystal. [1]

From Figure 2-2, we can see that X-ray beams A and B will travel in-phase towards the ordered lattice in a parallel fashion, producing constructive interference which will ultimately amplify the detected signal. The beam, B will travel a further distance relative to A, XYZ, which is related to the interplanar gap and the angle of incidence to produce the relationship shown in Equation 11:

$$XYZ = 2d_{hkl}\sin(\theta) \qquad (11)$$

Where d_{hkl} represents the interplanar gap between lattice planes, along with their orientation as defined by the miller indices (h, k, l). The Bragg angle is defined as θ and finally XYZ, the path difference. In order for constructive interference to be observed, the path difference must be equal to a whole number of wavelengths:

$$XYZ=n\lambda \qquad (12)$$

Where λ is the wavelength of the oncoming radiation and n an integer value. By equating both Equations 11 and 12, an expression for Bragg's law can be derived:[1]

$$2d_{hkl}\sin(\theta)=n\lambda \qquad (13)$$

In this whole thesis, Powder X-ray diffraction (PXRD) was carried out on a Rigaku MiniFlex 6G equipped with a D/teX Ultra detector, a 6-position (ASC-6) sample changer and Cu sealed tube ($K_{\alpha1}$ and $K_{\alpha2}$ wavelengths are 1.5406 and 1.5444 Å respectively) operating in the Bragg-Brentano geometry. A sample was carefully spread over a silicon zero-background holder and flattened with a glass slide, and then measured with a step size of 0.016° and time per step of 2° min^{-1}. PXRD was also performed directly on the work electrode surface for electrocatalytic stability studies using the fabricated holder as depicted in Figure 2-3. Due to the tiny catalysts deposited on the electrode surface the time per step was set to 0.75° min^{-1} to achieve higher intensities in the diffraction pattern. The obtained diffraction patterns of product were analysed by comparison with calculated patterns from the ICSD. Rietveld refinements [2] of the resulting PXRD pattern were also carried by GSAS-II software [3] to confirm the products. Refined parameters included unit cell parameters, sample displacement, strain, and crystallite broadening, as well as atomic position and U_{iso} for transition metals. Numbers in brackets give statistical deviations for the last significant digit. Standard deviations have been multiplied by the Berar factor to correct local correlations. Fitting profile (R_p) and weighed profile (R_{wp}) residuals are reported Background was fitted using shifted Chebyshev polynomic shape. Pseudo-Voigt function was used for peak shapes.

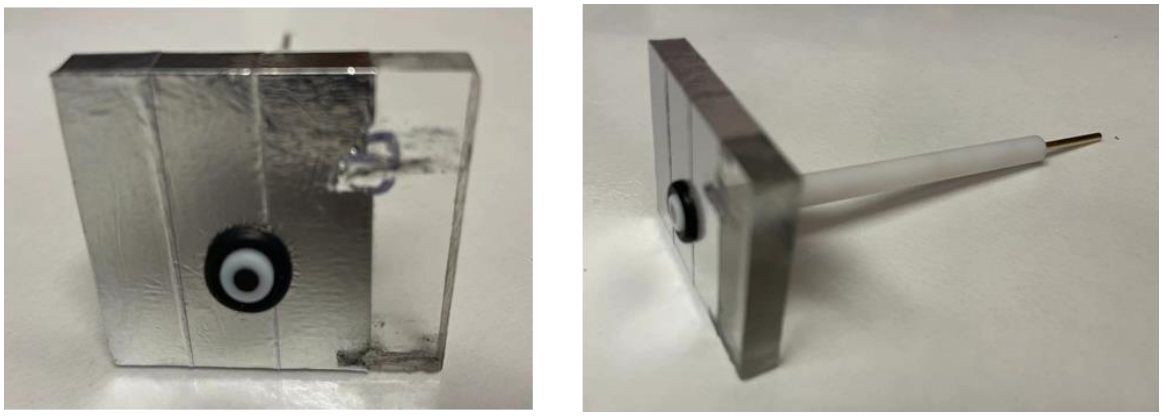

Figure 2-3: The holder designed for the characterisation of the catalyst by PXRD directly on the electrode surface before and after electrochemical stability measurements.

2.2.2. Scanning Electron Microscopy coupled with Energy Dispersive X-Ray Spectroscopy (SEM/EDX)

Scanning Electron Microscopy (SEM) was performed using a Phillips XL30 ESEM instrument equipped with an Oxford Instruments X-act spectrometer for Energy Dispersive X-ray Spectroscopy EDXS measurements. The INCA software was used for the data analysis. Cu foil was used as the calibration standard for the EDXS. The sample preparation involved dispersing *ca*. 1 mg of product in 1 ml of water on sonication for 5 minutes. 100 mL drop of resulting solution was casted on Cu foil producing a well-spread and homogenous coating on drying.

2.2.3. X-ray photoelectron spectroscopy (XPS)

In this thesis, The X-ray photoelectron spectroscopy (XPS) were performed by collaboration, all of samples needed to measure XPS were carefully packed and sent to Tomsk Polytechnic University, Russia. The testing was conducted using a Thermo Fisher Scientific XPS NEXSA spectrometer with a monochromated Al K alpha X-ray source operating at 1486.6 eV. The high-resolution spectra were recorded at the pass energy of 50 (eV) and energy resolution 0.1 (eV). The flood gun was used for the charge compensation. The analysed area was 200 μm^2.

2.3 Electrochemical measurements

2.3.1 Electrochemical Setup

All electrochemical measurements were performed using a Biologic SP-150 potentiostat with a three-electrode setup in a single cell compartment in 0.5 M H_2SO_4. As shown in Figure 2-4, catalysts deposited on to the surface of a glassy carbon electrode (surface area 0.071 cm^2) were used as working electrode. Carbon felt and 3 M Ag/AgCl were used as the counter and reference electrodes, respectively. Electrode potentials were converted to RHE scale by E(NHE) = E(Ag/AgCl) + 0.209 V +0.059×pH, and the ohmic resistances were compensated.

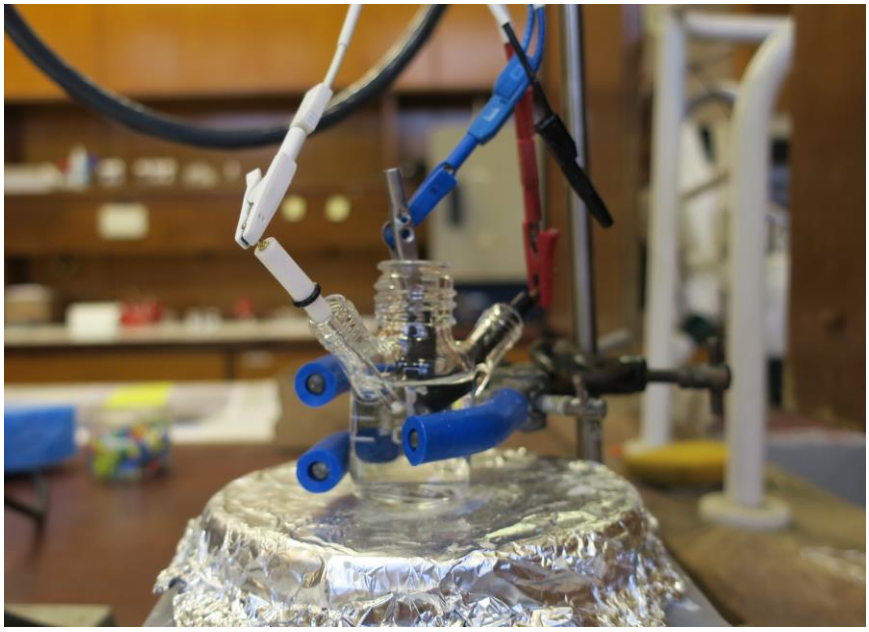

Figure 2-4: A picture of the three-electrode setup used in the electrochemical cell.

2.3.2. Working Electrodes Preparation

Electrochemical measurements were performed using a glassy carbon as a working electrode with a surface area of 0.071 cm^2 unless otherwise stated. Firstly, the glassy carbon electrode was cleaned with diamond polish on an alumina pad (IJ Cambria) for each measurement to avoid any adventitious impurities in the progress of electrocatalysts' assessment. Then the catalysts' inks were prepared by sonicating a mixture consisting of 1 mL DMF (99.9 %, Aldrich), 0.05 mL Nafion (5 wt. % in mixture of lower aliphatic alcohols and water, Aldrich) and 8 mg of product for 1 hour. After this time, 0.010 mL (corresponding to sample loading of *ca*. 1.13 mg cm^{-2} geometric) of the ink was drop cast on to the glassy carbon working electrode and allowed to dry naturally in air as shown in Figure 2-5.

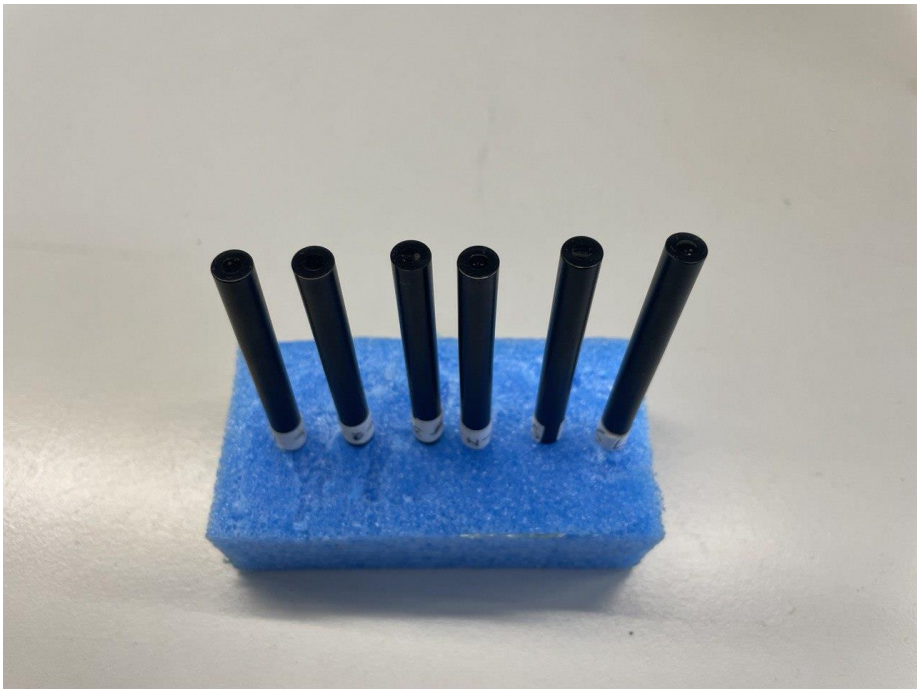

Figure 2-5: A collection of work electrodes, which were covered with electrocatalysts ink for use in the HER.

2.3.3. Voltammetry

Linear sweep voltammetry (LSV) is an electrochemical method used to study the current at a working electrode between a fixed potential range with a scan rate of 5 mV s^{-1}, which provides a specific reading of the currents achieved at a particular potential under this low scan rates. Cyclic voltammetry (CV) also is an electrochemical method applied for assessment catalysts, the voltage is swept in both reductive and oxidative directions between a fixed potential. LSV and CV measurements were performed on Biologic SP-150 potentiostat unless otherwise stated. The deposited glassy carbon was used as the working electrode, carbon felt as the counter and Ag/AgCl in 3 M NaCl as the reference electrode. 0.5 M H_2SO_4 used as electrolyte and measurements were carried out with a scan rate of 5 mV s^{-1} for LSV and 100 mV s^{-1} for CV. To remove the bubbles from the working electrode surface, the electrolyte kept under stirring. The experimental errors were obtained by performing at least three independent measurements and by taking the amount of variation between these measurements as an error.

2.3.4. Tafel slope analysis

Tafel slopes were obtained by linear sweep voltammetry with a scan rate of 5 mV s^{-1} through calculating the logarithm of the current density, which is plotted on the x-axis vs. the overpotential on the y-axis. The Tafel slope was observed from the gradient of the resulting

graph, which is a measure of the voltage required to increase the current density by an order of magnitude in mV per decade (mV dec^{-1}).

2.3.5. Electrochemical Impedance Spectroscopy (EIS)

Electrochemical Impedance Spectroscopy (EIS) was carried out in an identical electrochemical cell as the voltammetry techniques, but the electrolyte was kept static and Nyquist plots were obtained between a frequency range of 200 kHz to 100 mHz at various potentials.

2.3.6. Electrochemically Active Surface Area (ECSA)

The electrochemical active surface area (ECSA) was also performed in an identical electrochemical cell as the voltammetry techniques and obtained by sweeping the applied potential in a small potential range (in the non-Faradaic region where no charge-transfer reactions occur but absorption and desorption processes can take place) under the same conditions used for catalysis measurements.[4] When cycling the electrodes at different scan rates (v), the evolution of non-Faradaic current density (j) should scale linearly with the scan rate so that the slope gives the electrical double-layer capacitance ($C_{dI} = j/v$). The roughness factor is estimated by normalizing the double layer capacitance of the electrode with the double layer capacitance of a flat surface (ECSA = C_{dl}/C_{dlRef}). Using the roughness factor, the density of electrochemically active sites can be obtained by calculating the density of active sites on a flat surface multiplied by the roughness factor.

2.4. Gas Chromatography Measurements

Gas chromatography (GC) was used to confirm the production of hydrogen using an Agilent GC 7890 A with a thermal conductivity detector. The column used was a 30 metre-long 0.320 mm widebore HP-molesieve column (Agilent). The GC oven temperature was set to 27 °C and the carrier gas was Ar. The front inlet was set to 100 °C. The GC system was calibrated using certified standards of hydrogen at various concentrations (vol%) in Ar (CK Gas Products Limited, UK) before use. The Faradaic efficiency of samples were experimentally measured using a single cell two-electrode set up, which involved the catalyst-deposited glassy carbon working electrode and carbon felt counter electrode attached to a silver wire immersed in 0.5 M H_2SO_4. A known volume of electrolyte was removed to accurately determine the cell headspace. The cell was then sealed and degassed under argon for 30 minutes thus insuring an airtight system. Galvanostatic electrolysis was then performed with an applied current of –0.24 mA. At regular intervals, 25 µL samples of the headspace were directly injected into the GC. The expected volume percentages of hydrogen in the headspace were calculated by converting

the charge passed to an expected number of moles of gas, and then taking the volume of 1 mole of an ideal gas at standard temperature and pressure to be 22.4 L.

2.5. Density Functional Theory (DFT) calculation

In this thesis, all of computer calculation was done by our collaborators. Surface structures were optimized in Vienna Ab initio Simulation Package (VASP 5.4.4), which implemented Projector Augment Wave (PAW) based on plane-wave basis.[5] At least 10 Å of vacuum was implemented in our models to avoid layer interactions. Due to the large size of the unit cells, Γ-point was used to relax the structure. A Γ-point centred at 3 × 3 × 1 k-mesh was used for static energy calculations. The cut-off energy of plane wave basis was set at 550 eV. The exchange functional was the Perdew–Burke–Ernzerhof (PBE) of Generalized Gradient Approximation (GGA). In all calculations, the magnetic moments of the atoms were initially ferromagnetically aligned.

2.6. References

[1] P. Atkins, J. D. Paula, J. Keeler, *Atkins' Physical Chemistry*, Oxford University Press, Oxford, (**2014**) 976. ISBN:9780198847816.

[2] H.M. Rietveld, IUCr, A profile refinement method for nuclear and magnetic structures, *J. Appl. Crystallogr*. 2 (**1969**) 65–71. https://doi.org/10.1107/S0021889869006558.

[3] B.H. Toby, R.B. Von Dreele, GSAS-II: the genesis of a modern open-source all purpose crystallography software package, *J. Appl. Crystallogr*. 46 (**2013**) 544–549. https://doi.org/10.1107/S0021889813003531.

[4] S. Trasatti, O.A. Petrii, Real surface area measurements in electrochemistry, *J. Electroanal. Chem.* 327 (**1992**) 353–376. https://doi.org/10.1016/0022-0728(92)80162-W.

[5] G. Kresse, J. Furthmüller, Efficiency of ab-initio total energy calculations for metals and semiconductors using a plane-wave basis set, *Comput. Mater. Sci*. 6 (**1996**) 15–50. https://doi.org/10.1016/0927-0256(96)00008-0.

Chapter 3. Investigation of Co-Mo intermetallics as electrocatalysts for the HER

3.1. Introduction

There are two types of materials formed by two or more metallic elements, that is alloys and intermetallics. Alloys, are referred as solid solutions, are random mixtures of metals. However, intermetallics are compounds with a defined stoichiometry and crystal structure, with specific sites assigned for the atoms of each constituent element. As an example, the crystal structures of the disordered Co-Mo solid solution and the hexagonal Co_3Mo ordered phase are shown in Figure 3-1. Such ordering differentiates, the intermetallics display special superconducting and chemical properties, due to their strong internal order and mixed (metallic and covalent/ionic) bonding, which are not present in alloys. Alloys exhibit a lower thermal stability and properties of surface rearrangement and phase separation, result from its negative free energy of formation than intermetallics.[1] Moreover, random site occupancy of alloys limits the availability of catalyst active sites only to certain regions. Conversely, the regular structure of intermetallics would ensure homogeneity of the active sites.

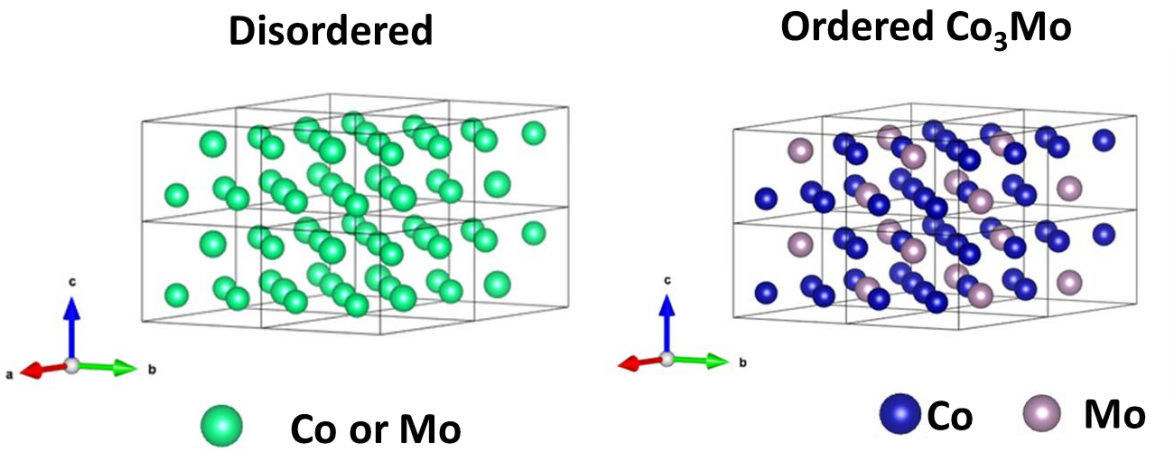

Figure 3-1: Crystal structure of disordered Co-Mo alloys and ordered hexagonal Co_3Mo.

As the electrochemical catalysts, intermetallics have been the choice for driving the hydrogen evolution reaction in alkaline media. As metallic alloys and intermetallic show electrocatalytic performance normally superior to their individual metal counterparts,[1–3] which has been known as synergistic effect and successfully exploited in alkaline media.[1,4,5] However, only a few attempts have been made to investigate the electrocatalytic performance of intermetallic with well-defined phase compositions in acidic electrolytes.[6–9] Research on pure-phased

metals intermetallic may provide a better understanding of their electrochemical properties. In this respect the Co–Mo system remain relatively unexplored. Based on the recent reports from Co_3Mo deposited on Ni foam for HER in 1M KOH [10,11] that delivered 68 mV at a benchmark current density of 10 mA cm^{-2}, it is interesting to understanding whether Co–Mo intermetallic system could be used in acidic media as well.

3.2. Aims

The aim of this chapter is to exploit a solid-state route to ordered Co-Mo system and test them as powders on glassy carbon electrodes. Within the Co-Mo phase diagram Co_3Mo and Co_7Mo_6 are two promising intermetallic that we aim to synthesis as powders and fully characterised. If identified as phase-pure products, they then be tested toward HER in acidic and alkaline media.

3.3. Synthesis and characterisation of pure-phase metal and intermetallics

3.3.1. Synthesis of the phase Co_7Mo_6

$Co_7Mo_6O_x$ precursor was prepared a citric acid route: 2376.8 mg (7.166 mmol) $Co(NO_3)_2{\cdot}6H_2O$ (Alfa Aesar, ACS reagent, ⩾ 99.0%), 1235.9 mg (1 mol) $(NH_4)_6Mo_7O_{24}{\cdot}4H_2O$ (Sigma-Aldrich, ACS reagent, ⩾ 99.0 %) and 3000 mg citric acid monohydrate, $C_6H_8O_7{\cdot}H_2O$ (Alfa Aesar, ⩾ 99.5 %) were added into a 150 ml Pyrex beaker and fully dissolved in 80 ml deionised water on stirring at room temperature. The water was evaporated at 120 ℃ resulting in foam looking products. The foams were calcined within the same beaker in air in a box furnace at 500 ℃ for 12 hours to eliminate any traces of carbon. The calcined foam was reground to black powder and confirmed as carbon-free by elemental analysis.

Co_7Mo_6 was synthesised by heating the oxide precursor prepared as described above under the flow of H_2 (5 %) / Ar gas. In a typical experiment, 200 mg of the oxide precursor were placed into a ceramic boat within a tube furnace. The samples were heated at 5 $^oC\ min^{-1}$ to 950 ℃ under the flow of H_2 (5 %) / Ar gas (a flow rate of 10 mL min^{-1}). After 10 hours of reaction time the furnace was cooled naturally to the ambient temperature and the synthesised products were reground with a pestle and mortar.

PXRD was utilised to evaluate the synthesised product, and the Figure 3-2 illustrates the results of product heated under 950 ℃. By comparing the prepared product PXRD pattern with those collected from the ICSD database, the resulting PXRD pattern peaks match fairly well with the peak positions of the simulated pattern for Co_7Mo_6, which adopts the structure of Fe_7W_6 (Space group: *R*-3*m* (166))[12]. There is a significant disorder within the crystal structure of the

studied sample (which however was identified as Co_7Mo_6 by EDX spectroscopy). The significant disorder (probably resulting in stacking faults along *c*-axis) may be avoided if a higher temperature were chosen. However, higher reaction temperature led to sintering of the powder and reducing of surface area making it unsuitable for any catalytic investigation (as well as making impossible to grind powder for PXRD). Therefore, the attempts to prepare a sample that would match the simulated pattern ideally were not pursued. Still, due to results from EDX spectroscopy we deemed the sample as phase-pure and thus, quite representative of the targeted Co_7Mo_6 material. This was further reinforced by the lack of any impurities that were expected if sample was not representative of phase pure Co_7Mo_6.

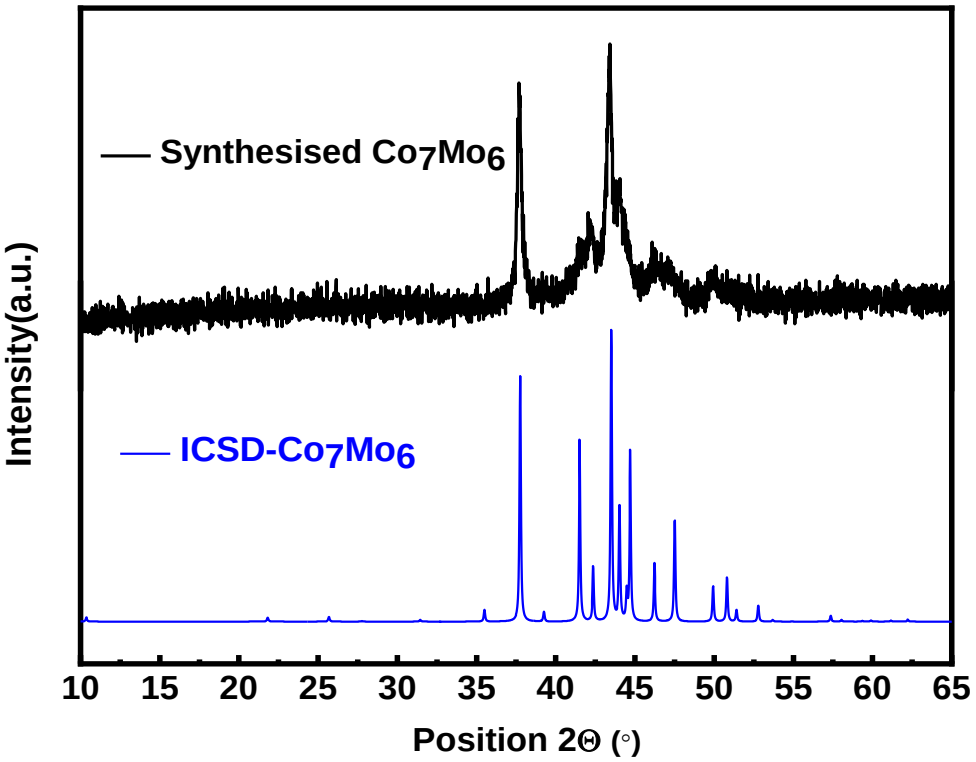

Figure 3-2: PXRD patterns of the resulting powder obtained by heating mixed precursor at 950 °C for 10 hours (top) in comparison with Co_7Mo_6 pattern as calculated from the ICSD database.

3.3.2. Synthesis of the phase Co_3Mo

Co_3Mo was made through similar method with Co_7Mo_6. First, 3055.92 mg (10.487 mmol) of $Co(NO_3)_2{\cdot}6H_2O$ (Alfa Aesar, ACS reagent, ⩾ 99.0%), 617.95 mg (0.5 mmol) and 3000 mg citric acid monohydrate, $C_6H_8O_7{\cdot}H_2O$ (Alfa Aesar, ⩾ 99.5 %) were added into a 150 ml Pyrex beaker and fully dissolved in 80 ml deionised water on stirring at room temperature. The water was evaporated at 120 ℃ resulting should be foam-liking products. The foams were calcined within the same beaker in air in a box furnace at 500 ℃ for 12 hours to eliminate any traces of carbon. The calcined foam was reground to black powder and confirmed as carbon-free by elemental analysis. The silica tube was then placed inside a tube furnace and annealed under 700 °C for 10 hours in 5% H_2 in Ar gas flow. There are clear Co impurity peaks observed at 48.6° from the PXRD pattern as shown in Figure 3-3. Hence, to get pure phase product, the resulting powder was reground with mortar and pestle again when the tube was cooled down to room temperature. The powder was placed back into the tube furnace again and reannealed under 850 °C for 5 hours in 5% H_2 in Ar gas flow.

The resulting PXRD pattern is shown in Figure 3-4 and illustrates a very good match with the simulated patterns for hexagonal Co_3Mo with the structure of Ni_3Sn (Space group: *P*63/*mmc* (194)). [13] The attempts to synthesis Co_3Mo at high temperature (to match the reaction temperature used for synthesis of Co_7Mo_6 for a better performance comparison between two intermetallic) was also carried out but the resulting powder exhibited a phase separation into Co_7Mo_6 and Co metal. This attempt was motivated by the assumption that a similar morphologies and surface areas products are more likely to be prepared at similar temperatures. Hence, a comparatively more reliable assessment about their electrochemical performance would be possible.

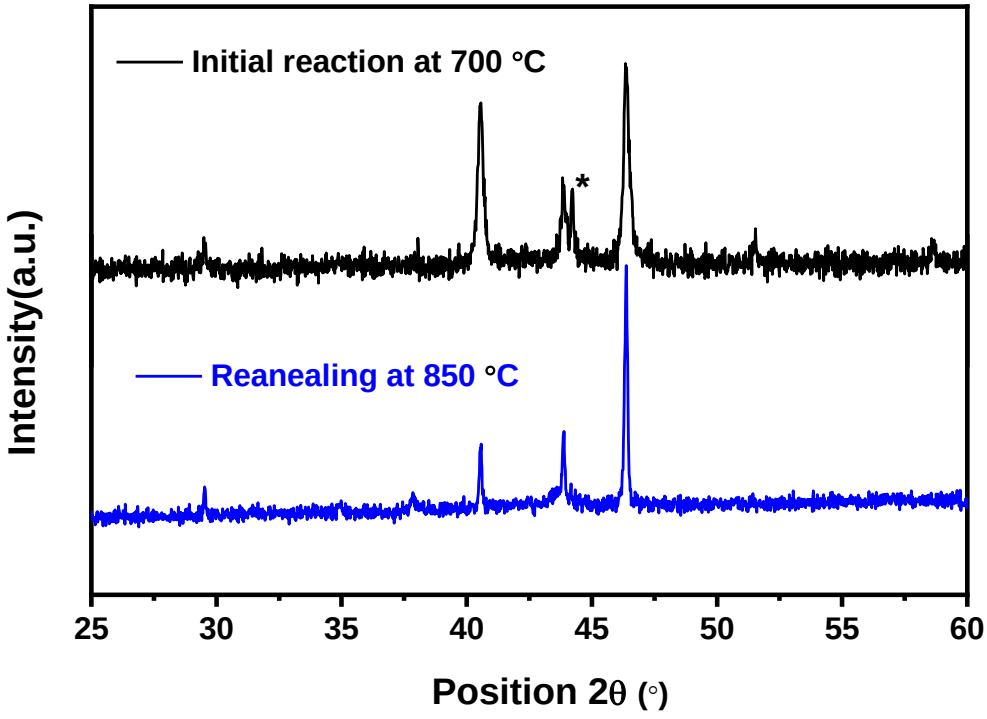

Figure 3-3: Comparison of Powder-XRD achieved by Co_3Mo intermetallic initial reaction result at 700 ℃ for 10 hours (* Co impurity peak) and reannealing at 850 ℃ for 5 hours(bottom).

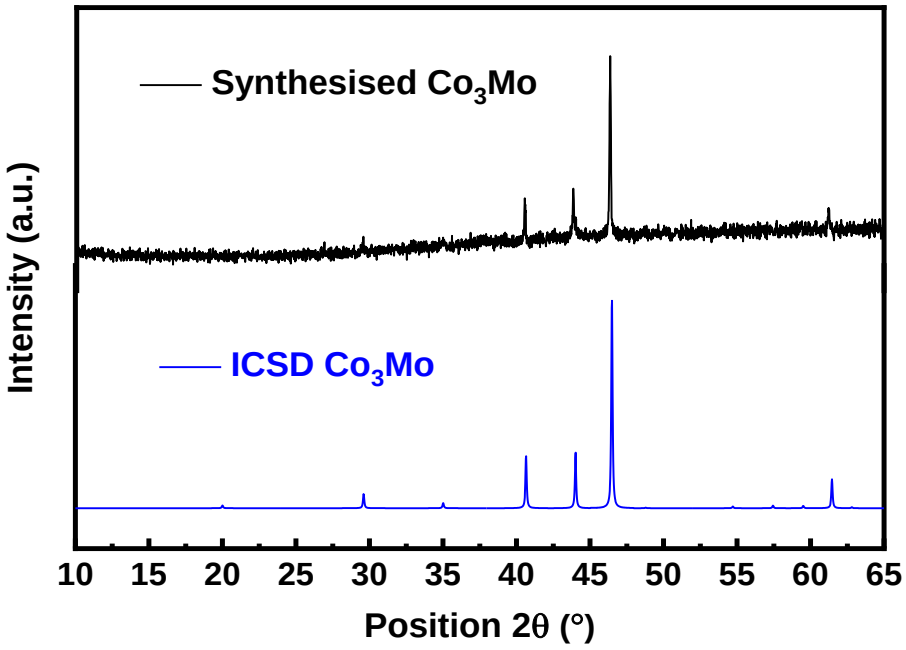

Figure 3-4: PXRD patterns of the resulting powder obtained by heating mixed precursor at 700 °C for 10 hours and 850 °C for 10 hours (black) in comparison with standard Co_3Mo as calculated from the ICSD database (blue).

3.3.3. Synthesis of Co and Mo metals

To study the performance of Co-Mo intermetallic toward the HER, the control experiments of Mo and Co metals were also carried out which were prepared by similar synthesis method. 150 mg (1.042 mmol) of MoO_3 powder was sandwiched between two silica wool pieces inside a silica tube (8 mm diameter and 20 mm long). The loading silica tube was then placed inside a tube furnace. And annealed under 950 °C for 10 hours in 5% H_2 in Ar gas. The obtained PXRD patterns illustrates that pure-phase Mo metal was synthesised by comparing with those simulated from the ICSD database as shown in Figure 3-5. Co metal was prepared by heating 150 mg (1.6138 mmol) $Co(OH)_2$ powder through identical experimental condition with Mo metal synthesising. The loading tube was heated under 350 °C for 5 hours in 5% H_2 Ar stream. The resulting PXRD pattern in the Figure 3-6 shows a good match with the simulated patterns collected from ICSD database with a single phase observed.

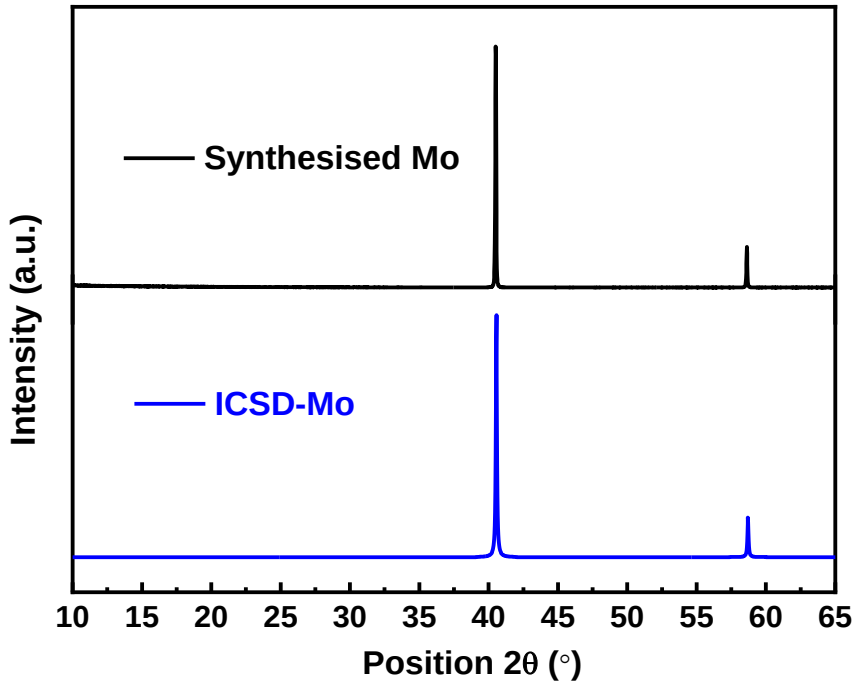

Figure 3-5: PXRD patterns of the resulting powder obtained by heating MoO_3 at 950 °C for 10 hours (top) in comparison with standard Mo as calculated from the ICSD database,

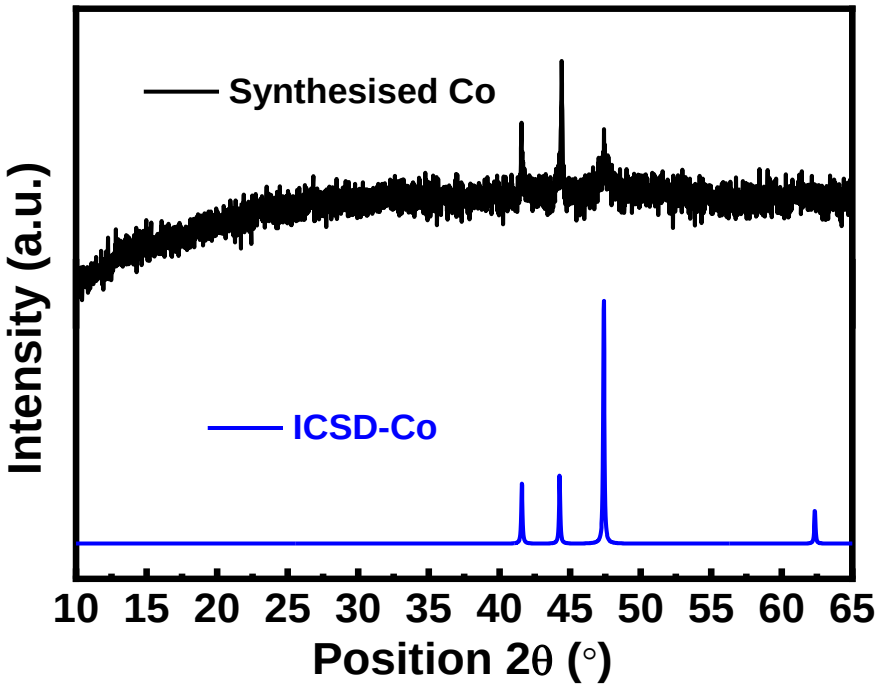

Figure 3-6: PXRD patterns of the resulting powder obtained by heating $Co(OH)_2$ at 350 °C for 5 hours (top) in comparison with standard Co as calculated from the ICSD database.

3.3.4. SEM and EDX analysis of phase Co_3Mo and Co_7Mo_6

To make the assessment for electrochemical catalysis more reliable, the morphology is another important fact to consider. Nanostructured materials would usually show an increased surface area which leads to the increased number of active sites. Therefore, it is important to compare the morphology of catalytically tested products. Here, the morphology of Co_3Mo observed from the SEM could be described as consisting of spherical-shaped particles with a diameter of *ca*. 300–500 nm (Figure 3-7 a), which is similar with Co_7Mo_6 (Figure 3-7 b). Despite the higher reaction temperature used for Co_7Mo_6 preparation it shows similar crystallite shapes and surface roughness as Co_3Mo. This suggests that samples are comparable in terms of morphology.

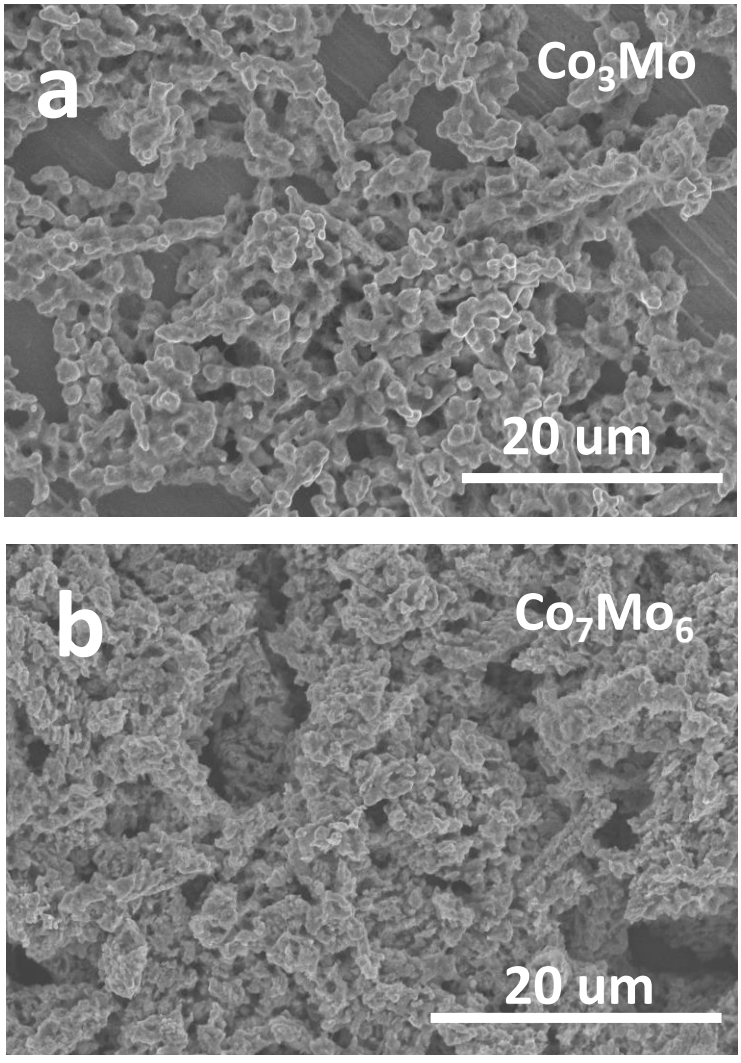

Figure 3-7: SEM image of (a) Co_3Mo and (b) Co_7Mo_6. The scale bar on both graphs is 20 μm. The sample preparation involved dispersing *ca*. 1 mg of intermetallic powder in 1 ml of hexane on sonication for 5 minutes. 100 μl drop of resulting solution cast on Cu foil.

To confirm the elements' distribution, the EDXS was used. It illustrated that Co_3Mo and Co_7Mo_6 are homogenous (Table 3-1). The average elements compositions are in line with the expected theoretical compositions ratios within the error of the measurements. The higher Mo content within the samples could be explained by the overlap between Cu (0.93 eV, L_α) and Co (0.76 eV, L_α), peaks which could lead to the underestimation of Co peak areas (Figure3-8). The Cu-peak was due to the X-ray beam penetrating down to Cu foil, which was used as a support for drop-casted sample in EDXS characterization.

Table 3-1: Elemental analysis of Co_3Mo and Co_7Mo_6 by EDXS. The results are the average of the values collected in several points across a sample and the errors present the standard deviations between the results at these points.

	Co_3Mo		**Co_7Mo_6**	
	Co	**Mo**	**Co**	**Mo**
at. % Exp.	73.57±1.79	28.5±2.1	50.55±0.82	49.5±0.82
at. % Theory	75	25	53.8	46.2

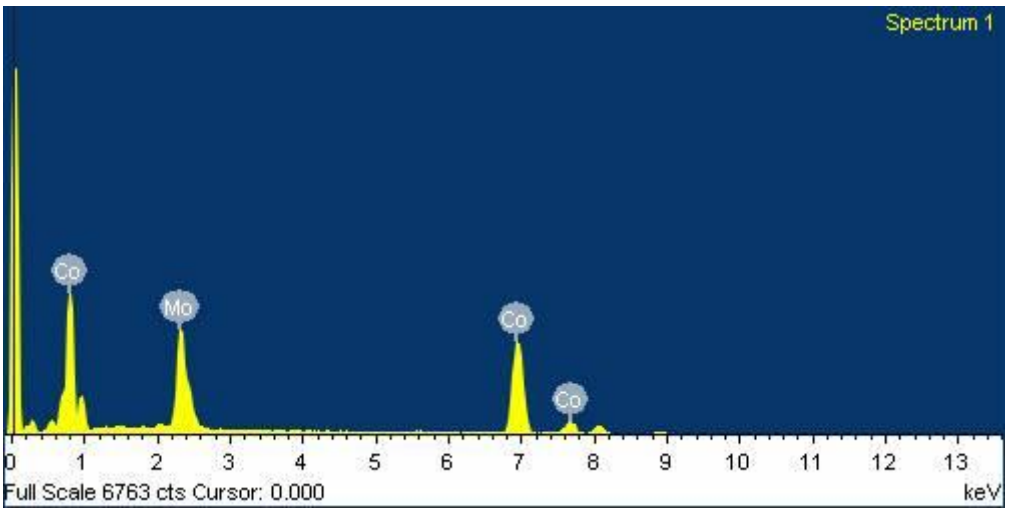

Figure 3-8: A representative EDXS spectrum of Co_3Mo sample. The peaks associated with Cu support are visible at 0.93 eV (Cu, L_α) and 8.04 eV (Cu, K_α).

3.3.5. Electrocatalytic activity of intermetallic

The Co_3Mo and Co_7Mo_6 intermetallic are interesting for the observation from electrochemistry point of view. Since both synthesised materials can show pure phase and similar roughness, the result of both intermetallic towards the HER could be accurately investigated. Here, LSV was used to investigate activity of Co_3Mo and Co_7Mo_6 as electrochemical catalysis in 0.5 H_2SO_4 solution, the overpotential values of 115 ± 8 mV and 160 ± 5 mV at the current density

10 mA cm^{-2} are observed from Co_3Mo and Co_7Mo_6 respectively, and higher overpotentials of 373 ± 7 mV and 411± 5 mV are achieved for Mo and Co at the same current density respectively (Figure 3-9). This observed overpotentials confidently make both Co_3Mo and Co_7Mo_6 intermetallic among the best electrocatalysts toward the HER in acidic media. [1,2,14]

To investigate the possible kinetics of the reaction, Tafel plots were studied and depicted in Figure 3-10. The resulting values of 71 ± 7 mV dec^{-1} and 84 ± 5 mV dec^{-1} are achieved from Co_3Mo and Co_7Mo_6 respectively, but which are outside the values for defined reaction mechanisms, i.e., 120 mV dec^{-1} (Volmer) and 40 mV dec^{-1} (Volmer-Heyrovsky).[14,15] Due to mass transport effects, Tafel slopes do not always follow perfect charge-transfer behaviour (Tafel behaviour) in powder materials.[16]

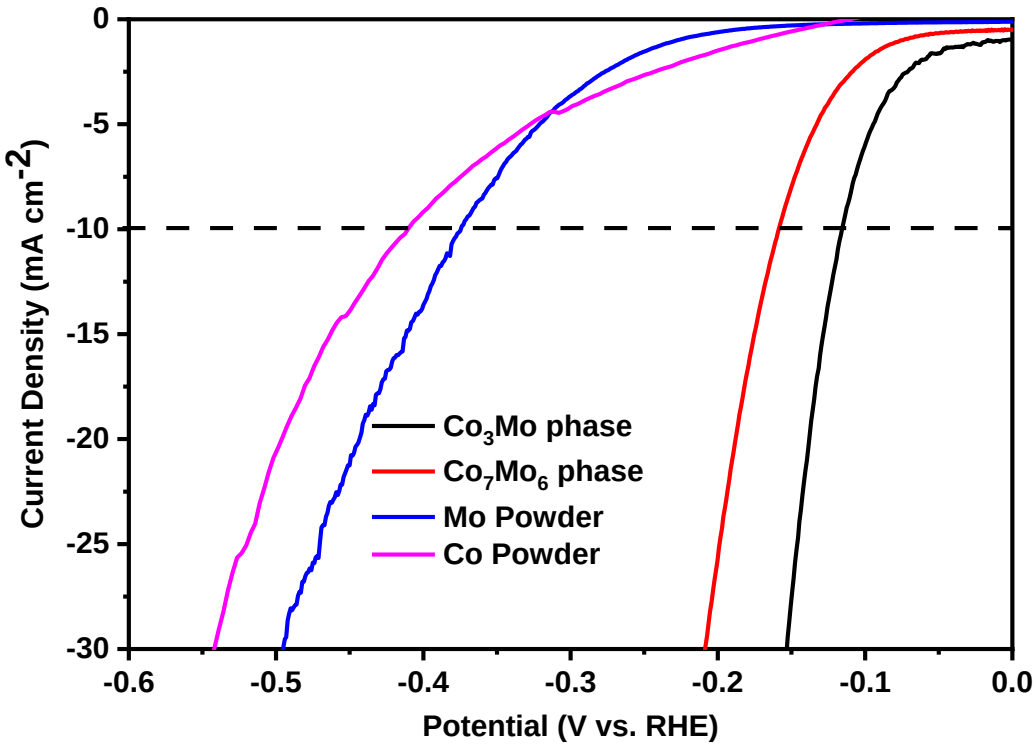

Figure 3-9: Electrochemical studies of Co-Mo intermetallic in 0.5 M H_2SO_4 electrolyte: Comparison of current densities achieved by Co_3Mo, Co_7Mo_6 as well as Mo and Co powders. The dashed line is guide to the eye at 10 mA cm^{-2}.

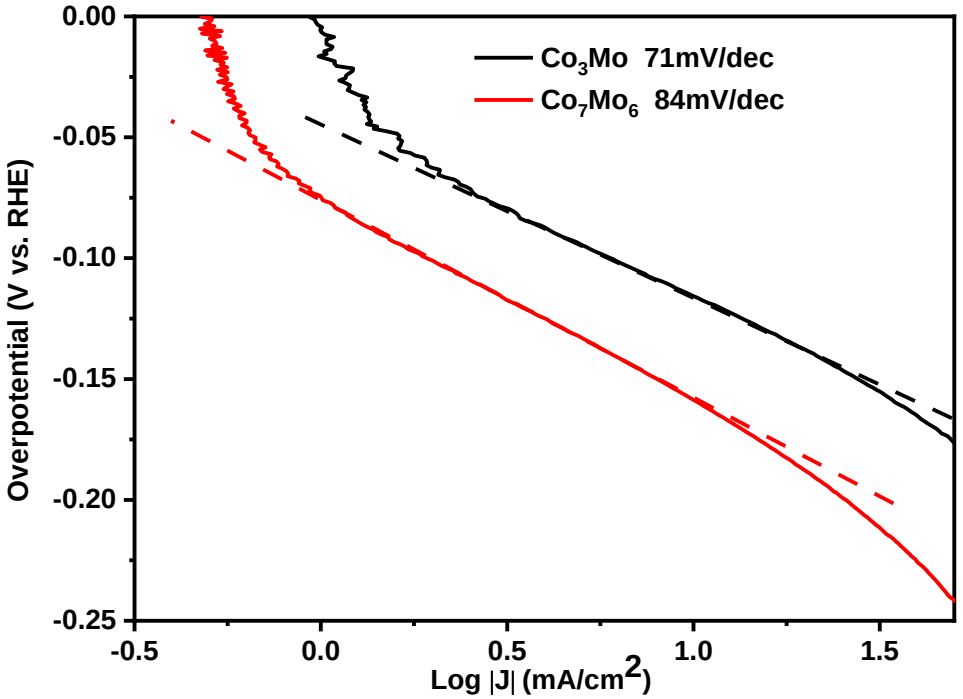

Figure 3-10: Tafel plots and corresponding Tafel slopes of Co_3Mo and Co_7Mo_6 in 0.5 M H_2SO_4 electrolyte. Catalysts were prepared on a glassy carbon working electrode as described in the experimental section. Carbon felt and 3 M Ag/AgCl were used as the counter and reference electrodes, respectively.

The stability of a catalyst is an important factor and must be assessed. In this respect, a constant potential over time were applied to evaluate electrocatalytic stability of the Co-Mo intermetallic (Figure 3-11). A clear decline in current densities observed for Co_3Mo, while the original values was retained over 16 hours without any evidence of decay for Co_7Mo_6. A good stability also was confirmed for Co_7Mo_6 upon cycling for 1000 times at a scan rate of 100 mV s^{-1}(Figure 3-12). The stability of Co_3Mo was also investigated by PXRD with the samples tested before and after 1000 times scanning directly on a glassy carbon electrode (Figure 3-13). The decomposition of the product was suggested by the disappearance of peak at *ca*. 43.8°. Comparing with Co_3Mo, the powder XRD of Co_7Mo_6 remain unchanged after 1000 times scanning (Figure 3-14), which indicted that higher Mo content could improve the Co-Mo intermetallic stability as electrocatalysts in acidic media, or this stability performance results from the high preparing reaction temperature (Co_3Mo was synthesised under 850°C but Co_7Mo_6 was prepared at 950°C). Thus, the Co-Mo system materials have potential as electrocatalysts to drive the HER and possibly even substitute expensive Pt.

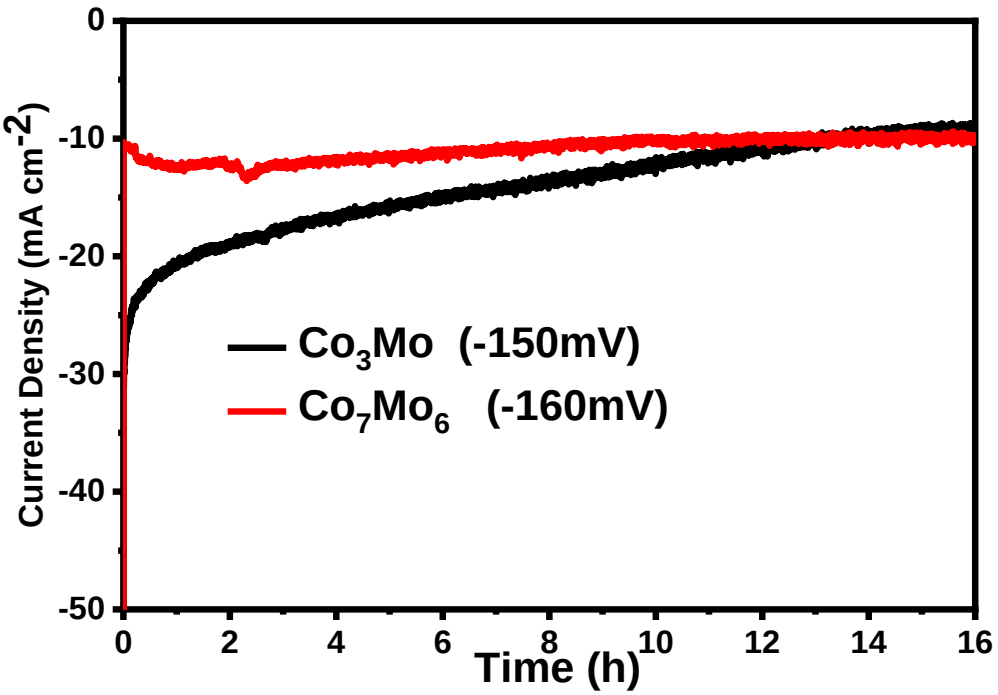

Figure 3-11: Chronoamperometry profiles of Co_3Mo and Co_7Mo_6 in 0.5 M H_2SO_4 at the applied potentials of 150 and 160 mV respectively. Experiments were performed using a three-electrode setup, with catalyst-deposited glassy carbon as the working electrode, 3 M Ag/AgCl as the reference and carbon felt as the counter electrode. Catalysts were prepared on a glassy carbon working electrode as described in the experimental section. Carbon felt and 3 M Ag/AgCl were used as the counter and reference electrodes, respectively.

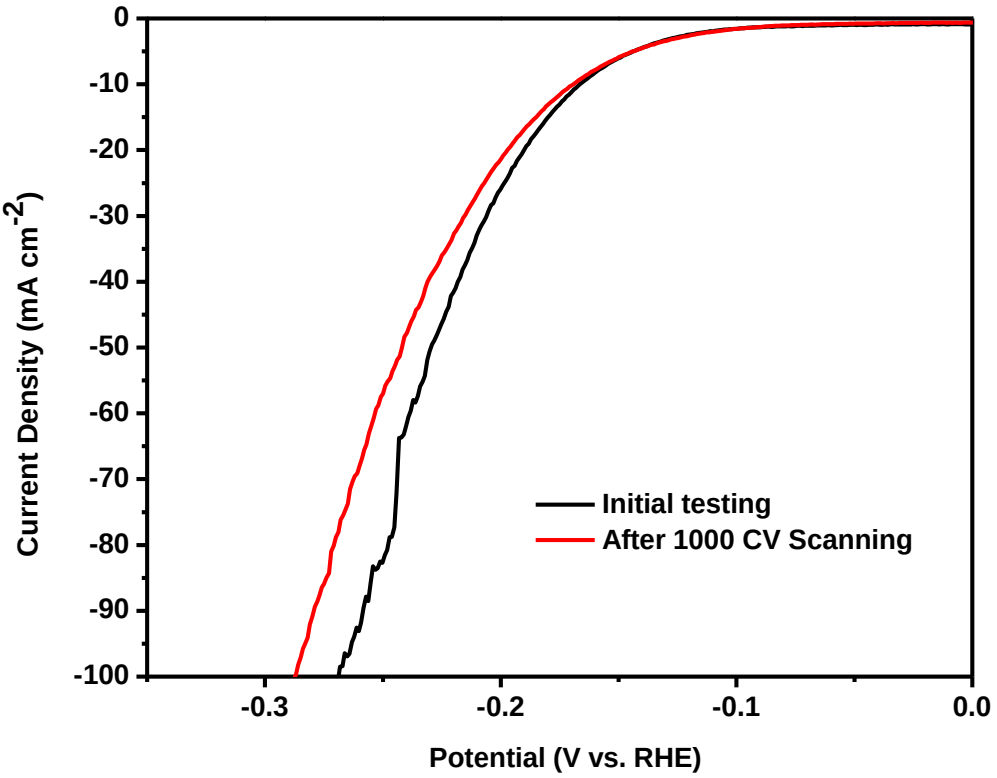

Figure 3-12: Comparison of current densities achieved by Co_7Mo_6 in 0.5M H_2SO_4 before and after 1000 scans at the scan rate of 100 mv s^{-1}.

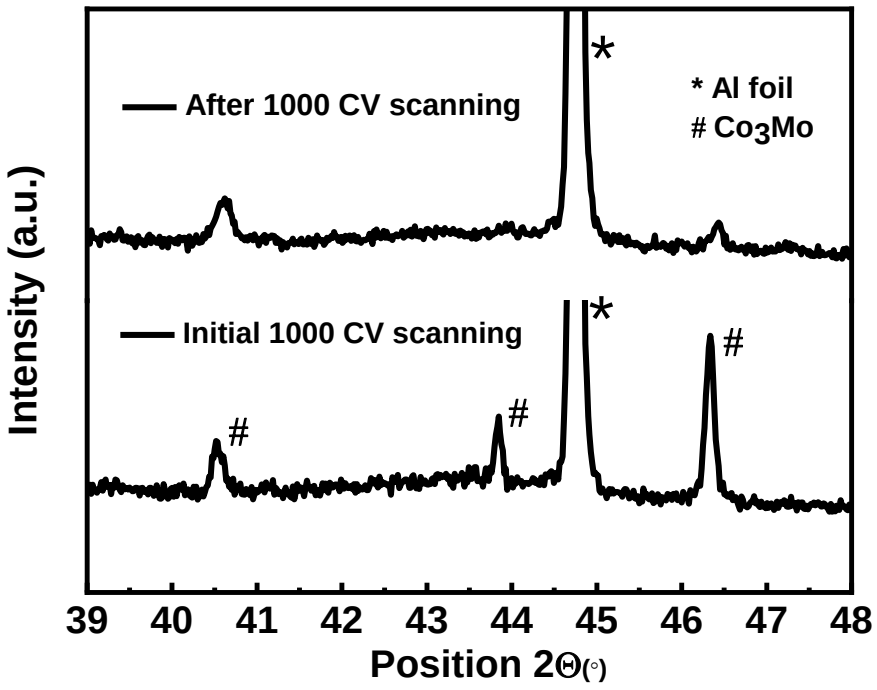

Figure 3-13: Comparison of Powder XRD pattern achieved by Co_3Mo in 0.5M H_2SO_4 before and after 1000 scans at the scan rate of 100 mV s^{-1}.

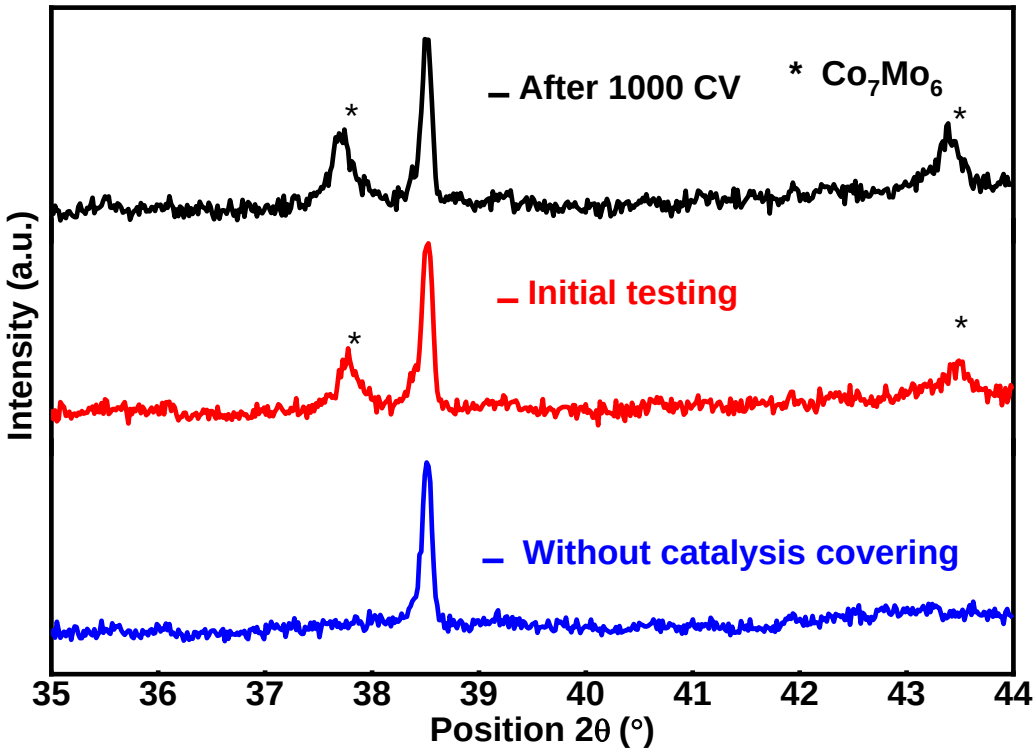

Figure 3-14: Comparison of Powder-XRD achieved by electrodes covered with phase Co_7Mo_6 and after 1000 CV scanning.

In addition, there are currently no electrochemical studies of Co_7Mo_6 in alkaline media. Therefore, it was interesting to study the performance of both intermetallics in 1 M KOH, LSV curves showed in Figure 3-15, and overpotentials of 120.5 ± 5 mV and 160 ± 5 mV at 10 mA cm^{-2} were observed by Co_3Mo and Co_7Mo_6, respectively. These seem high when compared with the reported Co_3Mo deposited on Ni foam (68 mV at 10 mA cm^{-2}). [11] However, immobilisation of Co_3Mo/Ni usually increase surface area as the currents are reported by normalisation to geometric surface area. Therefore, significantly lower OVP on Co_3Mo/Ni compared with free-standing Co_3Mo was expected which points out the importance of studying the catalytic performance in the absence of substrates.

Co_3Mo and Co_7Mo_6 also outperformed Co and Mo powder in alkaline media. Tafel slope was also investigated here, and the resulting 106 ± 9 mV dec^{-1} and 117 ± 5 mV dec^{-1} nearly to 120 mV dec^{-1} are achieved from Co_3Mo and Co_7Mo_6, respectively, as depicted in Figure 3-16. That values indicated that the electron transfer reaction leading to H-adsorption on the intermetallic catalyst surface is the rate determining step.[14,15] Finally, the stability of free-standing

Co_3Mo and Co_7Mo_6 as catalysts toward the HER in 1M KOH was evaluated as depicted in Figure 3-17. A clear fading of the current with time was still observed for Co_3Mo, which is in contrary to the previous report (reported high stability of Co_3Mo deposited on Ni foam and Cu substrate).[10,11]

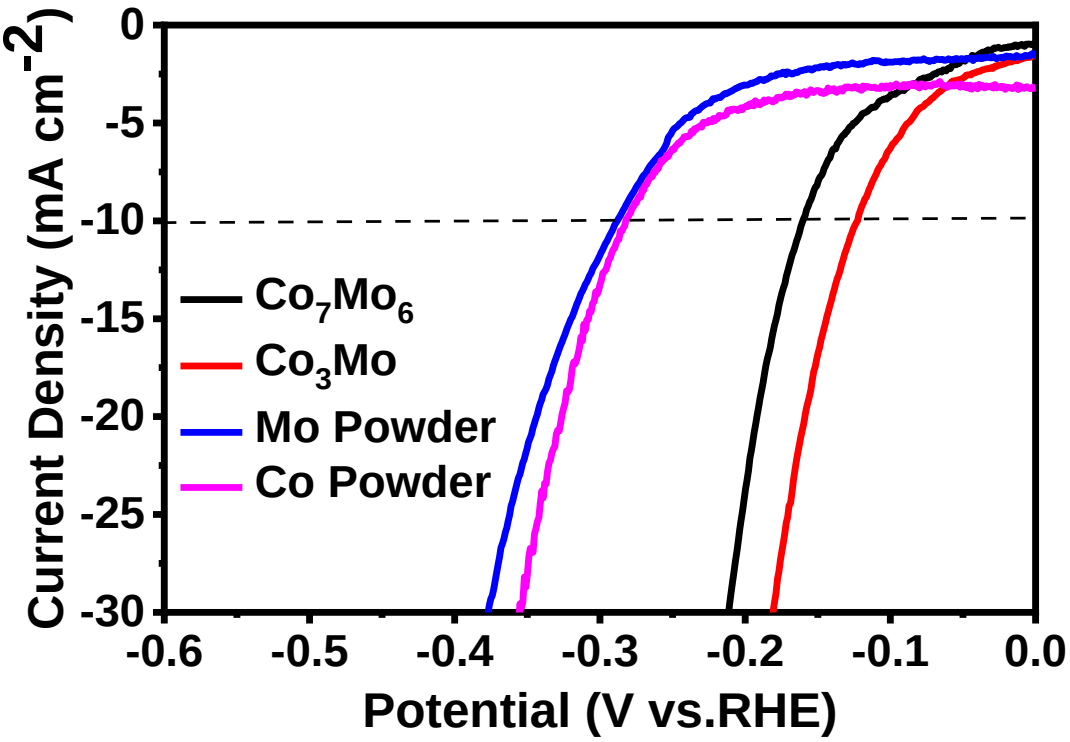

Figure 3-15: Comparison of current densities achieved by Co_3Mo, Co_7Mo_6 as well as Mo and Co powders in 1M KOH. The dashed line is guide to the eye at 10 mA cm^{-2}.

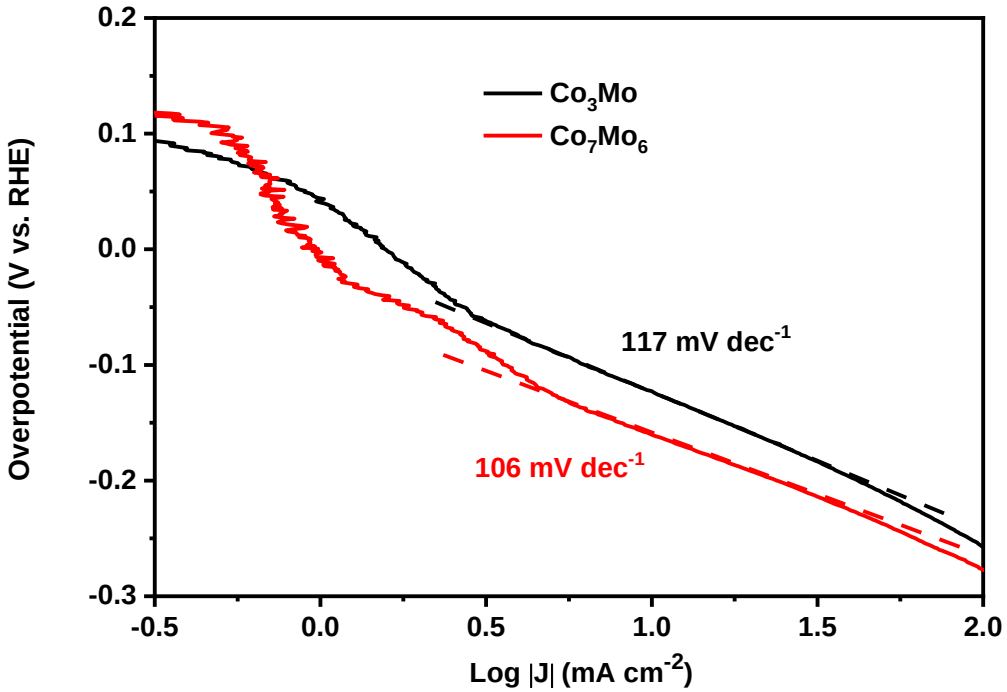

Figure 3-16: Tafel plots and corresponding Tafel slopes of Co_3Mo and Co_7Mo_6 in 1M KOH.

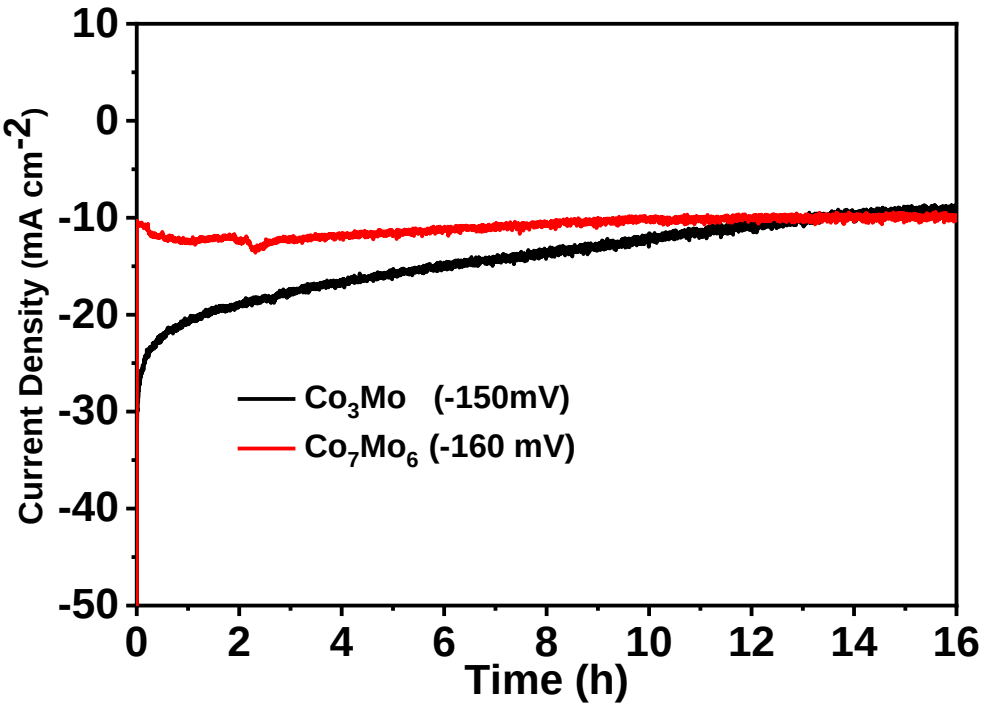

Figure 3-17: Controlled-potential chronoamperometry profile of Co_3Mo (black) and Co_7Mo_6 (red) in 1 M KOH under applied voltage of 123 mV and 140 mV corresponding to ca. 10 mA cm^{-2} respectively.

3.4. Conclusion

In conclusion, phase pure Co_3Mo and Co_7Mo_6 can be synthesised through heating the $CoMoO_x$ precursor. The evaluation of electrochemical performance points out that Co_3Mo in the free-standing form could routinely show good catalytic performance similar to previously studied classes of materials in acidic conditions. However, the poor stability makes it a suboptimal choice as an electrocatalyst for HER compared with Co_7Mo_6, which shows a marginally higher overpotential but keeps its performance unchanged after prolonged hours of stability testing.

3.5. References

[1] (a)ErmeteAntolini, Alloy vs. intermetallic compounds: Effect of the ordering on the electrocatalytic activity for oxygen reduction and the stability of low temperature fuel cell catalysts, *Applied Catalysis B: Environmental*. 217 (**2017**) 201-213 (b)M. Schalenbach, A.R. Zeradjanin, O. Kasian, S. Cherevko, K.J.J. Mayrhofer, A Perspective on Low-Temperature Water Electrolysis-Challenges in Alkaline and Acidic Technology, *Int. J. Electrochem. Sci*. 13 **(2018)** 1173–1226. https://doi.org/10.20964/2018.02.26.

[2] L. Rößner, M. Armbrüster, Electrochemical Energy Conversion on Intermetallic Compounds: A Review, *ACS Catal*. 9 (**2019**) 2018–2062. https://doi.org/10.1021/ACSCATAL.8B04566.

[3] M.M. Jaksic, Hypo–hyper-d-electronic interactive nature of synergism in catalysis and electrocatalysis for hydrogen reactions, *Electrochim. Acta*. 45 (**2000**) 4085–4099. https://doi.org/10.1016/S0013-4686(00)00525-9.

[4] A. Buttler, H. Spliethoff, Current status of water electrolysis for energy storage, grid balancing and sector coupling via power-to-gas and power-to-liquids: A review, Renew. *Sustain. Energy Rev*. 82 (**2018**) 2440–2454. https://doi.org/10.1016/J.RSER.2017.09.003.

[5] C.A.C. Sequeira, D.S.P. Cardoso, L. Amaral, B. Šljukić, D.M.F. Santos, On the performance of commercially available corrosion-resistant nickel alloys: A review, *Corros. Rev*. 34 (**2016**) 187–200. https://doi.org/10.1515/corrrev-2016-0014.

[6] D. Jin, A. Yu, Y. Lee, M.H. Kim, C. Lee, Ni_xRh_1−xbimetallic alloy nanofibers as a pH-universal electrocatalyst for the hydrogen evolution reaction: The synthetic strategy and fascinating electroactivity, *J. Mater. Chem. A*. 8 (**2020**) 8629–8637. https://doi.org/10.1039/D0TA02005B

[7] M. Schalenbach, F.D. Speck, M. Ledendecker, O. Kasian, D. Goehl, A.M. Mingers, B. Breitbach, H. Springer, S. Cherevko, K.J.J. Mayrhofer, Nickel-molybdenum alloy catalysts for the hydrogen evolution reaction: Activity and stability revised, *Electrochim. Acta*. 259 (**2018**) 1154–1161. https://doi.org/10.1016/J.ELECTACTA.2017.11.069.

[8] J.M.V. Nsanzimana, Y. Peng, M. Miao, V. Reddu, W. Zhang, H. Wang, B.Y. Xia, X. Wang, An Earth-Abundant Tungsten-Nickel Alloy Electrocatalyst for Superior Hydrogen Evolution, *ACS Appl. Nano Mater*. 1 (**2018**) 1228–1235. https://doi.org/10.1021/ACSANM.7B00383..

[9] J.G. Highfield, E. Claude, K. Oguro, Electrocatalytic synergism in Ni/Mo cathodes for hydrogen evolution in acid medium: A new model, *Electrochim. Acta*. 44 (**1999**) 2805–2814.

https://doi.org/10.1016/S0013-4686(98)00403-4.

[10] H. Shi, Y.T. Zhou, R.Q. Yao, W. Bin Wan, X. Ge, W. Zhang, Z. Wen, X.Y. Lang, W.T. Zheng, Q. Jiang, Spontaneously separated intermetallic Co_3Mo from nanoporous copper as versatile electrocatalysts for highly efficient water splitting, *Nat. Commun*. 11 (**2020**). https://doi.org/10.1038/S41467-020-16769-6.

[11] J. Chen, Y. Ge, Q. Feng, P. Zhuang, H. Chu, Y. Cao, W.R. Smith, P. Dong, M. Ye, J. Shen, Nesting Co_3Mo Binary Alloy Nanoparticles onto Molybdenum Oxide Nanosheet Arrays for Superior Hydrogen Evolution Reaction, *ACS Appl. Mater. Interfaces*. 11 (**2019**) 9002–9010. https://doi.org/10.1021/acsami.8b19148.

[12] J.B. Forsyth, L.M.D. Da Veiga, The structure of the μ-phase Co_7Mo_6, *Acta Crystallogr*. 15 (**1962**) 543–546. https://doi.org/10.1107/S0365110X62001401.

[13] L. Alte da Veiga, IUCr, Refinement of the structure of the phase Co_2Mo, *Acta Cryst*. 18 (**1965**) 855–857. https://doi.org/10.1107/S0365110X65002098.

[14] I. Roger, M.A. Shipman, M.D. Symes, Earth-abundant catalysts for electrochemical and photoelectrochemical water splitting, *Nat. Rev. Chem*. 1 (**2017**). https://doi.org/10.1038/S41570-016-0003.

[15] A. Lasia, Mechanism and kinetics of the hydrogen evolution reaction, *Int. J. Hydrogen Energy*. 44 (**2019**) 19484–19518. https://doi.org/10.1016/J.IJHYDENE.2019.05.183.

[16] D. Li, C. Batchelor-McAuley, R.G. Compton, Some thoughts about reporting the electrocatalytic performance of nanomaterials, *Appl. Mater. Today*. 18 (**2020**). https://doi.org/10.1016/J.APMT.2019.05.011.

Chapter 4. Investigation of cobalt molybdenum nitrides with η-carbide structure

Non-precious metal alloys could achieve good performance for driving the HER as discussed in Chapter 3. However, the poor stability and high reaction temperatures make Co-Mo alloys system a suboptimal choice for developing future electrocatalytic materials. As discussed in Chapter 3, the recent studies found that the binary transition metal nitrides tend to show better catalytic activity and durability for the HER in acidic media. In particular, MoN was found to have a better stability than Mo metal. Thus, the electrochemical properties of Co-Mo-based ternary nitrides are expected to improve compared with alloys.

4.1 Introduction

Although several examples of binary transition metal nitrides have been studied for the HER in acidic media, they tended to show a better stability compared with a stand-alone metal catalyst.[1] However, all of them were tested as composite systems. Therefore, it is difficult to tell whether the activity is due to the actual nitride performance or other factors such as morphology, impurities and/or substrate. Binary MoN serves as a good example, as the change of substrate from graphitic to N-doped carbon was shown to induce significant change in performance with overpotential (OVP) at 10 mA cm^{-2} shifting from 150 mV to almost 325 mV.[1] Similar results were observed on nanostructured MoN, which seemed to benefit from the use of N-doped carbon, with a huge shift from 62 mV to 258 mV in a bulk MoN.[2] It appears that despite being more stable under acidic conditions than Mo metal, MoN shows relatively high OVP when tested in free-standing form without support.

Surprisingly, ternary nitride electrocatalysts have remained relatively unexplored up to date in acidic media. Especially, there have been only limited number of studies into nitrides as electrocatalysts in the past, and those reported that had delivered reasonable performance were generally with poorly defined compositions, contained impurity phases or / and were composite materials as well.[3] Therefore, there is an imperative for phase pure ternary nitrides to be made and tested without obscuring effects of impurities and substrates. This is especially important when experiments are supported by computational studies as it allows for putting the predictions to the test.

In the literature several Co-Mo-based ternary nitrides have been reported to display WC structure.[4–6] However, this is quite unusual as this type ternary nitrides normally made in pure phase in η-carbide structure with the form of Co_3Mo_3N as shown in Figure 1.[7] The structure consists of the network of corner-sharing Mo_6N octahedra while Co-atoms are filling

the voids in-between. In addition, phase pure Co_3Mo_3N has been tested for electrochemical studying application only as catalyst for the oxygen evolution and oxygen reduction reaction in alkaline media.[8,9]

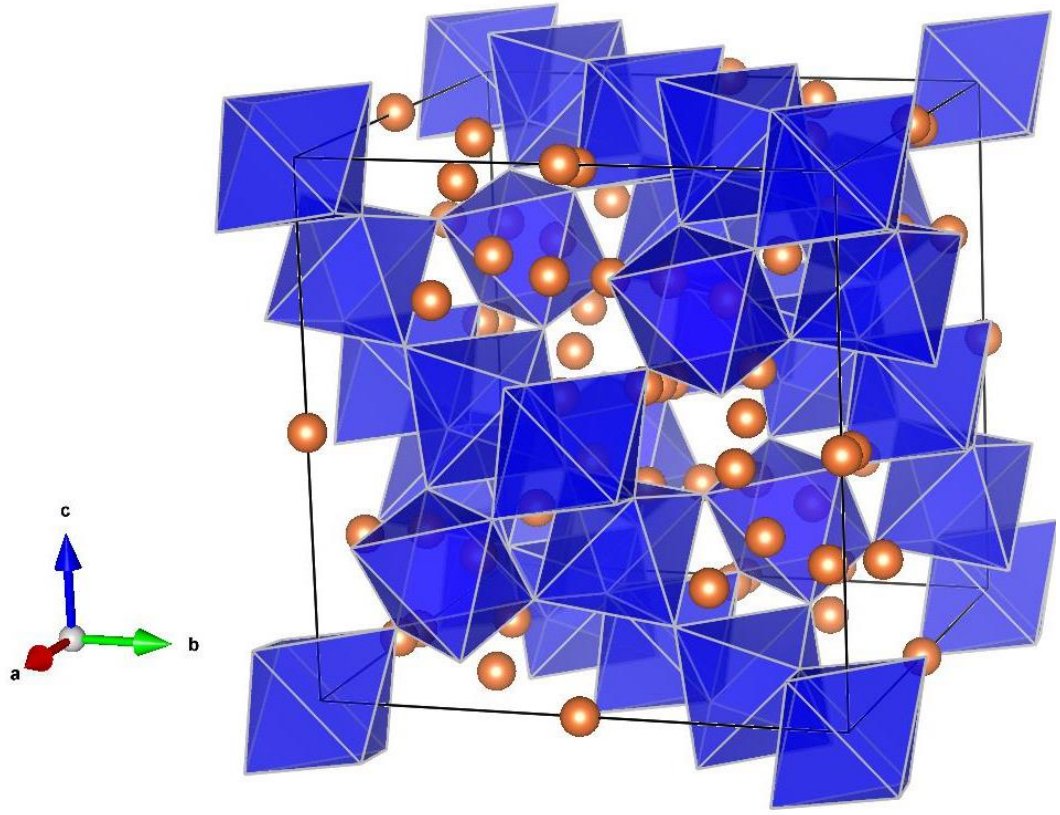

Figure 4-1. Crystal structure of Co_3Mo_3N showing the network of corner sharing Mo_6N-octahedra (blue). Mo and N atoms are omitted for clarity while Co-atoms are shown as orange spheres.

4.2. Aims

As Co_3Mo_3N could be synthesised in a single phase through the reaction of Co-Mo oxide precursor with H_2/N_2 gas mixture, [10] we aimed at using this route to synthesize of phase pure Co_3Mo_3N. To test whether Co-sites are electrocatalytic, the substitution of cobalt atom in Co_3Mo_3N with iron to form Fe_3Mo_3N was carried out. The partial removal of nitrogen from Co_3Mo_3N structure allows the formation of Co_6Mo_6N which could help with aim of studying the role of nitrogen-sites as catalytic for the HER.

4.3. Synthesis and characterisation of nitrides

4.3.1. Preparation of Co_3Mo_3N

Single phase Co_3Mo_3N was prepared through two steps: firstly, the Co-Mo oxide precursor was synthesised by using the citric acidic method with some modifications.[11,12] In this typical synthesis, 5.66 mmol $Co(NO_3)_2 \cdot 6H_2O$ (Alfa Aesar, ACS reagent, ⩾ 99.0%), 0.81 mmol $(NH_4)_6Mo_7O_{24} \cdot 4H_2O$ (Sigma-Aldrich, ACS reagent, ⩾ 99.0 %) and 22.6 mmol citric acid monohydrate, $C_6H_8O_7 \cdot H_2O$ (Alfa Aesar, ⩾ 99.5 %) were added into a 150 ml pyrex beaker and fully dissolved in 80 ml deionised water on stirring at room temperature. The water was evaporated at 120 ℃ resulting in foam looking products as depicted in Figure 4-2 (left).

The foams were calcined within the same beaker in air in a box furnace at 500 ℃ for 12 hours to eliminate any traces of carbon. The calcined foams of oxides grounded to black powders and confirmed as carbon-free by elemental analysis. Next, Co_3Mo_3N was synthesised by nitridation of the oxide precursor prepared as following. 200 mg of the precursor were placed into a ceramic boat within a tube furnace under flow of 5% H_2 in N_2 gas mixture with a flow rate of 10 mL / min. The heating rate was set at 5 ^oC / min and after 5 hours of reaction time at 750 ℃ the furnace was cooled naturally to the ambient temperature.

Figure 4-2: The foam of the oxide precursor prepared through citric acid routes for the CoMo-oxide precursor (left side with pink colour), the foam of the oxide precursor for the FeMo-oxide precursor (right side with black colour).

The resulting black powder was analysed in PXRD and showed a diffraction pattern displayed in Figure 4-3. The Rietveld refinement of PXRD data using the η-carbide-W_3Fe_3C structure-type as a model revealed that Co_3Mo_3N was a single phase product without any crystalline impurities (Table 4-1) The unit cell parameter of Co_3Mo_3N (a = 11.0139(3) Å) is smaller than values observed from the literature data for the products synthesised by nitridation of oxides either in NH_3 or H_2 (10 %) / N_2 mix, suggesting that the nitride synthesised in this work had slightly lower N-content.[10,11,13] This is in line with the results of elemental analysis for nitrogen (Co_3Mo_3N - Expt. N: 2.79±0.04 wt.%, Theory: N: 2.93 wt.% (Table 4-2)) that showed slightly lower N-content which is probably due to the lower temperature or / and lower H_2-content in syngas used here. In addition, the EDXS analysis collected in 3 random spots across the sample and the result showed that the ratio of Co to Mo is close to expected value as showed in Table 4-3, the purity is further confirmed.

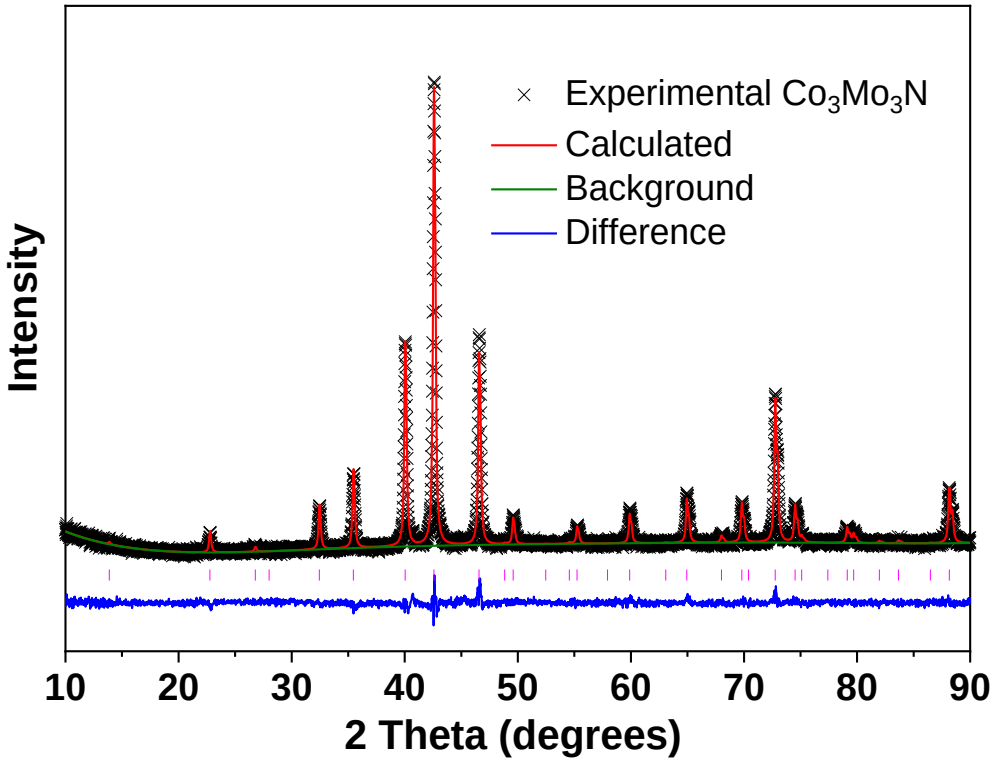

Figure 4-3: Rietveld refinement of PXRD data (CuK_α) for Co_3Mo_3N using the structure model based on reported Co_3Mo_3N structure (Space group: *Fd*-3*m*). Measured data are shown as crosses; the calculated profile is shown by a solid line through the measured data. The difference profile is shown along the bottom of the plot. Vertical bars represent the reflection positions for the phase.

Table 4-1: Structural parameters for the Rietveld refinement of the PXRD data collected on Co_3Mo_3N powder sample using structural model based on reported Co_3Mo_3N structure (Space group: *Fd*-3*m*) at ambient temperature. Estimated errors in the last digits are given in parentheses. The number of observations 4488, fitting profile (R_p)= 3.59%, weighed profile (R_{wp})= 5.10%.The value of the lattice constant a = 11.0139(3) Å. (Literature: a = 11.02089(14) Å prepared in H_2(10%)/ N_2; 11.027 Å and 11.038 Å prepared by ammonolysis of metal oxides in NH_3).[6,11,13,14]

	Site	x/a	y/b	z/c	Occupancy	B_{iso} (Å^2)
Mo	48*f*	0.3250(1)	0.125	0.125	1.0	0.0047(4)
Co1	32*e*	0.2922(1)	0.2922(1)	0.2922(1)	1.0	0.0071(9)
Co2	16*d*	0.5	0.5	0.5	1.0	0.0070(13)
N	16*c*	0	0	0	1.0	0.0038

Table 4-2: The results of microanalysis for nitrogen content in nitrides.

	Co_3Mo_3N	Co_6Mo_6N	Fe_3Mo_3N
N (Theory, wt. %)	2.93	1.48	2.98
N (experiment, wt. %)	2.79±0.04	1.23±0.05	2.92±0.07

Table 4-3: Results of the EDXS analysis collected in 3 random spots across the sample. The errors are calculated as additive of the standard deviation of the averages from 3 spots and instrumental error of 0.81 %. Due to the semi-qualitative nature of the detection of light elements by EDXS the N-content was excluded from the calculations.

Elemental composition	Co_3Mo_3N at. %		Co_6Mo_6N at. %		Fe_3Mo_3N at. %	
	Co	Mo	Co	Mo	Fe	Mo
Experiment	45.56±1.05	54.43±1.05	45.94±0.55	54.06±0.55	45.91±0.45	54.09±0.45
Theory	50	50	50	50	50	50

4.3.2. Preparation of Fe_3Mo_3N

Similar to synthesis Co_3Mo_3N, 5.66 mmol $Fe(NO_3)_3 \cdot 9H_2O$ (Alfa Aesar, ACS reagent, ≥ 99.0%), 0.81 mmol $(NH_4)_6Mo_7O_{24} \cdot 4H_2O$ (Sigma-Aldrich, ACS reagent, ⩾ 99.0 %) and 22.6 mmol citric acid monohydrate, $C_6H_8O_7 \cdot H_2O$ (Alfa Aesar, ⩾ 99.5 %) were added into a 150 ml pyrex beaker and fully dissolved in 80 ml deionised water on magnet stirring at room temperature. The water was evaporated at 120 ℃ resulting in foam looking products. The foams were calcined within the same beaker in air in a box furnace at 500 ℃ for 12 hours to eliminate any traces of carbon as shown in Figure 4-2 (right). The calcined foams of oxides were reground to black powders and confirmed as carbon-free by elemental analysis. Next, Fe_3Mo_3N was synthesised by nitridation of the oxide precursor prepared as following. 200 mg of the precursor were placed into a ceramic boat within a tube furnace under flow of 5% H_2 in N_2 gas mixture with a flow rate of 10 mL / min. The heating rate was set at 5 ^oC / min and after 5 hours of reaction time at 750 ℃ the furnace was cooled naturally to the ambient temperature.

The resulting black powder was analysed in PXRD as well and the Rietveld refinement of powder X-ray diffraction (PXRD) data using the η-carbide-W_3Fe_3C structure-type as a structural model revealed that Fe_3Mo_3N was pure phase as shown in Figure 4-4. The unit cell parameters of obtained Fe_3Mo_3N are a = 11.0707(8) Å (Table 4-4), which is in agreement with the literature data suggesting that the sample is close to ideal stoichiometry.[13] This is in line with the results of elemental analysis for nitrogen as showed in Table 4-2 and Table 4-3. At this point it should be stated we observed traces of carbon at *ca*. 0.1 wt. %. These are at the normal background level and we deem them unlikely to stem from ternary metal carbides as these would be detectable by PXRD.

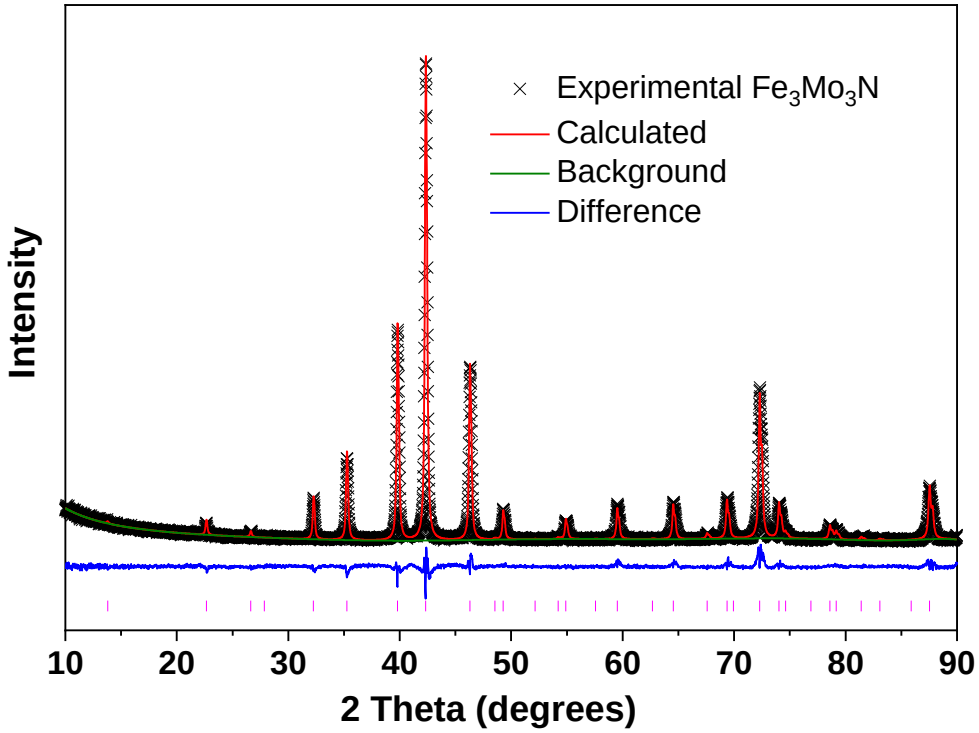

Figure 4-4: Rietveld refinement of PXRD data (CuK$_\alpha$) for Fe_3Mo_3N using the structure model based on reported Co_3Mo_3N structure (Space group: *Fd*-3*m*). Measured data are shown as crosses; the calculated profile is shown by a solid line through the measured data. The difference profile is shown along the bottom of the plot. Vertical bars represent the reflection positions for the phase.

Table 4-4: Structural parameters for the Rietveld refinement of the PXRD data collected on Fe_3Mo_3N powder sample using structural model based on reported Co_3Mo_3N structure (Space group: *Fd*-3*m*) at ambient temperature. Estimated errors in the last digits are given in parentheses. The number of observations 4488, fitting profile (R_p)= 9.90%, weighed profile (R_{wp})= 12.82%.The value of the lattice constant a = 11.0707(8) Å. (Literature: a = 11.07908 Å prepared in H_2(10%)/ N_2; 11.0859 Å and 10.9656 Å prepared by ammonolysis of metal oxides in NH_3).[13,15]

	Site	x/a	y/b	z/c	Occupancy	B_{iso} (Å^2)
Mo	48*f*	0.3202(4)	0.125	0.125	1.0	0.0048(4)
Fe1	32*e*	0.2926(6)	0.2926(6)	0.2926(6)	1.0	0.0087(3)
Fe2	16*d*	0.5	0.5	0.5	1.0	0.0031(4)
N	16*c*	0	0	0	1.0	0.0038

4.3.3. Preparation of Co_6Mo_6N

Nitrogen deficient nitride Co_6Mo_6N was prepared following a modified procedure described elsewhere.[10] In brief, 100 mg of oxide precursor were heated within the tube furnace using the same reaction conditions as for Co_3Mo_3N described above, except by using a H_2 (5 vol. %) / Ar gas mixture. The PXRD pattern of the resulting product was consistent with the previously reported one for Co_6Mo_6N. The Rietveld refinement of the PXRD data was also carried out to further confirm the single phase nature of the sample as shown in Figure 4-5 and Table 4-5. The unit cell parameter of a = 10.8810(1) Å was identified for this product, which is in an excellent match with the literature value of a = 10.8824 Å for samples determined as Co_6Mo_6N by neutron diffraction.[10] Importantly, the pure phase was further confirmed by elements analysis, the nitrogen content in this samples must be close to the theory value of 1.48 wt.%. this was confirmed by the elemental analysis on this samples with the result of 1.43 ± 0.04 wt.% closed to the expected value within the error of the measurement as shown in Table 4-2, the ratio of Co to Mo is close to expected value as shown in Table 4-3.

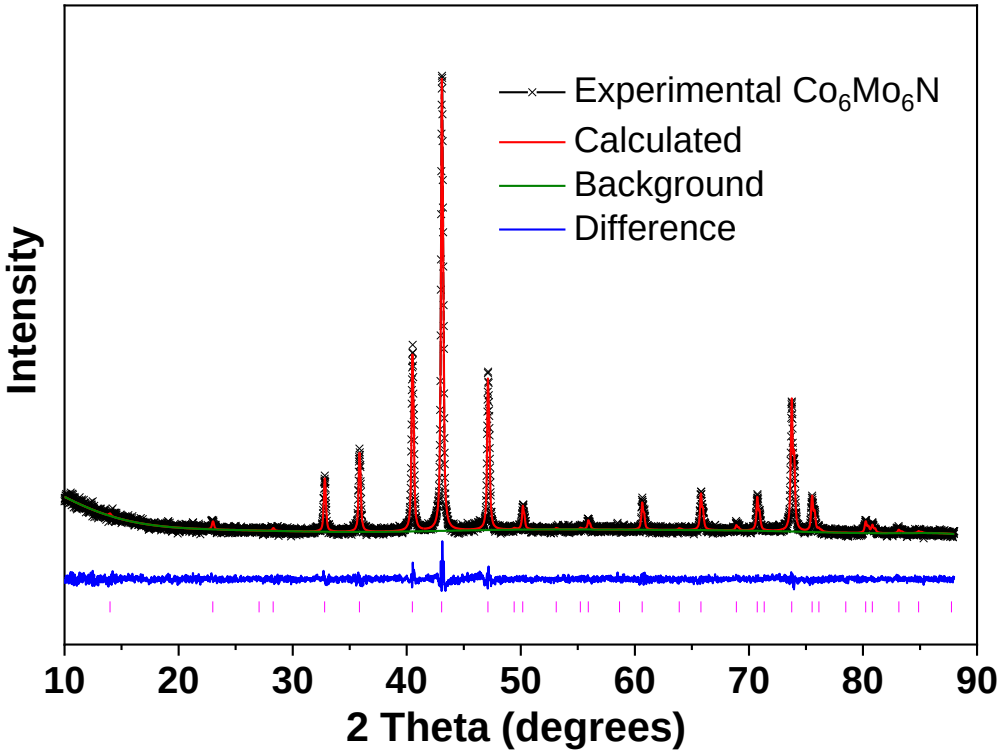

Figure 4-5: Rietveld refinement of PXRD data (CuKα) for Co_6Mo_6N using the structure model based on reported Co_6Mo_6C structure (Space group: *Fd*-3*m*). Measured data are shown as crosses; the calculated profile is shown by a solid line through the measured data. The difference profile is shown along the bottom of the plot. Vertical bars represent the reflection positions for the phase.

Table 4-5: Refined parameters for the Rietveld refinement of the PXRD data collected on Co_6Mo_6N powder sample using structural model based on the reported η-Co_6Mo_6C structure (Space group: *Fd*-3*m*) at ambient temperature. Estimated errors in the last digits are given in parentheses. The number of observations 4488, fitting profile (R_p)= 9.49%, weighed profile (R_{wp})= 8.55%. The value of the lattice constant a = 10.8810(1) Å. (Literature: a = 10.8824(16)Å[10])

	Site	x/a	y/b	z/c	Occupancy	B_{iso} (Å^2)
Mo	48*f*	0.3216(1)	0.125	0.125	1.0	0.0070(5)
Co1	32*e*	0.2936(1)	0.2936(1)	0.2936(1)	1.0	0.0078(3)
Co2	16*d*	0.5	0.5	0.5	1.0	0.0070(8)
N	8*a*	0.125	0.125	0.125	1.0	0.0038

4.4. Electrochemical investigation

4.4.1. Electrochemical investigation of Co_3Mo_3N

The composition of catalytic materials plays an important role in developing active cathodic materials for the HER, which is directly dependent on the overpotential used to operate the electrolyzer at significant current densities. Here, the obtained ternary nitride is of particular interest as electrocatalysis for HER activity because the samples were prepared in a single-phase form. This makes the understanding what role different elements play as electrocatalytic sites during the process of driving hydrogen production easier.

Co_3Mo_3N was deposited on the glassy carbon (GC) electrodes as described in Chapter 2 and tested by linear-sweep voltammetry in 0.5 M H_2SO_4 electrolyte (Figure 4-6, Red line). Co_3Mo_3N deliver an overpotential of 108 ± 8 mV at 10 mA cm^{-2} cathodic current density and are comparable to most reported nitride catalysts as list in Table 4-6. A very similar performance with Co_3Mo_3N was observed if part nitrogen content removed from its crystal to form Co_6Mo_6N (117 ± 12 mV) as shown in Figure 4-6 (Black line). This indicated that the nitrogen site is not the active site because a difference of performance would be observed in this case. To study role of the cobalt sites in this compound for electrocatalytic activity, we synthesised and tested Fe_3Mo_3N which crystallizes in the same structure as Co_3Mo_3N. However, a higher overpotential of 209 ± 8 mV at 10 mA cm^{-2} was observed from the free-standing Fe_3Mo_3N as shown in Figure 4-6 (blue line). Since replacing Co with Fe leads to deteriorated catalytic performance this points out that cobalt (rather than Mo) sites play the important role in the process of the HER.

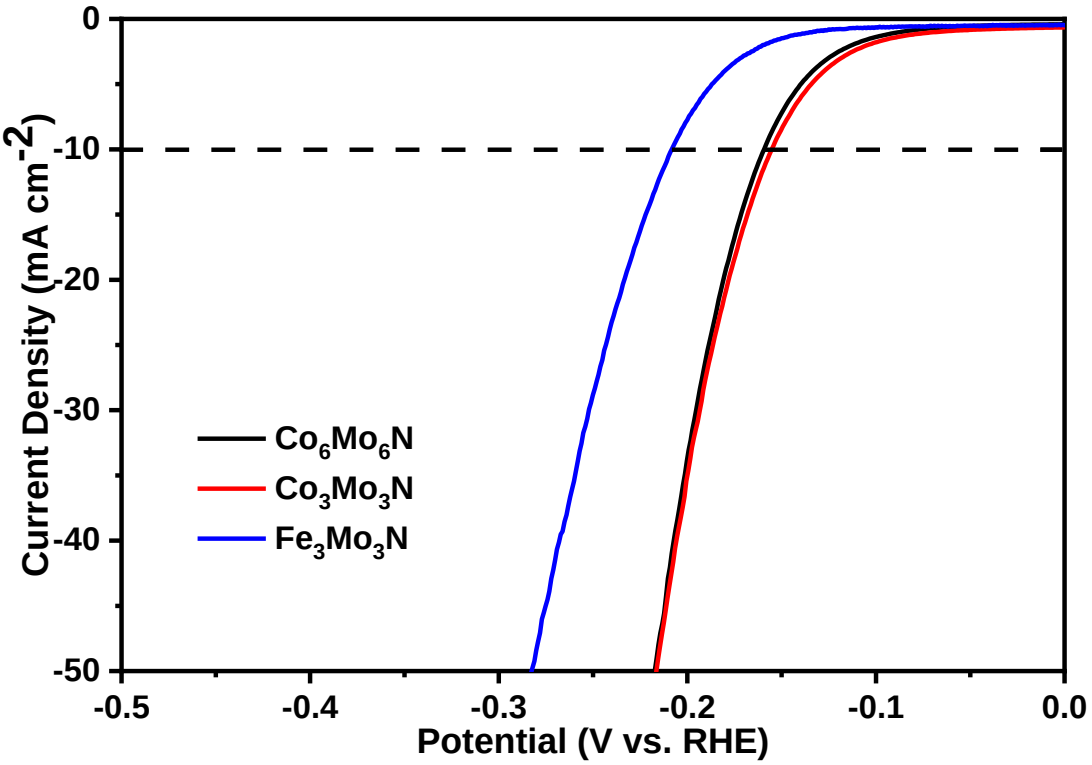

Figure 4-6: Comparison of the current densities achieved by Co_3Mo_3N (Red line), Co_6Mo_6N (Black line) and Fe_6W_6N (Blue line) in 0.5 M H_2SO_4. Catalysts were prepared on a glassy carbon working electrode as described in experimental section. An Ag/AgCl (3M KCl) reference and carbon felt counter electrode were used. Curves were obtained using linear sweep voltammetry with a scan rate of 5 mV s^{-1} and all resistance were compensated for resistance.

Table 4-6: Electrochemical properties of selected nitrides for HER in acidic media

Reported material description	**OVP at 10 mA/cm^2 (acidic media)**	**Tafel slope, mV dec^{-1}**	**ECSA mF/cm^2**	**Catalyst loading, mg/cm^2**	**Ref.**
$NiMoN_x$ / C nanosheet	–0.220 (0.1M $HClO_4$)@5 mA cm^{-2}	36	N/A	0.25	[3]
MoN / C nanosheet	–0.250 (0.1M $HClO_4$)@5 mA cm^{-2}	55	N/A	0.25	[3]
$Co_{0.6}Mo_{1.4}N_2$	–0.200 (0.1M $HClO_4$)	N/A	N/A	0.24	[14]
MoN Exfoliated	–0.290 (0.5M H_2SO_4)	90	1.56	N/A	[16]
MoN Bulk	–0.300 (0.5M H_2SO_4)@1 mA cm^{-2}	N/A	0.53	N/A	[16]
γ-Mo_2N	–0.300 (0.1M $HClO_4$)	N/A	N/A	1.15	[17]
Mo_2N / CNT–Graphene	–0.186 (0.5M H_2SO_4)	72	N/A	0.67	[18]
γ- Mo_2N	–0.381 (0.5M H_2SO_4)	108	N/A	0.12	[19]
MoN bulk	–0.258 (0.5M H_2SO_4)	134	0.69	0.145	[2]
Nanostructured MoN carbon	–0.128 (0.5M H_2SO_4)	52	18.59	0.285	[1]
MoN_x/NF	–0.148 (0.5M H_2SO_4)	114	11.01	N/A	[20]
Mo_2N/NC	-0.217(0.5M H_2SO_4)	115.7	N/A	0.5	[21]
Co_1Ni_1N	-0.142(0.5M H_2SO_4)	78.55	N/A	N/A	[22]
Co_2Ni_1N	-0.092(0.5M H_2SO_4)	55.30	N/A	N/A	[22]
Co_1Ni_2N	-0.171(0.5M H_2SO_4)	94.30	N/A	N/A	[22]

4.4.2. The investigation of intrinsic catalytic behaviour

The kinetics of the HER were studied by the analysis of corresponding Tafel plots; the similar Tafel slopes of 68.4 ± 5 mV and 69.7 ± 6 mV dec^{-1} were achieved by Co_3Mo_3N and Co_6Mo_6N respectively as shown in Figure 4-7. The observed values deviate significantly from the value of 40 mV dec^{-1} expected from Volmer – Heyrovsky mechanism which indicates that a more complex processes are at place. However, a higher value of 91.2 ± 5 mV per decade was observed for Fe_3Mo_3N than for Co-based nitrides. This is closer to the value of 120 mV dec^{-1} that is typically observed when Tafel mechanism is responsible for the HER, *e.g.*, when the adsorption of H^+ is rate limiting step. This again points out that the HER occurring on Co and Fe sites proceeds differently and as a result Co-sites are likely catalytic.

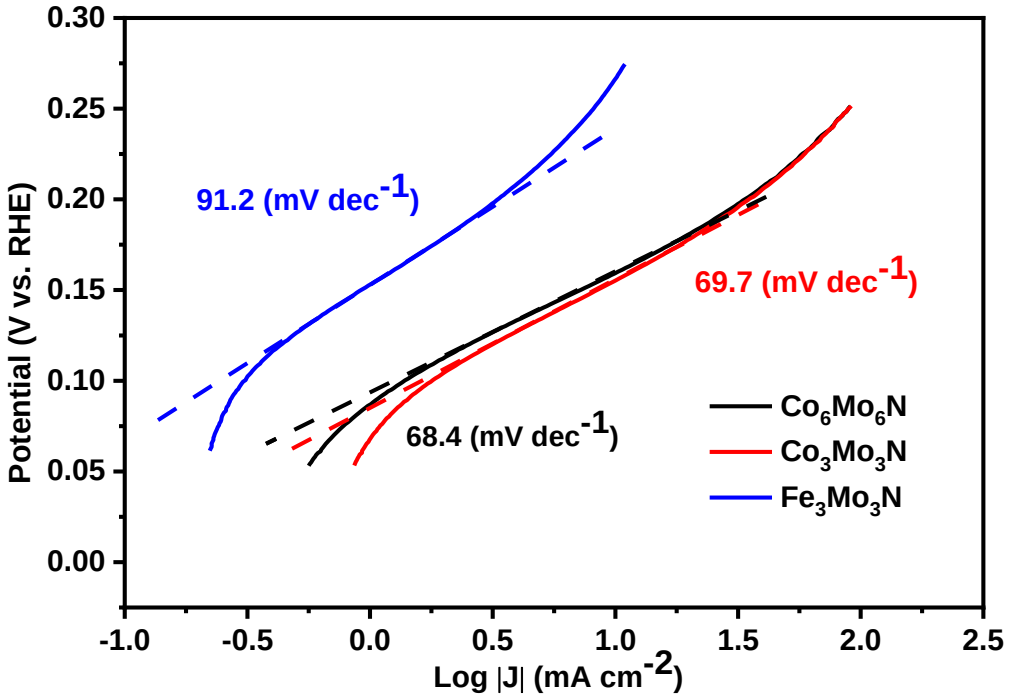

Figure 4-7: Tafel plots and corresponding Tafel slopes of Co_3Mo_3N (Red line), Co_6Mo_6N (Black line) and Fe_6W_6N (Blue line) in 0.5 M H_2SO_4 electrolyte. Slopes were obtained by linear sweep voltammetry with a scan rate of 5 mV s^{-1}. Dashed lines are provided as a guide to the eye. All current densities have been compensated for resistance.

Apart from the different reaction pathways on active site, there is another factor can influence the electrochemical performance. To test this, we carried out electrochemical impedance spectroscopy (EIS) experiments as shown in Figure 4-8. While Co_3Mo_3N and Co_6Mo_6N show almost the same charge-transfer resistance (R_{ct}) values of 32 Ω (*iR* compensated) and 31 Ω; the charge transfer resistance of 109 Ω in Fe_3Mo_3N is significantly higher. This suggest that

high charge-transfer properties and hydrogen evolution reaction kinetics in Co_3Mo_3N and Co_6Mo_6N catalysts as possible cause for improved performance over Fe_3Mo_3N.

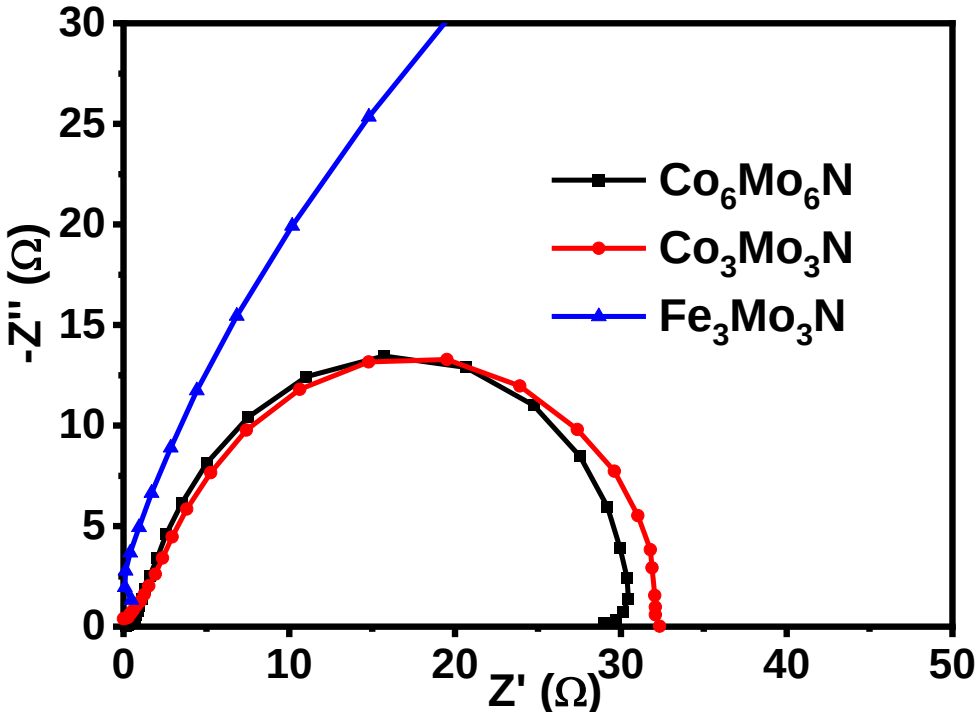

Figure 4-8: Nyquist plots showing electrochemical impedance spectroscopy at -150 mV (vs. RHE) in 0.5 M H_2SO_4 on the nitrides. Catalysts were prepared on a glassy carbon working electrode as described in the experimental chapter. Carbon felt and Ag/AgCl (3M KCl) were used as counter electrode and reference electrodes. All samples were compensated for iR.

In addition, as has been pointed out recently, the performance of catalysts could be estimated by the electrochemical active surface area (ECSA).[23,24] ECSA is directly proportional to double-layer capacitance (C_{dl}) which can be evaluated from CV curves obtained at various scan rates in the potential range. Therefore, C_{dl}, was proposed as the most appropriate method for evaluation of catalytic active surface in electrochemical system. As showed in Figure 4-9. Co_3Mo_3N and Co_6Mo_6N show almost identical C_{dl} values of 17.8 ± 0.9 and 16.9 ± 0.7 mF cm^{-2}, respectively, but a low value of 7.24 ± 0.5 mF cm^{-2} was achieved by Fe_3Mo_3N. That confirms that the cobalt sites should be active points for driving the hydrogen production. Since the morphology of a catalyst may play an important role in the catalytic properties, Scanning Electron Microscopy (SEM) was carried out to investigate the morphologies of Co_3Mo_3N, Co_6Mo_6N and Fe_3Mo_3N. Figure 4-10 demonstrate that the synthesised nitrides showed similar

morphology and surfaces. Therefore, the difference in performance is unlikely due to the morphology.

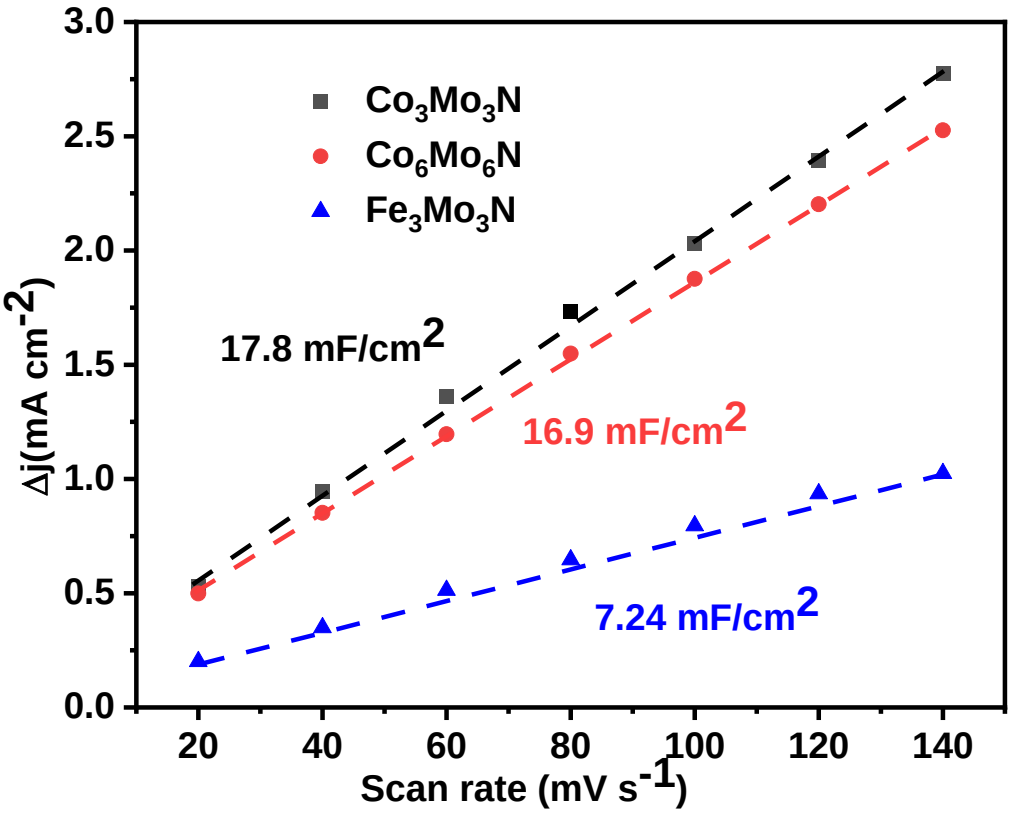

Figure 4-9: Charging current density differences ($\triangle j=j_a-j_c$) plotted against scan rates. The linear slope equivalent to twice of the double-layer capacitance C_{dl}, was used to represent the ECSA.

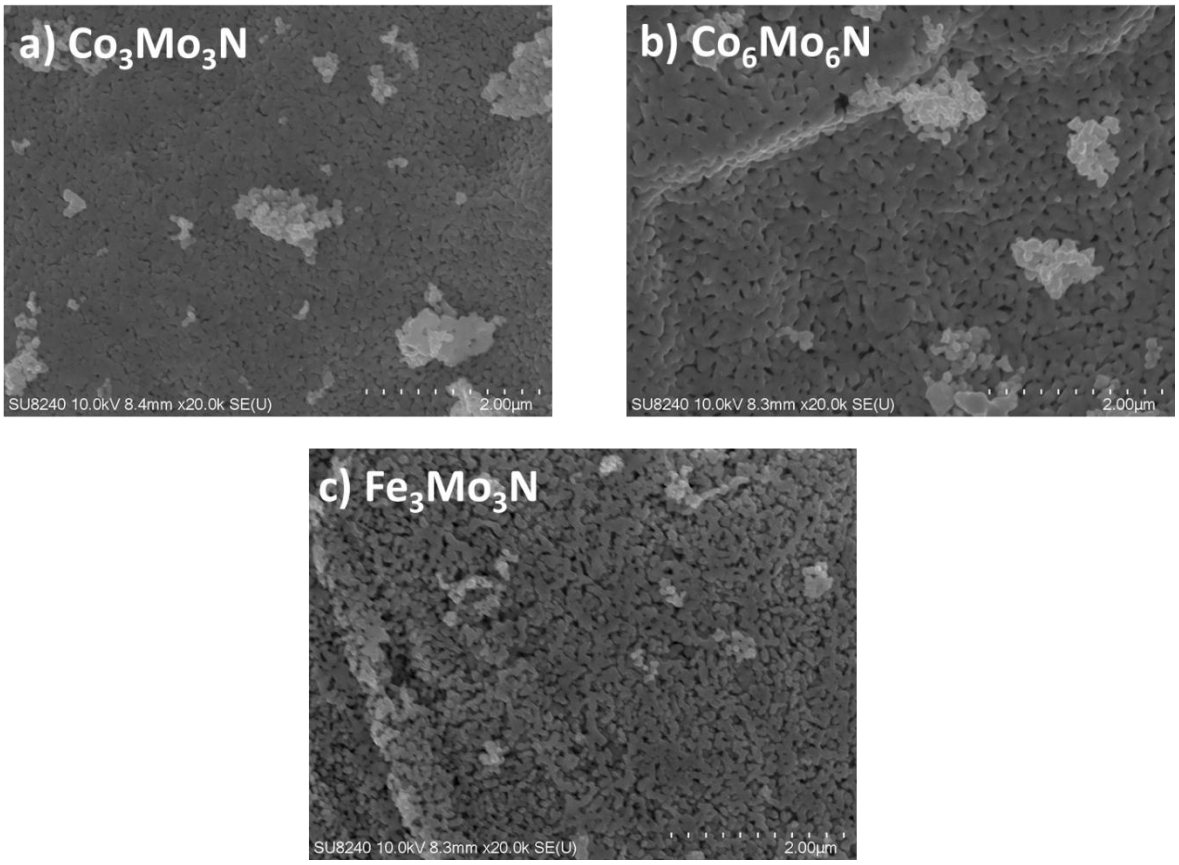

Figure 4-10: High magnification SEM images for (a) Co_3Mo_3N, (b) Co_6Mo_6N and (c) Fe_3Mo_3N synthesised under 750 ℃ with 5% H_2 in N_2 gas.

4.5. Stability studies of Co_3Mo_3N and Co_6Mo_6N

The testing of stability is a basic requirement for catalytic research. To investigate this, chronoamperometry was employed at a constant potential of 120 mV (vs. RHE) which corresponds to the overpotential required for the current density is -10 mA cm^{-2}. The current density remained stable when a constant potential was applied to Co_3Mo_3N deposited working electrode over 16 hours. Conversely, the decreasing of current density was observed from Co_6Mo_6N with time under the identical potential as shown in Figure 4-11. The experiment points out that Co_6Mo_6N is unstable. That a lower N-content reduces the stability was also found previously in the binary Mo-N system.[25] LSV investigation also showed that after 1000 CV cycles Co_6Mo_6N catalysts delivers significantly lower current densities (Figure 4-12), whereas the activity of Co_3Mo_3N remains unchanged (Figure 4-13).

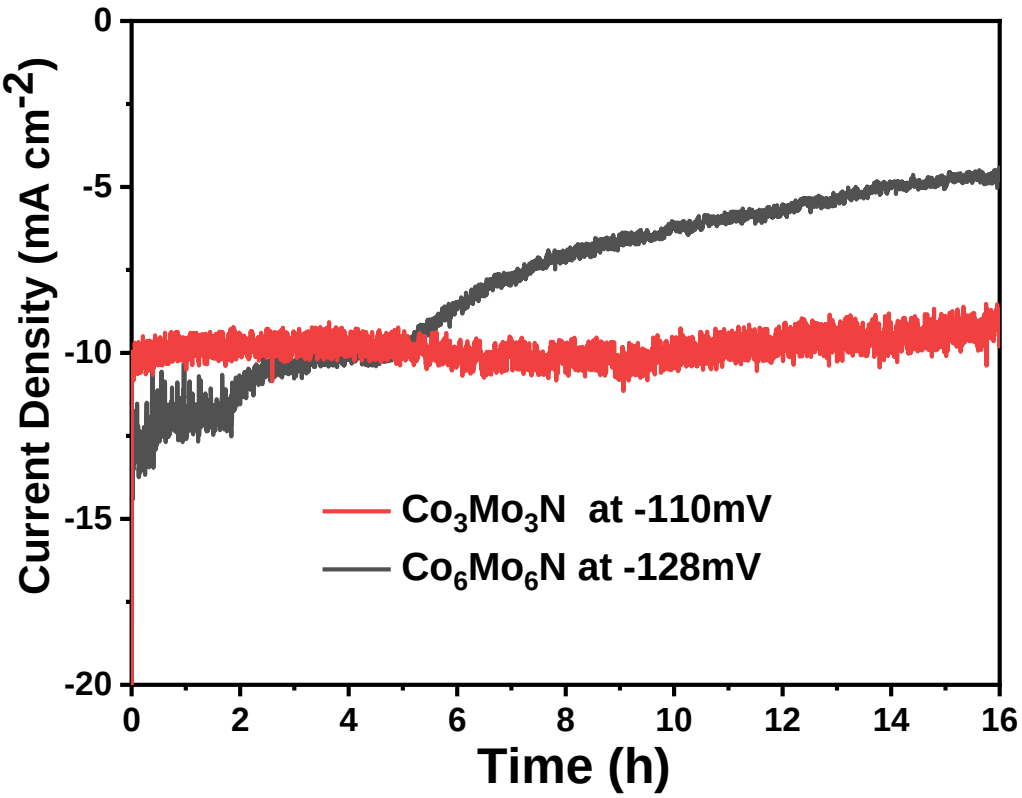

Figure 4-11: Chronoampermetry profile of Co_3Mo_3N and Co_6Mo_6N in 0.5 M H_2SO_4. The experiments were performed using a three-electrode step, with catalyst-deposited glassy carbon as the working electrode, 3 M Ag/AgCl as the reference and carbon felt as the counter electrode.

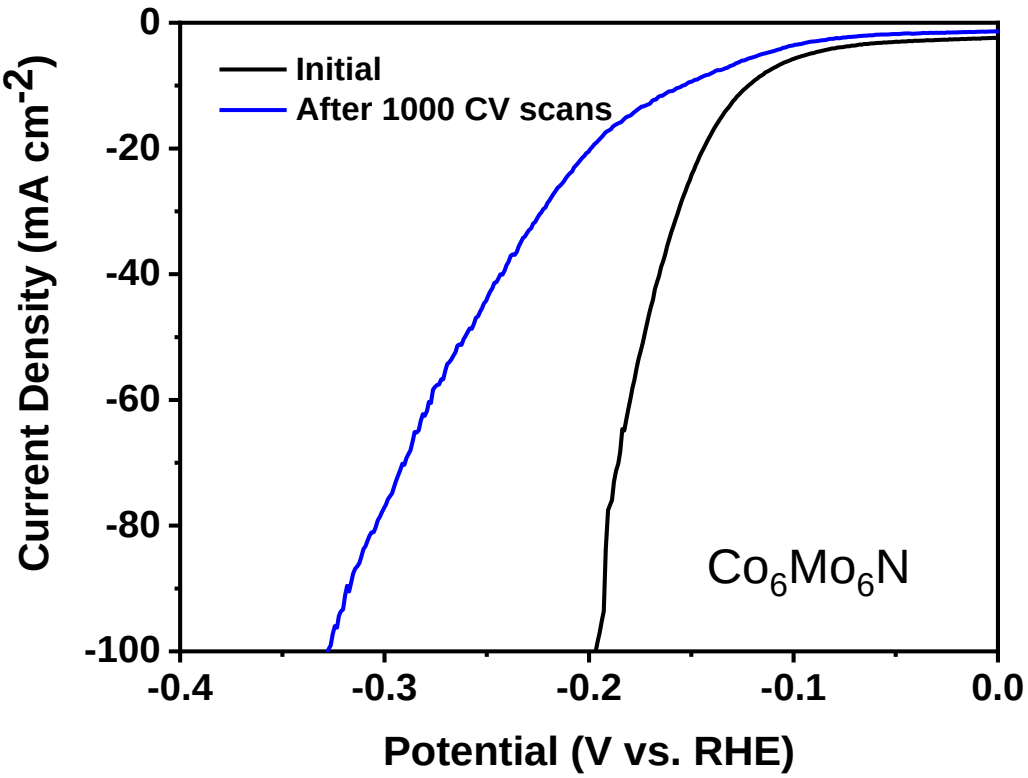

Figure 4-12: Comparison of the current densities achieved by Co_6Mo_6N catalyst in 0.5 M H_2SO_4 before and after 1000 cycles at the scan rate of 100mV s^{-1}.

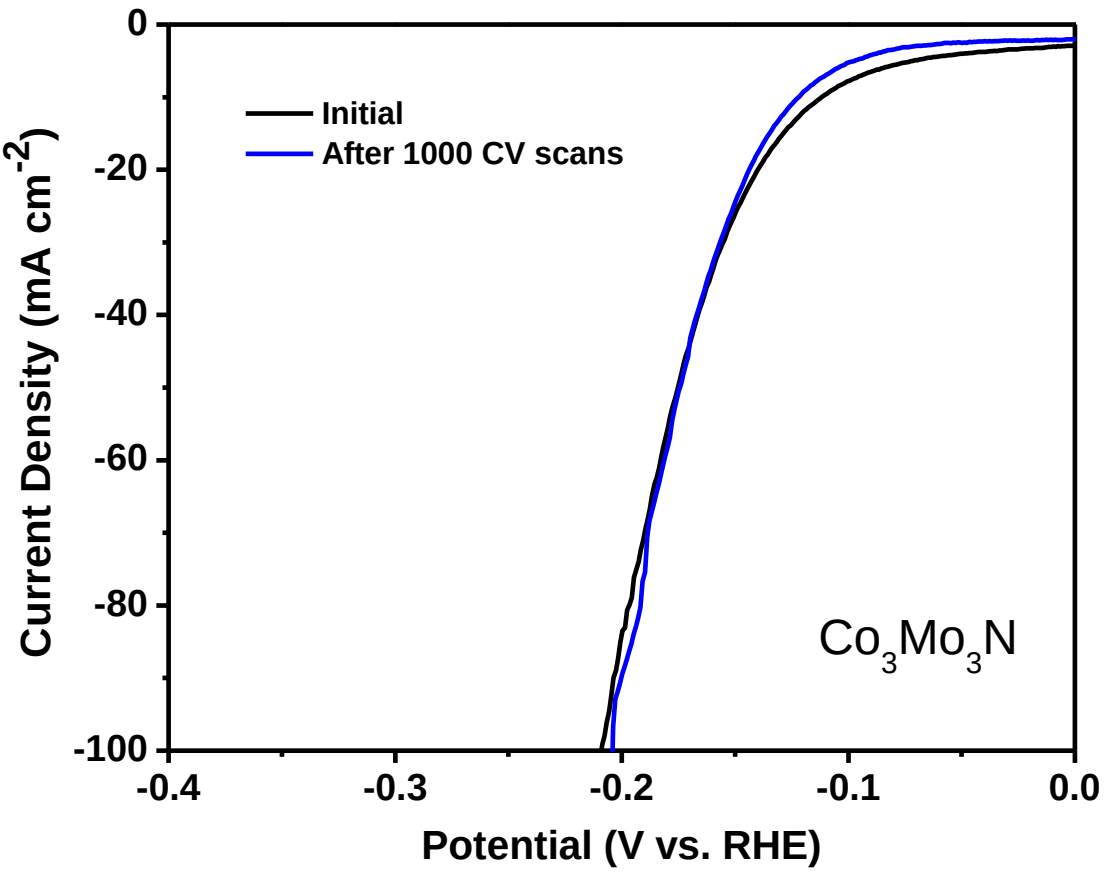

Figure 4-13: Comparison of the current densities achieved by Co_3Mo_3N catalyst in 0.5 M H_2SO_4 before and after 1000 cycles at the scan rate of 100mV s^{-1}.

The electrode with Co_3Mo_3N tested under electrochemical cycling conditions was also studied by PXRD. As such, the catalyst-deposited on glassy carbon electrode was cycled 1000 times between 0 V and -0.4 V (vs. Ag(AgCl)) and PXRD measurement was carried out directly on electrode before and after cycling. Figure 4-14 compares the PXRD patterns of Co_3Mo_3N before and after 1000 CV cycles and shows no obvious structure changes. In addition, the unit cell parameters of Co_3Mo_3N before (a = 11.004(3) Å) and after (a = 10.9980 (4) Å) 1000 cycles are identical within experimental error suggesting that the catalysts remain unchanged. In addition, XPS measurements were also carried out on Co_3Mo_3N for stability studying in 0.5 M H_2SO_4. Only minor difference was observed in the high-resolution Mo 3d, Co 2p and Mo 3p spectra before and after 1000 CV cycles as depicted in Figure 4-15 to Figure 4-17, which indicate that Co_3Mo_3N remains unchanged upon cycling.

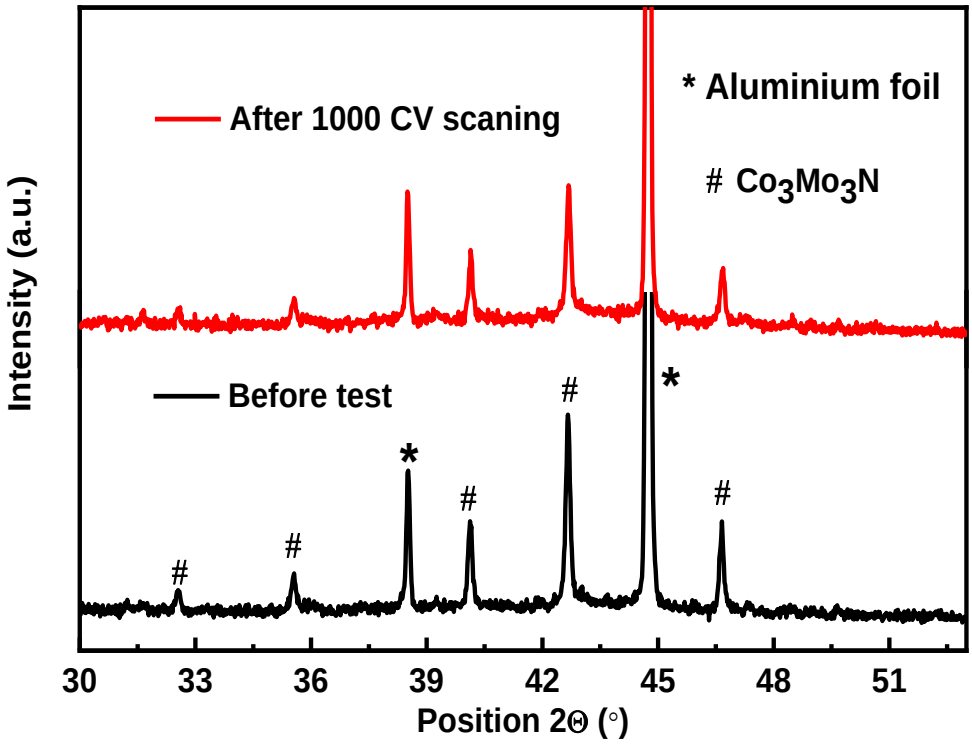

Figure 4-14: Comparison of XRD patterns recorded on Co_3Mo_3N before and after 1000 scans at the scan rate of 100 mv s^{-1} in 0.5M H_2SO_4.

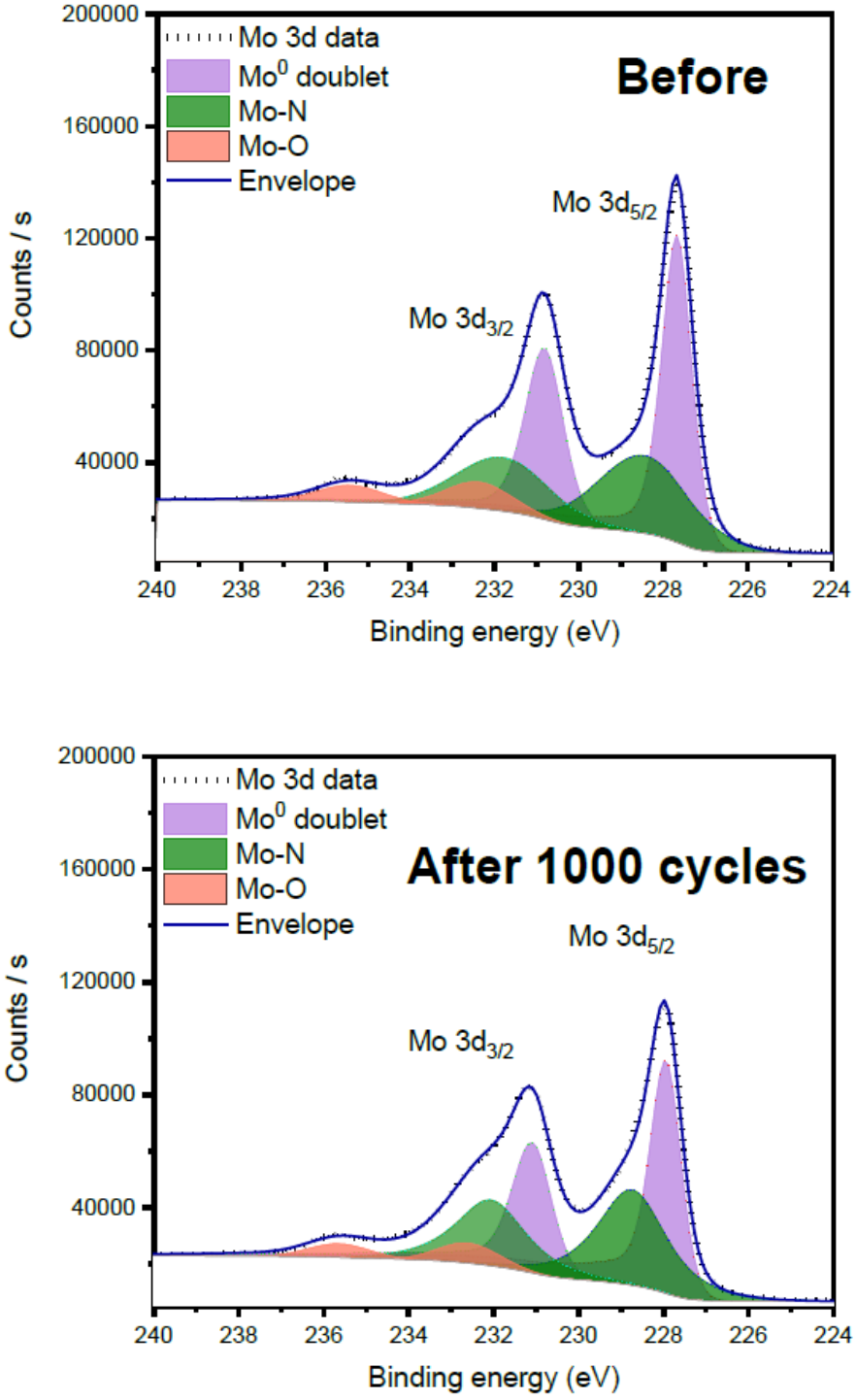

Figure 4-15: Experimental and deconvoluted high resolution Mo 3d XPS spectra before and after 1000 cycles in 0.5 M H_2SO_4.

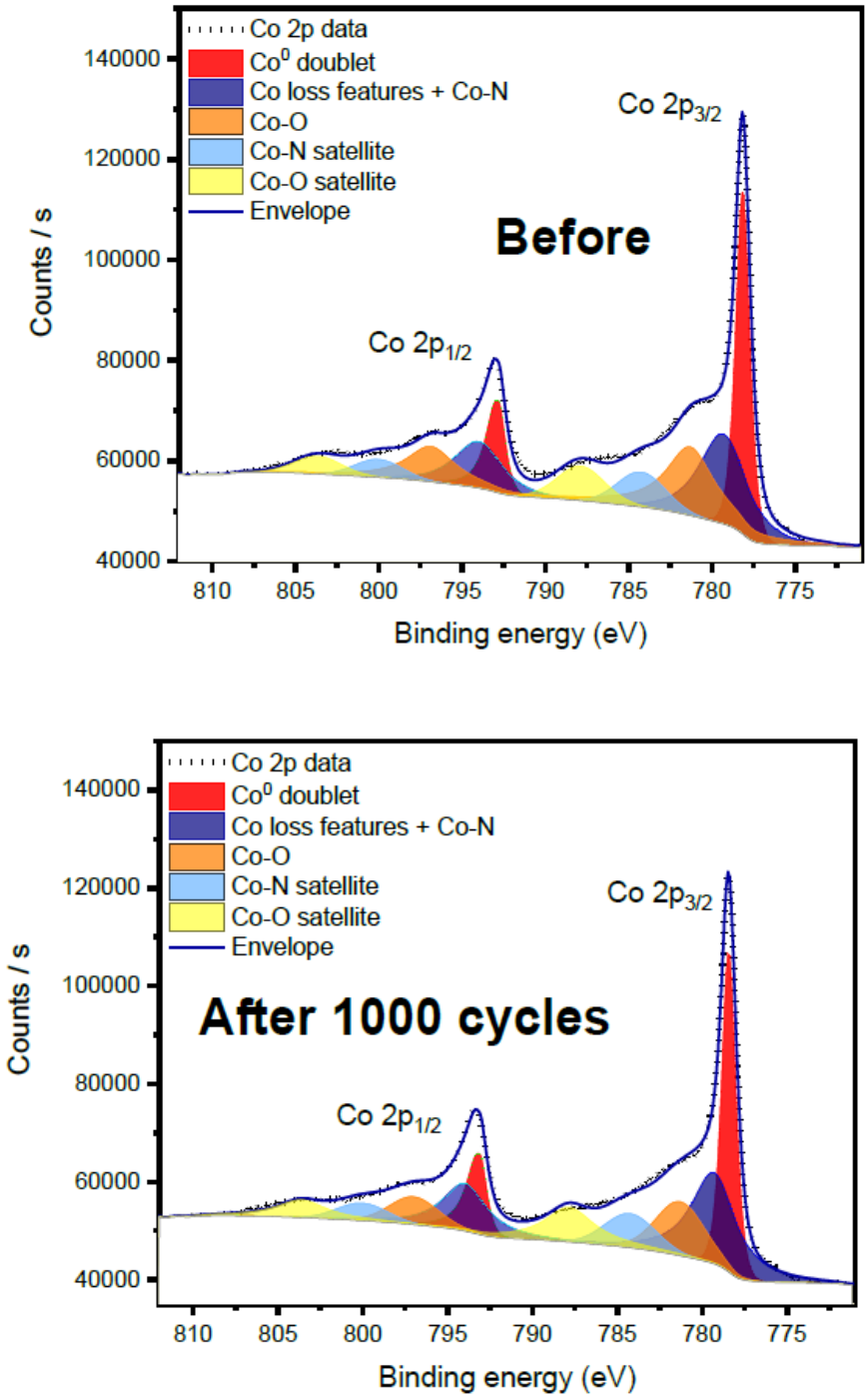

Figure 4-15: Experimental and deconvoluted high resolution Co 2p XPS spectra before and after 1000 cycles in 0.5 M H_2SO_4.

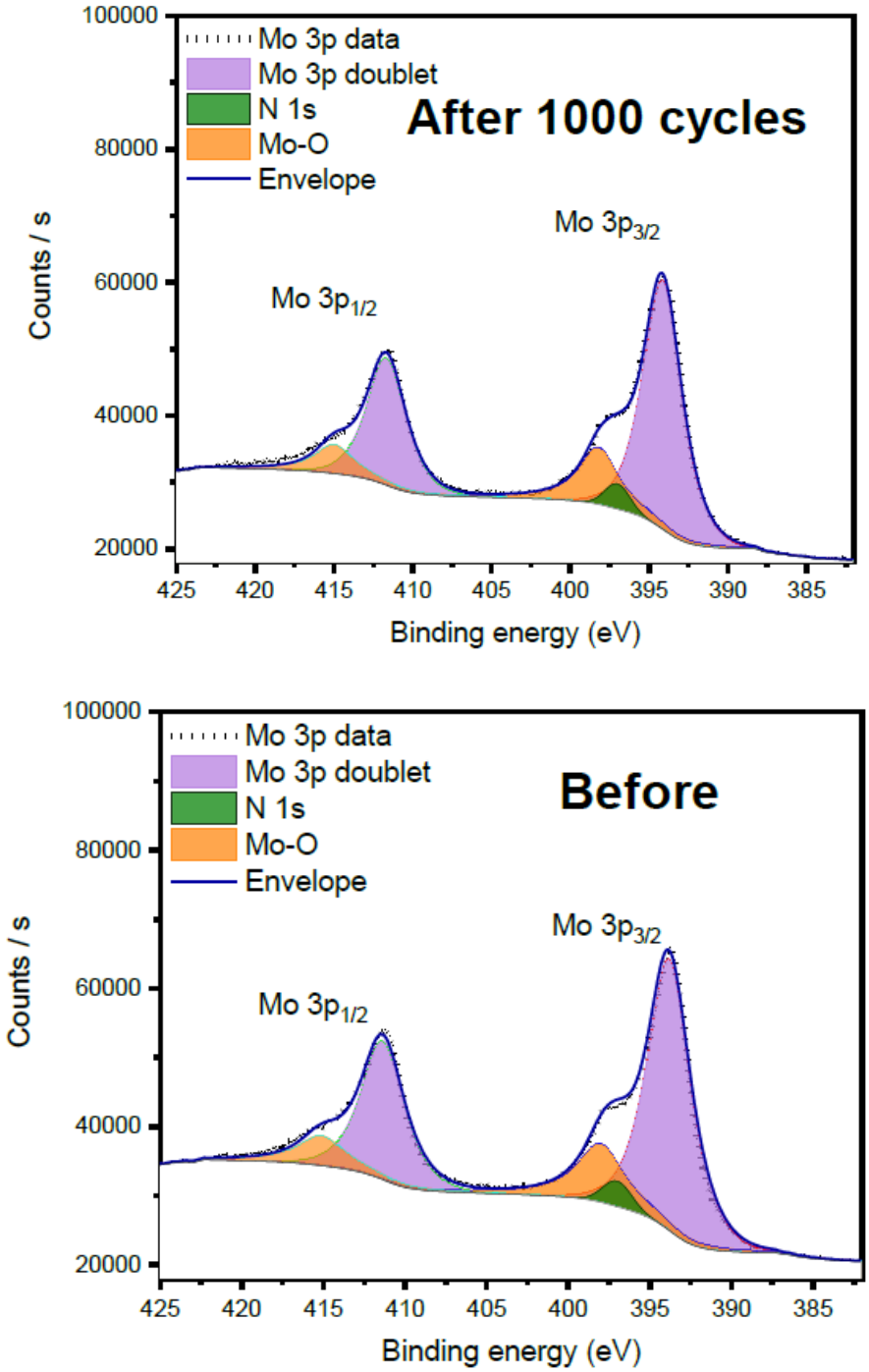

Figure 4-17: Experimental and deconvoluted high resolution Mo 3p XPS spectra before and after 1000 cycles in 0.5 M H_2SO_4.

4.6. Faradaic efficiency

The Faradaic efficiency could be determined by the relation between the experimentally determined percentage of hydrogen produced to the theoretical value calculated from the charge passed. Herein, gas chromatography measurement was conducted to determine the percentage of hydrogen produced from experiment. The detailed experiment was already discussed in chapter 2. In this case, the Faradaic efficiencies were determined to be 95.8 % for Co_3Mo_3N as depicted in Figure 4-18.

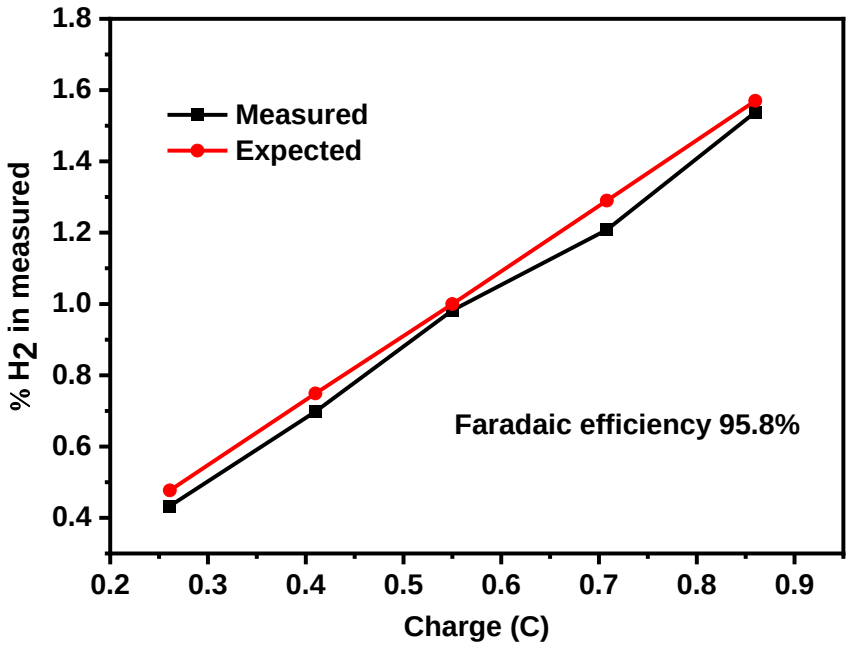

Figure 4-18: A representative trace of the proportion of H_2 (in vol. %) in the single-cell headspace during the electrolysis of Co_3Mo_3N at a constant current of 108 mA in 0.5 M H_2SO_4. Black squares show the proportion of H_2 (in vol. %) in the cell headspace determined using gas chromatography. The expected proportion of H_2 (in vol %) in the headspace was calculated from the charge passed.

4.7. Computational studies of potential active sites on Co_3Mo_3N

The above experimental part points out that the nitrogen sites had a minor responsibility for the catalytic behaviour which more N-content could increase the stability of nitrides for driving the HER in acidic media. Therefore, to rationalise the electrocatalysis behaviour of Co_3Mo_3N and $Co_3Mo_3N_{0.5}$, the DFT simulations of the electronic structure were carried out by our collaborators to identify the most possible reaction sites. Based on the previous theoretical studies, the (111)-face was found to be the most stable surface.[26] Here, ten Co_3Mo_3N-(111) surfaces (these surface structures are presented in Figure 4-19) were built and then evaluated the surface energies of the various slabs as depicted in Table 4-7 to obtain the stable surface with lowest energy. The resulting surface structure is shown in Figure 4-20.

Table 4-7: Surface energies (γ) of Co_3Mo_3N (111) surfaces. N_{Co}, N_{Mo} and N_N number of atoms within the block.

Surface index	**N_{Co}**	**N_{Mo}**	**N_N**	**γ (J m^{-2})**
Surface-0	100	120	44	1.927
Surface-1	112	120	44	3.013
Surface-2	112	132	44	3.421
Surface-3	116	132	44	3.419
Surface-4	128	132	48	3.096
Surface-5	132	132	48	3.026
Surface-6	132	144	48	2.739
Surface-7	144	144	48	3.133
Surface-8	144	156	48	3.337
Surface-9	148	156	60	2.603
Surface-10	148	168	60	2.008

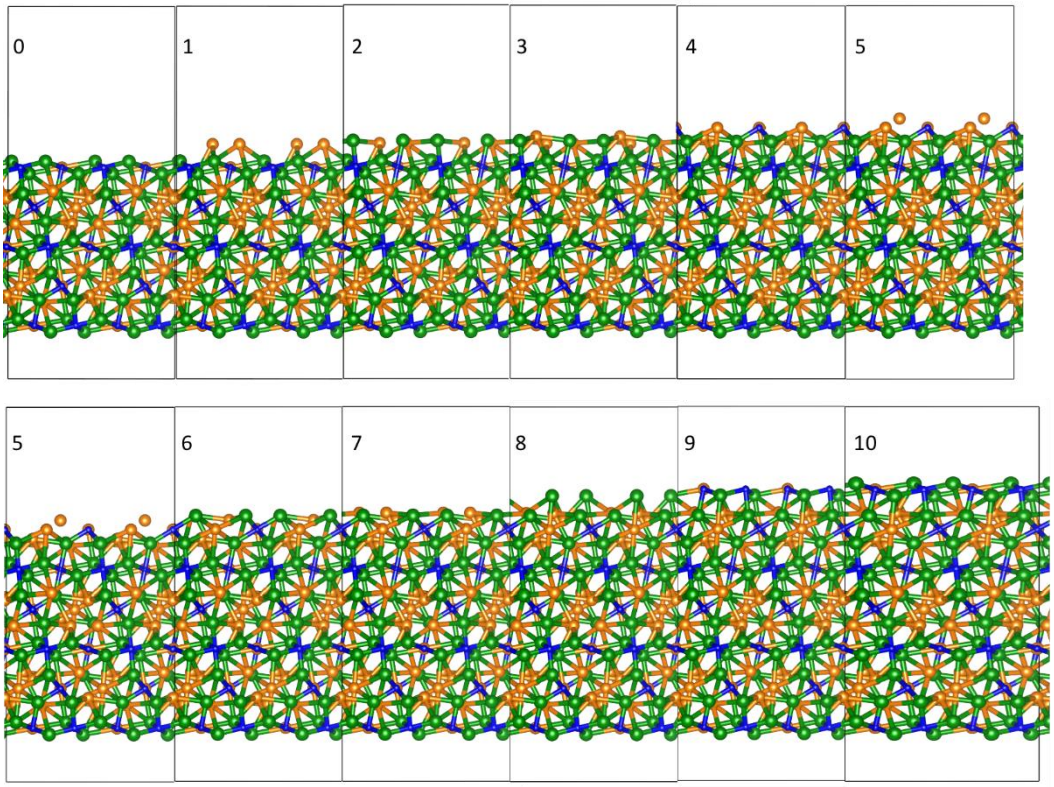

Figure 4-19: The ten possible Co_3Mo_3N-(111) termination blocks viewed along *c*-axis. Co, Mo and N are represented by orange, green and blue spheres.

The calculated free energies of hydrogen adsorption $\triangle G_H$ values for all of possible sites were list in Table 4-8, and the optimal sites that could participate in the catalytic reaction was shown in Figure 4-21. $\triangle G_H$ can be taken as the simplest first order descriptor for predicting the HER activity, and the closer this value is to zero, the closer the system is considered to the thermodynamic optimum.[3,27,28] In this simulation, the sites of hollow H_2-out has a $\triangle G_H$ = 0.03 eV. This value puts Co_3Mo_3N into the optimal range in comparison with transition metals when plotted against exchange current densities depicted in Figure 4-22. Therefore, this model explains well the low overpotential observed in Co_3Mo_3N.

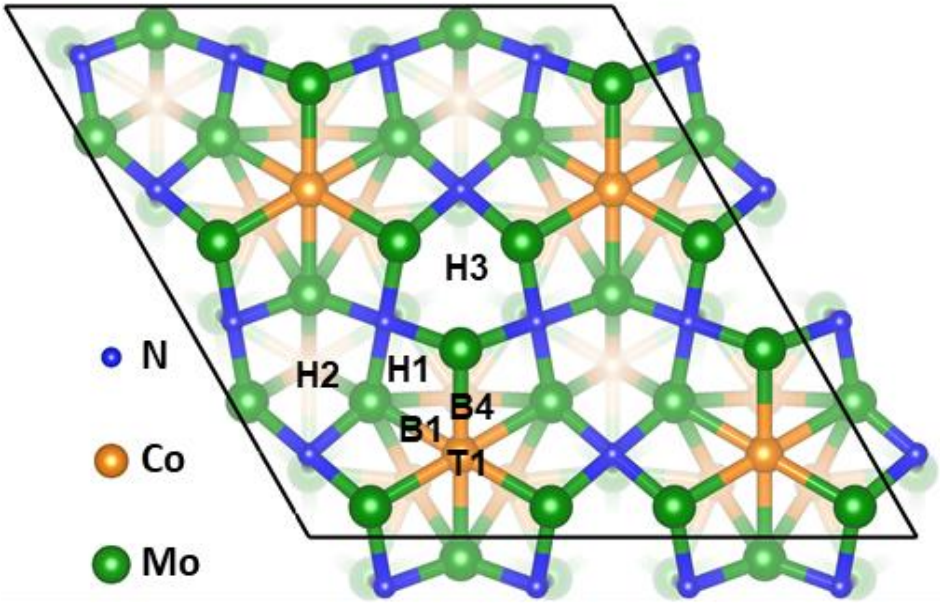

Figure 4-20: The most energetically favourable surface of Co_3Mo_3N and the optimal reaction sites for the HER in a single site model.

Table 4-8: The final adsorption sites and adsorption energy in Co_3Mo_3N after the optimisation of the model.

Material	**Co_3Mo_3N**
Adsorption	**$\triangle G_{Hads}$(eV)**
B1	-0.22
B4	-0.20
H1	-0.40
H2-IN	0.49
H3	-0.46
T1	0.36
H2-OUT	0.03

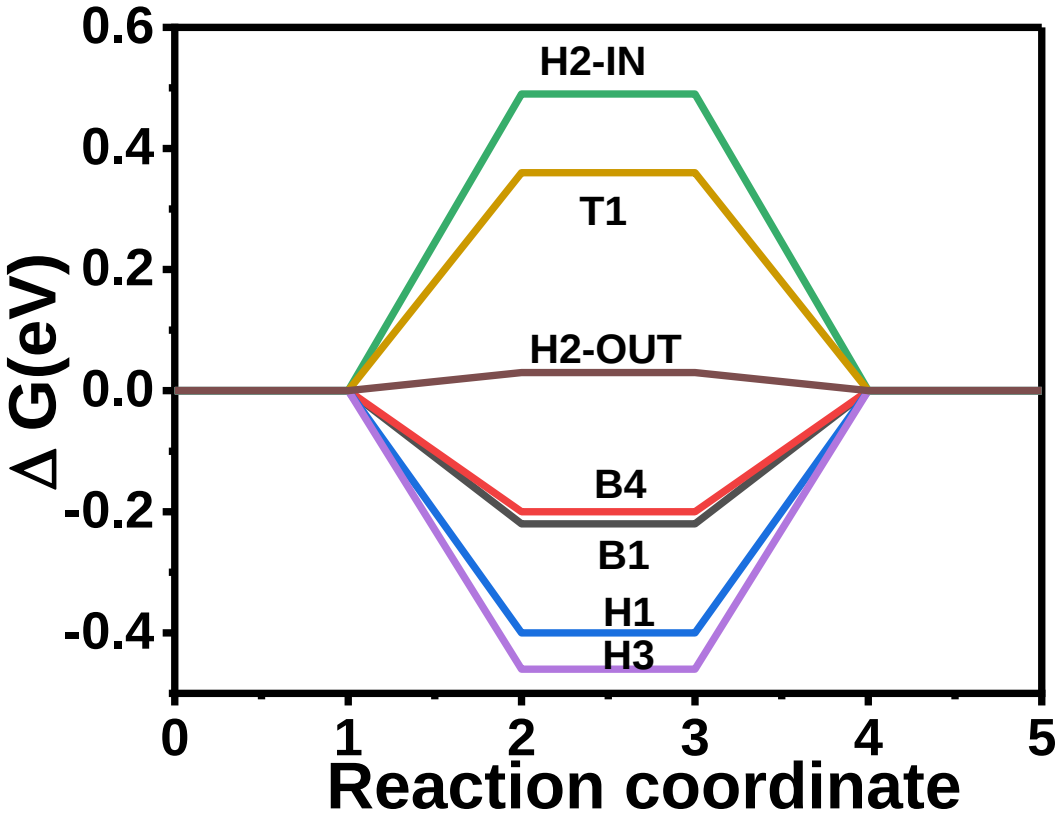

Figure 4-21: The free energy diagram of the possible reaction sites on the Co_3Mo_3N-(111) surface at pH = 0. The labels for the reaction sites correspond to the sites shown in (Figure 4-19).

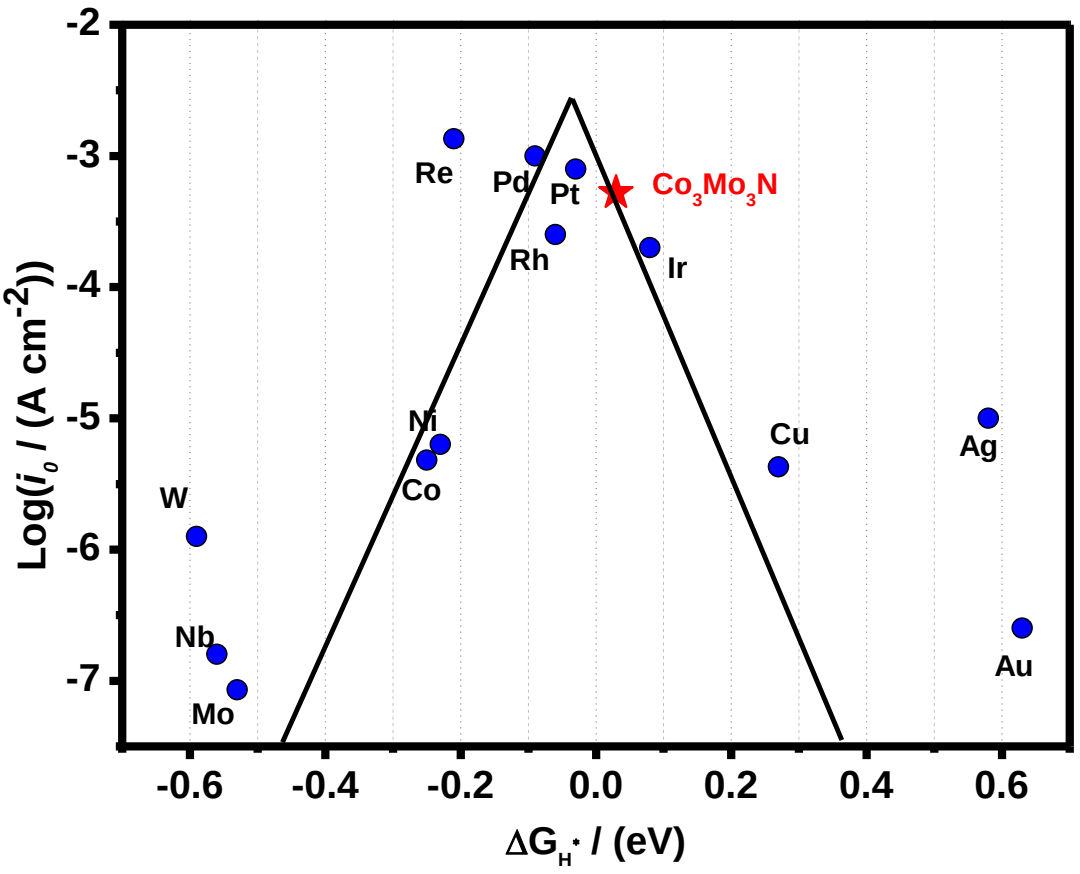

Figure 4-22: Volcano – plot built on the experimentally determined exchange current densities (values are taken from ref. [29]) as a function of the calculated free energy for hydrogen adsorption.

In addition, a striking similarity of total density of states (DOS) was observed between the surface with fully occupied nitrogen sites and the surface with a nitrogen vacancy (Figure 4-23 and Figure 4-24) suggesting that the overall electronic properties of the Co_3Mo_3N cannot be affected by the electron rearrangement due to N-vacancies. This explains the experimental findings that Co_3Mo_3N showed identical electrocatalytic performance in comparation with Co_6Mo_6N due to the N-vacancy could not influence the DOS of metal sites. However, the N-vacancy could destroy a network of [Mo_6N] octahedra in Co_3Mo_3N structure as shown in Figure 4-1, which may explain the lower catalytic stability of Co_6Mo_6N under long time electrolysis.

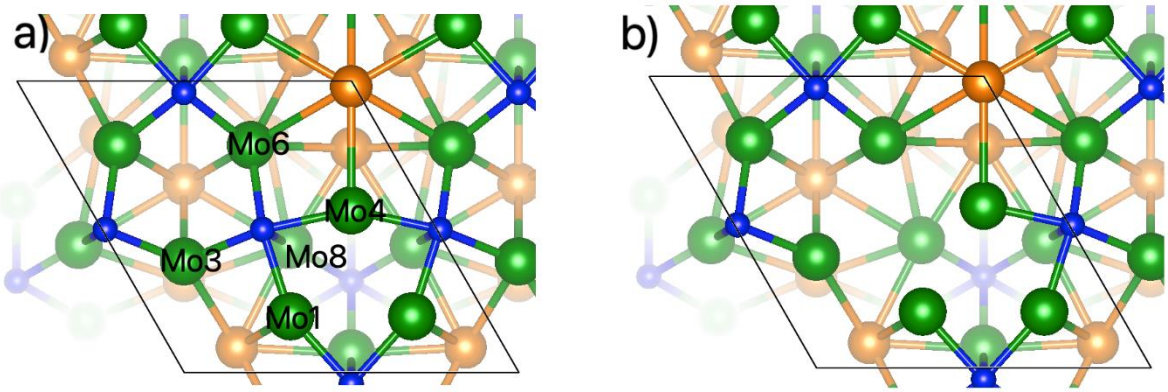

Figure 4-23: A magnified fragment of the original Co_3Mo_3N-(111) corresponding to the most stable surface (a); the Co_3Mo_3N-(111) with N-vacant site (b). Co, Mo and N are represented by orange, green and blue spheres.

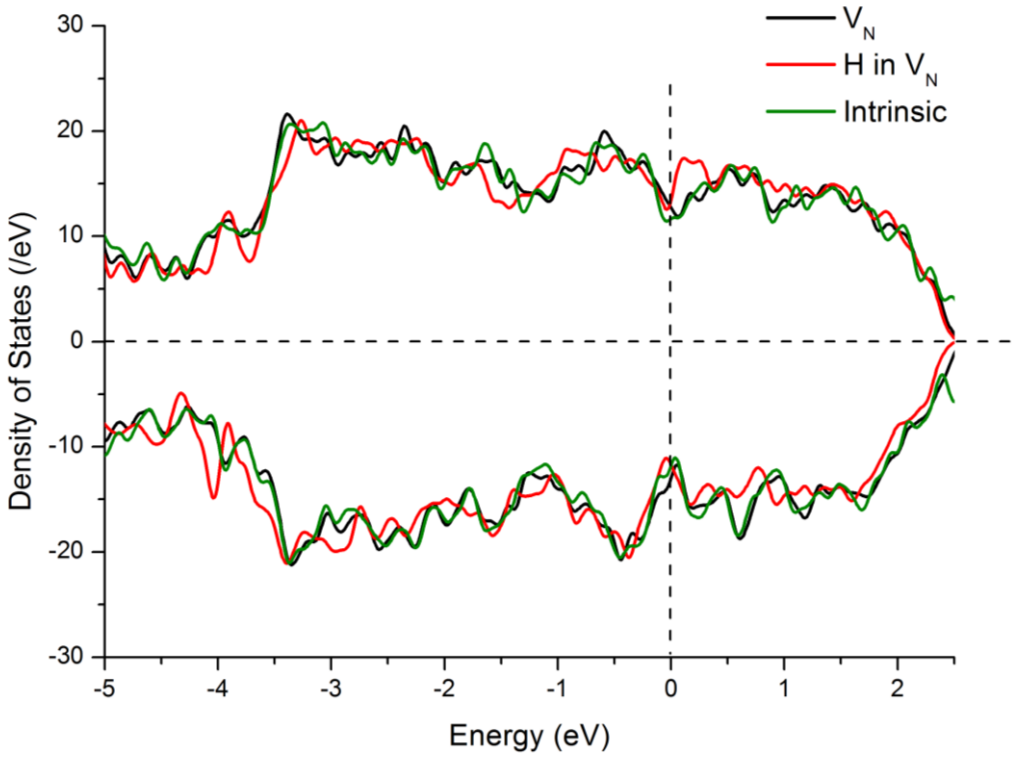

Figure 4-24: The total Density of States (DOS) of the intrinsic surface (green line), the surface with a N-vacancy (black line), and the surface that a H filled in the N-vacancy (red line).

4.8. Summary and conclusion

In summary, this chapter has focused on synthesis and characterising the cubic Co_3Mo_3N and understanding the origin of its catalytic activity for HER. By applying a solid-state route under H_2/N_2 gas flow, Co_3Mo_3N could be synthesised in a single phase, pure $Co_3Mo_3N_{0.5}$ was also obtained by annealing Co_3Mo_3N under H_2/Ar gas. Upon phase transition between Co_3Mo_3N and Co_6Mo_6N the morphology is retained, meaning that the catalytic activity can be investigated and compared with both materials exhibiting identical surface area. In this way, the electrochemical performance of both nitrides was investigated and showed minor difference between materials. Thus, the superior performance of Co_3Mo_3N is attributed to the metal sites, then the substitution of cobalt with iron to make free standard Fe_3Mo_3N was carried out. When tested electrochemically it is evident that overpotentials increased significantly, it points out that the catalytic active performance is from Co sites in Co_3Mo_3N composition, which is further investigated by DFT calculation (the Co-site ($\triangle G_H \sim 0$) appears to be catalytic point). The N-content plays an important role on the stability of the catalyst, the higher nitrogen occupancy in Co_3Mo_3N allows for prolonged electrolysis. Finally, a high value of Faradaic efficiency for Co_3Mo_3N further confirmed that the nitrides materials produce hydrogen making it attractive target for application in water electrolysis.

4.9. References

[1] J. Xiong, W. Cai, W. Shi, X. Zhang, J. Li, Z. Yang, L. Feng, H. Cheng, Salt-templated synthesis of defect-rich MoN nanosheets for boosted hydrogen evolution reaction, *J. Mater. Chem. A.* 5 (**2017**) 24193–24198. https://doi.org/10.1039/C7TA07566A.

[2] Y. Zhu, G. Chen, X. Xu, G. Yang, M. Liu, Z. Shao, Enhancing Electrocatalytic Activity for Hydrogen Evolution by Strongly Coupled Molybdenum Nitride@Nitrogen-Doped Carbon Porous Nano-Octahedrons, *ACS Catal.* 7 (**2017**) 3540–3547. https://doi.org/10.1021/acscatal.7b00120.

[3] W.F. Chen, K. Sasaki, C. Ma, A.I. Frenkel, N. Marinkovic, J.T. Muckerman, Y. Zhu, R.R. Adzic, Hydrogen-evolution catalysts based on non-noble metal nickel-molybdenum nitride nanosheets, *Angew. Chemie - Int. Ed.* 51 (**2012**) 6131–6135. https://doi.org/10.1002/ANIE.201200699.

[4] D. Errandonea, C. Ferrer-Roca, D. Martínez-Garcia, A. Segura, O. Gomis, A. Muñoz, P. Rodríguez-Hernández, J. López-Solano, S. Alconchel, F. Sapiña, High-pressure x-ray diffraction and ab initio study of Ni_2Mo_3N, Pd_2Mo_3N, Pt_2Mo_3N, Co_3Mo_3N, and Fe 3Mo3N: Two families of ultra-incompressible bimetallic interstitial nitrides, *Phys. Rev. B - Condens. Matter Mater. Phys.* 82 (**2010**) 174105. https://doi.org/10.1103/PHYSREVB.82.174105/FIGURES/6/MEDIUM.

[5] N. Schönberg, The tungsten carbide and nickel arsenide structures, *Acta Metall.* 2 (**1954**) 427–432. https://doi.org/10.1016/0001-6160(54)90062-0.

[6] T.J. Prior, P.D. Battle, Facile synthesis of interstitial metal nitrides with the filled β - manganese structure, *J. Solid State Chem.* 172 (**2003**) 138–147. https://doi.org/10.1016/S0022-4596(02)00171-8.

[7] Y. Sun, L. Wang, O. Guselnikova, O. Semyonov, J. Fraser, Y. Zhou, N. López, A.Y. Ganin, Revealing the activity of Co_3Mo_3N and $Co_3Mo_3N_{0.5}$ as electrocatalysts for the hydrogen evolution reaction, *J. Mater. Chem. A.* 10 **(2022**) 855–861. https://doi.org/10.1039/D1TA08389A.

[8] Y. Yuan, S. Adimi, T. Thomas, J. Wang, H. Guo, J. Chen, J.P. Attfield, F.J. DiSalvo, M. Yang, Co_3Mo_3N—An efficient multifunctional electrocatalyst, *Innov.* 2 (**2021**).

https://doi.org/10.1016/J.XINN.2021.100096.

[9] K. Zhang, L. Zhang, X. Chen, X. He, X. Wang, S. Dong, P. Han, C. Zhang, S. Wang, L. Gu, G. Cui, Mesoporous cobalt molybdenum nitride: A highly active bifunctional electrocatalyst and its application in lithium-O_2 batteries, *J. Phys. Chem. C*. 117 (**2013**) 858–865. https://doi.org/10.1021/jp310571y.

[10] S.M. Hunter, D. McKay, R.I. Smith, J.S.J. Hargreaves, D.H. Gregory, Topotactic nitrogen transfer: Structural transformation in cobalt molybdenum nitrides, *Chem. Mater*. 22 (**2010**) 2898–2907. https://doi.org/10.1021/cm100208a.

[11] J.O. Conway, T.J. Prior, Interstitial nitrides revisited – A simple synthesis of M_xMo_3N (M = Fe, Co, Ni), *J. Alloys Compd*. 774 (**2019**) 69–74. https://doi.org/10.1016/J.JALLCOM.2018.09.307.

[12] N. Bion, F. Can, J. Cook, J.S.J. Hargreaves, A.L. Hector, W. Levason, A.R. McFarlane, M. Richard, K. Sardar, The role of preparation route upon the ambient pressure ammonia synthesis activity of Ni_2Mo_3N, *Appl. Catal. A Gen*. 504 (**2015**) 44–50. https://doi.org/10.1016/J.APCATA.2014.10.030.

[13] S.K. Jackson, R.C. Layland, H.C. Zur Loye, The simultaneous powder X-ray and neutron diffraction refinement of two η-carbide type nitrides, Fe_3Mo_3N and Co_3Mo_3N, prepared by ammonolysis and by plasma nitridation of oxide precursors, *J. Alloys Compd*. 291 (**1999**) 94–101. https://doi.org/10.1016/S0925-8388(99)00484-3.

[14] B. Cao, G.M. Veith, J.C. Neuefeind, R.R. Adzic, P.G. Khalifah, Mixed close-packed cobalt molybdenum nitrides as non-noble metal electrocatalysts for the hydrogen evolution reaction, *J. Am. Chem. Soc*. 135 (**2013**) 19186–19192. https://doi.org/10.1021/JA4081056.

[15] D. Errandonea, C. Ferrer-Roca, D. Martínez-Garcia, A. Segura, O. Gomis, A. Muñoz, P. Rodríguez-Hernández, J. López-Solano, S. Alconchel, F. Sapiña, High-pressure x-ray diffraction and ab initio study of Ni_2Mo_3N, Pd_2Mo_3N, Pt_2Mo_3N, Co_3Mo_3N, and Fe_3Mo_3N: Two families of ultra-incompressible bimetallic interstitial nitrides, *Phys. Rev. B - Condens. Matter Mater. Phys*. 82 (**2010**). https://doi.org/10.1103/PHYSREVB.82.174105.

[16] J. Xie, S. Li, X. Zhang, J. Zhang, R. Wang, H. Zhang, B. Pan, Y. Xie, Atomically-thin

molybdenum nitride nanosheets with exposed active surface sites for efficient hydrogen evolution, *Chem. Sci*. 5 (**2014**) 4615–4620. https://doi.org/10.1039/C4SC02019G.

[17] W.F. Chen, S. Iyer, S. Iyer, K. Sasaki, C.H. Wang, Y. Zhu, J.T. Muckerman, E. Fujita, Biomass-derived electrocatalytic composites for hydrogen evolution, *Energy Environ. Sci*. 6 (**2013**) 1818–1826. https://doi.org/10.1039/C3EE40596F.

[18] D.H. Youn, S. Han, J.Y. Kim, J.Y. Kim, H. Park, S.H. Choi, J.S. Lee, Highly active and stable hydrogen evolution electrocatalysts based on molybdenum compounds on carbon nanotube-graphene hybrid support, *ACS Nano*. 8 (**2014**) 5164–5173. https://doi.org/10.1021/NN5012144.

[19] L. Ma, L.R.L. Ting, V. Molinari, C. Giordano, B.S. Yeo, Efficient hydrogen evolution reaction catalyzed by molybdenum carbide and molybdenum nitride nanocatalysts synthesized via the urea glass route, *J. Mater. Chem. A*. 3 (**2015**) 8361–8368. https://doi.org/10.1039/C5TA00139K.

[20] R. Ramesh, D.K. Nandi, T.H. Kim, T. Cheon, J. Oh, S.H. Kim, Atomic-Layer-Deposited MoNx Thin Films on Three-Dimensional Ni Foam as Efficient Catalysts for the Electrochemical Hydrogen Evolution Reaction, *ACS Appl. Mater. Interfaces*. 11 (**2019**) 17321–17332. https://doi.org/10.1021/ACSAMI.8B20437.

[21] Y.J. Song, Z.Y. Yuan, One-pot Synthesis of Mo_2N/NC Catalysts with Enhanced Electrocatalytic Activity for Hydrogen Evolution Reaction, *Electrochim. Acta*. 246 (**2017**) 536–543. https://doi.org/10.1016/J.ELECTACTA.2017.06.086.

[22] X. Feng, H. Wang, X. Bo, L. Guo, Bimetal-Organic Framework-Derived Porous Rodlike Cobalt/Nickel Nitride for All-pH Value Electrochemical Hydrogen Evolution, *ACS Appl. Mater. Interfaces*. 11 (**2019**) 8018–8024. https://doi.org/10.1021/ACSAMI.8B21369.

[23] C. Zhang, Y. Huang, Y. Yu, J. Zhang, S. Zhuo, B. Zhang, Sub-1.1 nm ultrathin porous CoP nanosheets with dominant reactive {200} facets: a high mass activity and efficient electrocatalyst for the hydrogen evolution reaction, *Chem. Sci*. 8 (**2017**) 2769–2775. https://doi.org/10.1039/C6SC05687C.

[24] B. Zhang, Y.H. Lui, H. Ni, S. Hu, Bimetallic $(Fe_xNi_{1-x})_2P$ nanoarrays as exceptionally

efficient electrocatalysts for oxygen evolution in alkaline and neutral media, *Nano Energy*. 38 (**2017**) 553–560. https://doi.org/10.1016/J.NANOEN.2017.06.032.

[25] M. Kozejova, V. Latyshev, V. Kavecansky, H. You, S. Vorobiov, A. Kovalcikova, V. Komanicky, Evaluation of hydrogen evolution reaction activity of molybdenum nitride thin films on their nitrogen content, *Electrochim. Acta*. 315 (**2019**) 9–16. https://doi.org/10.1016/J.ELECTACTA.2019.05.097.

[26] C.D. Zeinalipour-Yazdi, J.S.J. Hargreaves, C.R.A. Catlow, DFT-D3 Study of Molecular N_2 and H_2 Activation on Co_3Mo_3N Surfaces, *J. Phys. Chem. C*. 120 (**2016**) 21390–21398. https://doi.org/10.1021/acs.jpcc.6b04748.

[27] J. Greeley, T.F. Jaramillo, J. Bonde, I. Chorkendorff, J.K. Nørskov, Computational high-throughput screening of electrocatalytic materials for hydrogen evolution, *Nat. Mater*. 5 (**2006**) 909–913. https://doi.org/10.1038/NMAT1752.

[28] J. Kibsgaard, C. Tsai, K. Chan, J.D. Benck, J.K. Nørskov, F. Abild-Pedersen, T.F. Jaramillo, Designing an improved transition metal phosphide catalyst for hydrogen evolution using experimental and theoretical trends, *Energy Environ. Sci*. 8 (**2015**) 3022–3029. https://doi.org/10.1039/C5EE02179K.

[29] J.K. Nørskov, T. Bligaard, A. Logadottir, J.R. Kitchin, J.G. Chen, S. Pandelov, U. Stimming, Trends in the Exchange Current for Hydrogen Evolution, *J. Electrochem. Soc*. 152 (**2005**) J23. https://doi.org/10.1149/1.1856988.

Chapter 5: Investigation of Co_6W_6N as electrocatalysts for the HER

The results in the previous chapter showed that Co_6Mo_6N is a suitable catalyst in acidic media, which showed the overpotential of 110 ± 8 mV at j = -10 mA / cm^2. This electrochemical catalytic behaviour presents an opportunity for studies of isostructural nitrides because Co_6Mo_6N showed poor durability upon prolonged electrolysis (suggesting degradation under continuously applied potential). Other isostructural materials may be more stable and thus, more suitable in electrolysers. In this chapter, the synthesis, characterisation, and electrocatalytic of previously unreported isostructural Co_6W_6N is discussed. It is also compared with Fe_6W_6N in order to confirm the role Co catalytic sites.

5.1 Introduction

5.1.1 η-Co_6Mo_6C structure-type based materials

As discussed in Chapter 1, several ternary compounds with η-carbide structure were reported. These include carbides: Fe_6Mo_6C, Co_6Mo_6C, Fe_6W_6C, Ni_6Mo_6C, and Co_6W_6C.[1][2][3] A reasonable electrocatalytic performance was observed for some of them, such as hydrogen evolution reaction, oxygen evolution reaction, and hydrazine oxide.[3][4][5] There are only few reports on nitrides, which include: Co_6Mo_6N, that can be formed by heating Co_3Mo_3N in H_2/Ar gas flow.[6][7] Other metal nitrides, Fe_6W_6N and Ni_6W_6N, were also reported to be prepared by the hot isostatic pressing technique.[8][9] Only Co_6Mo_6N was electrochemically tested. As discussed in Chapter 4 the computational studies suggested that cobalt atoms are probably act as the main active sites in Co_6Mo_6N.[10] Therefore, if Co-sites are indeed catalytic, one should expect at least similar performance from Co_6W_6N. As there have been no reports of synthesis of this nitride one can speculate that its crystal structure should be similar to Co_6Mo_6N as displayed in Figure 5-1 which consists of network of corner-sharing W_6N octahedra while Co-atoms are interlinked in-between the octahedra. The similarity with Co_6Mo_6N offers the opportunity to investigate the previously discussed route of reaction between mixed oxide precursor and H_2/N_2 gas for synthesis of Co_6W_6N.

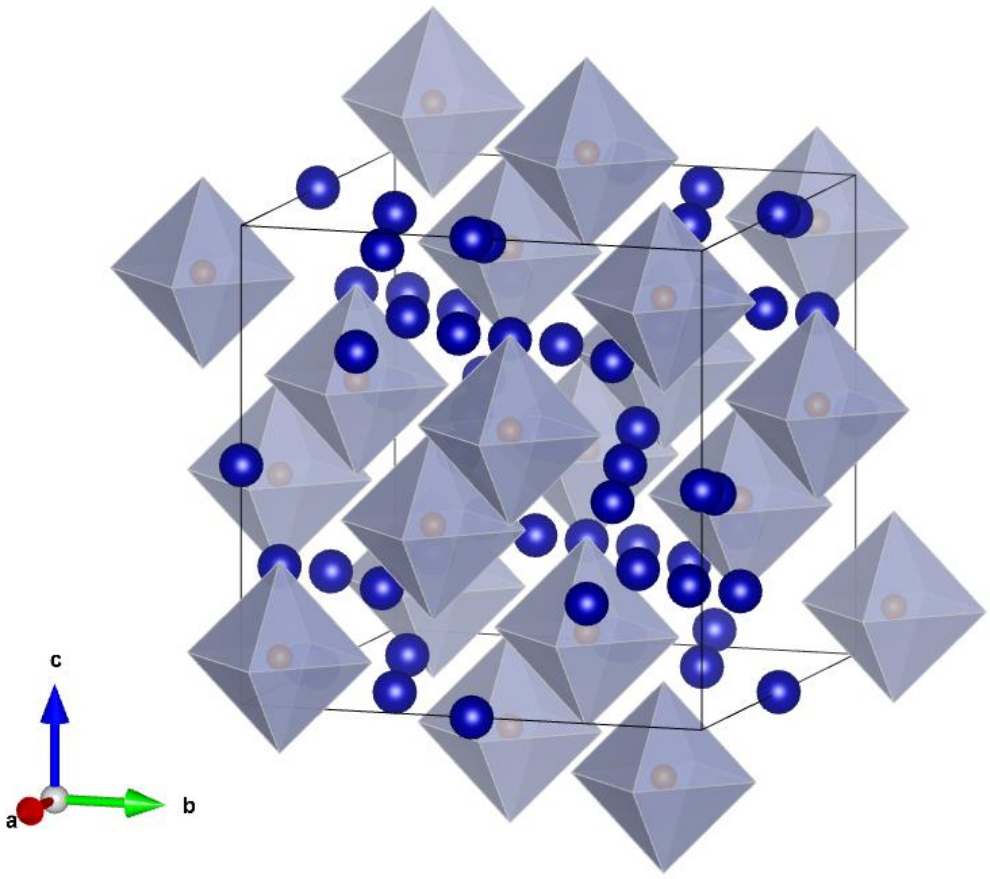

Figure 5-1: The proposed crystal structure of Co_6W_6N showing the composition of Co atoms and W_6N-octahedra. Co-atoms are shown as blue spheres.

5.1.2 Aims

The aim of this work was to investigate the solid-state route to Co_6W_6N under H_2/N_2 gas flow. If successful, the substitution of cobalt atom in Co_6W_6N with iron to form Fe_6W_6N would be carried out for comparison. The aim of comparing these two nitrides is to confirm whether Co-sites play a crucial role in electrochemical performance and whether the W-based nitrides are more stable in comparison with Co_6Mo_6N analogues described in the previous chapter.

5.2 Synthesis and characterisation of Co_6W_6N

5.2.1 Preparation of Co_6W_6N

As this nitride has not been reported before, work was carried out to find the optimal reaction conditions that could lead to a single phase sample. First, the cobalt-tungsten-based oxide precursor was prepared by adding dropwise 20 mL of 0.25 M solution of $Na_2WO_4 \cdot 2H_2O$ (Alfa Aesar, ACS reagent, ≥ 99.0%) to 20 mL of 0.25 M solution of $CoCl_2 \cdot 6H_2O$ (Hopkin Williams, ACS reagent, ≥ 99.0%) upon stirring. The resulting solution was allowed to stir for 2 hours

under ambient condition. After solidification, the precipitate was isolated using vacuum filtration and dried overnight in an oven at 120 ℃ resulting in a precursor consisting of metal oxides. Then, the synthesis of Co_6W_6N was initially tried by nitridation of the precursor at 750 ℃ in H_2 (5 vol. %) / N_2 gas mixture with a flow rate of 5 mL / min for 5 hours which was similar to reaction conditions used for Co_3Mo_3N as discussed in Chapter 4. The resulting black powder was analysed in PXRD and showed a diffraction pattern displayed in Figure 5-2. As there is no match between the simulated and experimental patterns further investigation at higher temperatures were followed. However, the PXRD data collected on products obtained at higher reaction temperature of 800 ℃ and 850 ℃ (Figure 5-3 and 5-4) showed that the targeted phase of Co_6W_6N was still not observed.

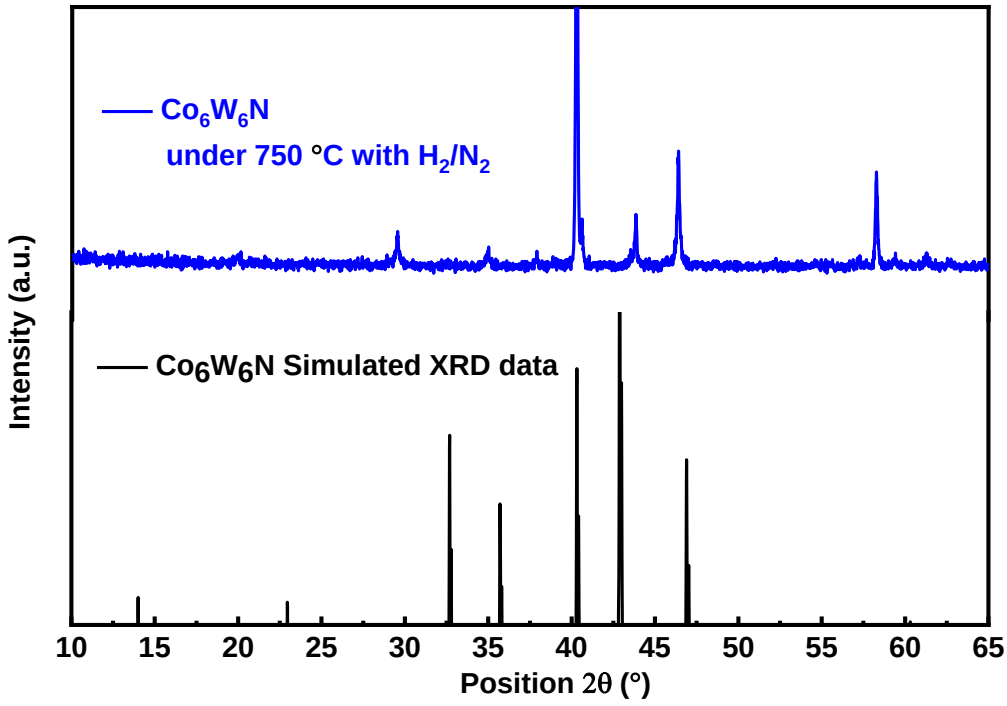

Figure 5-2: Comparison of PXRD pattern of obtained Co_6W_6N samples under 750 ℃ with 5 % H_2 in N_2 with simulated Co_6W_6N XRD data.

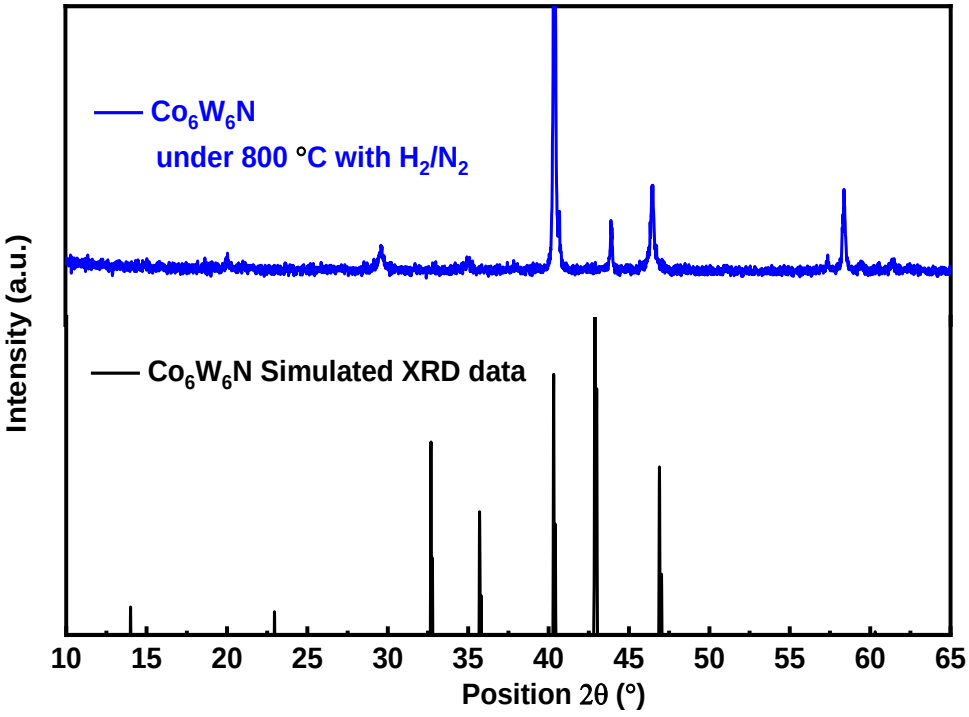

Figure 5-3: Comparison of PXRD pattern of obtained Co_6W_6N samples under 800 °C with 5 % H_2 in N_2 with simulated Co_6W_6N XRD data.

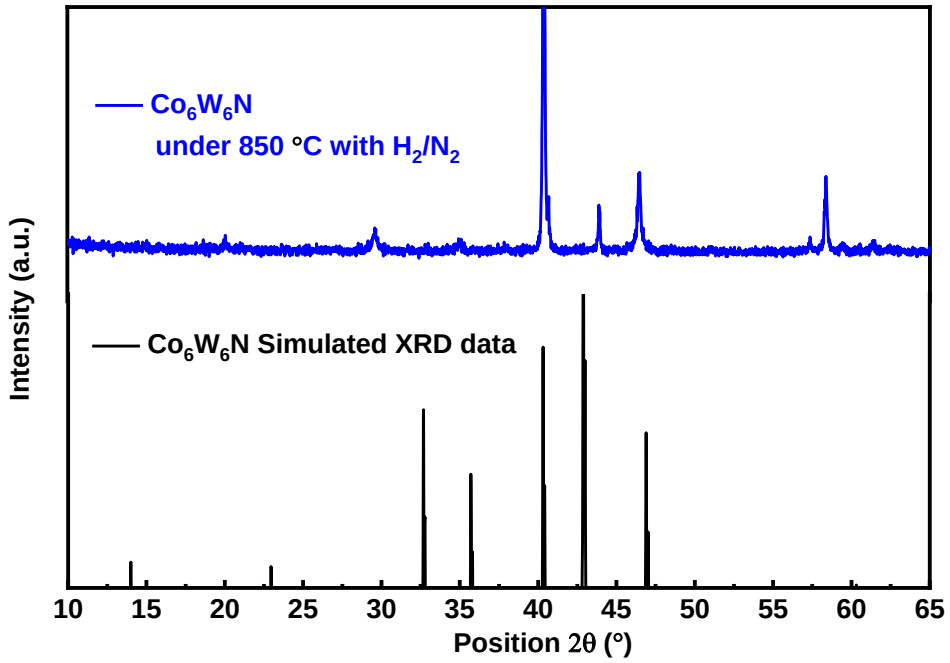

Figure 5-4: Comparison of PXRD pattern of obtained Co_6W_6N samples under 850 °C with 5 % H_2 in N_2 with simulated Co_6W_6N XRD data.

As the attempts to prepare the products solely in H_2/N_2 gas mixture, the urea method was adapted with some modification for the synthesis of Co_6W_6N.[11] Figure 5-5 shows the schematic of the experiment that was carried out using urea as assisting nitrogen source in addition to H_2 (5 vol. %) / N_2 gas mixture.

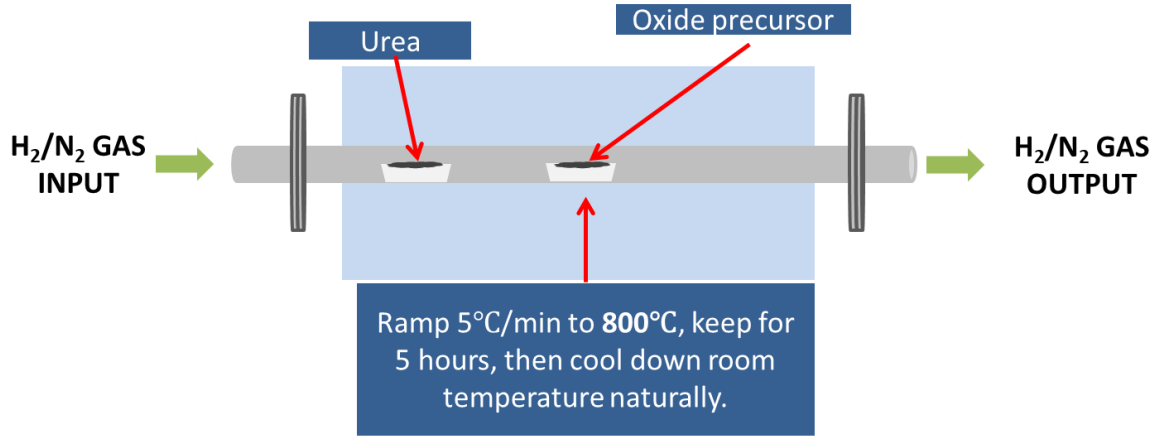

Figure 5-5: An illustrative schematic of equipment for synthesising samples with urea under 5% H_2 in N_2 gas mixture flow.

It was possible to observe the consistent Co_6W_6N peaks at 32.9°, 35.9°, 43.1°and 47.3° under 750 °C reaction temperature with some unidentified impurities at 40.3°, 16.5° and 58.3° (Figure 5-6). The PXRD pattern of sample prepared at 800 °C was deemed as single phase of Co_6W_6N. Therefore, Rietveld refinement of the powder XRD data was carried against the structure model to confirm the purity of the product (Figure 5-7). The result confirmed that Co_6W_6N is the only product, and no impurity was present. The structural parameters are summarized in Table 5-1. The resulting unit cell parameter a = 10.8811(9) Å is substantially smaller than a = 11.0995 Å as previously reported for Co_3W_3N [12] indirectly confirming that the resulting product is probably Co_6W_6N. However, the unit cell parameter is practically the same as previously reported in Co_6W_6C (a = 10.894 Å) [13] suggesting the possibility that the presence of urea may had been a possible source of carbon thus, leading to the formation of carbide. Therefore, the chemical analysis was carried out to determine the possible carbon as well as nitrogen content.

There was no carbon detected in the synthesised product and as shown in Table 5-2 the nitrogen content in Co_6W_6N is close to the expected theoretical value. In addition, Co and W contents were determined by the Energy Dispersive Xray (EDX) analysis and were found close to the

expected values (Table 5-3). Therefore, the bulk characterization showed that the nitride was made as a pure phase and free from impurities.

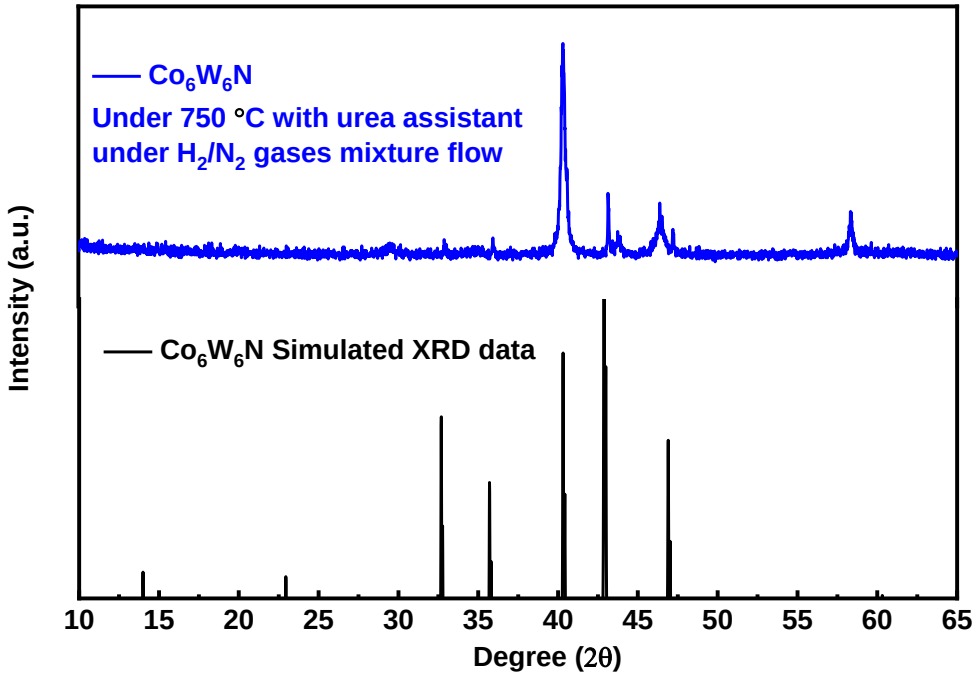

Figure 5-6: Comparison of PXRD pattern of obtained Co_6W_6N samples under 750 ℃ with 5 % H_2 in N_2 (urea assisted) with simulated Co_6W_6N XRD data.

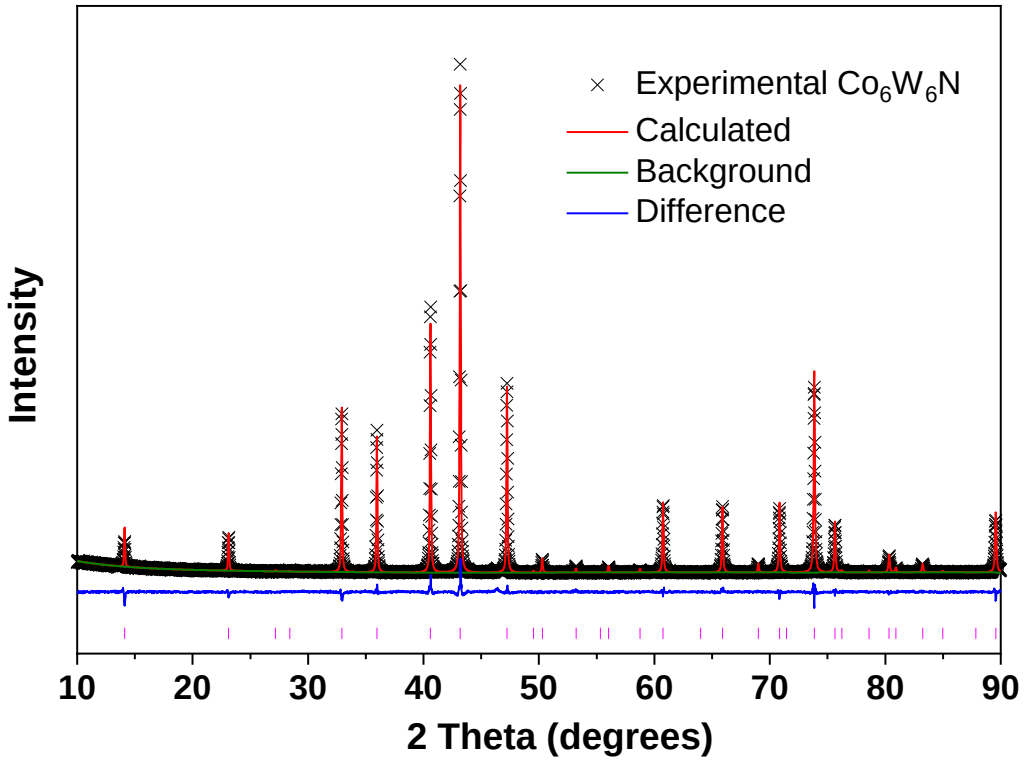

Figure 5-7: Rietveld refinement of PXRD data (CuK_α) for Co_6W_6N prepared at 800 °C with 5 % H_2 in N_2 (urea assisted) using the structure model based on reported Co_3Mo_3N structure (Space group: *Fd*-3*m*). Measured data are shown as crosses; the calculated profile is shown by a solid line through the measured data. The difference profile is shown along the bottom of the plot. Vertical bars represent the reflection positions for the phase.

Table 5-1: Structural parameters for the Rietveld refinement of the PXRD data collected on Co_6W_6N powder sample using structural model based on η-Co_6Mo_6C structure-type (Space group: *Fd*-3*m*) at ambient temperature. Estimated errors in the last digits are given in parentheses. The number of observations 4787, fitting profile (R_p)= 5.10%, weighed profile (R_{wp})= 6.85%. The value of the lattice constant a = 10.8802(8) Å.

	Site	x/a	y/b	z/c	Occupancy	B_{iso} (Å^2)
W	48*f*	0.22574(6)	0.12500	0.12500	1.0	0.0080(3)
Co1	32*e*	0.29218(3)	0.29218(3)	0.29218(3)	1.0	0.0075(2)
Co2	16*d*	0.50000	0.50000	0.50000	1.0	0.0018(3)
N	8*a*	0.12500	0.12500	0.12500	1.0	0.0100

Table 5-2: Results of the chemical microanalysis for the nitrogen element in ternary nitrides prepared in this work.

	Co_6W_6N	Fe_6W_6N
N (Expected, wt. %)	0.95	0.96
N (Experiment, wt. %)	0.94±0.07	0.82±0.10

Table 5-3: Metal content in Co_6W_6N and Fe_6W_6N from EDX analysis.

	Co_6W_6N		Fe_6W_6N	
Elemental composition	Co, at. %	W, at. %	Fe, at. %	W, at. %
Experiment	49.84±0.63	50.16±0.63	50.03±0.65	49.97±0.65
Theory	50	50	50	50

5.2.2. Synthesis of Fe_6W_6N

The full substitution of cobalt atoms in Co_6W_6N structure with iron atoms could be employed to study the intrinsic catalytic activity. Therefore, the identical method of preparing Co_6W_6N was used to synthesise Fe_6W_6N. The reaction procedure involved 20 mL of 0.25 M solution of $FeCl_2 \cdot 4H_2O$ (Hopkin Williams, ACS reagent, ≥ 98.0%) added dropwise to 20 mL of 0.25 M solution of $Na_2WO_4 \cdot 2H_2O$ (Alfa Aesar, ACS reagent, ≥ 99.0%). The relevant solution was allowed to stir for 2 hours under ambient condition. After solidification, the insoluble product was isolated using vacuum filtration and dried overnight in an oven at 120 ℃ resulting in the relevant precursor consisting of metal oxides. The synthesis of both nitrides was carried out by nitridation of the oxide precursors at 800 ℃ in H_2 (5 vol. %) / N_2 gas mixture with a flow rate of 5 mL / min for 5 hours using urea as an additional nitrogen source.

PXRD of the resulting powders revealed diffraction pattern that were consistent with that of the Co_6W_6N. The Rietveld refinement of the data (Figure 5-8) revealed the unit cell of a = 10.9348(3) Å for Fe_6W_6N (Table 5-4). The value of the unit cell parameter observed in this work is consistent with the one reported in the literature a = 10.937 Å.[8]

Chemical and EDXS analyses were carried out to determine the composition as before (Table 5-2 and Table 5-3). No carbon impurities were detected in the synthesised product. However, the nitrogen content was slightly below the expected theoretical values, while Fe and W

contents are close to the expected values. That means that the synthesised nitride was possibly free from impurities.

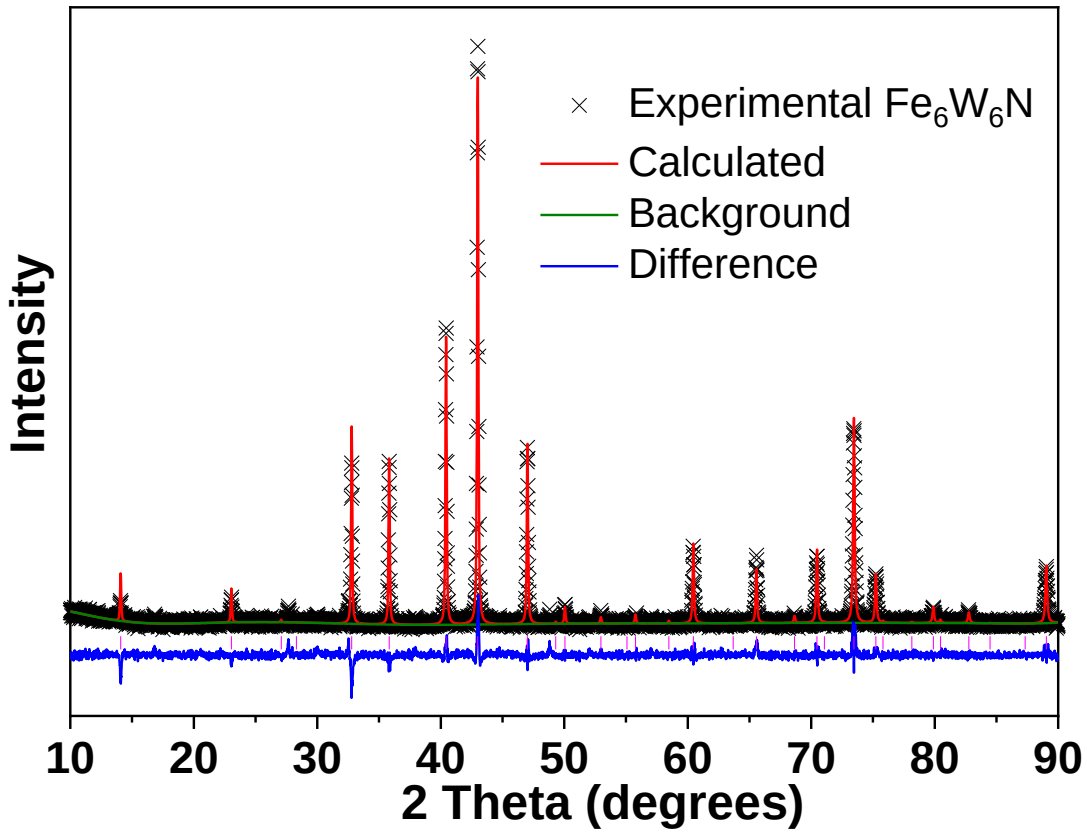

Figure 5-8: Rietveld refinement of PXRD data (CuK_α) for Fe_6W_6N using the structure model based on reported Co_6Mo_6C structure (Space group: *Fd*-3*m*). Measured data are shown as crosses; the calculated profile is shown by a solid line through the measured data. The difference profile is shown along the bottom of the plot. Vertical bars represent the reflection positions for the phase.

Table 5-4: Structural parameters for the Rietveld refinement of the PXRD data collected on Fe_6W_6N powder sample using structural model based on η-Co_6Mo_6C structure-type (Space group: *Fd*-3*m*) at ambient temperature. Estimated errors in the last digits are given in parentheses. The number of observations 4787, fitting profile (R_p)= 8.99%, weighed profile (R_{wp})= 11.61%. The value of the lattice constant a = 10.9373(8) Å. The B_{iso} were not refined and were fixed at 0.01 for all atoms as they tended to show negative values.

	Site	x/a	y/b	z/c	Occupancy	B_{iso} (Å^2)
W	48*f*	0.32390(7)	0.12500	0.12500	1.000	0.0080(2)
Fe1	32*e*	0.29218	0.29218	0.29218	1.000	0.0075(7)
Fe2	16*d*	0.50000	0.50000	0.50000	1.000	0.0018(4)
N	8*a*	0.12500	0.12500	0.12500	1.000	0.00380

5.3. Electrochemical investigations

5.3.1. Electrochemical investigation of Co_6W_6N

The development of active cathodic materials for the HER depends on maximizing the values of the current densities at the lowest overpotential possible. However, impurities can often obscure the results making it difficult to compare between isostructural materials as it is hard to judge whether the performance is due to the main phase or impurities. From the characterization Co_6W_6N was found as a single phase making direct comparison with Co_6Mo_6N (which was also a single phase) possible. As the nitrogen sites were found to play only a minor role in catalytic performance [10] it offers the opportunity to confirm that Co-sites in Co_6W_6N are indeed catalytically active as the molybdenum was specifically substituted by tungsten. Figure 5-9 (red line) shows a typical polarization curve of Co_6W_6N (measured in 0.5 M H_2SO_4 electrolyte and recorded in the HER overpotential range between 0 and -0.6 V at a scan rate of 5 mV/s with iR correction). Low overpotential of 150 ± 8 mV was achieved at 10 mA cm^{-2} cathodic current density which is comparable (117 ± 12 mV) to the Co_6Mo_6N as discussed in previous chapter and reported elsewhere.[10] This suggests that the substitution of molybdenum with tungsten leads to similar catalytic performance and thus, further confirms that Co-sites are catalytic. The slightly higher overpotential may be explained by higher reaction temperature that was necessary for synthesis of a single-phase Co_6W_6N sample. We were unable to synthesise Fe_6Mo_6N but it was possible to make phase pure Fe_6W_6N. When tested electrochemically it is evident that overpotentials increased significantly. The

overpotential of 414 ±18 mV for Fe_6W_6N was observed. This affirms that cobalt sites play key role in the HER activity as otherwise the substitution for Fe would not have such dramatic effect.

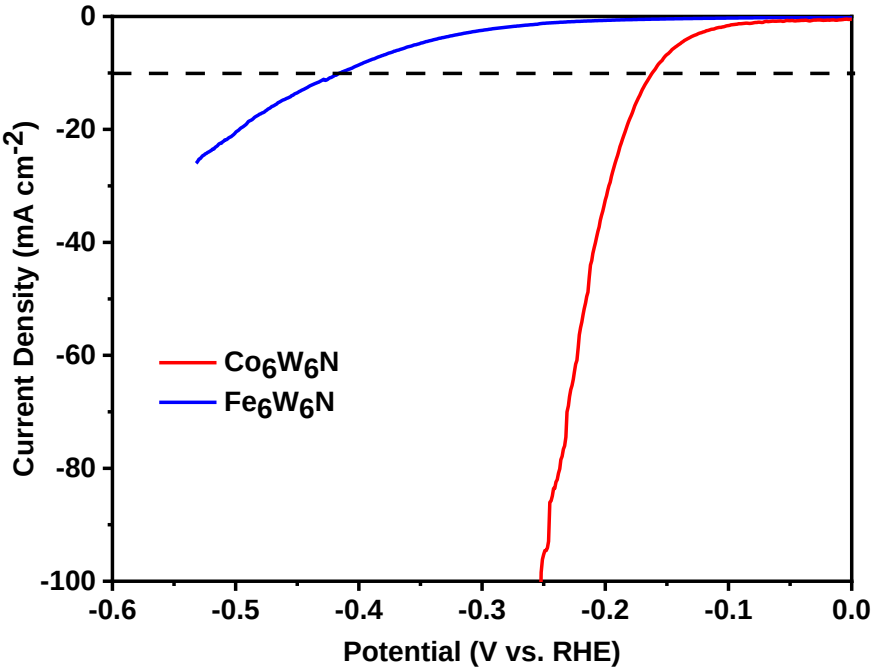

Figure 5-9: Comparison of the current densities achieved by Co_6W_6N (red line) and Fe_6W_6N (blue line) in 0.5 M H_2SO_4. Catalysts were prepared on a glassy carbon working electrode as described in experimental section. An Ag/AgCl (3M KCl) reference and carbon felt counter electrode were used. Curves were obtained using linear sweep voltammetry with a scan rate of 5 mV s^{-1} and all resistance were compensated for resistance.

5.3.2. The studying of intrinsic catalysis behaviours.

The as-measured ternary nitride catalysis polarization curves do not directly reflect the possible reaction mechanism. Therefore, the corresponding Tafel plots were obtained from polarization measurement and shown in Figure 5-10 (the details for the analysis of the Tafel slops was discussed in method section). Co_6W_6N show Tafel slopes of 73.9 ± 1.5 mV per decade. While the value of 179.5 ± 6.8 mV per decade was observed for Fe_6W_6N catalyst. The extremely high Tafel slope for Fe_6W_6N points out that the HER is rate-limited by Volmer step, *i.e.*, the adsorption of H is extremely weak. As described in the previous chapter, Co_6W_6N behaves similar to Co_6Mo_6N and does not follow any classical mechanism suggesting a more complex reaction mechanism. [14] [15][16]

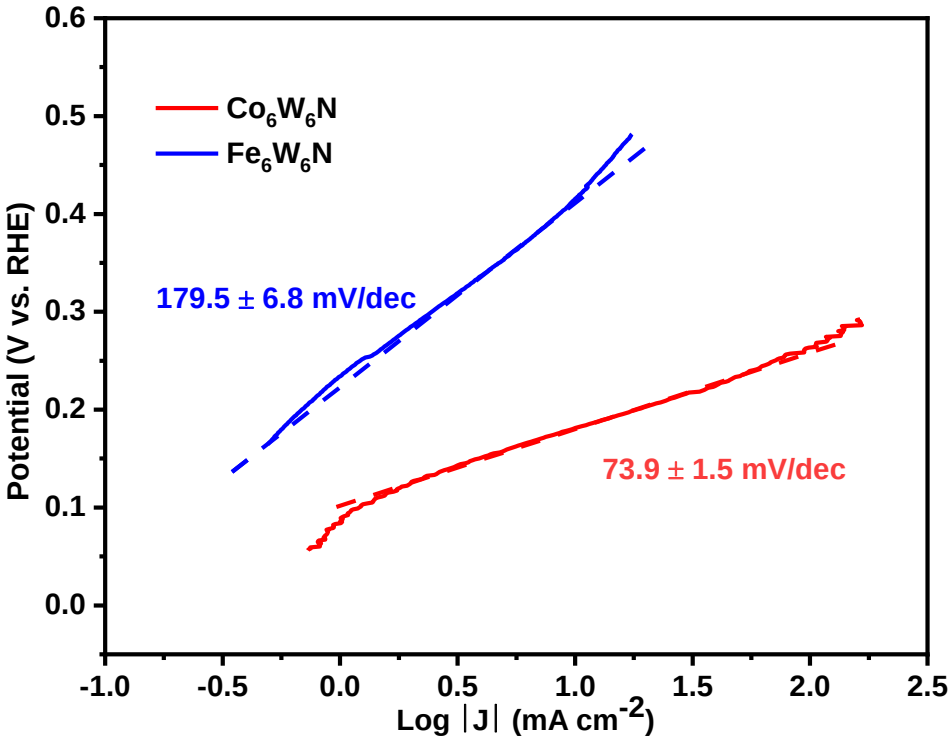

Figure 5-10: Tafel plots and the corresponding Tafel slopes of Co_6W_6N (red line) and Fe_6W_6N (blue line) in 0.5 M H_2SO_4 electrolyte. Slopes were obtained by linear sweep voltammetry with a scan rate of 5 mV s^{-1}. Dashed lines are provided as a guide to the eye. All current densities have been compensated for resistance.

Electrochemically active surface area (ECSA) is considered a factor for the intrinsic activity of the electrocatalyst in the HER.[17] Double layer capacitance, C_{dl}, is directly proportional to ECSA.[17][18] Therefore, the values of C_{dl} were evaluated from CV curves recorded at various scan rates in the potential range of -0.08 V to –0.04 V (*vs.* Ag | AgCl) as shown in Figure 5-11. The higher C_{dl} values of 2.56 ± 0.4 mF cm^{-2} were measured on Co_6W_6N electrocatalysts, but a low value of 0.19 ± 0.1 mF cm^{-2} was observed on Fe_6W_6N. One can hypothesise that the double layer capacitance is due to the adsorption of hydrogen on the surface of the catalyst. And the low values confirm that the hydrogen adsorption on the surface of Fe_6W_6N electrocatalyst is limited which appears in line with the high Tafel slope values.

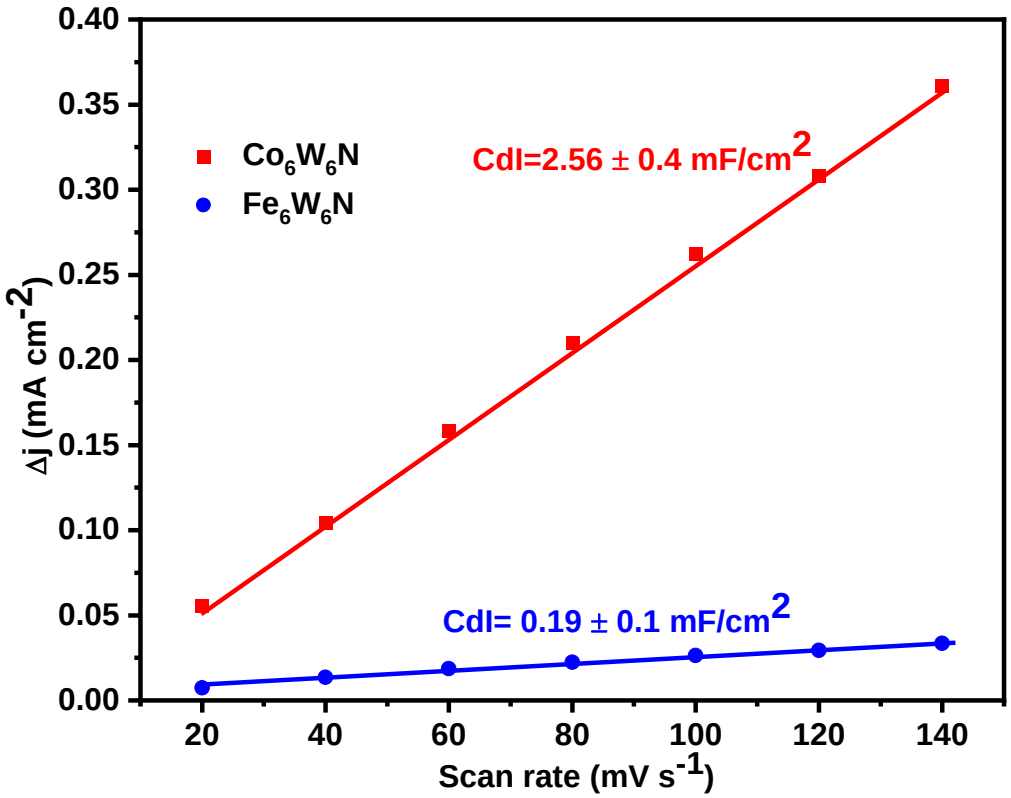

Figure 5-11: Charging current density differences ($\triangle j=j_a-j_c$) plotted against scan rates. The linear slope equivalent to twice of the double-layer capacitance C_{dl}, was used to represent the ECSA.

Although ECSA suggests that there are significantly more catalytic sites in Co_6W_6N it is possible that the higher numbers are simply due to the morphology of the catalyst. Scanning Electron Microscopy (SEM) was carried out to investigate the morphologies of the prepared samples (detailed information in Experimental chapter). Figure 5-12 shows that the three synthesized nitrides showed similar surface, and this was unsurprising as identical reaction conditions were employed. Therefore, the poor catalytic performance of Fe_6W_6N is intrinsic and can be explained solely by the presence of Fe-sites. Overall, the Tafel slopes, ECSA, and SEM studies point out that cobalt sites play an important role in driving the HER in Co_6W_6N.

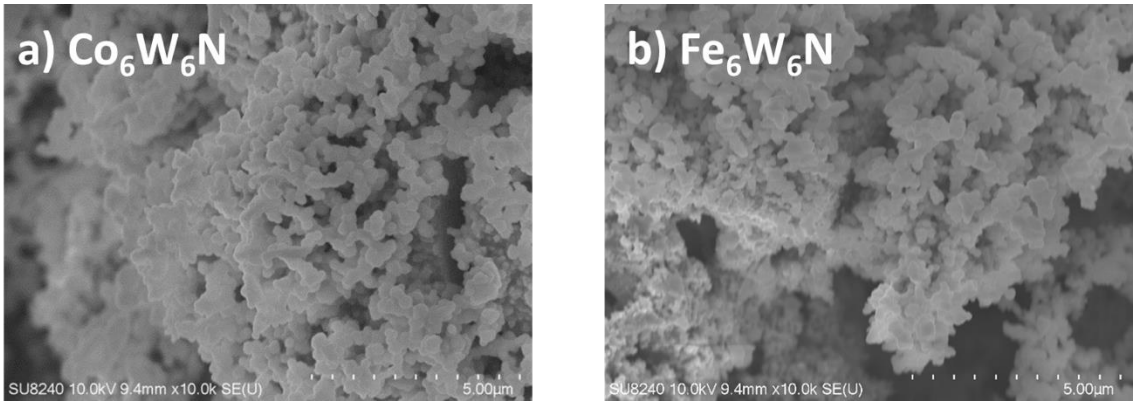

Figure 5-12: High magnification SEM images for (a) Co_6W_6N and (b) Fe_6W_6N synthesised under 800 ℃ via melamine method.

5.3.3. Investigation into electrochemical stability of Co_6W_6N.

The catalyst durability is important for water electrolysis. Chronopotentiometry and CV cycling are two main and efficient techniques that are used to determine the stability of a catalyst. Here, both were applied to measure the stability of Co_6W_6N in acidic electrolyte. The polarization curves of Co_6W_6N electrocatalyst were collected before and after 1000 CV cycling under an unchanging scanning rate of 100 mV s^{-1}, and it showed no significant decay in current density as reported in Figure 5-13.

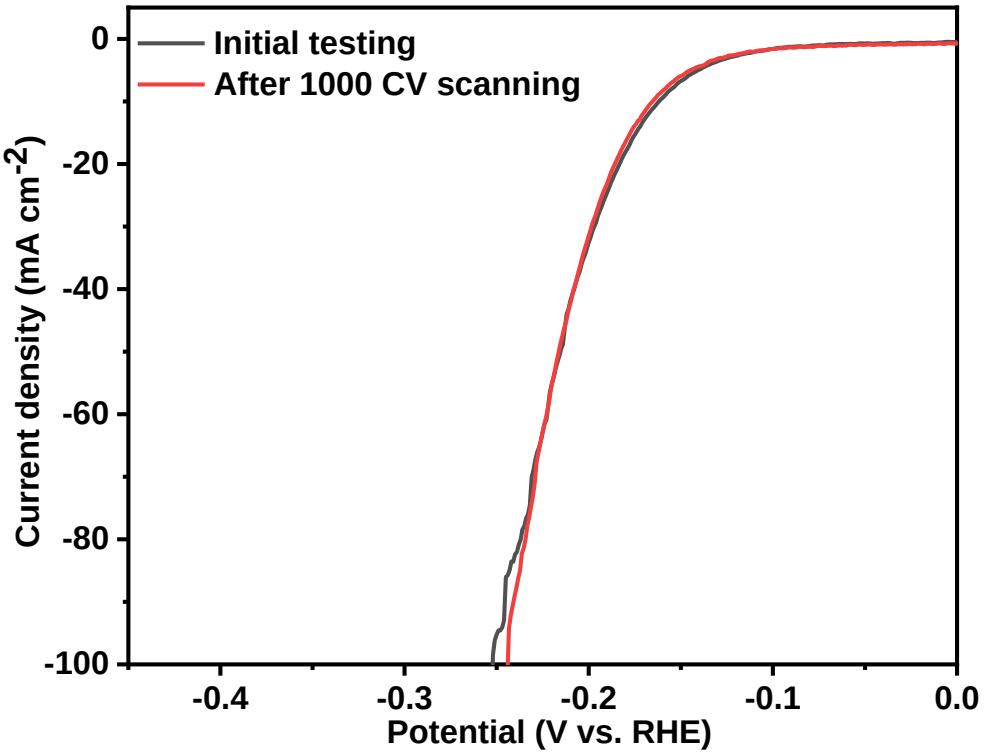

Figure 5-13: Comparison of the current densities achieved by Co_6W_6N before and after 1000 cycles in 0.5 M H_2SO_4. The red line illustrates the current densities achieved immediately after the 1000 cycle scan and shows the overpotential and current density remain unchanged from the original value.

Similarly, Co_6W_6N retained the benchmark current density of 10 mA cm^{-2} over for 16 hours when chronoamperometrically tested under a constant applied potential of 155 mV in 0.5 M H_2SO_4 (Figure 5-14). This is in a strong contrast with Co_6Mo_6N that was found unstable.[10] This suggests that a possible cause for the stability is the presence of W within the structure. Additionally, PXRD patterns of Co_6W_6N samples were collected before and after stability experiments Figure 5-15. There seems be the peaks split after 1000 CV scanning, it may result from the hydrogen being inserted into interstitials during durability testing. No other significant changes can be seen from XRD plots for Co_6W_6N electrocatalyst. Finally, the stability of Co_6W_6N allowed us to measure the Faradaic efficiency of H_2 production. The theoretically expected amount of H_2 is close to the experimental values (Figure 5-16), thereby confirming that Co_6W_6N is indeed produces hydrogen. This makes Co_6W_6N a durable and efficient catalyst that holds potential to be used in PEMEL.

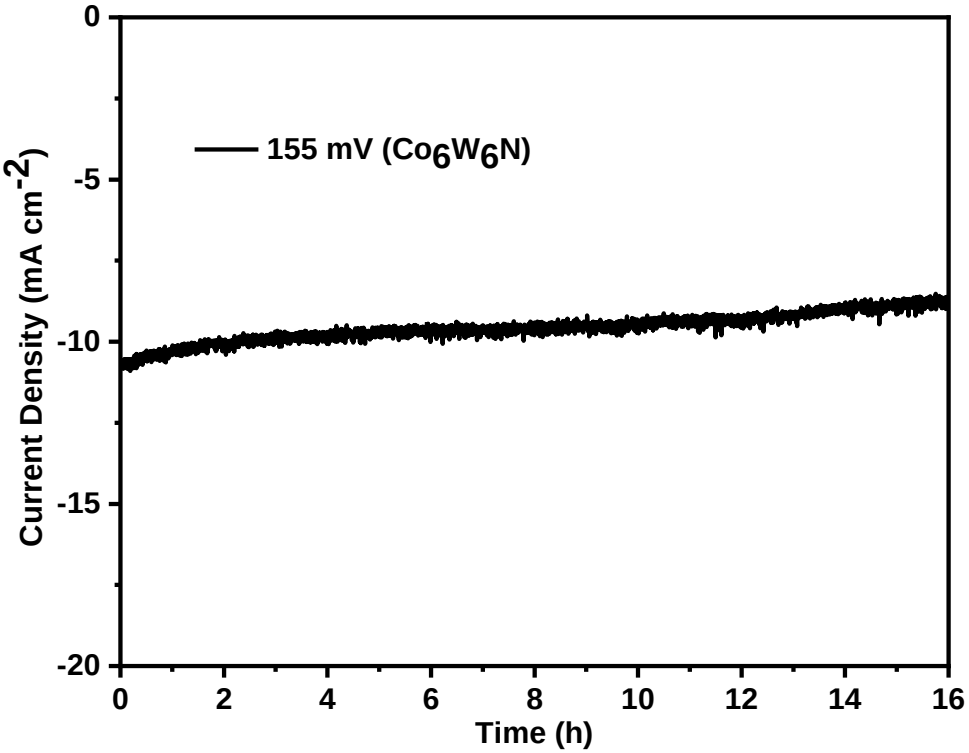

Figure 5-14: Chronoamperometry profile of nanocrystalline pure Co_6W_6N in 0.5 M H_2SO_4. The applied potential was chosen as the value corresponding to j= -10 mA cm^{-2}. Experiments were performed using a three-electrode step, with catalyst-deposited glassy carbon as the working electrode, Ag/AgCl (3 M KCl) as the reference and carbon felt as the counter electrode.

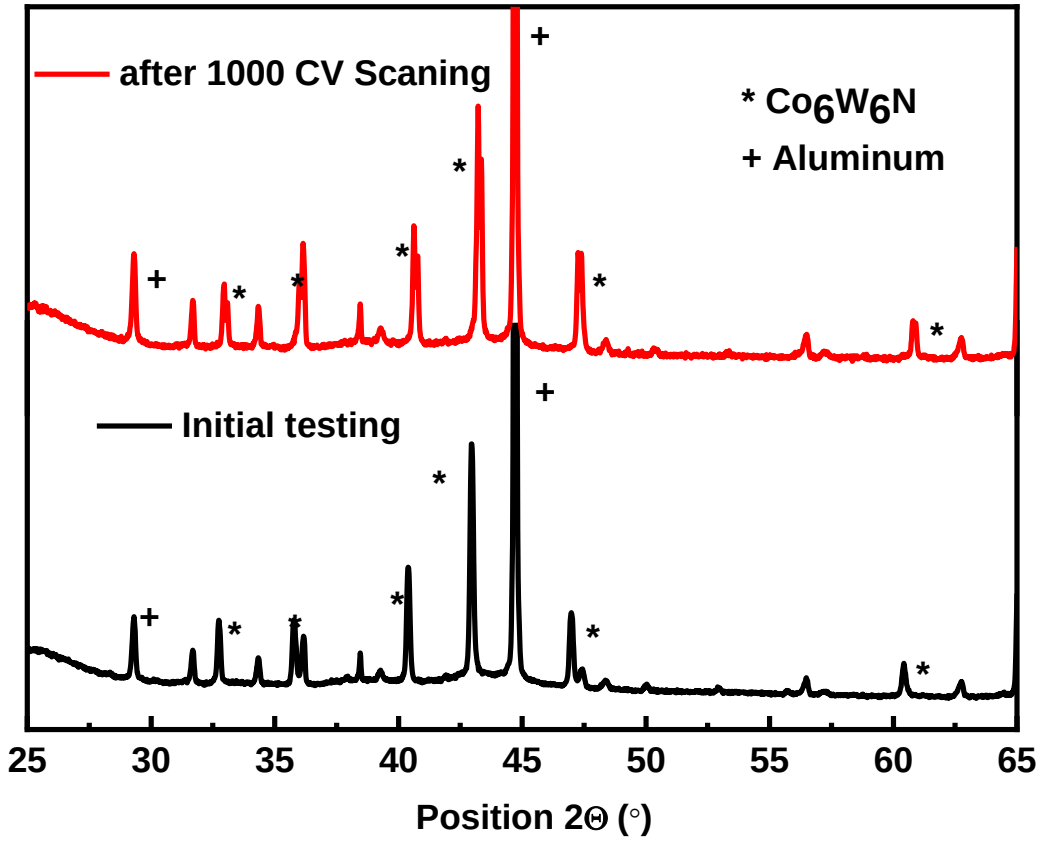

Figure 5-15: The PXRD patterns collected on Co_6W_6N before and after 1000 cycles in 0.5 M H_2SO_4.

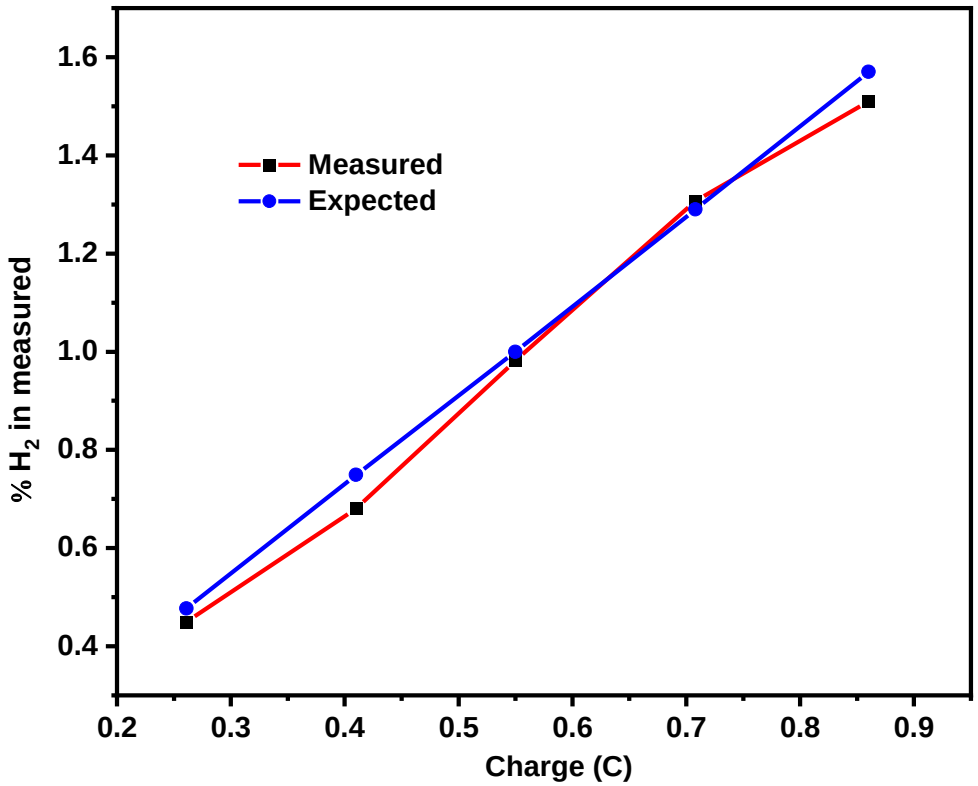

Figure 5-16: A representative trace of the proportion of H_2 (in vol. %) in the single-cell headspace during the electrolysis of Co_6W_6N at a constant current of 108 mA in 0.5 M H_2SO_4. Black squares show the proportion of H_2 (in vol. %) in the cell headspace determined using gas chromatography. The expected proportion of H_2 (in vol %) in the headspace was calculated from the charge passed.

5.4 Conclusion

This work produced an experimental route for the synthesis of a novel Co_6W_6N, noble metal free electrocatalyst. Co_6W_6N showed significantly lower overpotential and Tafel slopes compared with the isostructural Fe_6W_6N suggesting that Co-sites are electrocatalytically active for the hydrogen evolution reaction in acidic condition. The higher electrochemical stability of Co_6W_6N compared with Co_6Mo_6N suggest that the presence of tungsten within the structure leads to improved electrochemical stability. However, the mechanism for stabilisation was not established. Co_6W_6N illustrates that a simple strategy that involved a substitution of the transition metal could help with the improvement of key catalytic properties such as catalytic activity and the stability of catalyst.

5.5 References

[1] Y.N. Regmi, B.M. Leonard, General synthesis method for bimetallic carbides of group VIIIA first row transition metals with molybdenum and tungsten, *Chem. Mater*. 26 (**2014**) 2609–2616. https://doi.org/10.1021/cm500076v.

[2] J.M. Newsam, A.J. Jacobson, L.E. McCandlish, R.S. Polizzotti, The structures of the η-carbides Ni_6Mo_6C, Co_6Mo_6C, and $Co_6Mo_6C_2$, *J. Solid State Chem*; 75:2 (**1988**) 296–304. https://doi.org/10.1016/0022-4596(88)90170-3.

[3] M. Zhang, J. Zhu, B. Liu, Y. Hou, C. Zhang, J. Wang, J. Niu, Ultrafine Co_6W_6C as an efficient anode catalyst for direct hydrazine fuel cells, *Chem. Commun*. 57 (**2021**) 10415–10418. https://doi.org/10.1039/D1CC03446D.

[4] J. Chen, B. Ren, H. Cui, C. Wang, J. Chen, B. Ren, H. Cui, C. Wang, Constructing Pure Phase Tungsten-Based Bimetallic Carbide Nanosheet as an Efficient Bifunctional Electrocatalyst for Overall Water Splitting, *Small*. 16 (**2020**) 1907556. https://doi.org/10.1002/SMLL.201907556.

[5] J. Gao, J. Yang, X. Cai, Z. Xing, H. Xu, G. Li, Facile preparation of Co_6W_6C/W@NC electrocatalyst for hydrogen evolution reaction using transition metal substituted polyoxometalates as precursor, *Mater. Lett*. 271 (**2020**) 127722. https://doi.org/10.1016/J.MATLET.2020.127722.

[6] S.M. Hunter, D. McKay, R.I. Smith, J.S.J. Hargreaves, D.H. Gregory, Topotactic nitrogen transfer: Structural transformation in cobalt molybdenum nitrides, *Chem. Mater*. 22 (**2010**) 2898–2907. https://doi.org/10.1021/cm100208a.

[7] S.M. Hunter, D.H. Gregory, J.S.J. Hargreaves, M. Richard, D. Duprez, N. Bion, A study of $^{15}N/^{14}N$ isotopic exchange over cobalt molybdenum nitrides, *ACS Catal*. 3 (**2013**) 1719–1725. https://doi.org/10.1021/cs400336z.

[8] T. Waki, S. Terazawa, Y. Tabata, Y. Murase, M. Kato, K. Hirota, S. Ikeda, H. Kobayashi, K. Sato, K. Kindo, H. Nakamura, HIP synthesis of *η*-carbide-type nitrides Fe_3W_3N and Fe_6W_6N and their magnetic properties, *J. Alloys Compd*. 509 (**2011**) 9451–9455. https://doi.org/10.1016/J.JALLCOM.2011.07.025.

[9] K.S. Weil, P.N. Kumta, Structural Characterization of a Series of New Ternary pg-Nitride Compounds, *MRS Online Proc. Libr.* 1998 4951. 495 (**1997**) 221–226.

https://doi.org/10.1557/PROC-495-221.

[10] Y. Sun, L. Wang, O. Guselnikova, O. Semyonov, J. Fraser, Y. Zhou, N. López, A.Y. Ganin, Revealing the activity of Co_3Mo_3N and $Co_3Mo_3N_{0.5}$ as electrocatalysts for the hydrogen evolution reaction, *J. Mater. Chem. A.* 10 (**2022**) 855–861. https://doi.org/10.1039/D1TA08389A.

[11] Y. Yuan, S. Adimi, X. Guo, T. Thomas, Y. Zhu, H. Guo, G.S. Priyanga, P. Yoo, J. Wang, J. Chen, P. Liao, J.P. Attfield, M. Yang, A Surface-Oxide-Rich Activation Layer (SOAL) on Ni_2Mo_3N for a Rapid and Durable Oxygen Evolution Reaction, *Angew. Chemie Int. Ed.* 59 (**2020**) 18036–18041. https://doi.org/10.1002/ANIE.202008116.

[12] K.S. Weil, P.N. Kumta, Synthesis and structural investigation of a new ternary transition metal nitride, Co_3W_3N, *J. Alloys Compd.* 265 (**1998**) 96–103. https://doi.org/10.1016/S0925-8388(97)00283-1.

[13] C.B. Pollock, H.H. Stadelmaier, The eta carbides in the Fe−W−C and Co−W−C systems, *Metall. Trans.* 1970 14. 1 (**1970**) 767–770. https://doi.org/10.1007/BF02811752.

[14] Y. Sun, A.Y. Ganin, The Synergistic Effects of Alloying on the Performance and Stability of Co_3Mo and Co_7Mo_6 for the Electrocatalytic Hydrogen Evolution Reaction, *Hydrog.* 2020, Vol. 1, Pages 11-21. 1 (**2020**) 11–21. https://doi.org/10.3390/HYDROGEN1010002.

[15] D. Li, C. Batchelor-McAuley, R.G. Compton, Some thoughts about reporting the electrocatalytic performance of nanomaterials, *Appl. Mater. Today*. 18 (**2020**) 100404. https://doi.org/10.1016/J.APMT.2019.05.011.

[16] A. Lasia, Mechanism and kinetics of the hydrogen evolution reaction, *Int. J. Hydrogen Energy*. 44 (**2019**) 19484–19518. https://doi.org/10.1016/J.IJHYDENE.2019.05.183.

[17] F. Rosalbino, D. Macciò, A. Saccone, G. Scavino, Study of Co–W crystalline alloys as hydrogen electrodes in alkaline water electrolysis, *Int. J. Hydrogen Energy*. 39 (**2014**) 12448–12456. https://doi.org/10.1016/J.IJHYDENE.2014.06.082.

[18] J.C. McGlynn, T. Dankwort, L. Kienle, N.A.G. Bandeira, J.P. Fraser, E.K. Gibson, I. Cascallana-Matías, K. Kamarás, M.D. Symes, H.N. Miras, A.Y. Ganin, The rapid

electrochemical activation of $MoTe_2$ for the hydrogen evolution reaction, *Nat. Commun*. 2019 101. 10 (**2019**) 1–9. https://doi.org/10.1038/s41467-019-12831-0.

Chapter 6. Investigation of $Fe_xNi_{2-x}Mo_3N$ (x = 0 - 1.25) as electrocatalysts for the HER

Apart from the nitrides with η-carbide structures (Co_3Mo_3N, Fe_3Mo_3N, Co_6Mo_6N and Co_6W_6N) that were already discussed in Chapter 4 and Chapter 5, two other nitrides (Co_2Mo_3N and Ni_2Mo_3N) with the Mo_3Al_2C structure are interesting targets for the investigation.[1–6] Recent reports showed that Co_2Mo_3N cannot be reduced under H_2 to nitrogen-deficient phase in comparison with Co_3Mo_3N.[2,4] Furthermore, Co_2Mo_3N contains only two equivalents of Co compared with Co_3Mo_3N. Therefore, it could be used as a good testing subject to probe that Co-sites are indeed catalytic, and as one would expect a poorer performance from this nitride if this were the case.

6.1. Introduction

The nitrides adopting the Mo_3Al_2C structure [7–9] are described by a cubic cell (space group symmetry $P4_132$). As displayed in Figure 6-1 either Co_2Mo_3N or Ni_2Mo_3N consists of corner-sharing Mo_6N octahedra with Co and Ni forming a network by filling the space between the octahedra (by occupying 8*c*-Wickoff sites). Ni_2Mo_3N is commonly prepared by nitridation of a relevant oxide precursor by NH_3,[3,4] H_2/N_2,[7] or using urea under N_2.[10] Ni_2Mo_3N was electrochemically tested and showed a reasonable activity towards both the hydrogen and oxygen evolution processes in alkaline media.[11–13] However, compared with Ni_2Mo_3N, the isostructural Co_2Mo_3N has remained relatively unexplored. It is challenging to synthesise through phase pure Co_2Mo_3N since Co_3Mo_3N exist and tends to form. Therefore, Co_2Mo_3N catalysts that are tested electrochemically contained impurities. Specifically, the tested products prepared in NH_3 contained Co_3Mo_3N as impurity [2,7] and those obtained in H_2/N_2 consisted of phase mixtures of Co_2Mo_3N, Co_3Mo_3N and β-$Mo_2N_{0.78}$.[6] Access to a phase pure Co_2Mo_3N is important for understanding of its catalytic behaviour towards the HER.

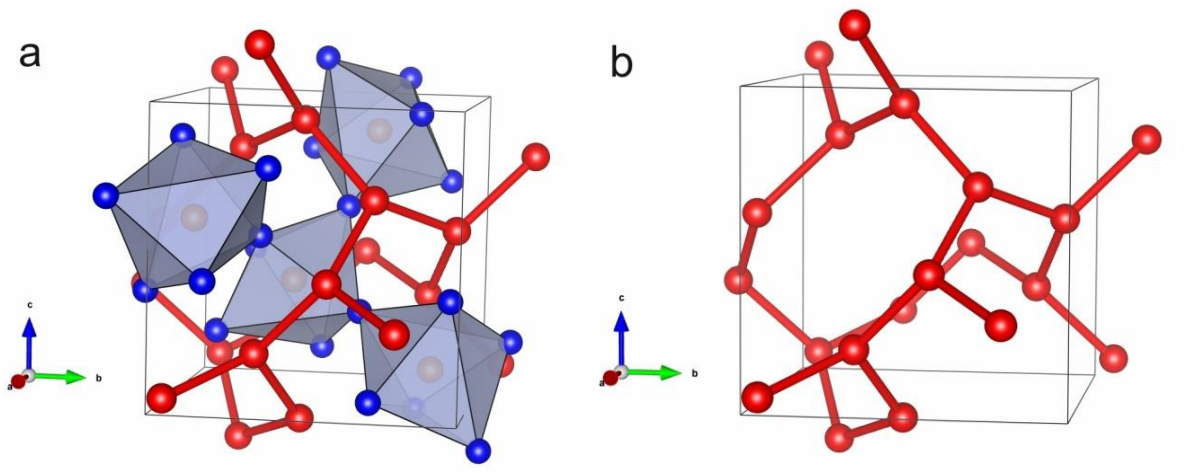

Figure 6-1: Crystal structure of (Co or Ni)$_2$Mo$_3$N displaying a network of vertex-sharing Mo$_6$N octahedra (a); the network of Co or Ni atoms interpenetrating the structure with Mo and N atoms omitted for clarity (b). **Co** or **Ni** – red; **Mo** – blue; **N** – orange spheres.

6.2. Aims

The aim of this work is to develop the reaction protocol and synthesise phase-pure Co_2Mo_3N or Ni_2Mo_3N through a sol-gel route. If successful, these materials would be used for the electrochemical studies to probe the intrinsic electrocatalytic activity of these ternary nitrides. In addition, the solid solutions could be formed to make isostructural $Fe_xNi_{2-x}Mo_3N$ compounds. The specific substitution of Ni by Fe should provide some information about the role of Ni in catalytic performance of Ni_2Mo_3N. This information could then provide an insight into the role different metals play in the process of electrolysis.

6.3. Synthesis and characterisation of Co_2Mo_3N and $Fe_xNi_{2-x}Mo_3N$ (x = 0-1.25)

The samples were synthesised using a similar method as Co_3Mo_3N which is discussed in Chapter 4.

6.3.1. Synthesis and characterisation of Co_2Mo_3N

Firstly, Co-Mo based oxide precursor was prepared by a citric method: 3.77 mmol $Co(NO_3)_2 \cdot 6H_2O$ (Alfa Aesar, ACS reagent, ≥ 99.0%), 0.81 mmol $(NH_4)_6Mo_7O_{24} \cdot 4H_2O$ (Sigma-Aldrich, ACS reagent, ≥ 99.0 %) and 20 mmol citric acid monohydrate, $C_6H_8O_7 \cdot H_2O$ (Alfa Aesar, ≥ 99.5 %) were added into a 150 ml pyrex beaker and fully dissolved in 80 ml deionised water by stirring at room temperature. The water was evaporated at 120 °C resulting in foam looking products. The foams were calcined within the same beaker in air in a box furnace at 500 °C for 12 hours to eliminate any traces of carbon, and then the calcined foam was ground to powder. Co_2Mo_3N was synthesised by nitridation of the oxide precursor

prepared as described above. In a typical experiment, 200 mg of the oxide precursor were placed into a ceramic boat within a tube furnace. The samples were heated at 5 °C min^{-1} to 850 °C under the flow of H_2 (5 %) / N_2 gas (a flow rate of 10 mL min^{-1}). After 5 hours of reaction time the furnace was cooled naturally to the ambient temperature and the synthesised products were reground with a pestle and mortar.

The resulting material was measured by PXRD and as single phase was confirmed by comparison with the simulated pattern Rietveld refinement on the data was undertaken. The refinement of the data based on a Mo_3Al_2C structure (space group $P4_132$) rapidly converged. The fitted X-ray diffraction pattern is shown in Figure 6-2 and the refined structural parameters are presented in Table 6-1.

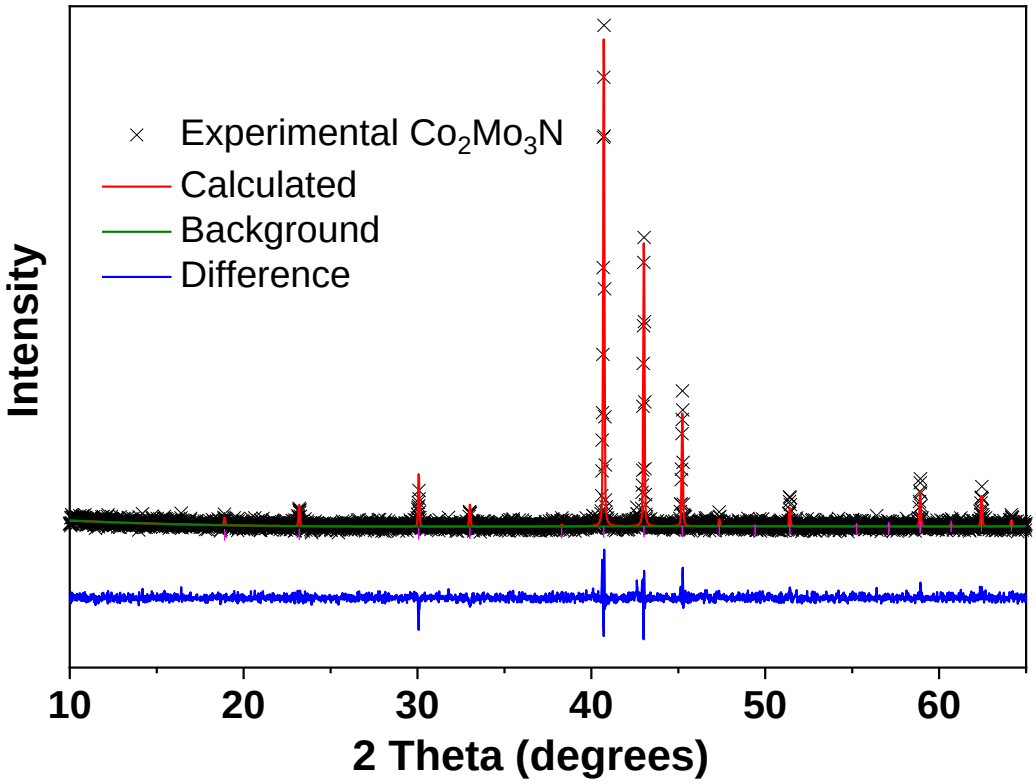

Figure 6-2: Rietveld refinement of PXRD data (CuK_α) for Co_2Mo_3N using the structure model based on reported Co_2Mo_3N structure (Space group: $P4_132$). Measured data are shown as crosses; the calculated profile is shown by a solid line through the measured data. The difference profile is shown along the bottom of the plot. Vertical bars represent the reflection positions for the phase.

Table 6-1: Structural parameters for the Rietveld refinement of the PXRD data collected on Co_2Mo_3N powder sample using structural model based on Mo_3Al_2C structure-type (Space group: $P4_132$) at ambient temperature. Estimated errors in the last digits are given in parentheses. The number of observations 5333, fitting profile (R_p)= 6.63%, weighed profile (R_{wp})= 8.63%. The value of the lattice constant a = 6.6548(2) Å. (Literature: a = 6.6653 Å prepared in H_2(10%)/ N_2;).[7]

	Site	x/a	y/b	z/c	Occupancy	B_{iso} (Å^2)
Mo	12*d*	0.1250	0.2051(3)	0.4551(3)	1.0000	0.0266(8)
Co	8*c*	0.0675(4)	0.0675(4)	0.0675(4)	1.0000	0.0075(5)
N	4*a*	0.3750	0.3750	0.3750	1.0000	0.2500

SEM investigation of the samples was undertaken after, and representative SEM images are presented in Figure 6-3. It is evident that the samples comprised of small particles and overall morphology resembled a sponge which is consistent with the previously published work. In addition, the EDX analysis carried out at different parts of the sample showed an average atomic ratio Co / Mo = 40.8 / 59.2 (Table 6-2). However, this value is within experimental error of the expected ratio (40 / 60 for Co_2Mo_3N).

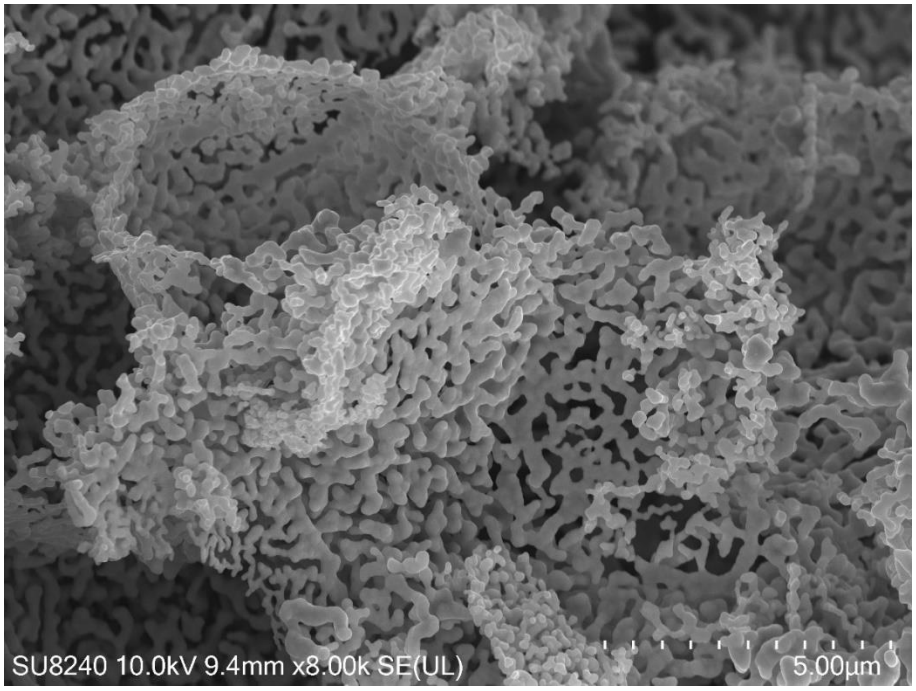

Figure 6-3: SEM image of Co_2Mo_3N prepared by reaction of oxide precursor for 5 h at 850 °C.

Table 6-2: Metal content in Co_2Mo_3N and $Fe_xNi_{2-x}Mo_3N$ (x = 0 – 1.25) samples based on the results of EDX analysis. It should be noted that nitrogen as light element cannot be detected reliably and therefore, it was excluded from the EDX analysis. The standard deviations were calculated based on averaging the results on at least five points collected at different parts of the sample.

Targeted composition	**Ni, at. % Experiment / Theory**	**Mo, at. % Experiment / Theory**	**Fe, at. % Experiment / Theory**	**Co, at. % Experiment / Theory**
Ni_2Mo_3N	40.53±0.84 / 40	59.47±0.84 / 60		
$Fe_{0.5}Ni_{1.5}Mo_3N$	30.86±0.85 / 30	59.14±0.85 / 60	10.00±0.85 /10	
$FeNiMo_3N$	20.23±0.68 / 20	60.18±0.68 / 60	19.59±0.68 / 20	
$Fe_{1.25}Ni_{0.75}Mo_3N$	15.03±0.57 / 15	60.52±0.57 / 60	24.45±0.57 / 25	
Co_2Mo_3N		59.24±0.63 / 60		40.76±0.63 / 40

6.3.2. Synthesis and characterisation of Ni_2Mo_3N

Identical experimental method as for Co_2Mo_3N was applied to the synthesis of Ni_2Mo_3N. Specifically, 3.77 mmol $Ni(NO_3)_2 \cdot 6H_2O$ (Alfa Aesar, ACS reagent, ≥ 99.0%) was used to replace 3.77 mmol $Co(NO_3)_2 \cdot 6H_2O$, other steps were kept unchanged. The resulting PXRD patterns are presented in Figure 6-4. Rietveld refinement of PXRD data against model based on the Mo_3Al_2C structure (space groups $P4_132$) showed that Ni_2Mo_3N was single phase sample. Detailed crystal data are summarised in Table 6-3. In contract to the products prepared by methods which involved ammonia gas, our PXRD patterns showed no evidence for the presence of impurity (like Mo_2N or Mo) in the final product.[3,10,11,14,15]

SEM image (Figure 6-5) of Ni_2Mo_3N is very similar to the prepared Co_2Mo_3N above. It shows that the synthetic method and reaction temperature led to the same morphology. EDX showed an atomic ratio Ni:Mo of 40.53:59.47 within experimental error of the expected ratio (40:60 for Ni_2Mo_3N) as summarized in Table 6-2.

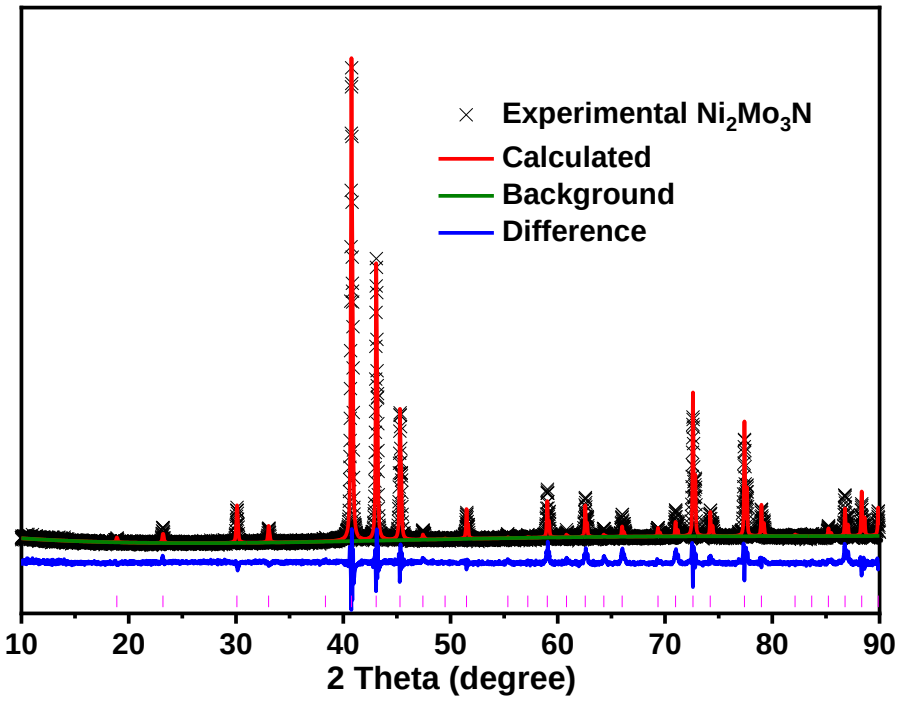

Figure 6-4: Rietveld refinement of PXRD data (CuK$_\alpha$) for Ni_2Mo_3N using the structure model based on reported Ni_2Mo_3N structure (Space group: $P4_132$). Measured data are shown as crosses; the calculated profile is shown by a solid line through the measured data. The difference profile is shown along the bottom of the plot. Vertical bars represent the reflection positions for the phase.

Table 6-3: Structural parameters for the Rietveld refinement of the PXRD data collected on Ni_2Mo_3N powder sample using structural model based on Mo_3Al_2C structure-type (Space group: $P4_132$) at ambient temperature. Estimated errors in the last digits are given in parentheses. The number of observations 5333, fitting profile (R_p)= 8.35%, weighed profile (R_{wp})= 11.00%. The value of the lattice constant a = 6.6321(1) Å. (Literature: a = 6.6340 Å prepared in H_2/ N_2; 6.6335 Å , 6.6324 Å and 6.6327 Å prepared in H_2/N_2, 6.6305 Å and 6.6364 Å prepared by ammonolysis of metal oxides in NH_3, and 6.6208 Å prepared by urea method).[3,10,11,14,15]

	Site	x/a	y/b	z/c	Occupancy	B_{iso} (Å^2)
Mo	12*d*	0.1250	0.2018(2)	0.4518(2)	1.0000	0.0200(9)
Ni	8*c*	0.0628(3)	0.0628(3)	0.0628(3)	1.0000	0.0266(1)
N	4*a*	0.3750	0.3750	0.3750	1.0000	0.2500

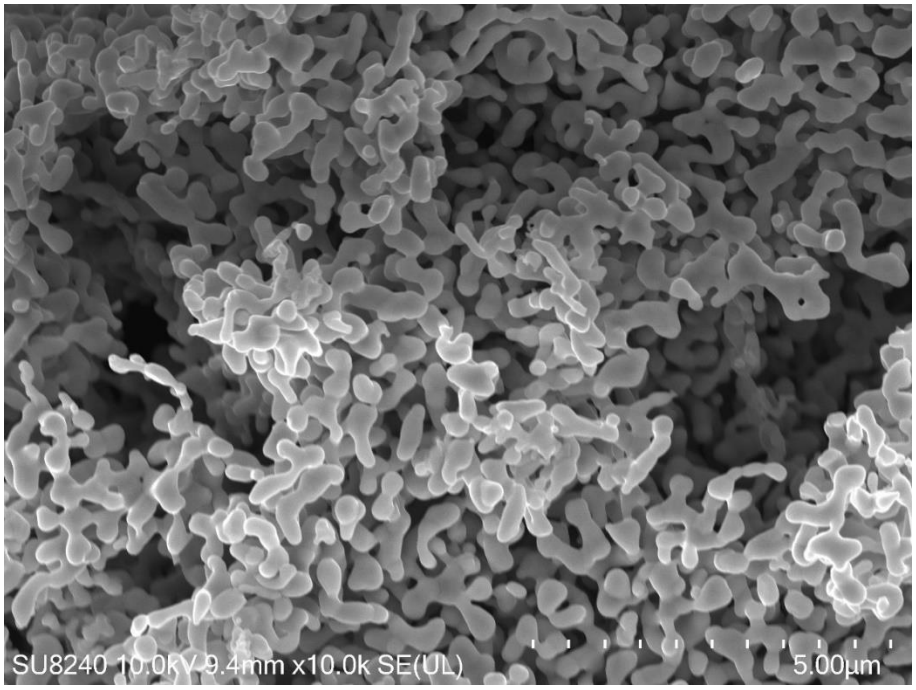

Figure 6-5: SEM image of Ni_2Mo_3N prepared through nitridation of a precursor synthesised by Pechini method for 5 hrs at 850 ℃.

6.3.3. Synthesis and characterisation of $Fe_xNi_{2-x}Mo_3N$ (x = 0.5, 1 or 1.25)

The attempts to replace either cobalt or nickel atoms with iron in the above two samples were carried out. $Fe(NO_3)_3 \cdot 9H_2O$ (Fisher Chemical, Analytical reagent grade) was used to make a precursor in addition to either $Co(NO_3)_2 \cdot 6H_2O$ or $Ni(NO_3)_2 \cdot 6H_2O$. The other reaction steps were unchanged. However, the Co_2Mo_3N and Fe_3Mo_3N phases were observed from the attempts to make $Fe_xCo_{2-x}Mo_3N$ as demonstrated by an example of sample with the nominal composition $FeCoMo_3N$ in Figure 6-6. These two phases (Co_2Mo_3N with the unit cell a = 6.6632Å and Fe_3Mo_3N with the unit cell a = 11.0856 Å, both are identical with reported value 6.6653 Å[7] and 11.07808 Å[15], respectively) invariably were main components of the reaction mixture.

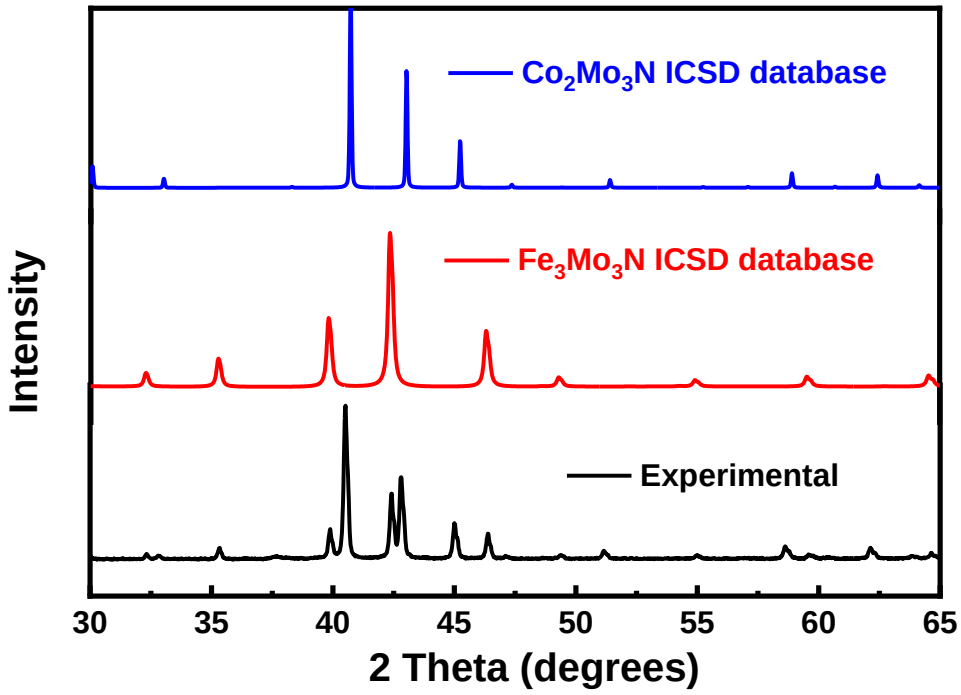

Figure 6-6: PXRD pattern for $FeCoMo_3N$ synthesised by annealing FeCo-Mo oxide precursor under H_2/N_2 gas flow at 850°C.

The stoichiometry of the precursors for synthesis of $Fe_xNi_{2-x}Mo_3N$, are summarized in Table 6-4. PXRD patterns of the resulting powders were consistent with the formation of a relevant single phase products. From the Rietveld refinement of the PXRD data collected on resulting powder (Figure 6-7 to Figure 6-9), the experimental data were found to converge rapidly consistent with a Mo_3Al_2C structure with space group $P4_132$. The structural parameters are presented in Table 6-5 to Table 6-7.

In addition, the morphology retained after replacing some nickel atoms from the Ni_2Mo_3N compounds as depicted in Figure 6-10 to Figure 6-12 and EDX showed an atomic ratio within experimental error of the expected ratio as presented in Table 6-2, which make the evaluation of electrochemistry more reliable.

Table 6-4: Quantities of reagents used in the synthesis of iron nickel molybdenum nitride $Fe_xNi_{2-x}Mo_3N$ (x = 0.5, 1 and 1.25)

x	$Ni(NO_3)_2 \cdot 6H_2O$	$Fe(NO_3)_3 \cdot 9H_2O$	$(NH_4)_6Mo_7O_{24} \cdot 4H_2O$	Citric acid monohydrate
0.5	2.83mmol	0.94mmol	0.81mmol	20mmol
1	1.88mmol	1.89mmol	0.81mmol	20mmol
1.25	1.41mmol	2.36mmol	0.81mmol	20mmol

Table 6-5: Structural parameters for the Rietveld refinement of the PXRD data collected on $Fe_{0.5}Ni_{1.5}Mo_3N$ powder sample using structural model based on Mo_3Al_2C structure-type (Space group: $P4_132$) at ambient temperature. Estimated errors in the last digits are given in parentheses. The number of observations 5333, fitting profile (R_p)= 4.42%, weighed profile (R_{wp})= 6.47%. The value of the lattice constant a = 6.6464(2) Å. (Literature: a = 6.6479 Å prepared in H_2/ N_2.[16]

	Site	x/a	y/b	z/c	Occupancy	B_{iso} (Å^2)
Mo	12*d*	0.1250	0.2018(2)	0.2018(2)	1.0000	0.0014(4)
Ni	8*c*	0.0688(8)	0.0688(8)	0.0688(8)	0.7500	0.0013(7)
Fe	8*c*	0.695(2)	0.695(2)	0.695(2)	0.2500	0.0024
N	4*a*	0.37500	0.37500	0.37500	1.0000	0.0025

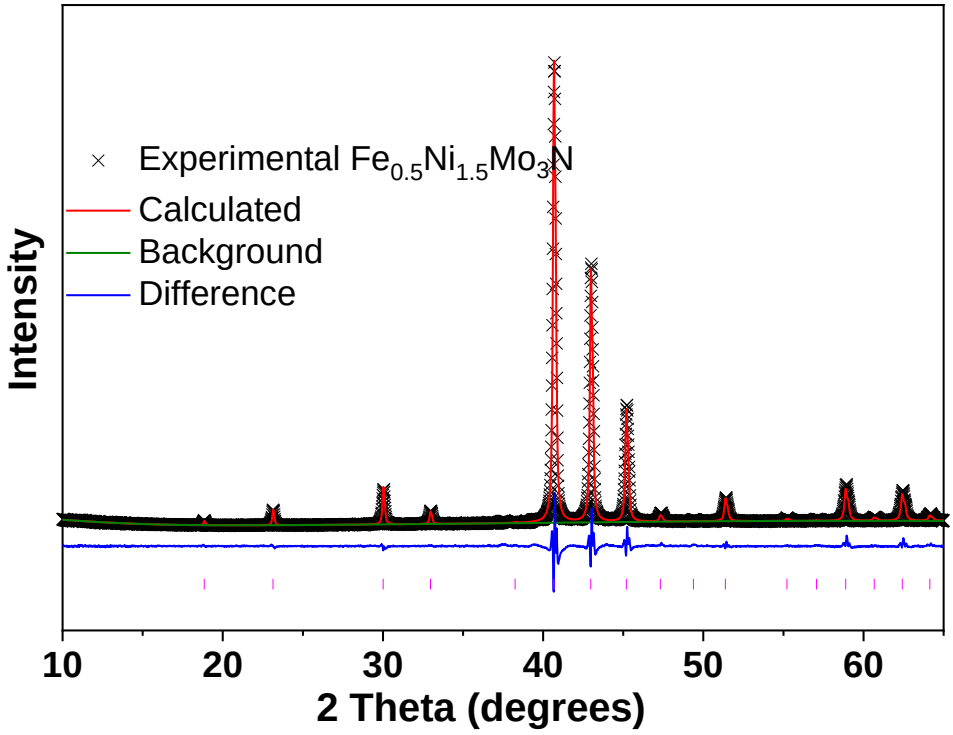

Figure 6-7: Rietveld refinement of PXRD data (CuK$_\alpha$) for $Fe_{0.5}Ni_{1.5}Mo_3N$ using the structure model based on reported Ni_2Mo_3N structure (Space group: $P4_132$). Measured data are shown as crosses; the calculated profile is shown by a solid line through the measured data. The difference profile is shown along the bottom of the plot. Vertical bars represent the reflection positions for the phase.

Table 6-6: Structural parameters for the Rietveld refinement of the PXRD data collected on $FeNiMo_3N$ powder sample using structural model based on Mo_3Al_2C structure-type (Space group: $P4_132$) at ambient temperature. Estimated errors in the last digits are given in parentheses. The number of observations 5333, fitting profile (R_p)= 5.00%, weighed profile (R_{wp})= 7.14%. The value of the lattice constant a = 6.6634(3) Å. (Literature: a = 6.663 Å prepared in H_2/ N_2.[16]

	Site	x/a	y/b	z/c	Occupancy	B_{iso} (Å^2)
Mo	12*d*	0.1250	0.2034(2)	0.4534(2)	1.0000	0.0010(3)
Ni	8*c*	0.0688(4)	0.0688(4)	0.0688(4)	0.5000	0.0005(5)
Fe	8*c*	0.0648(4)	0.0648(4)	0.0648(4)	0.5000	0.0036(9)
N	4*a*	0.3750	0.3750	0.3750	1.0000	0.0025

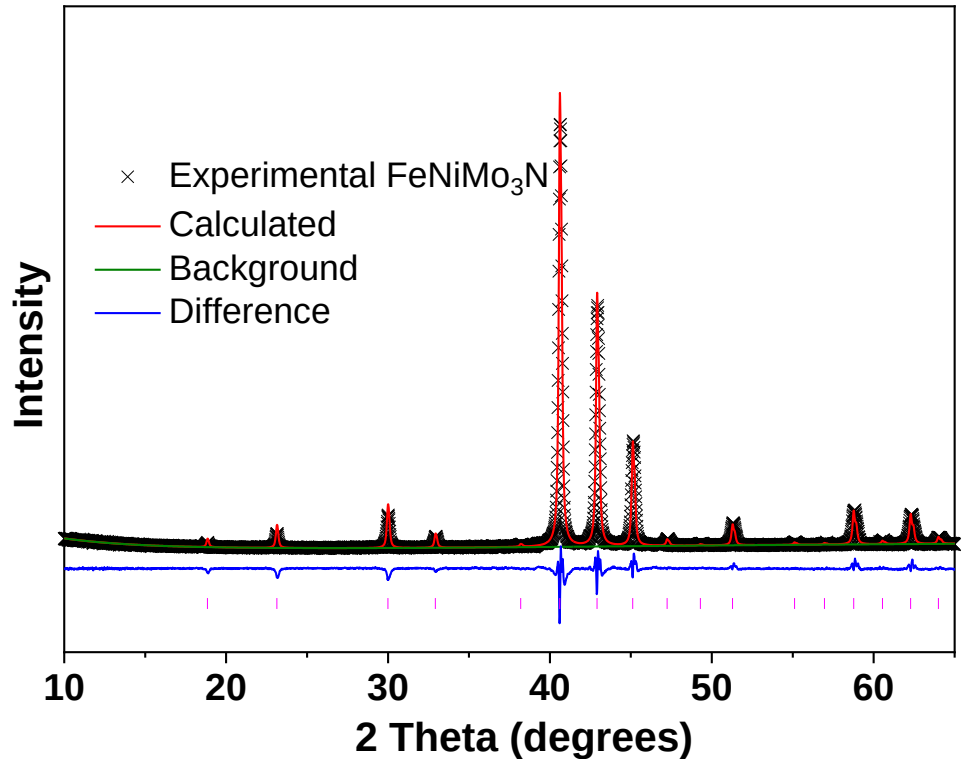

Figure 6-8: Rietveld refinement of PXRD data (CuK_α) for $FeNiMo_3N$ using the structure model based on reported Ni_2Mo_3N structure (Space group: $P4_132$). Measured data are shown as crosses; the calculated profile is shown by a solid line through the measured data. The difference profile is shown along the bottom of the plot. Vertical bars represent the reflection positions for the phase.

Table 6-7: Structural parameters for the Rietveld refinement of the PXRD data collected on $Fe_{1.25}Ni_{0.25}Mo_3N$ powder sample using structural model based on Mo_3Al_2C structure-type (Space group: $P4_132$) at ambient temperature. Estimated errors in the last digits are given in parentheses. The number of observations 5333, fitting profile (R_p)= 4.74%, weighed profile (R_{wp})= 6.88%. The value of the lattice constant a = 6.6702(4) Å. (Literature: a = 6.6722 Å prepared in H_2/ N_2.[16]

	Site	x/a	y/b	z/c	Occupancy	B_{iso} (Å^2)
Mo	12*d*	0.12500	0.2035(2)	0.4530(2)	1.0000	0.00092
Ni	8*c*	0.0656(8)	0.0656(8)	0.0656(8)	0.3750	0.00092
Fe	8*c*	0.0689(8)	0.06890	0.0689(8)	0.6250	0.00096
N	4*a*	0.37500	0.37500	0.37500	1.0000	0.00096

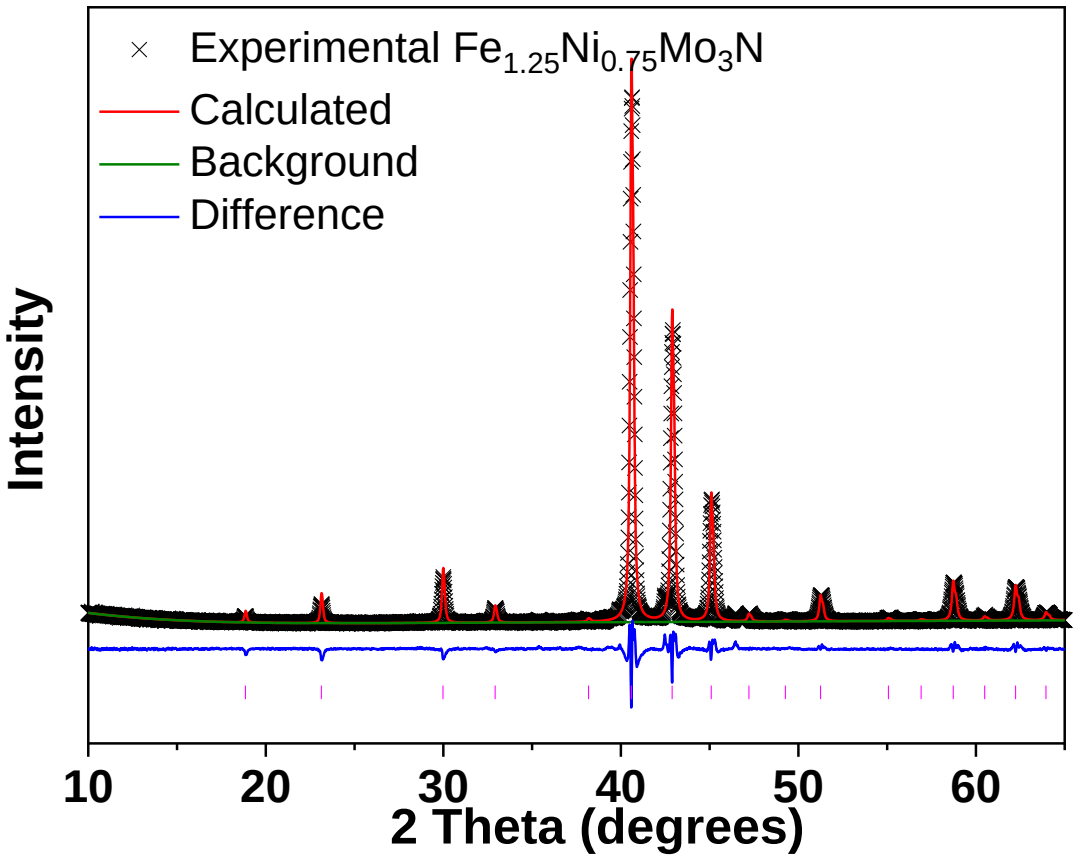

Figure 6-9: Rietveld refinement of PXRD data (CuK_α) for $Fe_{1.25}Ni_{0.75}Mo_3N$ using the structure model based on reported Ni_2Mo_3N structure (Space group: $P4_132$). Measured data are shown as crosses; the calculated profile is shown by a solid line through the measured data. The difference profile is shown along the bottom of the plot. Vertical bars represent the reflection positions for the phase.

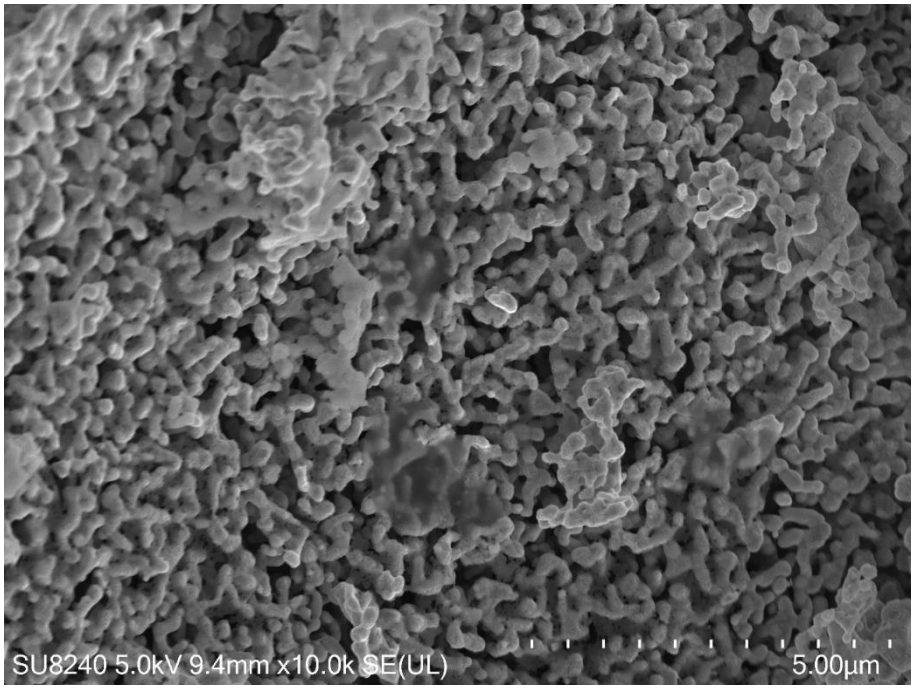

Figure 6-10: High magnification SEM images for $Fe_{0.5}Ni_{1.5}Mo_3N$ synthesised at 850 ℃ with 5% H_2 in N_2 gas flow.

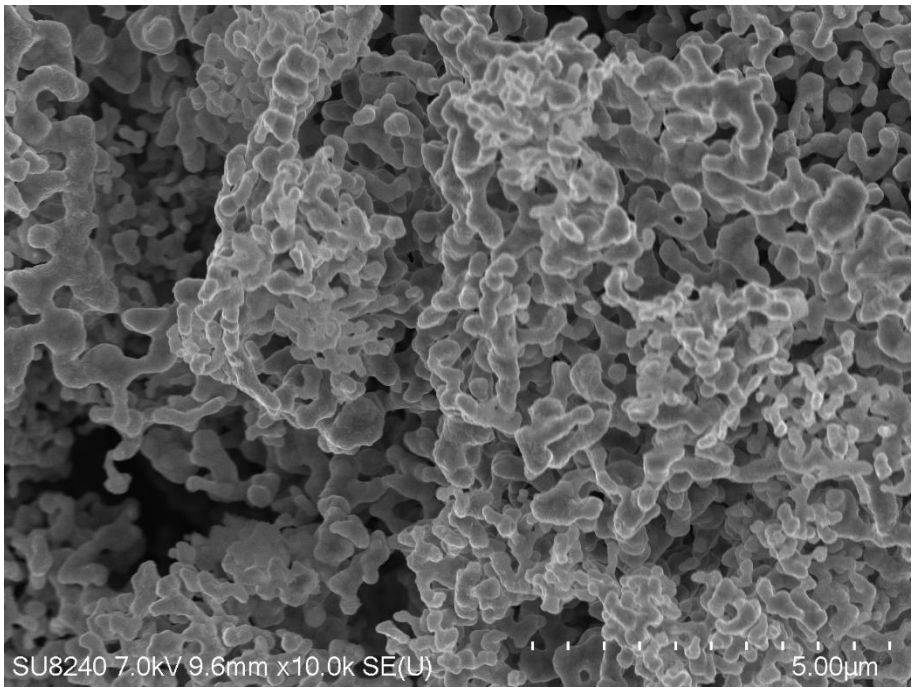

Figure 6-11: High magnification SEM images for $FeNiMo_3N$ synthesised at 850 ℃ with 5% H_2 in N_2 gas flow.

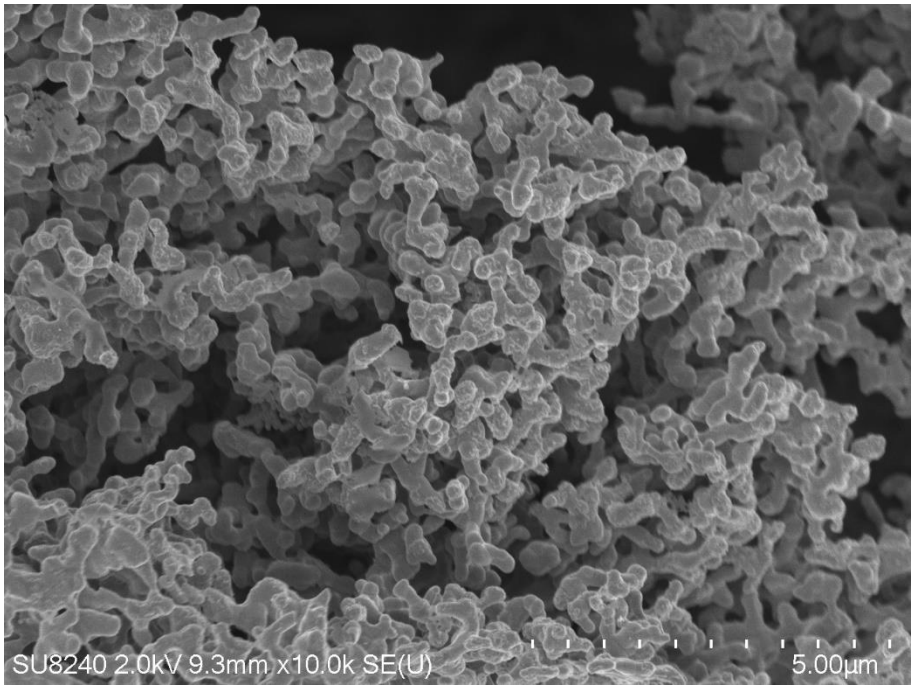

Figure 6-12: High magnification SEM images for $Fe_{1.25}Ni_{0.75}Mo_3N$ synthesised under 850 ℃ 5% H_2 in N_2 gas flow.

6.4 Electrochemical investigation of Co_2Mo_3N and Ni_2Mo_3N

6.4.1 The catalysts activity Studies of Co_2Mo_3N and Ni_2Mo_3N

LSV studies of Co_2Mo_3N and Ni_2Mo_3N with a scan rate of 5 mV s^{-1} revealed that samples can achieve high current densities (Figure 6-13). In addition, the overpotential required for reaching j = –10 mA cm^{-2} was achieved at the identical overpotentials of 149 ± 8 mV and 156 ± 6 mV by Co_2Mo_3N and Ni_2Mo_3N, respectively. The nearly identical overpotential values indicate that Co and Ni sites are probably responsible for the hydrogen production. This is in line with the previous studies (Chapter 4 - 5) as well as computational work that found the cobalt and nickel atoms showed the same ability of absorption hydrogen.[17]

Additionally, there is only a minor difference between Tafel plots as shown in Figure 6-14, with the slope of Co_2Mo_3N of 106 ±3 mV dec^{-1} which is identical with the Tafel slope of Ni_2Mo_3N (112 ± 3 mV dec^{-1}). Therefore, the similarity in overpotentials and reaction kinetics at j = –10 mA cm^{-2} between both nitrides further suggests that cobalt and nickel atoms do not appear to lead to differences in the performance.

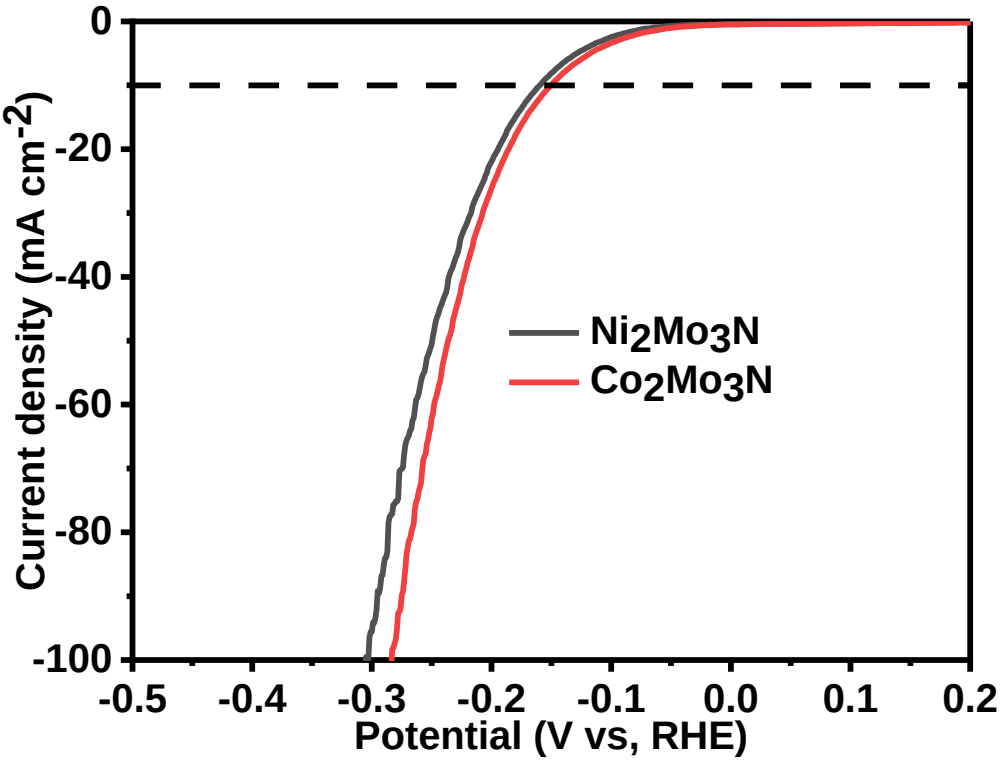

Figure 6-13: Electrochemical studies on Co_2Mo_3N and Ni_2Mo_3N in 0.5 M H_2SO_4: the current density obtained by linear sweep voltammetry at a scan rate of 5 mV s^{-1}, dashed line provides a guide to the eye at a current density of 10 mA cm^{-2}.

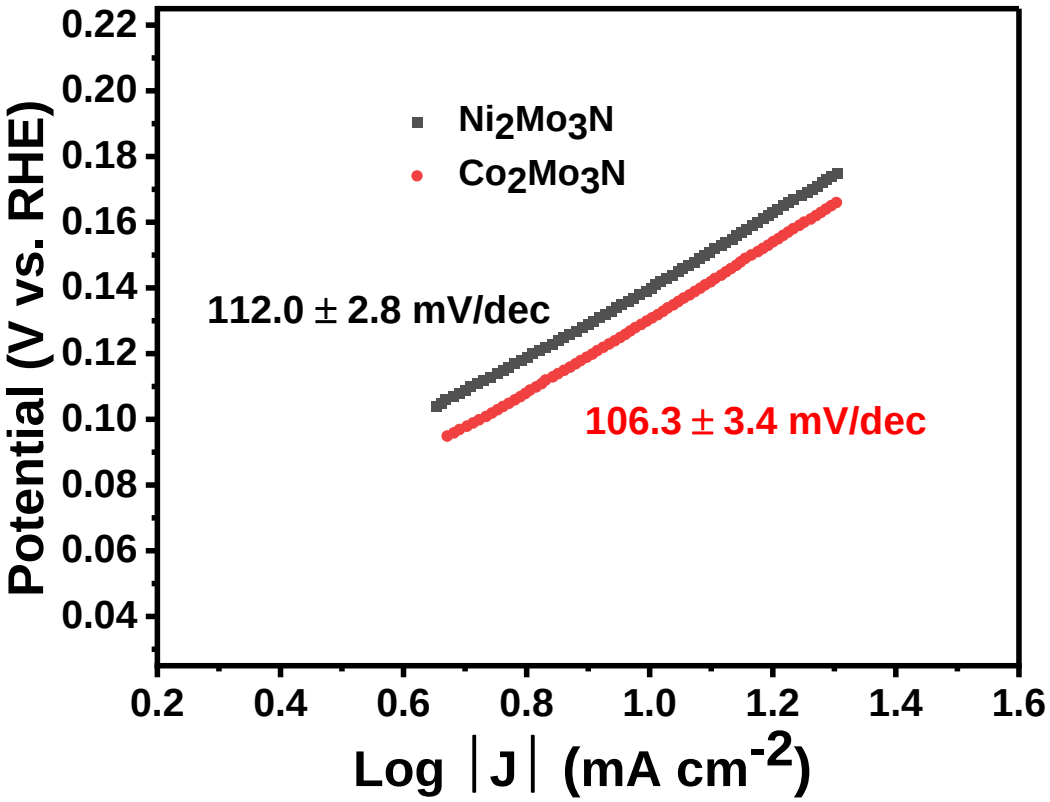

Figure 6-14: Comparison of corresponding Tafel slopes between Co_2Mo_3N and Ni_2Mo_3N. All current densities were corrected for resistance.

Identical high current densities under low potentials were achieved by nitrides of Co_2Mo_3N and Ni_2Mo_3N, but this cannot give information about the intrinsic activity of both nitrides. Even though cobalt and nickel appear like active sites for the HER based on our assessment. Alternative hypothesis is also possible if we assume that Mo or N are strongly catalytic than the similarity in catalytic performance between Co_2Mo_3N and Ni_2Mo_3N could be due to the fact that Co and Ni do not participate, so their catalytic activity is negligibly low and all activity originates from Mo or N. In particular, Sang *et al*. found that the nitrogen sites are catalytic for the HER in Ni_2Mo_3N nitride.[13] Therefore, to investigate whether N sites (Or possibly Mo sites are active) we attempted to replace Co and Ni with Fe. If the hypothesis that either N or Mo sites are active is correct than we should expect no change in performance upon substitution. As was mentioned before we were unable to replace Co for Fe in Co_2Mo_3N but it was possible to make $Fe_xNi_{2-x}Mo_3N$ solid solutions.

A significantly higher overpotential of 200 ± 9 mV at 10 mA cm^{-2} was observed in the material with the composition $Fe_{0.5}Ni_{1.5}Mo_3N$, and with more nickel atoms replaced by iron atoms in Ni_2Mo_3N structure, poorer performances of the nitride's compounds were observed as depicted

in Figure 6-15 and Table 6-8. In addition, there is an evident difference in Tafel slopes and the relevant plots (Figure 6-16). The Tafel slopes of $Fe_xNi_{2-x}Mo_3N$ (x =0 – 1.25) are all higher than 120 mV dec^{-1}. This represents a change in reaction kinetics when nickel atoms are replaced with iron in Ni_2Mo_3N. According to our hypothesis, if Mo or N sites were catalytic than replacing Ni for Fe (the nitrogen content is unchanged when replacing Ni for Fe as shown in Table 6-9) would not have significant impact given the fact that the morphology of all samples is identical. However, this is not the case and thus, the experiments indicated that the nickel plays an important role and highly probable active sites for the HER.

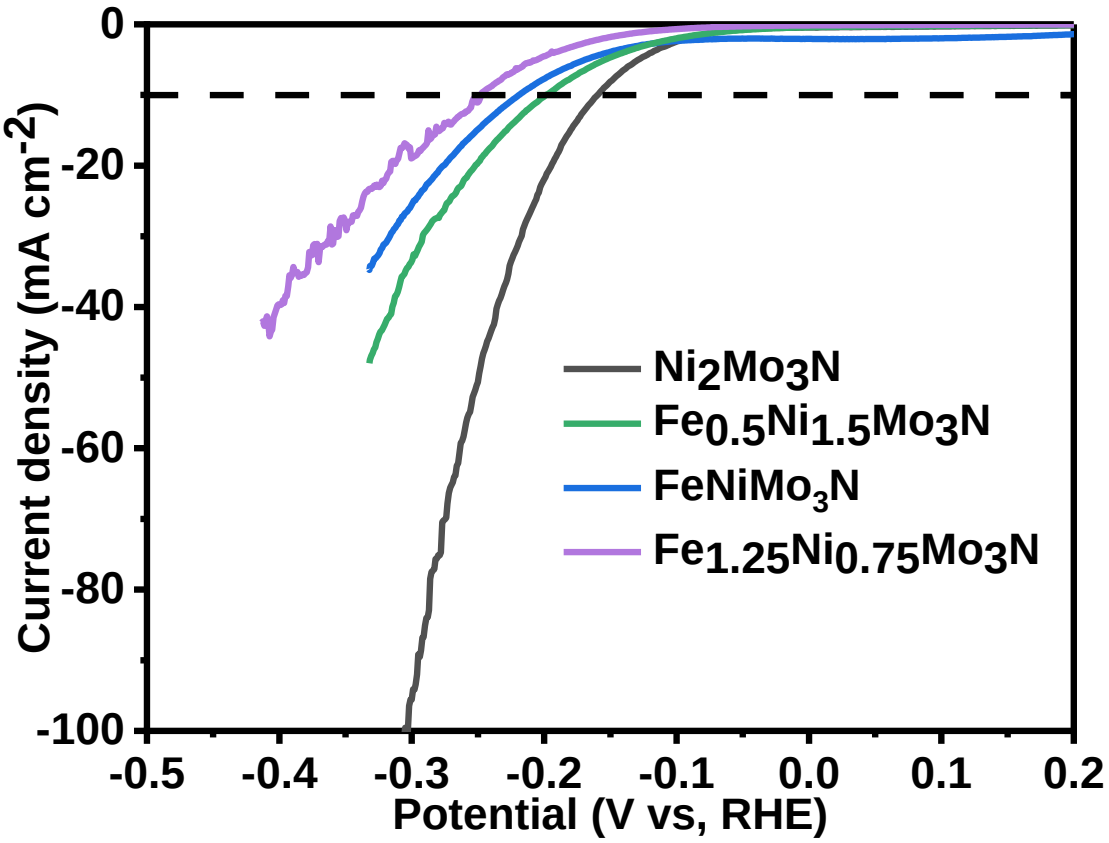

Figure 6-15: Electrochemical studies on Ni_2Mo_3N, $Fe_{0.5}Ni_{1.25}Mo_3N$, $FeNiMo_3N$ and $Fe_{1.25}Ni_{0.75}Mo_3N$ in 0.5 M H_2SO_4: the current density obtained by linear sweep voltammetry at a scan rate of 5 mV s^{-1}, dashed line provides a guide to the eye at a current density of 10 mA cm^{-2}.

Table 6-8: Summary of electrochemical properties of the ternary metal nitride electrocatalysts for the HER under acidic media

	OVP(at 10 mA cm^{-2})	Tafel slope (mv dec^{-1})	EIS(Ω)	ECSA (mF cm^{-2})
Co_2Mo_3N	149 ± 8	106.3 ±3.4	80 ± 9	10.9 ± 1.1
Ni_2Mo_3N	158 ± 10	112.0 ± 2.8	79 ± 7	10.8 ± 0.9
$Fe_{0.5}Ni_{1.5}Mo_3N$	200± 9	131.3 ± 4.8	109 ± 8	5.7 ± 0.8
$FeNiMo_3N$	217± 11	135.9 ± 7.4	138 ± 9	2.2 ± 0.6
$Fe_{1.25}Ni_{0.75}Mo_3N$	248± 10	124.3 ± 2.8	178 ± 7	1.4 ± 0.4

Table 6-9: Microanalysis for CHN elemental nitrogen content

	Co_2Mo_3N wt. %	Ni_2Mo_3N wt. %	$Fe_{0.5}Ni_{1.5}Mo_3N$ wt. %	$FeNiMo_3N$ wt. %	$Fe_{1.25}Ni_{0.75}Mo_3N$ wt. %
Experiment	3.28	3.3	3.26	3.19	3.22
Theory	3.34	3.34	3.35	3.36	3.37

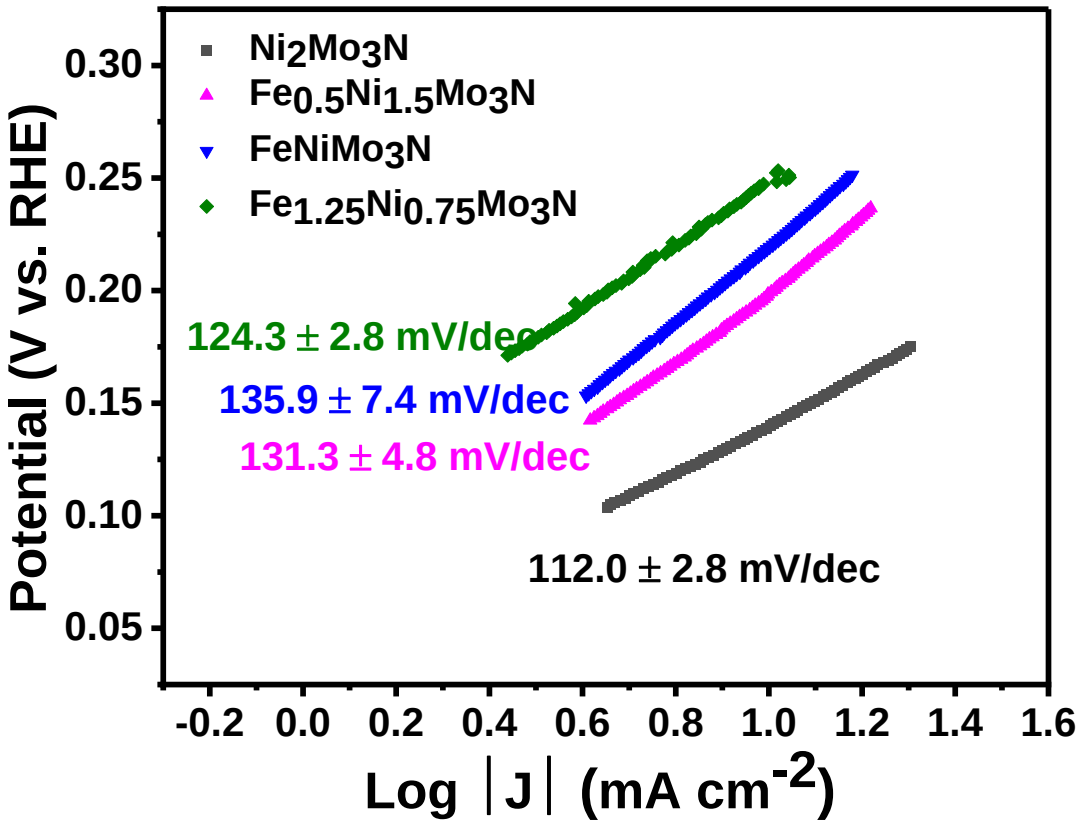

Figure 6-16: Tafel plots and corresponding Tafel slopes. All current densities were corrected for resistance.

In addition, we carried out a comparative study of the catalyst in this work using electrochemical surface area evaluation. ECSA is directly proportional to double-layer capacitance (C_{dl}) which can be evaluated from cyclic voltammetry (CV) curves obtained at various scan rates in the potential range of 0.02 V to –0.02 V (vs Ag | AgCl) as depicted in Figure 6-17 and Table 6-8. the similarity of the catalytic behaviour between Co_2Mo_3N and Ni_2Mo_3N was further confirmed by ECSA, with the similar higher C_{dl} values of 10.9 ± 1.1 mF cm^{-2} and 10.8 ± 0.9 mF cm^{-2}, respectively. Comparing to lower values of $Fe_{0.5}Ni_{1.5}Mo_3N$ (5.7 ± 0.8 mF cm^{-2}), $FeNiMo_3N$ (2.2 ± 0.6 mV dec^{-1}) and $Fe_{1.25}Ni_{0.75}Mo_3N$ (1.4 ± 0.4 mV dec^{-1}), which indicated that the active sites reduced with replacing of nickel content with iron in Ni_2Mo_3N structure and further suggest that neither Mo or N could be active centres for the HER.

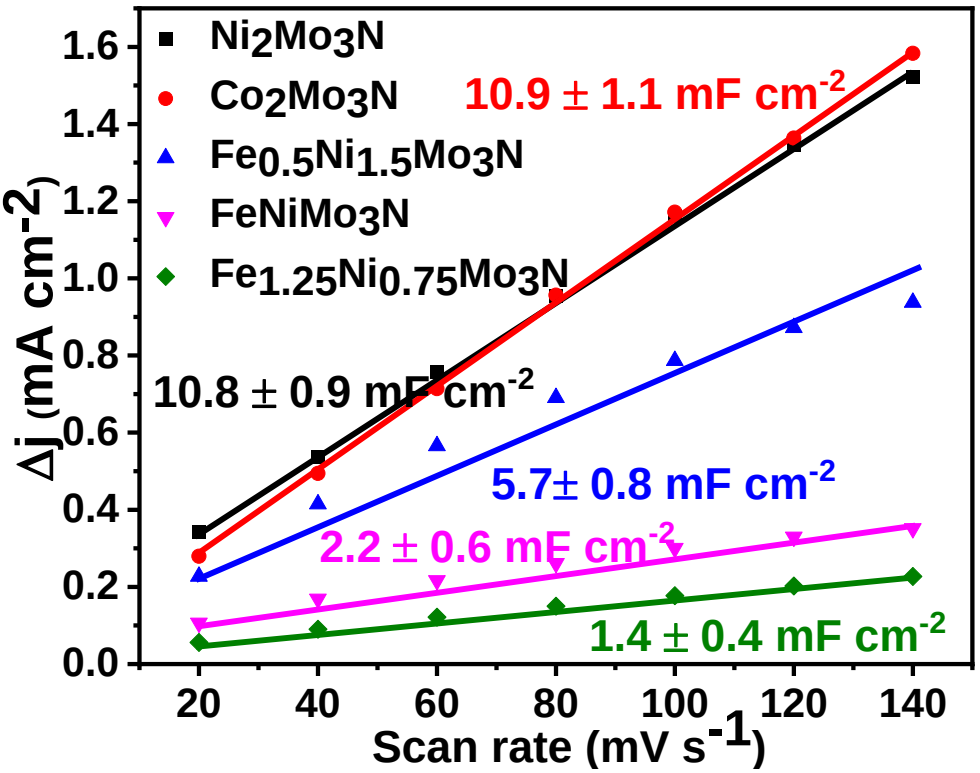

Figure 6-17: Current density differences of nitrides plotted against scan rates. The double layer capacitances (C_{dl}) measured at 140 mV (vs. RHE) in 0.5 M H_2SO_4. Catalysts were prepared on a glassy carbon working electrode as described in the experimental chapter. A 3 M Ag/AgCl reference and carbon felt counter electrode were used.

Further, we also carried out electrochemical impedance spectroscopy (EIS) experiments as depicted in Figure 6-18, the same charge-transfer resistance (both *iR* compensated) values of R_{ct} = 80 ± 9 Ω and R_{ct} = 79 ± 7 Ω observed for Co_2Mo_3N and Ni_2Mo_3N, are lower that the values of $Fe_{0.5}Ni_{1.5}Mo_3N$ (109 ± 8 Ω), $FeNiMo_3N$ (138 ± 9 Ω) and $Fe_{1.25}Ni_{0.75}Mo_3N$ (178 ± 7 Ω), which is suggests that high charge-transfer properties obtained in Co_2Mo_3N and Ni_2Mo_3N nitrides, conductivity decreased with nickel replaced by iron in Ni_2Mo_3N structure and led to inferior catalytic properties for driving the HER on this materials.

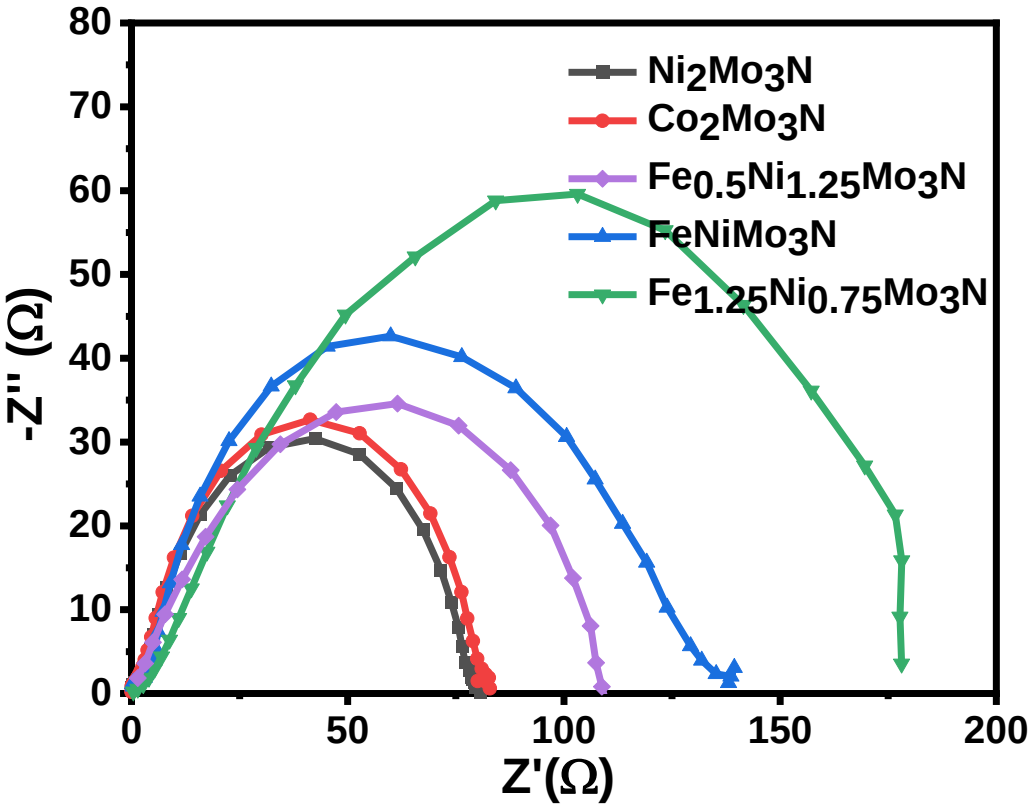

Figure 6-18: Nyquist plots showing electrochemical impedance spectroscopy on synthesised nitrides at -128 mV (vs. RHE) in 0.5M H_2SO_4. Catalysts were prepared on a glassy carbon working electrode as described in the experimental chapter. A 3 M Ag/AgCl reference and carbon felt counter electrode were used. This corresponds well with the iR compensation.

6.4.2 Stability Studies of Co_2Mo_3N and Ni_2Mo_3N

The longevity of the catalyst is a key factor in the search for earth-abundant electrocatalysts, as nanoscale catalysts tend to degrade with time, resulting in the loss of activity.[18] Since Co_2Mo_3N and Ni_2Mo_3N showed good performance as catalysts for the HER assessing their durability is important. Initially, the electrochemical stability of both nitrides was assessed using cyclic voltammetry. This is involved sweeping the applied potential for 1000 times between +0.2 V and -0.55 V (vs. RHE) in 0.5 M H_2SO_4. Figure 6-19 and Figure 6-20 showed a comparison of the current densities achieved during the initial cycle and 1000th cycle of Co_2Mo_3N and Ni_2Mo_3N, respectively. After 1000 CV scans, there was no obvious difference between initial and cycled materials. Both nitrides remained stable, the current densities achieved initial and after 1000 cycles are identical under a given potential. Additionally, after the cycling, the PXRD pattern of both nitrides were obtained to observe any difference related to the crystal structure. As depicted in Figure 6-21 and Figure 6-22, which show the PXRD

pattern of Co_2Mo_3N and Ni_2Mo_3N before and after 1000 cycles, respectively, there are no evident structural changes.

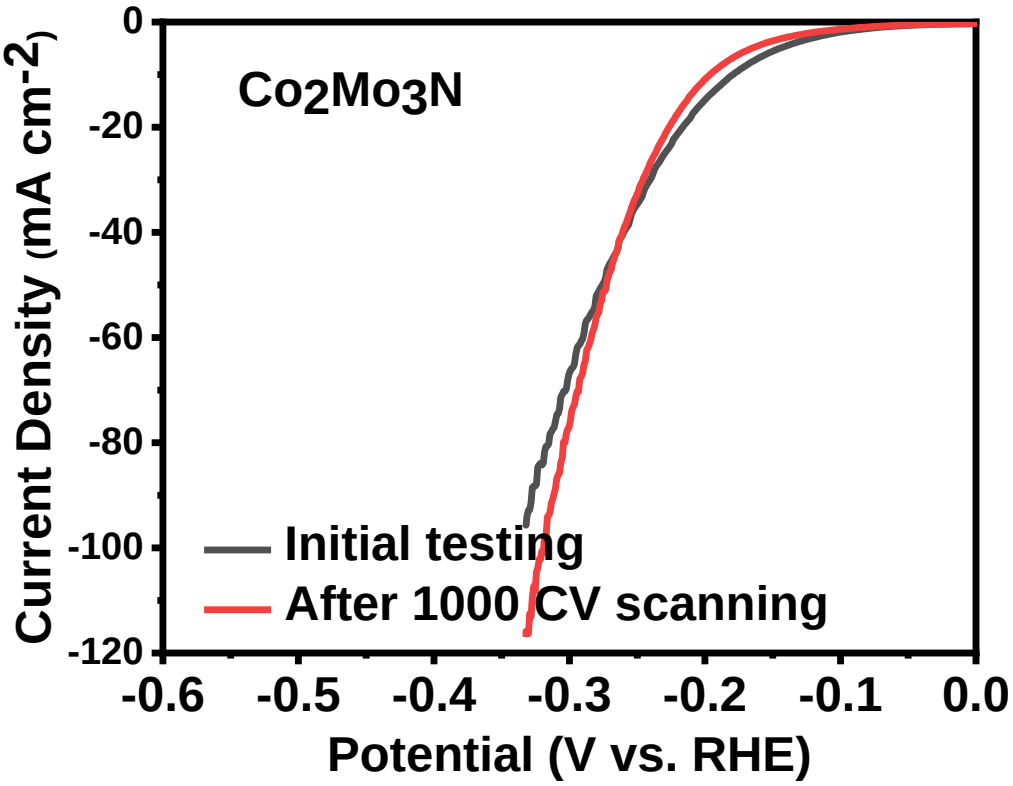

Figure 6-19: Comparison of the current density achieved by Co_2Mo_3N before and after 1000 cycles in 0.5 M H_2SO_4. Red lines represent the initial cycle and black lines represent the 1000th cycle. Catalysts were prepared in a glassy carbon working electrode as described in the experiment chapter. A 3 M Ag/AgCl reference and carbon felt counter electrode were used. Curves were obtained using linear sweep voltammetry at a scan rate of 100 mV s^{-1} and all resistance were compensated for.

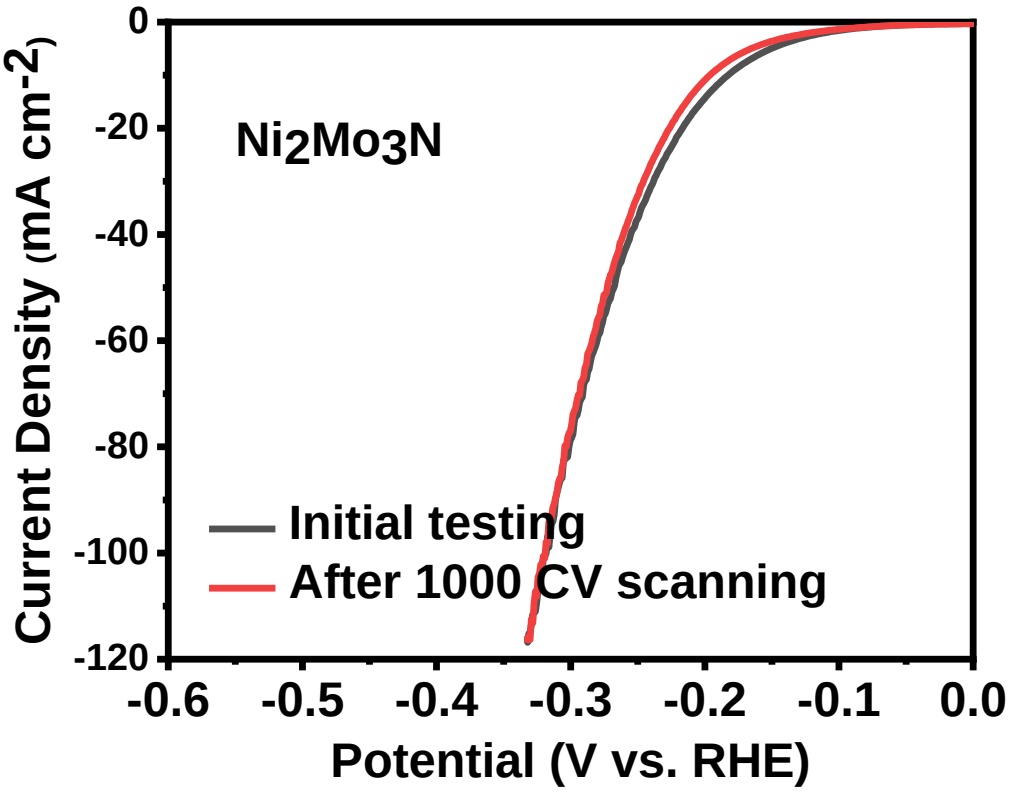

Figure 6-20: Comparison of the current density achieved by Ni_2Mo_3N before and after 1000 cycles in 0.5 M H_2SO_4. Red lines represent the initial cycle and black lines represent the 1000th cycle. Catalysts were prepared in a glassy carbon working electrode as described in the experiment chapter. A 3 M Ag/AgCl reference and carbon felt counter electrode were used. Curves were obtained using linear sweep voltammetry at a scan rate of 100 mV s^{-1} and all resistance were compensated for.

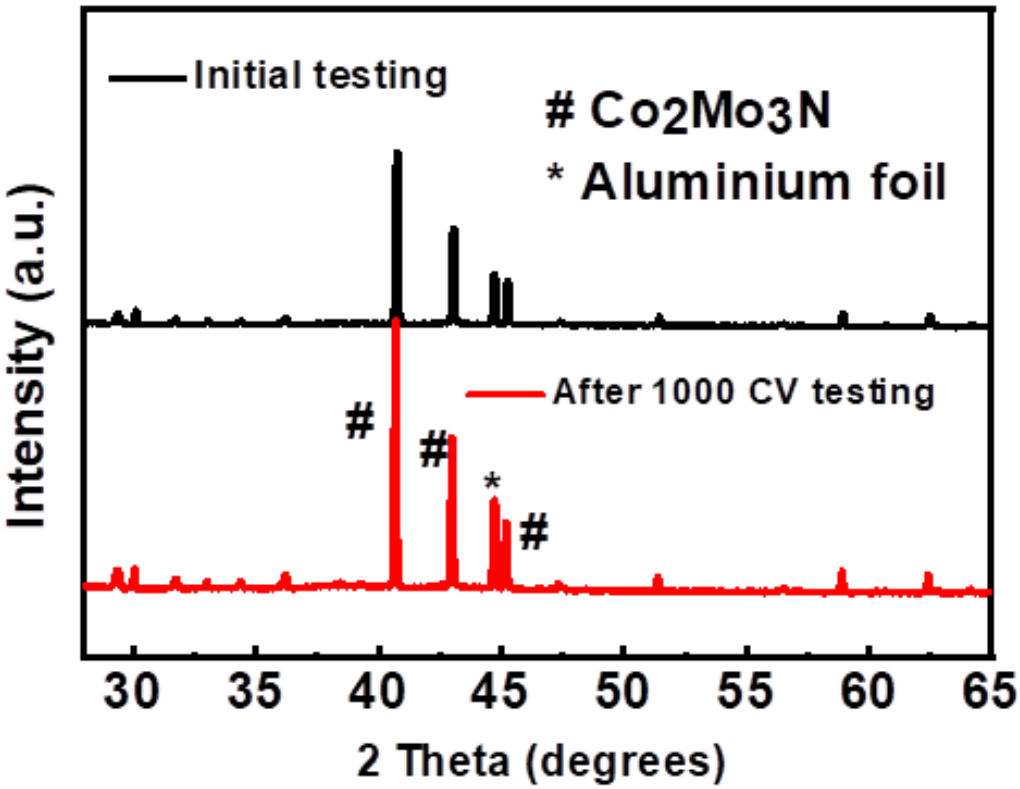

Figure 6-21: comparison of the PXRD pattern of Co_2Mo_3N before and after 1000 CV scanning. Patterns were measured directly on the surface of the glassy carbon working electrode on which the catalyst ink was deposited.

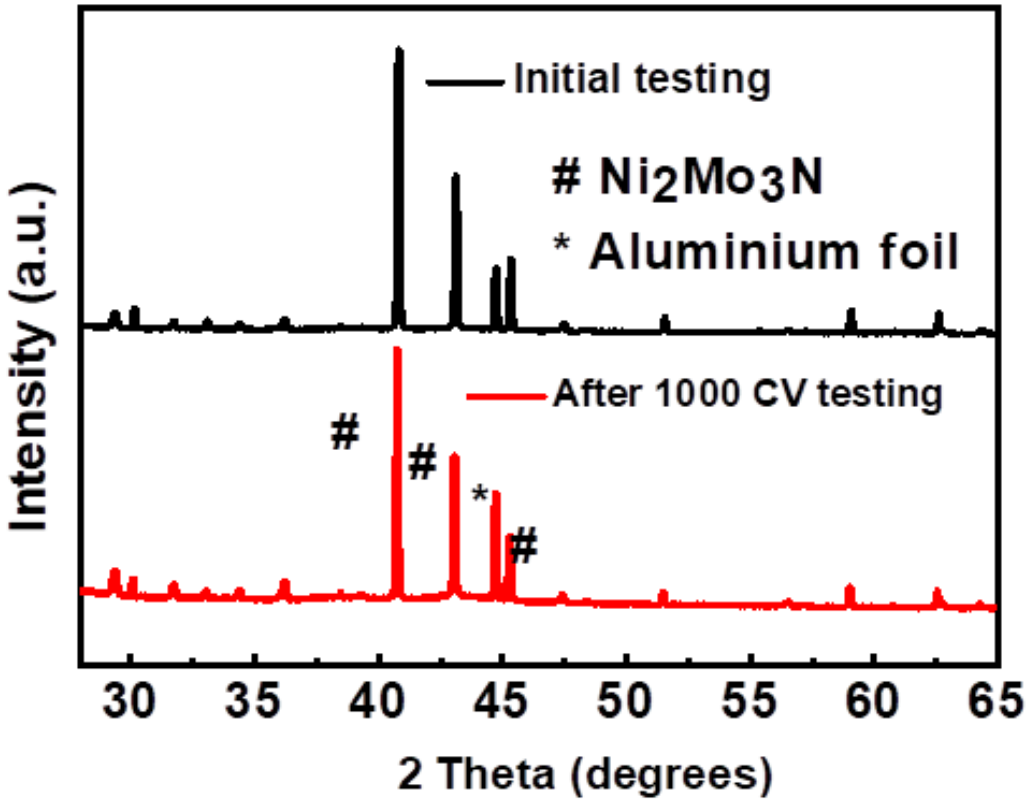

Figure 6-22: Comparison of the PXRD pattern of Ni_2Mo_3N before and after 1000 CV scanning. Patterns were measured directly on the surface of the glassy carbon working electrode on which the catalyst ink was deposited.

6.5 Conclusion

In summary, the successful synthesis of phase pure Co_2Mo_3N and Ni_2Mo_3N allowed us to perform the reliable assessment of their catalytic performance. Both catalysts demonstrate nearly identical electrocatalytic activity towards the HER. To study the intrinsic activity, the single phase samples of $Ni_{1.5}Fe_{0.5}Mo_3N$, $NiFeMo_3N$ and $Ni_{0.75}Fe_{1.25}Mo_3N$ were also prepared under the identical reaction condition. The comparison of the electrochemical performance revealed that the higher overpotentials were observed as nickel atoms were replaced by iron atoms in Ni_2Mo_3N structure. This indicated that the nickel atoms play decisive role in catalytic activity while Mo and N are probably inactive.

6.6 References

[1] P.S. Herle, M.S. Hegde, K. Sooryanarayana, T.N. Guru Row, G.N. Subbanna, Ni_2Mo_3N: A New Ternary Interstitial Nitride with a Filled *β*-Manganese Structure , *Inorg. Chem.* 37 (**1998**) 4128–4130. https://doi.org/10.1021/IC980211T.

[2] P. Adamski, D. Moszyński, M. Nadziejko, A. Komorowska, A. Sarnecki, A. Albrecht, Thermal stability of catalyst for ammonia synthesis based on cobalt molybdenum nitrides, *Chem.* Pap. 73 (**2019**) 851–859. https://doi.org/10.1007/S11696-018-0642-0/FIGURES/7.

[3] N. Bion, F. Can, J. Cook, J.S.J. Hargreaves, A.L. Hector, W. Levason, A.R. McFarlane, M. Richard, K. Sardar, The role of preparation route upon the ambient pressure ammonia synthesis activity of Ni_2Mo_3N, *Appl. Catal. A Gen*. 504 (**2015**) 44–50. https://doi.org/10.1016/J.APCATA.2014.10.030.

[4] S. Al Sobhi, N. Bion, J.S.J. Hargreaves, A.L. Hector, S. Laassiri, W. Levason, A.W. Lodge, A.R. McFarlane, C. Ritter, The reactivity of lattice nitrogen within the Ni_2Mo_3N and $NiCoMo_3N$ phases, *Mater. Res. Bull*. 118 (**2019**) 110519. https://doi.org/10.1016/J.MATERRESBULL.2019.110519.

[5] A. Daisley, The role of composition on the ammonia synthesis activity of nitrides, carbonitrides, carbides and osmium based compounds, (**2020**). https://ethos.bl.uk/OrderDetails.do?uin=uk.bl.ethos.818753 (accessed 28 September 2022).

[6] A. Daisley, L. Costley-Wood, J.S.J. Hargreaves, The Role of Composition and Phase upon the Lattice Nitrogen Reactivity of Ternary Molybdenum Nitrides, *Top. Catal.* 64 (**2021**) 1021–1029. https://doi.org/10.1007/S11244-021-01432-1/TABLES/3.

[7] T.J. Prior, P.D. Battle, Facile synthesis of interstitial metal nitrides with the filled *β*-manganese structure, *J. Solid State Chem*. 172 (**2003**) 138–147. https://doi.org/10.1016/S0022-4596(02)00171-8.

[8] W. Jeitschko, H. Nowotny, F. Benesovsky, Ein Beitrag zum Dreistoff: Molybdän-Aluminium-Kohlenstoff - Die Phase Mo_3Al_2C, *Monatshefte Für Chemie*. 94 (**1963**) 247–251. https://doi.org/10.1007/BF00900244.

[9] W. Jeitschko, H. Nowotny, F. Benesovsky, Phasen mit aufgefüllter β-Manganstruktur,

Monatshefte Für Chemie Und Verwandte Teile Anderer Wissenschaften 1964 954. 95 (**1964**) 1212–1218. https://doi.org/10.1007/BF00904716.

[10] Y. Yuan, S. Adimi, X. Guo, T. Thomas, Y. Zhu, H. Guo, G.S. Priyanga, P. Yoo, J. Wang, J. Chen, P. Liao, J.P. Attfield, M. Yang, A Surface-Oxide-Rich Activation Layer (SOAL) on Ni_2Mo_3N for a Rapid and Durable Oxygen Evolution Reaction, *Angew. Chemie - Int. Ed.* 59 (**2020**) 18036–18041. https://doi.org/10.1002/anie.202008116.

[11] P. Zhou, X. Lv, Y. Gao, Z. Liang, Y. Liu, Z. Wang, P. Wang, Z. Zheng, Y. Dai, B. Huang, Synthesis of novel cubic Ni_2Mo_3N and its electronic structure regulation by vanadium doping towards high-efficient HER electrocatalyst, *Electrochim. Acta*. 337 (**2020**) 135689. https://doi.org/10.1016/J.ELECTACTA.2020.135689.

[12] S.H. Park, S.H. Kang, D.H. Youn, Direct One-Step Growth of Bimetallic Ni_2Mo_3N on Ni Foam as an Efficient Oxygen Evolution Electrocatalyst, *Mater*. 2021, Vol. 14, Page 4768. 14 (**2021**) 4768. https://doi.org/10.3390/MA14164768.

[13] S.H. Park, T.H. Jo, M.H. Lee, K. Kawashima, C.B. Mullins, H.K. Lim, D.H. Youn, Highly active and stable nickel-molybdenum nitride (Ni_2Mo_3N) electrocatalyst for hydrogen evolution, *J. Mater. Chem. A.* 9 (**2021**) 4945–4951. https://doi.org/10.1039/D0TA10090K.

[14] S. Al Sobhi, J.S.J. Hargreaves, A.L. Hector, S. Laassiri, Citrate-gel preparation and ammonia synthesis activity of compounds in the quaternary $(Ni,M)_2Mo_3N$ (M = Cu or Fe) systems, *Dalt. Trans.* 48 (**2019**) 16786–16792. https://doi.org/10.1039/C9DT03673C.

[15] J.O. Conway, T.J. Prior, Interstitial nitrides revisited – A simple synthesis of M_xMo_3N (M = Fe, Co, Ni), *J. Alloys Compd*. 774 (**2019**) 69–74. https://doi.org/10.1016/J.JALLCOM.2018.09.307.

[16] T.J. Prior, S.E. Oldham, V.J. Couper, P.D. Battle, Ferromagnetic nitrides with the filled β-Mn structure: $Fe_{2-x}M_xMo_3N$ (M = Ni, Pd, Pt), *Chem. Mater*. 17 (**2005**) 1867–1873. https://doi.org/10.1021/CM047859Q.

[17] J.K. Nørskov, T. Bligaard, A. Logadottir, J.R. Kitchin, J.G. Chen, S. Pandelov, U. Stimming, Trends in the Exchange Current for Hydrogen Evolution, *J. Electrochem.*

Soc. 152 (**2005**) J23. https://doi.org/10.1149/1.1856988/META.

[18] A.B. Laursen, P.C.K. Vesborg, I. Chorkendorff, A high-porosity carbon molybdenum sulphide composite with enhanced electrochemical hydrogen evolution and stability, *Chem. Commun*. 49 (**2013**) 4965–4967. https://doi.org/10.1039/C3CC41945B.

Chapter 7: Transition metal nitrides based on anti-perovskite structure used as electrocatalysts for Hydrogen Evolution Reaction

7.1 Introduction

Anti-perovskite based materials have found applications in electrocatalysis,[1,2] as their relatively simple crystal structure allows for high flexibility in elemental composition. As shown by the example of Co_3SnN in Figure 7-1 each of the elements within the structure could be replaced with other metals on the Sn and Co cations sites, respectively, and nitrogen with carbon.[3]

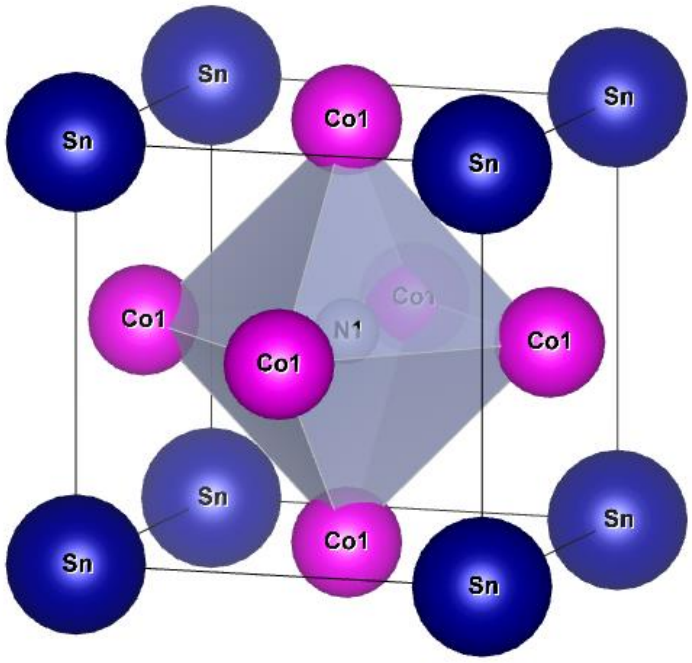

Figure 7- 1: The idealised anti-perovskite structure exemplified by Co_3SnN with the positions of N at cell origin; Co_6N octahedral polyhedron framework with N at the cell centre.

This structure creates a wide range of various anti-perovskite based materials. The nitride based anti-perovskites could be defined by a general formulae X_3AN where A typically a main group element and X is the transition metal. Depending on the nature of A and X some of these nitrides can exhibit a good conductivity[4] making them a promising target for electrocatalytic applications. There is an indication that anti-perovskite based materials are capable to withstand high current densities in alkaline media which is a wildly used electrolyte in industrial electrolysers.[1,5] Therefore, they may be a viable alternative to Ni based alloys which are currently considered state-of-the-art cathode materials in alkaline media due to their

high activity and availability.[6–9] However, the chemical stability of most metal alloys still presents challenges for application of metal alloys in water electrolysis.[10,11] Therefore, finding more stable and active cathode materials is important for the production of hydrogen from alkaline water electrolysis. Despite the simple crystal structure, wide elemental flexibility in the composition, corrosion stability, and conductivity, the anti-perovskite materials have rarely been employed in the field of electrocatalysis.[2,12,13]

Ammonia is a common source of nitrogen for the synthesis of metal nitrides including those with the anti-perovskite structure.[14–17] However, ammonia gas is difficult to handle and therefore use of solid precursors such as melamine or urea has been investigated in the past. Melamine decomposes into C_3N_4 at 560 ^oC and releases ammonia gas. Further heating of C_3N_4 leads to decomposition into radical species containing nitrogen or carbon. Therefore, melamine was used as a nitrogen source for the synthesis of binary nitrides (CrN, AlN, BN, TiN, TaN and VN) from the reaction between oxide precursors and melamine.[18,19] In addition, this melamine method was used for the synthesis of two anti-perovskite nitrides Co_3SnN and Ni_3ZnN.[20] However, the reported synthesis relied on the sealing of melamine and relevant oxide precursors into a quartz ampoule which is suboptimal as it requires specialized equipment. The high vapour pressure of the produced decomposition products as well as the possibility of carbide impurities makes this method quite challenging to apply. Therefore, a new optimised process was employed in this work.

7.2 Synthesis and characterisation of a family of anti-perovskite nitrides

As described in detail in the Experimental Chapter 2 we developed a simplified apparatus that allowed us to carry out the reaction between melamine (300mg) and the mixture (100mg) of metals in a tube furnace (Figure 7-2). In short, stoichiometric amounts of metal powders and melamine (similar to the previous report[19]) were initially mixed and placed into a smaller size quartz ampoule which was then inserted into a larger one. The setup was then placed into 5% H_2 in N_2 flow within a tube furnace to protect the products from the ambient atmosphere. However, cobalt and tin metals impurities were invariably present in the resulting product as was evidenced by evaluation of the PXRD pattern (Figure 7-3).

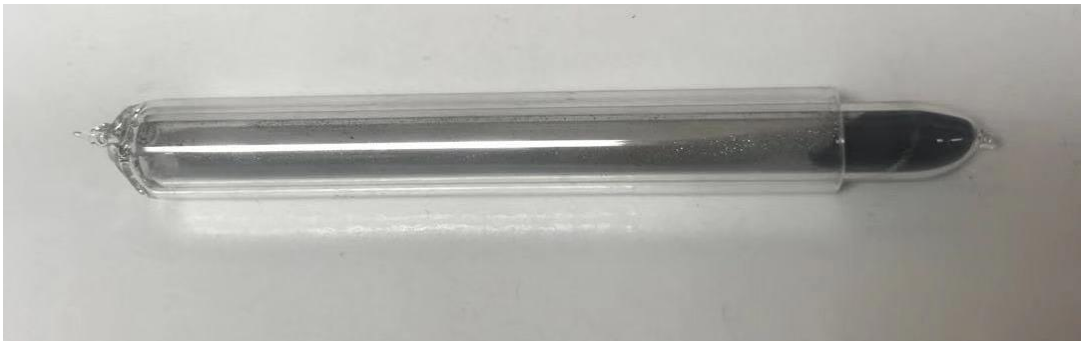

Figure 7-2: A photo of the experimental setup used for the reaction between melamine and metal (oxide) precursors in a configuration when all products are mixed together.

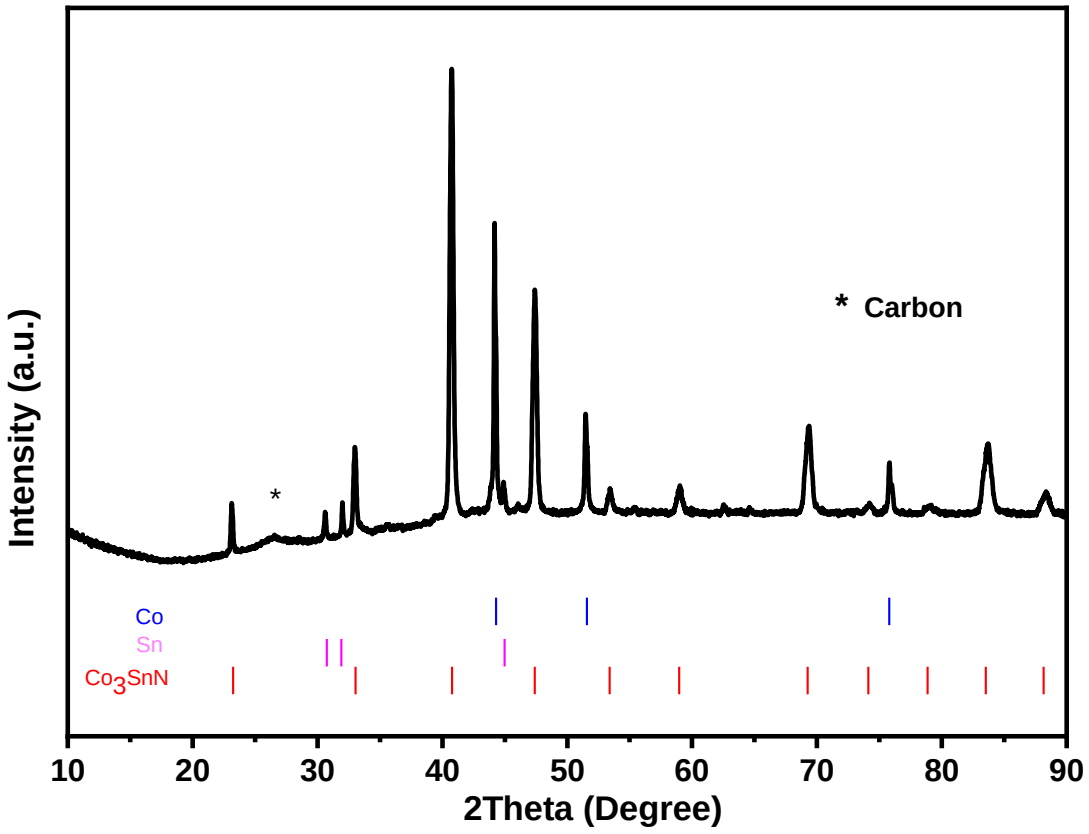

Figure 7-3: The XRD pattern of product prepared by mixing metals precursor with melamine under 650 ℃ for 2 hours.

Figure 7-4: A photo of the experimental setup used for the reaction between melamine and metal (oxide) precursors in a configuration when melamine and metals powders are separated.

Therefore, a different strategy was employed by placing the stoichiometric 100mg of cobalt and tin metal powders at the bottom of the larger ampoule while melamine (300mg) was loaded at the bottom of the smaller ampoule. The small ampoule was then carefully inserted into the larger one to avoid the mixing of metals powders and melamine, as shown in Figure 7-4. The product obtained using this configuration was confirmed by PXRD as a single phase Co_3SnN. The Rietveld refinement of PXRD data showed an excellent fit to the model based on the Co_3ZnC structure-type (Figure 7-5). All of the diffraction peaks were matched with a cubic lattice and were found consistent with the space group *Pm*-3*m*. The unit cell parameter a = 3.83726(9) Å is comparable to the previously reported of a = 3.8513 Å.[20] Additional parameters are detailed in Table 7-1.

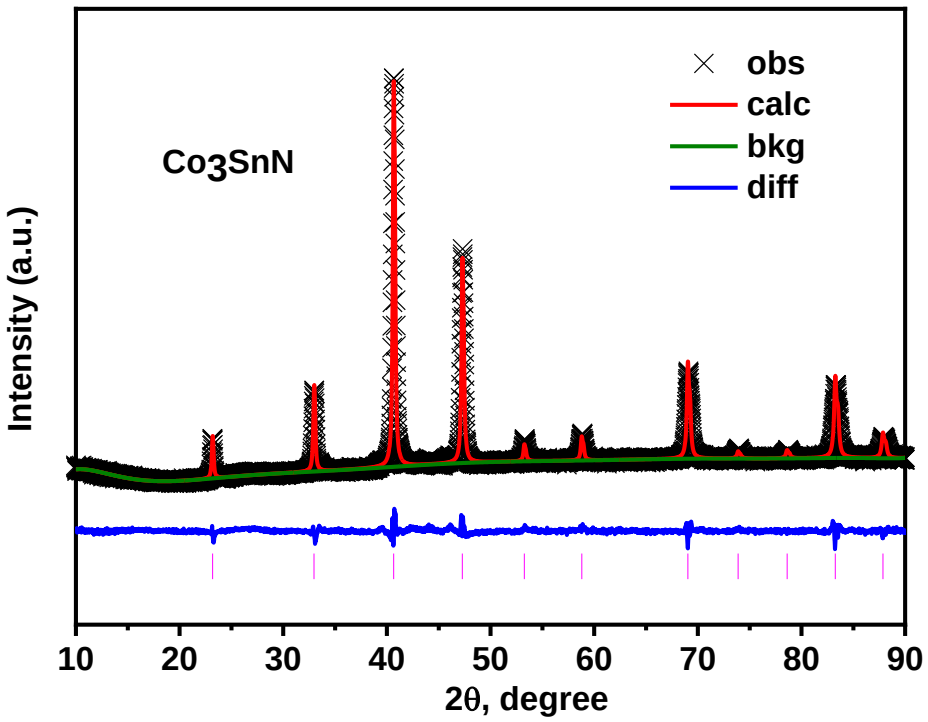

Figure 7-5: Rietveld refinement of PXRD data (CuK_{α}) for Co_3SnN prepared under 650℃ using the model structure based on reported Co_3ZnC structure (Space group: *Pm*-3*m*). Measured datapoints are shown as crosses; the calculated profile is shown by a solid line through the measured data. The difference profile is shown along the bottom of the plot. Vertical bars represent the reflection positions for the phase.

Table 7-1: Structural parameters for the Rietveld refinement of the PXRD data collected from Co_3SnN powder sample using structural model based on Co_3ZnC structure-type (Space group: *Pm*-3*m*) at ambient temperature. Estimated errors in the last digits are given in parentheses. The number of observations 5333, fitting profile (R_p)= 4.94%, weighed profile (R_{wp})= 6.25%. The value of the lattice constant a = 3.83726(9) Å, reported value a = 3.8253 Å by ammonia route;[21] a = 3.8531 Å in a sealed ampoule with melamine.[20]

	Site	x/a	y/b	z/c	Occupancy	B_{iso} (Å^2)
Sn	1*b*	0	0	0	1.000	0.008(2)
Co	3*c*	0	0.5	0.5	1.000	0.013(9)
N	1*a*	0.5	0.5	0.5	1.000	0.006

Since the isolation of Co_3SnN was a success, an attempt to synthesise Fe_3SnN was carried out under the same condition (300mg melamine,100 mg mixture of metals and the reaction temperature is 650 ℃) as for Co_3SnN but by using Fe metal instead of Co metal. The PXRD pattern of the product is shown in Figure 7-6, the compound crystallizes with the same cubic structure as Co_3SnN but with a bigger unit cell parameter a = 3.89532(3) Å which is similar to previously reported Fe_3SnN of a = 3.8818 Å.[22,23] A more detail information is given Table 7-2. To the best of our knowledge, this is the first Fe_3SnN synthesis through the melamine route and due to the simplicity of the protocol this may prove to be advantageous over NH_3 based approach.[23,24]

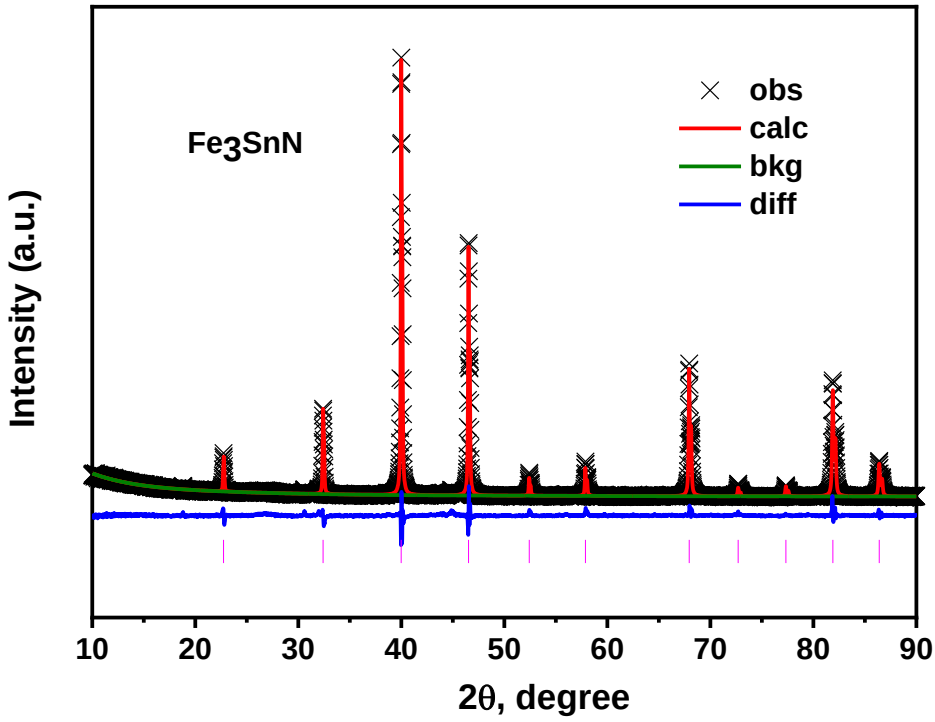

Figure 7-6: Rietveld refinement of PXRD data (CuK$_\alpha$) for Fe_3SnN prepared under 650℃ using the structure model based on reported Co_3ZnC structure (Space group: *Pm*-3*m*). Measured datapoints are shown as crosses; the calculated profile is shown by a solid line through the measured data. The difference profile is shown along the bottom of the plot. Vertical bars represent the reflection positions for the phase.

Table 7-2: Structural parameters for the Rietveld refinement of the PXRD data collected on Fe_3SnN powder sample using structural model based on Co_3ZnC structure-type (Space group: *Pm*-3*m*) at ambient temperature. Estimated errors in the last digits are given in parentheses. The number of observations 5333, fitting profile (R_p)= 9.71%, weighed profile (R_{wp})= 11.65%. The value of the lattice constant a = 3.8964(2) Å, reported values a = 3.8371 Å ammonia and hydrogen;[25] a = 3.8818 Å ammonia hydrogen gas flow;[22] a = 3.8818 Å ammonia hydrogen gas flow.[23]

	Site	x/a	y/b	z/c	Occupancy	B_{iso} (Å^2)
Sn	1*b*	0	0	0	1.000	0.005(2)
Fe	3*c*	0	0.5	0.5	1.000	0.013(2)
N	1*a*	0.5	0.5	0.5	1.000	0.004

Similarly, the synthesis of Co_3ZnN from the reaction of melamine (300mg) and mixture (100mg) of cobalt and zinc used as metal precursors was attempted and led to the single phase product according to the PXRD (Figure 7-7). All the diffraction peaks could be matched with the cubic structure while the Rietveld refinement of the data gave the unit cell parameter a = 3.75893(3) Å, which is close to the reported value of a =3.764 Å.[26] The detailed information is summarized in Table 7-3. This is also the first report of preparing Co_3ZnN through this melamine route. This indicated that this method could be widely used for the synthesis.

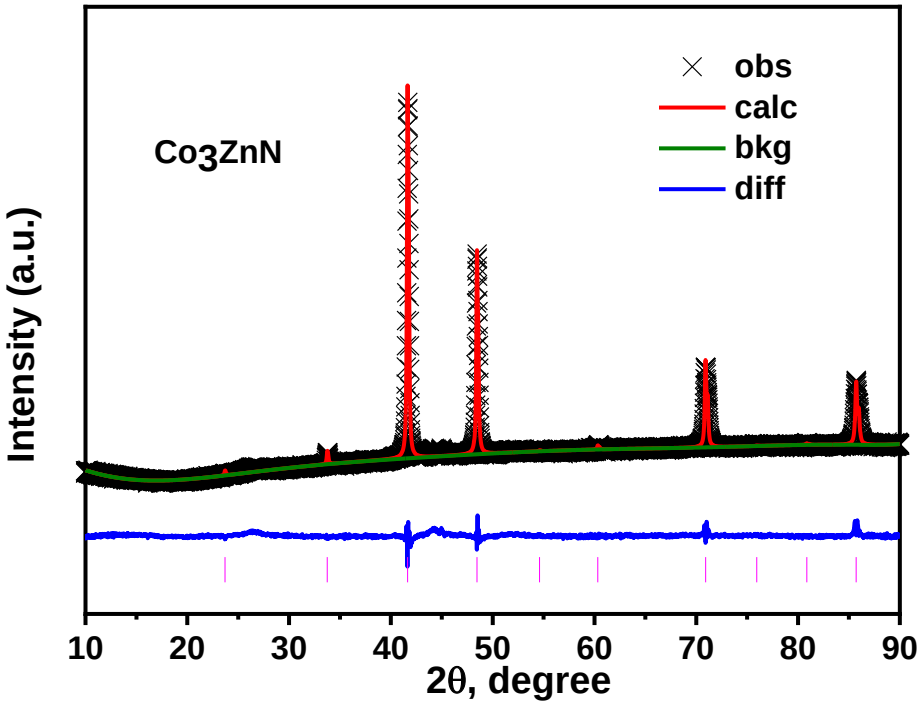

Figure 7-7: Rietveld refinement of PXRD data (CuK$_\alpha$) for Co_3ZnN prepared under 650℃ using the structure model based on reported Co_3ZnC structure (Space group: *Pm*-3*m*). Measured data are shown as crosses; the calculated profile is shown by a solid line through the measured data. The difference profile is shown along the bottom of the plot. Vertical bars represent the reflection positions for the phase.

Table 7-3: Structural parameters for the Rietveld refinement of the PXRD data collected on Co_3ZnN powder sample using structural model based on Co_3ZnC structure-type (Space group: *Pm*-3*m*) at ambient temperature. Estimated errors in the last digits are given in parentheses. The number of observations 5333, fitting profile (R_p)= 3.57%, weighed profile (R_{wp})= 4.65%. The value of the lattice constant a = 3.7573(6) Å, reported values a = 3.7585 Å ammonia method;[27] a = 3.7640 Å ammonia method;[26] a = 3.7580 Å ammonia method.[28]

	Site	x/a	y/b	z/c	Occupancy	B_{iso} (Å^2)
Zn	1*b*	0	0	0	1.000	0.005(4)
Co	3c	0	0.5	0.5	1.000	0.011(9)
N	1*a*	0.5	0.5	0.5	1.000	0.013

Meanwhile, the synthesis of Co_3InN with the same melamine contents and reaction temperatures was attempted as well, but here 100mg of mixture about cobalt metal powder and In_2O_3 was used instead of metal. According to the XRD pattern of the product in Figure 7-8, single phase was observed, and all the diffraction peaks could be matched with the cubic structure while the Rietveld refinement of the data gave the unit cell parameter a = 3.8509(8) Å, which is close to the report value of a =3.764 Å and a = 3.854 Å.[29] and detail information showed in Table 7-4.

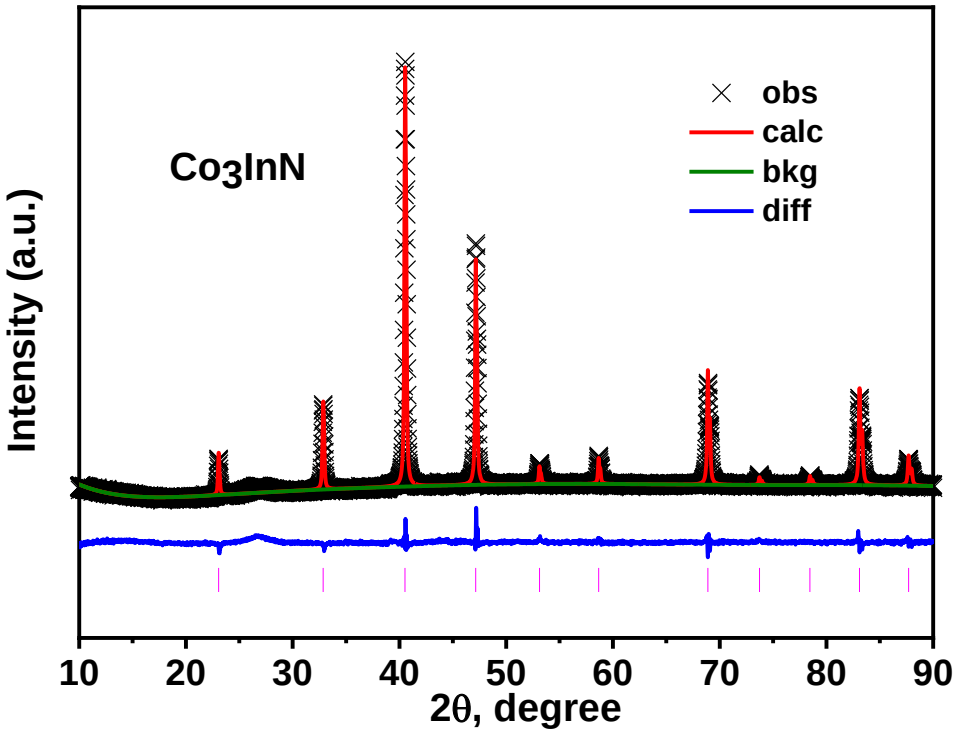

Figure 7-8: Rietveld refinement of PXRD data (CuK_α) for Co_3InN prepared under 650°C using the structure model based on reported Co_3ZnC structure (Space group: *Pm*-3*m*). Measured data are shown as crosses; the calculated profile is shown by a solid line through the measured data. The difference profile is shown along the bottom of the plot. Vertical bars represent the reflection positions for the phase.

Table 7-4: Structural parameters for the Rietveld refinement of the PXRD data collected on Co_3InN powder sample using structural model based on Co_3ZnC structure-type (Space group: *Pm*-3*m*) at ambient temperature. Estimated errors in the last digits are given in parentheses. The number of observations 5333, fitting profile (R_p)= 4.50%, weighed profile (R_{wp})= 5.79%. The value of the lattice constant a = 3.8509(8) Å, reported values a = 3.8567(2) Å ammonia method;[27] a = 3.8540 Å ammonia method;[29] a = 3.8518 Å.[30]

	Site	x/a	y/b	z/c	Occupancy	B_{iso} (Å^2)
In	1*b*	0	0	0	1.000	0.009(6)
Co	3*c*	0	0.5	0.5	1.000	0.007(8)
N	1*a*	0.5	0.5	0.5	1.000	0.013

Energy dispersive X-ray spectroscopy (EDXS) was used to confirm the chemical compositions of the nitrides (Table 7-5). Based on the measurements the compositions were normalized to the stoichiometry of the cation in the *A*-position of A_3XN (*i.e.* In, Sn and Zn) and established as: $Co_{3.03\pm0.09}In_{1\pm0.08}N$; $Co_{2.90\pm0.09}Sn_{1.00\pm0.09}N$; $Co_{3.21\pm0.09}Zn_{1.00\pm0.08}N$ and $Fe_{2.92\pm0.06}Sn_{1.00\pm0.08}N$. With exception of Co_3ZnN (which showed substantially higher amount of Co, partial 1*b* sites may occupied by Co atom in this case, and resulting formula could be $Co_3(Zn_{0.95}Co_{0.05})N$)). The compositions of the other samples were consistent with the expected 3:1 ratio within the standard deviations.

Table 7-5: The elemental analysis of Co_3SnN, Co_3ZnN, Co_3InN and Fe_3SnN by EDXS. The results are the average of values collected in several points across a sample and the errors present the standard deviations between the values at these points.

	Co_3InN		**Co_3SnN**		**Co_3ZnN**		**Fe_3SnN**	
	Co	**In**	**Co**	**Sn**	**Co**	**Zn**	**Fe**	**Sn**
at. % Exp.	75.18±2.21	24.82±2.03	74.38±2.41	25.62±2.23	75.58±3.21	24.42±2.58	74.47±1.54	25.53±1.98
at. % Theory	75	75	75	25	75	25	75	25

7.3 Electrocatalytic performance for the hydrogen evolution on Co_3SnN, Co_3ZnN, Co_3InN and Fe_3SnN

The powders were processed into inks and drop-casted onto a glassy carbon working electrodes as described in detail in the experimental section (Chapter 2). They were then tested in 1M KOH in a 3-electrode configuration by linear sweep voltammetry.

A reasonable electrocatalytic behaviour was observed from Co_3ZnN which reached a voltage of 188±9 mV at -10mA cm^{-2} (Figure 7-9, blue line). In comparison, Co_3InN (Figure 7-9, green line) and Co_3SnN (Figure 7-9, red line) reached a current density of -10 mA cm^{-2} under a potential of 128±15 mV and 151±12 mV. Fe_3SnN was also tested, and a substantially higher potential (274 ±10 mV) was required to drive current density of -10 mA cm^{-2}. To achieve the high current density of -100 mA cm^{-2} the potentials of 237± 18 mV (Co_3SnN), 276±13 mV (Co_3InN) and 355±21mV (Co_3ZnN) were required. This makes Co_3SnN probably most promising targets for catalysis toward HER in alkaline media as higher currents often >500 mA cm^{-2} are preferred for a better efficiency. Evidently the poor performance of Fe_3SnN (that did not even achieve reasonable current densities) suggests that Co-plays key role in the catalytic performance.

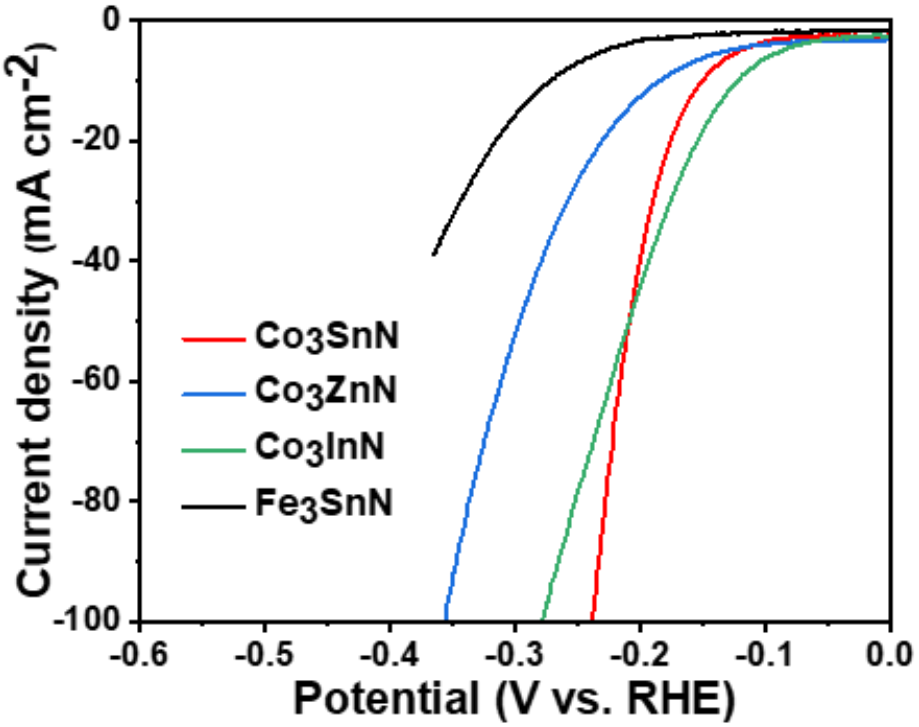

Figure 7-9: Comparison of the current densities achieved by Co_3SnN (red line), Fe_3SnN (black line), Co_3ZnN (blue line) and Co_3InN (green line) in 1 M KOH electrolyte. Catalysts were prepared on a glassy carbon working electrode as described in Chapter 2. A 3M Ag/AgCl reference and carbon felt counter electrode were used. Curves were obtained using linear sweep voltammetry with a scan rate of 5 mV s^{-1} and all resistance were compensated for resistance

The electrochemical impedance spectroscopy (EIS) experiments were also carried out to understand the activity of the nitrides (Figure 7-10). There is a reduction in charge transfer resistance (R_{CT}) values: 820 Ω (Fe_3SnN); 234 ±11 Ω (Co_3ZnN), 120±7 Ω (Co_3InN) and 91±8 Ω (Co_3SnN). Analysis of Co-based compounds suggest a certain trend as the charge transfer resistance seems to decrease along the period from Zn to Sn. Remarkably, there is a huge difference between the values observed on Fe_3SnN and Co_3SnN which indicates that Co-sites play crucial role in improving the reaction process.

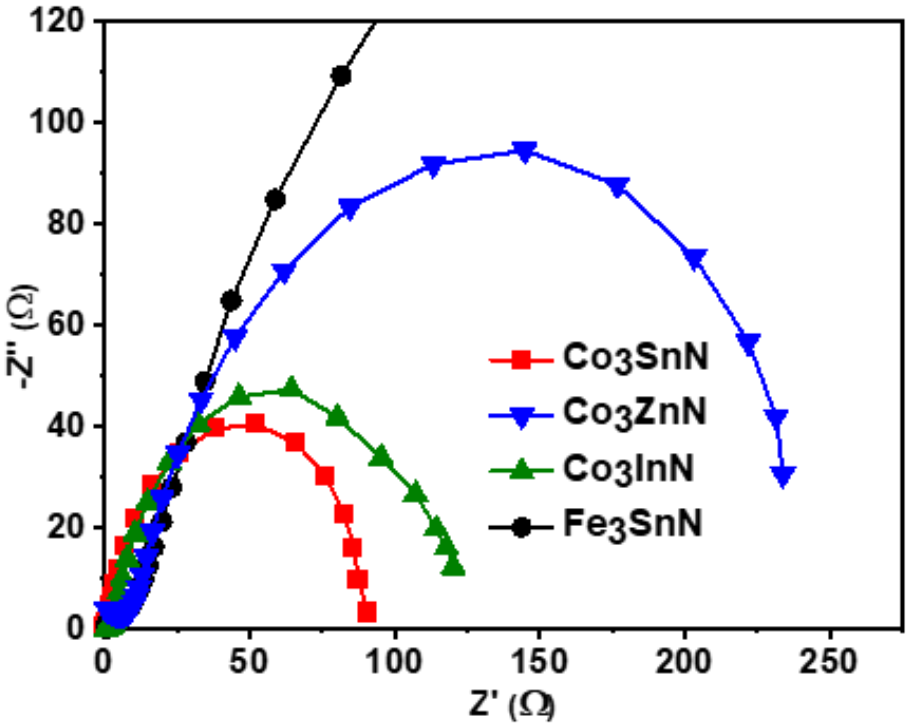

Figure 7-10: Nyquist plots showing electrochemical impedance spectroscopy at -150 mV (vs. RHE) in 1M KOH on the nitrides. Catalysts were prepared on a glassy carbon working electrode as described in the experimental chapter. Carbon felt and Ag/AgCl (3M KCl) were used as counter electrode and reference electrodes. All samples were compensated for iR.

The above results suggest that Co_3SnN is probably the most promising compound for future use as an electrocatalysts toward HER in alkaline electrolysers. However, the stability is also an important parameter to be considered for a state-of-the-art catalyst. The investigation of stability of Co_3SnN was carried out using chronoamperometry measurement at a constant voltage of -140 mV versus RHE in 1 M KOH. The current density gradually drifted from the original values over 16 hours of testing suggesting that there may be some decay over time (Figure 7-11). Similarly, Co_3SnN shows some changes upon cycling for 1000 times at a scan rate of 100 mV s^{-1}. LSV data were collected before and after 1000 CV scans and there is an evident change in the current density after 1000's cycle (Figure. 7-12). This suggests that degradation may take place over time making Co_3SnN unsuitable for applications in electrolysers. To investigate possible changes after stability testing, the PXRD was measured on the catalyst (*ex-situ* but directly on the glassy carbon electrode) before and after 1000 cycles (Figure 7-13). However, no significant changes were observed which excludes the bulk degradation of the sample as the primary cause of the reduction in electrochemical performance

with time. It is highly likely that any changes appear on the surface and could not be detected by PXRD.

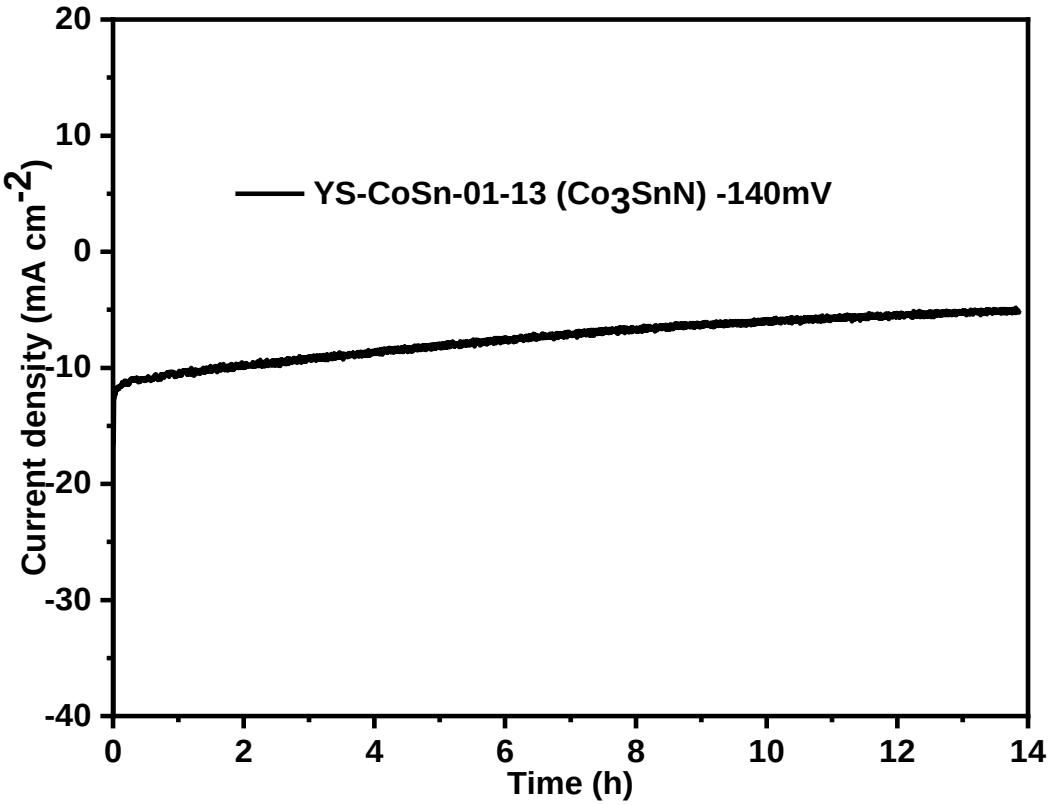

Figure 7-11: Chronoamperometry profile of Co_3SnN in 1 M KOH at an applied potential of 140 mV (*vs*. RHE). Experiments were performed using a three electrodes setup, with catalyst-deposited on glassy carbon as the working electrode, 3 M Ag/AgCl was used as the reference and carbon felt as the counter electrode.

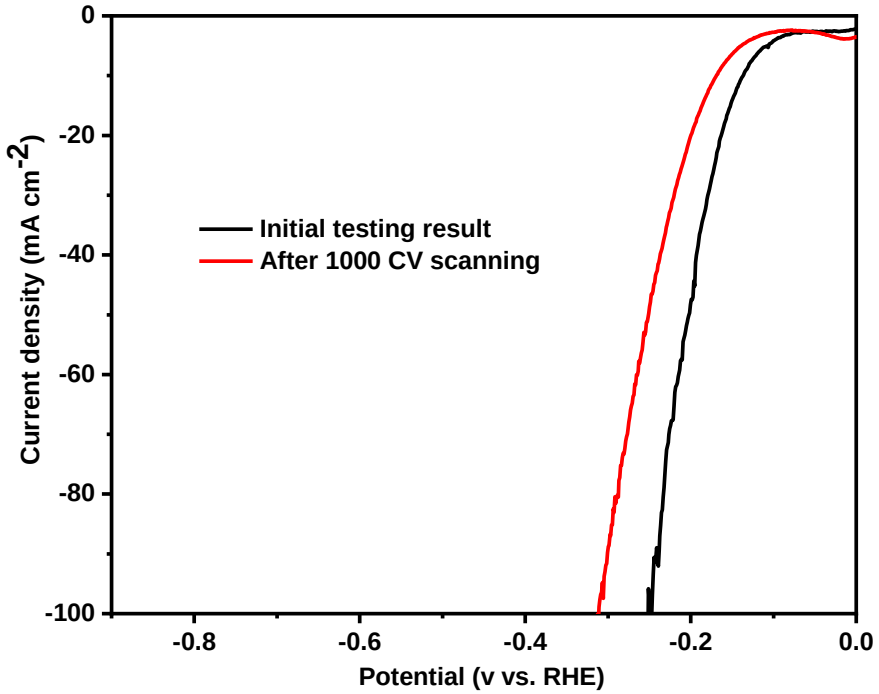

Figure 7-12: Comparison of the current densities achieved by Co_3SnN before and after 1000 cycles in 1 M KOH.

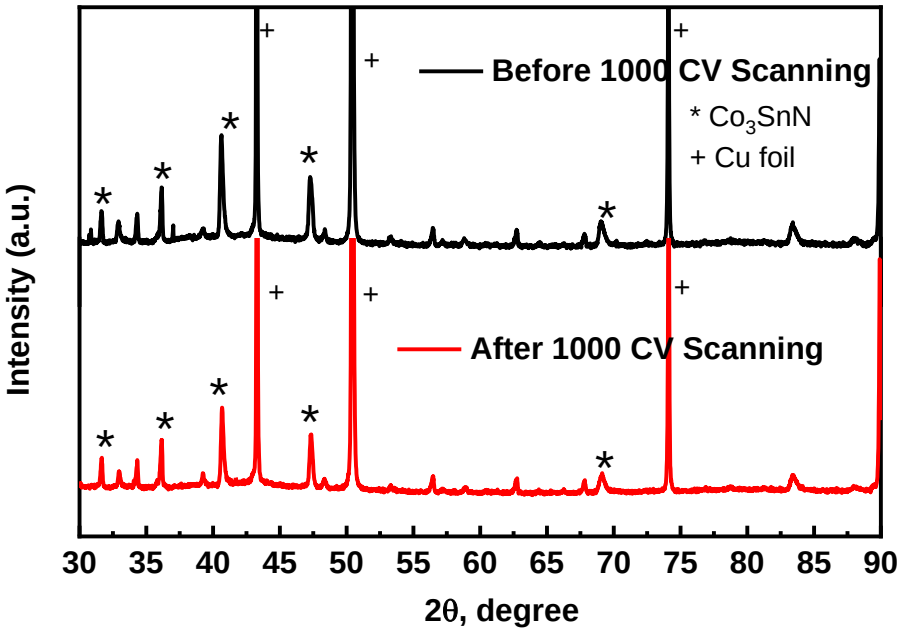

Figure 7-13: The PXRD patterns collected on Co_3SnN before and after 1000 cycles in 1 M KOH.

Finally, the difference in morphology between four tested samples could be a reason for a difference in the catalytic activity.[31] The Scanning Electron Microscopy (SEM) images reveal that the morphologies of Co_3SnN (Figure 7-15a), Co_3ZnN (Figure 7-15b), Co_3InN (Figure 7-15c) are identical and could be described as consisting of agglomerates of spherical particles. However, Fe_3SnN (Figure 7-15d) is somewhat different and consist of well-defined platelets therefore, we could not rule out completely that catalytic performance difference between Co_3SnN and Fe_3SnN may be due to a change in morphology. However, as the particle sizes in Co_3SnN are significantly larger than in Fe_3SnN it is unlikely that it has significantly larger surface area which would typically lead to an improved catalytic performance due to higher number of catalytic sites.

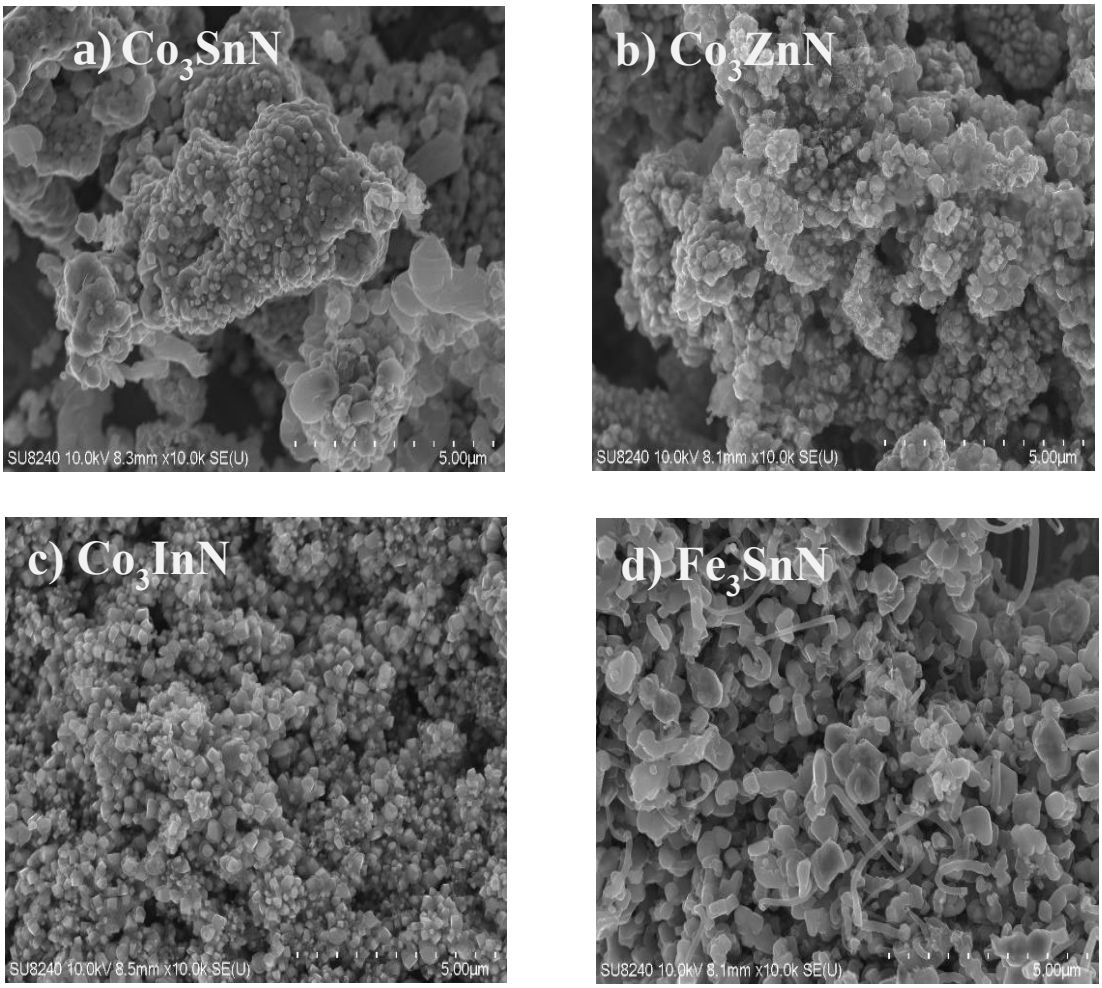

Figure 7-14: High magnification SEM images for (a) Co_3SnN, (b) Co_3ZnN (c) Co_3InN and (d) Fe_3SnN synthesised under 650 ℃ via melamine method.

7.4 Conclusion

In conclusion, single phase the anti-perovskite Co_3SnN, Co_3ZnN, Co_3InN and Fe_3SnN can be prepared through melamine synthesis method. To the best of our knowledge this is a first report on the investigation of the activity of anti-perovskite Co_3SnN towards HER in alkaline conditions. The evaluation of electrochemical performance points out that the anti-perovskite Co_3SnN exhibits a low overpotential suggesting a confident performance for the electrocatalytic water splitting. A better stability is, however, desired for this material to be applied for the hydrogen evolution reaction in alkaline media at an industrial scale.

7.5 References

[1] H. Zhang, W. Xia, H. Shen, W. Guo, Z. Liang, K. Zhang, Y. Wu, B. Zhu, R. Zou, Antiperovskite Intermetallic Nanoparticles for Enhanced Oxygen Reduction, *Angew. Chemie - Int. Ed*. 59 (**2020**) 1871–1877. https://doi.org/10.1002/anie.201911943.

[2] Y. Zhu, G. Chen, Y. Zhong, Y. Chen, N. Ma, W. Zhou, Z. Shao, A surface-modified antiperovskite as an electrocatalyst for water oxidation, *Nat. Commun*. 2018 91. 9 (**2018**) 1–9. https://doi.org/10.1038/s41467-018-04682-y.

[3] R. Niewa, Metal-Rich Ternary Perovskite Nitrides, *Eur. J. Inorg. Chem*. 2019 (**2019**) 3647–3660. https://doi.org/10.1002/EJIC.201900756.

[4] B. He, C. Dong, L. Yang, X. Chen, L. Ge, L. Mu, Y. Shi, $CuNNi_3$: a new nitride superconductor with antiperovskite structure, *Supercond. Sci. Technol*. 26 (**2013**) 125015. https://doi.org/10.1088/0953-2048/26/12/125015.

[5] R.L. LeRoy, Industrial water electrolysis: Present and future, *Int. J. Hydrogen Energy*. 8 (**1983**) 401–417. https://doi.org/10.1016/0360-3199(83)90162-3.

[6] C.A.C. Sequeira, D.S.P. Cardoso, L. Amaral, B. Šljukić, D.M.F. Santos, On the performance of commercially available corrosion-resistant nickel alloys: A review, *Corros. Rev*. 34 (**2016**) 187–200. https://doi.org/10.1515/corrrev-2016-0014.

[7] A. Buttler, H. Spliethoff, Current status of water electrolysis for energy storage, grid balancing and sector coupling via power-to-gas and power-to-liquids: A review, *Renew. Sustain. Energy Rev*. 82 (**2018**) 2440–2454. https://doi.org/10.1016/J.RSER.2017.09.003.

[8] A. Baroutaji, T. Wilberforce, M. Ramadan, A.G. Olabi, Comprehensive investigation on hydrogen and fuel cell technology in the aviation and aerospace sectors, *Renew. Sustain. Energy Rev*. 106 (**2019**) 31–40. https://doi.org/10.1016/J.RSER.2019.02.022.

[9] Z. Chehade, C. Mansilla, P. Lucchese, S. Hilliard, J. Proost, Review and analysis of demonstration projects on power-to-X pathways in the world, *Int. J. Hydrogen Energy*. 44 (**2019**) 27637–27655. https://doi.org/10.1016/J.IJHYDENE.2019.08.260.

[10] M.T.M. Koper, Thermodynamic theory of multi-electron transfer reactions: Implications for electrocatalysis, *J. Electroanal. Chem*. 660 (**2011**) 254–260.

https://doi.org/10.1016/J.JELECHEM.2010.10.004.

[11] Y. Sun, A.Y. Ganin, The Synergistic Effects of Alloying on the Performance and Stability of Co_3Mo and Co_7Mo_6 for the Electrocatalytic Hydrogen Evolution Reaction, *Hydrog*. 2020, Vol. 1, Pages 11-21. 1 (**2020**) 11–21. https://doi.org/10.3390/HYDROGEN1010002.

[12] J.H. Shim, S.K. Kwon, B.I. Min, Electronic structures of antiperovskite superconductors $MgXNi_3$ (X = B, C, and N), *Phys. Rev. B - Condens. Matter Mater. Phys*. 64 (**2001**) 1805101–1805104. https://doi.org/10.1103/PHYSREVB.64.180510.

[13] T. He, Q. Huang, A.P. Ramirez, Y. Wang, K.A. Regan, N. Rogado, M.A. Hayward, M.K. Haas, J.S. Slusky, K. Inumara, H.W. Zandbergen, N.P. Ong, R.J. Cava, Superconductivity in the non-oxide perovskite $MgCNi_3$, *Nat*. 2001 4116833. 411 (**2001**) 54–56. https://doi.org/10.1038/35075014.

[14] N. Yao, P. Li, Z. Zhou, Y. Zhao, G. Cheng, S. Chen, W. Luo, Hydrogen Evolution Reaction: Synergistically Tuning Water and Hydrogen Binding Abilities Over Co_4N by Cr Doping for Exceptional Alkaline Hydrogen Evolution Electrocatalysis (Adv. Energy Mater. 41/2019) , *Adv. Energy Mater*. 9 (**2019**) 1970159. https://doi.org/10.1002/AENM.201970159.

[15] W.F. Chen, K. Sasaki, C. Ma, A.I. Frenkel, N. Marinkovic, J.T. Muckerman, Y. Zhu, R.R. Adzic, Hydrogen-evolution catalysts based on non-noble metal nickel-molybdenum nitride nanosheets, *Angew. Chemie - Int. Ed*. 51 (**2012**) 6131–6135. https://doi.org/10.1002/ANIE.201200699.

[16] J. Shi, Z. Pu, Q. Liu, A.M. Asiri, J. Hu, X. Sun, Tungsten nitride nanorods array grown on carbon cloth as an efficient hydrogen evolution cathode at all pH values, *Electrochim. Acta*. 154 (**2015**) 345–351. https://doi.org/10.1016/J.ELECTACTA.2014.12.096.

[17] X. Jia, Y. Zhao, G. Chen, L. Shang, R. Shi, X. Kang, G.I.N. Waterhouse, L.-Z. Wu, C.-H. Tung, T. Zhang, Water Splitting: Ni_3FeN Nanoparticles Derived from Ultrathin NiFe-Layered Double Hydroxide Nanosheets: An Efficient Overall Water Splitting Electrocatalyst; *Adv. Energy Mater*. 6 (**2016**). https://doi.org/10.1002/AENM.201670063.

[18] M. Lei, H.Z. Zhao, H. Yang, B. Song, W.H. Tang, Synthesis of transition metal carbide nanoparticles through melamine and metal oxides, *J. Eur. Ceram. Soc*. 28 (**2008**) 1671–1677. https://doi.org/10.1016/J.JEURCERAMSOC.2007.11.013.

[19] H. Zhao, M. Lei, X. Chen, W. Tang, Facile route to metal nitrides through melamine and metal oxides, *J. Mater. Chem*. 16 (**2006**) 4407–4412. https://doi.org/10.1039/B611381H.

[20] D. Hirai, H. Tanaka, D. Nishio-Hamane, Z. Hiroi, Synthesis of anti-perovskite-type carbides and nitrides from metal oxides and melamine, *RSC Adv*. 8 (**2018**) 42025–42031. https://doi.org/10.1039/C8RA07581F.

[21] C. Liu, X. Tao, X. Kan, X. Liu, C. Zhang, S. Feng, Y. Yang, Q. Lv, J. Hu, M. Shezad, Spin-glass behavior in Co-based antiperovskite compound SnNCo3, *Appl. Phys. Lett*. 116 (**2020**). https://doi.org/10.1063/1.5140434.

[22] T. Scholz, A.L. Görne, R. Dronskowski, Itinerant nitrides and salt-like guanidinates – The diversity of solid-state nitrogen chemistry, *Prog. Solid State Chem*. 51 (**2018**) 1–18. https://doi.org/10.1016/J.PROGSOLIDSTCHEM.2017.04.001.

[23] T. Scholz, R. Dronskowski, Improved Ammonolytic Synthesis, Structure Determination, Electronic Structure, and Magnetic Properties of the Solid Solution $Sn_xFe_{4-x}N$ ($0 \leq x \leq 0.9$), *Inorg. Chem*. 54 (**2015**) 8800–8807. https://doi.org/10.1021/ACS.INORGCHEM.5B01510.

[24] T. Scholz, R. Dronskowski, Spin-glass behavior of $Sn_{0.9}Fe_{3.1}N$: An experimental and quantum-theoretical study, *AIP Adv*. 6 (**2016**) 055107. https://doi.org/10.1063/1.4948984.

[25] Z. Zhao, D. Xue, Z. Chen, F. Li, Preparation and Characterization of gH-Fe_3SnN, *Phys. Stat. Sol*. 174 (**1999**). https://doi.org/10.1002/(SICI)1521-396X(199907)174:1.

[26] Y. Yuan, L. Yang, B. He, E. Pervaiz, Z. Shao, M. Yang, Cobalt-zinc nitride on nitrogen doped carbon black nanohybrids as a non-noble metal electrocatalyst for oxygen reduction reaction, *Nanoscale*. 9 (**2017**) 6259–6263. https://doi.org/10.1039/C7NR02264F.

[27] Y. Goto, A. Daisley, J.S.J. Hargreaves, Towards anti-perovskite nitrides as potential

nitrogen storage materials for chemical looping ammonia production: Reduction of Co_3ZnN, Ni_3ZnN, Co_3InN and Ni_3InN under hydrogen, *Catal. Today*. 364 (**2021**) 196–201. https://doi.org/10.1016/J.CATTOD.2020.03.022.

[28] T. Yamazaki, A. Uehara, K. Kozawa, Y. Kimisima, M. Uehara, Chemical phase separation of superconductive and ferromagnetic domains in $ZnNNi_3$-XCo_x, *Adv. Condens. Matter Phys*. 2012 (**2012**) 902812. https://doi.org/10.1155/2012/902812.

[29] W.H. Cao, B. He, C.Z. Liao, L.H. Yang, L.M. Zeng, C. Dong, Preparation and properties of antiperovskite-type nitrides: $InNNi_3$ and $InNCo_3$, *J. Solid State Chem*. 182 (**2009**) 3353–3357. https://doi.org/10.1016/J.JSSC.2009.10.002.

[30] T.S. Lehmann, B. Blaschkowski, R. Niewa, Electrochemical Bulk Synthesis of Ternary Nitride Perovskites: Co_3InN and Ni_3InN, *Eur. J. Inorg. Chem.* 2019 (**2019**) 1709–1713. https://doi.org/10.1002/EJIC.201900013.

[31] Y. Liu, J. Wu, K.P. Hackenberg, J. Zhang, Y.M. Wang, Y. Yang, K. Keyshar, J. Gu, T. Ogitsu, R. Vajtai, J. Lou, P.M. Ajayan, B.C. Wood, B.I. Yakobson, Self-optimizing, highly surface-active layered metal dichalcogenide catalysts for hydrogen evolution, *Nat. Energy*. 2 (**2017**). https://doi.org/10.1038/NENERGY.2017.127.

8. Conclusion and Outlook

The work described in this thesis has investigated binary metal alloys and their ternary nitrides for the electrocatalytic activity. The solid-state methods were utilized to synthesis the products. Firstly, phase pure Co_3Mo and Co_7Mo_6 were synthesised through heating precursor of stoichiometry Co_3MoO_x or $Co_7Mo_6O_x$. The evaluation of electrochemical performance points out that Co_3Mo in the free-standing form could routinely show good catalytic performance in acidic conditions. However, the poor stability makes it a suboptimal choice as an electrocatalyst for HER compared with Co_7Mo_6, which shows a marginally higher overpotential but keeps its performance unchanged after prolonged hours of stability testing.

To obtain the catalysts with catalytic active performance and long-time durability. The cubic Co_3Mo_3N with the η-carbide type structure was prepared in a single phase by a solid-state route under H_2/N_2 gas flow, and pure Co_6Mo_6N was also obtained by annealing Co_3Mo_3N under H_2/Ar gas. The electrochemical performance of both nitrides was investigated and showed minor difference between materials. Thus, the superior performance of Co_3Mo_3N is attributed to the metal sites, and more nitrogen composition can help improve the catalysts stability. To detect which metal sites is active, the substitution of cobalt with iron to make free standard Fe_3Mo_3N was carried out. When tested electrochemically it is evident that overpotentials increased significantly. This points out that the catalytic active performance is from Co sites, which is further investigated by DFT calculation (the Co-site ($\triangle G_H \sim 0$) appears to be catalytic point). The N-content plays an important role on the stability of the catalyst, the higher nitrogen occupancy in Co_3Mo_3N allows for prolonged electrolysis. In addition, in composition of Co_6Mo_6N, the substitution of molybdenum with tungsten was carried out. Intriguingly, as noble metal free electrocatalyst, Co_6W_6N showed significantly lower overpotential, compared with the isostructural Fe_6W_6N suggesting that Co-sites are electrocatalytically active for the hydrogen evolution reaction in acidic condition. Interestingly, the higher electrochemical stability of Co_6W_6N compared with Co_6Mo_6N suggest that the presence of tungsten within the structure leads to improved catalytic performance. Co_6W_6N illustrates that a simple strategy that involved a substitution of the transition metal could help with the improvement of key catalytic properties such as catalytic activity and the stability of catalyst.

Following this discussion on ternary nitrides with the η-carbide type structure, attention was shifted to phase pure Co_2Mo_3N and Ni_2Mo_3N with the filled β-manganese structure exclusively, with focus on the study of the intrinsic activity as the electrocatalytic activity for the HER. Due

to the identical performance observed from both catalysts, the single phase samples of $Ni_{1.5}Fe_{0.5}Mo_3N$, $NiFeMo_3N$ and $Ni_{0.75}Fe_{1.25}Mo_3N$ were also prepared under the identical reaction condition. The comparison of the electrochemical performance revealed that the higher overpotentials were observed as nickel atoms were replaced by iron atoms in Ni_2Mo_3N structure. This indicated that the nickel atoms play decisive role in catalytic activity comparing to Mo and N sites.

At the same time, single phase the anti-perovskite Co_3SnN, Co_3ZnN, Co_3InN and Fe_3SnN were prepared through melamine synthesis method. The evaluation of electrochemical performance points out that the anti-perovskite Co_3SnN exhibits a low overpotential suggesting an excellent performance for the electrocatalytic water splitting. A better stability is, however, desired for this material to be applied for the hydrogen evolution reaction in alkaline media at an industrial scale.

This thesis has explored the intrinsic activity in transition metal intermetallic and ternary nitrides, beginning with the catalysts synthesis to identify the catalytic performance toward HER. Through the substitution of the elements in one type of catalysis, we have obtained a comprehensively understanding on the role of various elements played in single phase samples. Cobalt and nickel compositions as active sites usually play an important role for driving hydrogen production. Although molybdenum, nitrogen, tungsten and tin play minor role in activity, they could improve the durability of catalysts. This makes opportunities for Co_3Mo_3N, Co_6W_6N, Ni_2Mo_3N, Co_2Mo_3N, and Co_3SnN materials as electrocatalysts to be applied for the hydrogen evolution reaction in industrial. Although the OVP reported on pure Co_3Mo_3N, Co_6W_6N, Ni_2Mo_3N, Co_2Mo_3N, and Co_3SnN is slightly higher than most reported compositional materials in literature, a huge potential about applying those Co or Ni dominated nitrides for hydrogen production in a large scale when immobilized them on substrate (such as Ni foam or carbon clothes). Take Co_3Mo_3N as example, an OVP compared to Pt was observed from Co_3Mo_3N deposited on Ni foam. In short, this thesis providing further insight into the origins of electrocatalytic activity in Co or Ni dominated ternary transition metals nitrides.